Development and Assessment of a Neural Network Approach for Retrieving Aerosol Properties from Multispectral, Multiangle Polarization Measurements

by

ALEXANDRA TSEKERI

A dissertation submitted to the Graduate Faculty in Earth and Environmental Sciences in partial fulfillment of the requirements for the degree of Doctor of Philosophy, The City University of New York

2012

This manuscript has been read and accepted for the
Graduate Faculty in Earth and Environmental Sciences in satisfaction
of the dissertation requirement for the degree of Doctor of Philosophy.

Prof. Barry M. Gross

Date

Chair of Examining Committee

Dr. Yehuda L. Klein

Date

Executive Officer

Prof. Fred Moshary
Dr. Jacek Chowdhary
Prof. William Rossow
Supervisory Committee

Abstract

DEVELOPMENT AND ASSESSMENT OF A NEURAL NETWORK APPROACH FOR RETRIEVING AEROSOL PROPERTIES FROM MULTISPECTRAL, MULTIANGLE POLARIZATION MEASUREMENTS

by

Alexandra Tsekeri

Advisor: Professor Barry M. Gross

Quantifying the microphysical properties of aerosols is crucial for quantifying global climate forcings. Satellite based aerosol retrievals usually rely on intensity measurements of the scattered light, but this approach has been proven inadequate for retrieving the complex refractive index and shape of aerosols, as well as the contamination from the ground surfaces. It is with these limitations in mind that we plan to improve the quality and scope of aerosol retrievals, by making use of the full capabilities of current and future polarimetric sensor systems. In order to utilize the increased information content on aerosol optical thickness (AOT), size distribution, shape and single scattering albedo (SSA), intrinsically available in multispectral-multiangle polarimetric observations, we make use of suitably constructed neural networks (NNs). We focus our analysis initially on simple retrievals over the ocean, in order to best assess the potential of the NNs as a practical approach and to identify any possible limitations. In particular, we find that, by choosing a suitable combination of inputs and outputs, based on principal component analysis (PCA), we can develop a robust NN retrieval trained on synthetic datasets. We further show the value of using cascaded NNs, to improve

retrieval accuracy. Consequently, we demonstrate the potential and limitations of this approach on real aircraft instrument data from the Research Scanning Polarimeter (RSP). Discrepancies in the retrievals are found to be due to limitations from the use of spherical particle assumptions and preliminary efforts to overcome this restriction are identified. It is our belief that the value of these methods, in comparison to existing local inversion schemes, will further increase with the expected magnification of data sizes on future missions, such as the Aerosol-Cloud-Ecosystem (ACE) Mission.

Acknowledgments

During my graduate studies in CUNY I was very fortunate to work with Professor Barry Gross, who provided his guidance and constant support, especially during times of crisis. I hope he continues giving the opportunity to students to pursue their interests in the field, allowing them this way to grow to professionals that enjoy and appreciate their work.

I was also fortunate to be close to Dr. Jacek Chowdhary, thus having the privilege of his valuable advice on theoretical, as well as practical matters throughout my study. He stirred up my interest on the polarization retrieval techniques, reviling a path that, although more complicated, seemed to point to the right direction. And I think I am starting seeing the nice view now…

And finally, Professor William Rossow, for his guidance and help throughout the years, as well as his inspirational classes and his shattering common logic.

Lastly, I would like to thank the people who facilitated greatly the practical challenges I had to face, Dr. Kirk Knobelspiesse and Dr. Brian Cairns, for their valuable help with the codes and the datasets of the Research Scanning Polarimeter.

Table of contents

List of Tables

List of Figures

Chapter 1

Introduction

Aerosols are tiny suspended particles in the atmosphere, with sizes ranging from few nanometers to some tenths of micrometers. In order to understand the large scale effects aerosols may have on the environment and climate, it is critical to monitor their microphysical properties (like size distribution and chemical composition) and their loadings globally. Due to their high spatial and temporal variability though, effective monitoring of aerosol properties on a global scale is possible only through satellite observations [Hansen et al., 1997]. Therefore, the quality of satellite aerosol retrieval algorithms is crucial for better understanding their behavior and impact on the Earth system.

Aerosols play a very important role in the physical and chemical processes in the atmosphere, having thus a significant impact on air quality. They have been linked to heart and lung related diseases, with asthma being the most common, caused mainly by the smaller particles, which, penetrating deeper into the lung tissue, produce lung and cardiac distress [EPA, 1996]. The seriousness of their impact on human health has led EPA to provide strict guidelines on ambient

aerosol concentrations[1]. One consequence of this concern are the significant research efforts to connect satellite integrated column retrievals to surface particulate concentrations. Clearly, being able to partition more accurately aerosol loadings into fine and coarse modes, would improve current approaches, which rely mainly on AOT [Zhang et al., 2009, Szykman et al., 2004]. These issues however are not central to the climate with aspects, for which we are most concerned in this thesis.

Most central to our motivation is the fact that aerosols have also a significant effect on Earth's climate, both directly and indirectly, which is very difficult to quantify accurately. Their direct effect, depending on the class of aerosol that is being considered, is due to reflection and absorption of the incoming sunlight, causing cooling or warming, respectively, of the planet. In particular, different aerosols can have different proportions of absorption and scattering and a critical parameter for assessing their direct climate forcing is the ratio of their scattering to their total extinction (scattering + absorption) of light (i.e. SSA -see section 2.2.2.1).

In fact, in order to quantify the aerosol direct effect on the climate, it is not sufficient to look only at their extensive properties, such as the optical depth, but we need to quantify also their intensive properties, namely the size distribution, shape and chemical composition (refractive index), along with their SSA. The problem of quantifying the aerosol direct effect lies particularly on the difficulty of pulling out these intensive properties. This is the reason why the resulting error bars, associated with the direct forcings of aerosols are remarkably large (see Figure 1-1), especially in comparison to the warming forcings of the green house gases (GHGs). To decrease these uncertainties, we need to monitor the spatial and temporal distribution of

[1]EPA sets the 24-hour exposure standard at 35 μg/m^3 (http://www.dec.ny.gov/).

relevant aerosol properties over the globe, with an accuracy that can be used to assess both, Global Climate Models (GCMs) and more regional climate models.

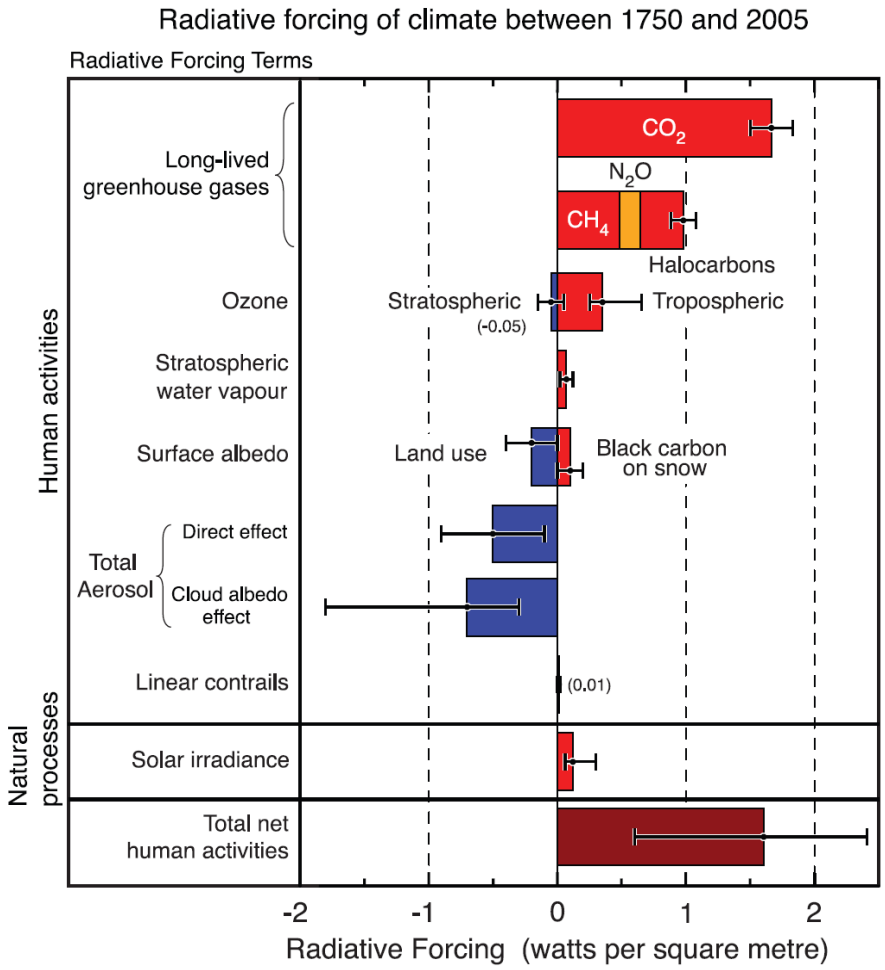

Figure 1-1. Climate forcings from different atmospheric components (source: [IPCC, 2007])

The aerosol indirect effect on the radiation balance is even more difficult to quantify. That is because it involves processes, which alter the cloud characteristics in the presence of aerosols, but, unfortunately, the mechanisms underlying these processes are not well understood yet [IPCC, 2007]. For example, aerosols can significantly "pull" water vapor from the cloud

environment resulting in a larger number of smaller water droplets upon nucleation. Therefore, aerosols tend to push the cloud droplet size distribution towards smaller droplets, which, for a given water vapor mass, results in clouds with larger albedoes and subsequent cooling of the Earth. Although quantifying the indirect effect is very difficult, better monitoring of the aerosol microphysical properties can be incorporated into cloud dynamic algorithms, in order to understand better understand its mechanisms and reduce its uncertainties [Kaufman and Koren, 2006, Lohmann and Diehl, 2006].

Comprehensive analysis of how errors in climate forcings can be connected to the uncertainties of the aerosol property retrievals, imposes severe accuracy demands and requirements on the measuring capabilities of the satellite sensors [Mishchenko et al., 2004] and on the sophistication of the retrieval algorithms (see also discussion in section 4.1.1). In particular, to achieve accuracies which can ultimately reduce the uncertainty of quantifying the aerosol effects on climate, the uncertainties in the currently retrieved aerosol properties must be reduced, while unmeasured still aerosol microphysical properties must be monitored (see Table 4-1).

Reaching these accuracies is challenging, due to both the limited capabilities of the present monitoring satellite instruments and the limitations of the applied inversion techniques. For example, the old style nadir looking intensity measurement approach is not suitable and passive radiometry sensors must ultimately provide the angular distribution and spectral variation of the total, as well as the polarized intensity of the scattered light. Actually, as

emphasized in Mishchenko et al., [2004], the required retrieval accuracies can be achieved only through synergetic algorithms, which combine passive and active remote sensing data.

This sharp increase, not only in the number of measurements, but also in the number of required retrieved parameters, makes imperative the exploration of totally unfamiliar methods for the inversion of these data, since the old inversion methods are impractical to use with such large dimensionalities. For example, for the preprocessed look-up-tables (LUTs) in a scheme like this, not only does the size of the data measurements expand geometrically, but the dimensionality of the parameters LUTs increases significantly. Besides taxing the data storage resources, the CPU demands of multidimensional interpolation become completely impractical, growing geometrically with the data size.

While current approaches are focused on optimal estimation methods, which make use of information theoretical approaches, such methods have limitations due to convergence issues, which become more severe with increasing parameter dimension, lack of information in the measurements and possible multicollinearities in the measurements and in the retrieved parameters. In addition, the required time for the retrieval increases seriously, reducing thus the real-time capacity of the inversion, especially for future polarimetric imagers.

Therefore, in order to be able to actually use all the available data in an efficient manner, we focus on more data-centered tools, such as the NN approach. Such approaches seek to develop statistical correspondences between the measurements and the aerosol parameters, based on large scale modeling of the associations connecting input measurements to the underlying aerosol parameters.

This thesis is focused on exploring the potential, and the limitations, of the NN approach for analyzing very large multiangle – multispectral polarized data. While such measurements were supposed to be available by 2011 with the launch of GLORY, which would have carried onboard the Aerosol Polarimetry Sensor (APS) [Mishchenko et al., 2007], the unfortunate failure of the mission made this impossible. We are thus forced to use existing data from the high altitude aircraft measurements of a similar instrument, the RSP [Cairns et al., 1999]. RSP provides a very good substitute for the APS approach. It is hoped, of course, it is hoped that these techniques will find use in the future launch of APS (estimated after 2014[2]) or in future planned missions, such as ACE.

In pursuing this effort, we have limited our study to oceanic retrievals, since the details of the ground contamination add a very complex level of difficulty, including the difficulties in getting clean calibration signals, making it hard to account for angular misalignments. On the other hand, ocean observations allow sun glint to make these corrections easier and turn the focus on the retrieval algorithm and not on the systemic engineering issues of the data scenes.

In this chapter, we provide the necessary background and motivation for our efforts. In section 1.1 we present the general framework about the nature of the aerosols. In section 1.2 we discuss the impact of the aerosols on the climate. In section 1.3 we continue with a discussion on the capabilities and limitations of current satellite aerosol retrieval approaches

[2] The mission is currently waiting for approval. If this happens, its launch target date will be the summer of 2014 (from personal communication with Dr. Jacek Chowdhary).

and their anticipated future improvements. We close this introduction with section 1.4, where we give a brief description of the advantages and weaknesses of the NN approach for our retrieval, along with some more specific elements about it, such as the need to preprocess the data with PCA and the configuration of the NN cascading scheme we use.

1.1. Aerosol classes

Aerosols can be natural or anthropogenic, with the first being usually larger (or "coarse") and the latter being smaller (or "fine"). The distinction between natural and anthropogenic groups is not always clear, since sometimes the processes generating the particles can be a combination of both factors. However, the attribution of the coarse size to natural aerosols and of fine size to anthropogenic aerosols is a useful preliminary classifier and such a distinction is feasible by remote sensing.

In particular, the aerosol size distribution is modeled as a log-normal bimodal distribution (see section 4.2.1) with a "fine" mode, for small particles, and a "coarse" mode, for bigger particles such as dust or sea salt (Figure 1-2). There is also a third mode, containing ultra-fine particles, which do not interact though with the light measured by the remote sensing instruments and, thus, their monitoring is not possible from space. This mode is also less relevant from a climate standpoint, since ultrafine particles accumulate rapidly into larger particles and, thus, they are not significant on a global scale. Of course, near the emission

sources these particles pose significant health risks, but this is beyond the scope of satellite aerosol monitoring.

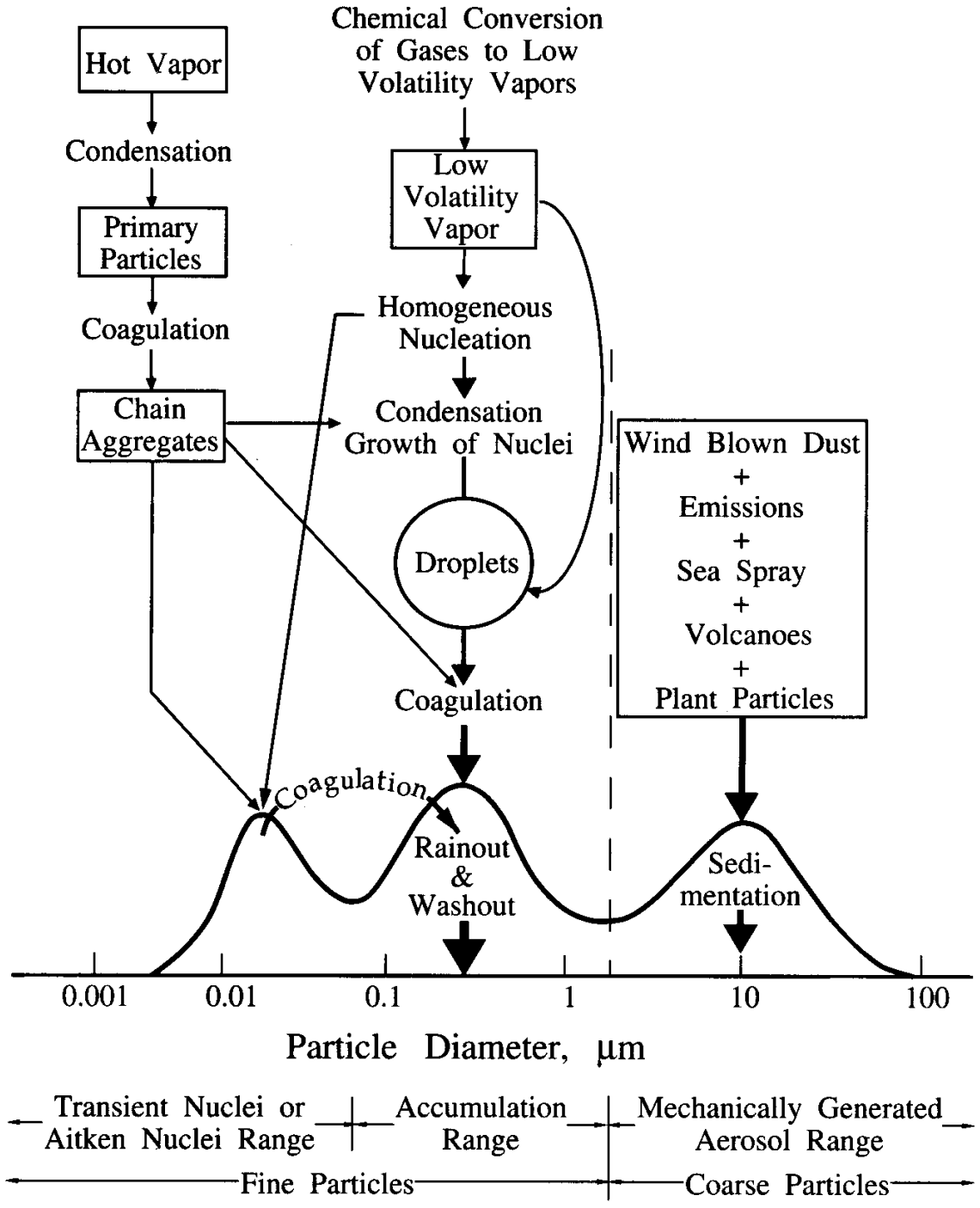

Figure 1-2. The sources and sinks of atmospheric aerosols, along with their ultrafine, fine and coarse modes of their size distribution (source: [Seinfeld and Pandis, 1998]).

Most aerosol retrieval algorithms model aerosols as homogeneous spheres with a composition expressed by a complex refractive index [Dubovik et al., 2002], despite the fact that they are usually mixtures of more than one components and they can take any shape. The sphericity assumption, in particular, can cause significant inaccuracies in the retrieved microphysical parameters, if the particle shape deviates appreciably from that of a sphere, as is the case for mineral dust aerosols [Dubovik et al., 2006]. Although the need to incorporate the particle non-sphericity in the retrieval algorithms is widely recognized, the use of non-spherical models in practical applications is limited, mainly due to their limited range of applicability and the CPU time they require to incorporate the additional degrees of freedom.

Our retrieval algorithm considers spherical particles only, since this is a quite common assumption for the aerosols above oceanic scenes. This assumption is gradually challenged though, as discussed in section 4.3.1.3 and seen from the examination of the real RSP data in chapter 5. Thus, we recognize the importance of incorporating in our retrieval the non-sphericity of the particles above oceanic scenes and this is one of our immediate future plans (see also the discussion in chapter 6).

An indicative classification of the aerosol types, based on the Intergovernmental Panel on Climate Change's Fourth Assessment Report [IPCC, 2007], is given in Appendix I.

1.2. Aerosol effect on climate

1.2.1. Aerosol direct effect

The direct effect relates to the scattering or the absorption of the incoming sunlight. When scattering occurs, the forcing posed on climate is negative, whereas for absorption it is positive, driving the Earth's temperature to lower or higher values, respectively. The estimation of the aerosol direct effect requires the knowledge of the aerosol spectral SSA, phase function and spectral optical thickness (defined in sections 2.2.1 and 2.2.2). The SSA provides the sign of the forcing (negative or positive for cooling or heating), while the phase function and optical thickness determine the magnitude of the forcing [Hansen et al., 1997].

The greatest uncertainty in quantifying the aerosol direct effect comes from the high uncertainty in the retrieval of the spectral SSA. As seen in [Mishchenko and Travis, 1997a, b], the total intensity-only measurements do not contain enough information to retrieve the SSA, while the retrievals which combine total intensity with polarized intensity measurements provide a far more accurate estimation of the SSA. Even for the latter ones though, the required accuracy is not always reached [Chowdhary et al., 2005, Waquet et al., 2009, Knobelspiesse et al., 2011a, b].

1.2.2. The aerosol indirect effect

Aerosols affect Earth's climate indirectly also, acting as cloud condensation nuclei (CCN) and, subsequently, altering the cloud properties in the atmosphere. This phenomenon is very poorly understood and its quantification comes with a very high uncertainty (Figure 1-1).

1.2.2.1 First indirect effect

The first indirect effect, or the "Twomey effect", is the increasing of the droplet number in the cloud, which results in the increasing of the cloud reflecting area and thus its albedo [Twomey, 1980]. This phenomenon produces more reflecting clouds in the atmosphere and imposes a negative forcing on the climate.

1.2.2.2. Second indirect effect

The formed cloud droplets are smaller in size, thus the cloud precipitation is suppressed and its lifetime is prolonged. This effect, together with the first indirect effect, result in more reflecting clouds that stay longer in the atmosphere, having a cooling effect on the climate.

1.2.2.3. Semi-direct effect

The semi-direct effect is the impact of the absorbing aerosols to cloud formation and dissipation. Absorbing aerosols (i.e. soot) increase the temperature of their surrounding air by re-emitting the absorbed light. Thus, the atmosphere stability is improved and the formation of clouds is suppressed. Moreover, they can also cause evaporation of the cloud droplets and dissipation of existing clouds. This phenomenon imposes then a positive forcing on the climate.

Two more indirect effects, reported in the IPCC fourth assessment report, [2007], are the "glaciation indirect effect" and the "thermodynamic effect", which are even more poorly understood. Overall, it does not seem safe to even try to quantify the indirect effect yet, since

the scientific understanding of its mechanisms is still very poor. However, as discussed above, it is certainly crucial that better aerosol microphysical properties are obtained, so that future modeling efforts can provide some guidelines into estimating how the characteristics of the aerosols can affect these mechanisms. In particular, since the research for the indirect effect is mainly focused on modelling sub-modules, in an effort to match observations of clouds and radiative properties, it is clear that the aerosol "inputs" must be as good as possible [Lohmann and Hoose, 2009].

1.3. Aerosol retrieval approaches

Satellite observations have the ability to provide a global, unperturbed and total-atmospheric-column picture of the aerosols in the atmosphere[3], which can not be achieved by any other type of measurement (like ground or *in situ* measurements). It is also quite clear that the existing satellite instrument capabilities and the subsequent algorithms used to retrieve the aerosol properties, are far from optimal, resulting to large uncertainties in aerosol monitoring, which propagate errors in the estimation of the aerosol effects on climate.

As clearly depicted in the work of Mishchenko and Travis [1997a, b], the effective aerosol monitoring is feasible only through the combination of the total intensity with the polarized intensity of light, measured in multiple wavelengths and viewing angles. In particular, measurements at the shorter wavelengths (UV, VIS) contain information about the fine particle

[3] The active satellite remote sensing instruments trace also the vertical distribution of the aerosols along the atmospheric column.

properties, whereas measurements at the longer wavelengths (NIR) contain information about the coarse particle properties. Moreover, measurements in different viewing angles provide information about the angular features of the particle scattering, which depends on the particle microphysical properties (size, shape and refractive index), as well. The spectral and angular information varies for different satellite instruments, whereas the majority of sensors do not provide polarization measurements. Thus, in order to compensate for their restricted information content, their retrievals have to rely heavily on a-priori assumptions. The use of such assumptions, though, imposes large uncertainties in the retrieved aerosol parameters, which can grow even bigger, if the intensity of light is not measured with the required radiometric accuracy [Mishchenko and Travis, 1997b].

Our algorithm, for the retrieval of the optical and microphysical properties of the aerosols in the atmosphere, is particularly well-suited for the APS approach, which combines multispectral, multiangle measurements of the total intensity and the linearly polarized intensity of light [Mishchenko et al., 2007]. As already mentioned though, the APS data will not be available before its possible future re-launch, thus, the data used in this study are taken from the RSP. The RSP has participated in many experiments and has collected a wealth of information, which have been used to evaluate the APS approach and, in more general terms, to highlight the importance of polarization measurements for aerosol retrievals [Chowdhary et al., 2001, 2002, 2005, 2006, Waquet et al., 2009, Knobelspiesse et al., 2011a, b].

1.3.1. Measuring capabilities and aerosol products of available satellite sensors

Table 1-1 presents an indicative summary of the operational aerosol retrieval approaches as presented in the IPCC fourth assessment report IPCC, [2007], ordered according to the level of increasing sensor sophistication and inversion approach.

Table 1-1. Satellite sensors for aerosol retrievals

Satellite instrument	Period of measurements	Spectral bands	Viewing angles	Polarization measurements	Retrieved aerosol parameters
AVHRR	1979 to present	0.63, 0.87, 3.7, 10.5 and 11.5 μm	1	no	AOT
TOMS	1979 to present	0.33 and 0.36 μm	1	no	AOT
MODIS	2000 to present	12 bands (0.41 to 2.1 μm)	1	no	AOT
MISR	2000 to present	4 bands (0.47 to 0.86 μm)	9	no	AOT, Ångstrom exponent
POLDER	Nov. 1996 to June 1997, Apr. 2003 to Oct. 2003, Jan. 2005 to present	8 bands (from 0.44 to 0.91 μm)	multiple	yes	AOT, Ångstrom exponent

1.3.1.1. Advanced Very High Resolution Radiometer (AVHRR) approach

AVHRR has only two channels, in the VIS and NIR, and measures only the total intensity of light along a fixed viewing angle. This approach is obviously far from optimal and it provides

only a rough estimate of the AOT at the VIS channel above the ocean [Husar et al., 1997, Ignatov and Stowe, 2002]. The AVHRR data are important nonetheless, since they provide a continuous record since 1979. The same is true for the AOT product from the Total Ozone Mapping Spectrometer (TOMS), which is retrieved above both, ocean and land [Torres et al., 2002], with a quite limited accuracy also.

1.3.1.2. Moderate Resolution Imaging Spectrometer (MODIS) approach

MODIS performs multispectral measurements of light, along twelve bands in the VIS and NIR (from 0.41 to 2.1 μm). It measures only the total intensity of light at one fixed viewing angle. From these measurements, MODIS provides the AOT above the ocean [Tanré et al., 1997] and a relatively accurate estimation of the AOT above land (except bright surfaces) [Kaufman et al., 1997].

MODIS measurements are widely used in the aerosol community. Their main advantage is their spatial and temporal resolution, as well as their broad swath coverage. Moreover, the broad multispectral capacity, including a 2.2 μm channel, makes it easier to separate ground from aerosol signals.

Furthermore, MODIS flies on the Terra and Aqua satellites on the A-train configuration [Anderson et al., 2005], which was planned to include GLORY also, thereby providing a combination of passive and active satellite instrument data, crucial for future synergetic retrievals.

1.3.1.3. Multi-angle Imaging Spectro-Radiometer (MISR) approach

MISR measures only the total intensity of light in four bands in the VIS, but it also provides angular information along nine different viewing angles. It retrieves the AOT above the ocean [Kahn et al., 2001] and land, including bright surfaces, like deserts [Martonchik et al., 2004]. It also provides an estimation of the Ångstrom exponent, as well. Furthermore, its multiangle capabilities introduce the possibility of determining the height of plumes, by looking at complex spatial patterns in multiangle configurations providing a stereo-projection approach, which, however, clearly dissipates away from the emission source [Kahn et al., 2010].

1.3.1.4. Polarization and Directionality of the Earth's Reflectances (POLDER) approach

POLDER was the first sensor, which incorporated polarization measurements from space in aerosol retrievals. It measures the total intensity and the polarized intensity of light in eight bands in the VIS (from 440 to 910 nm), along multiple viewing angles. Its main deficiency is the lack of measurements in the NIR part of the spectrum, which does not make possible the retrieval of the coarse particles properties. It also lacks measurements in the short wavelength channels (λ< 440 nm), which would resolve better the aerosol absorbing properties. Due to these limitations, POLDER retrieves only the AOT and the Ångstrom exponent above the ocean [Deuzé et al., 2000] and the AOT above the land [Deuzé et al., 2001].

1.3.2. Future aerosol retrieval approaches

1.3.2.1. Aerosol Polarimetry Sensor (APS) approach

As mentioned above, the APS is planned to provide a more complete approach towards accurate retrievals, since it combines multiangle measurements (at 255 viewing angles) of the total intensity and the polarized intensity of light, along nine bands in the VIS and NIR (from 410 to 2120 nm), with very high radiometric and polarimetric accuracy [Mishchenko et al., 2007]. Its main deficiency is its narrow swath, since it performs along-track measurements.

Until APS re-launch (estimated sometime after 2014), the RSP instrument will continue to provide data and evaluate the APS approach for retrieving the aerosol properties above ocean and land. In particular, we demonstrate that the RSP measurements can be used to successfully retrieve most of the aerosol microphysical properties (effective radius and effective variance of the size distribution, real part of refractive index) and the AOT above ocean. Other studies have also shown the capabilities of RSP for retrieving the aerosol microphysical properties and the AOT above the ocean and land [Chowdhary et al., 2001, 2002, 2005, 2006, Waquet et al., 2009]. The retrieval of the SSA is in general successful above the ocean, whereas above the land, is more uncertain [Waquet et al., 2009]. Furthermore, the ability of the RSP approach to retrieve simultaneously the oceanic characteristics and the aerosol properties has been demonstrated as well, in Chowdhary et al., [2001, 2002, 2005, 2006]. Finally, the potential of a simultaneous retrieval of aerosol and cloud properties is discussed by Knobelspiesse et al., [2011b].

1.3.2.2. Aerosol Cloud Ecosystems Mission (ACE) approach

ACE is a future mission (estimated launching in 2021), which will carry on board passive and active instruments [Starr, 2011]. For aerosol monitoring, it will use an imaging polarimeter, with multispectral, multiangle measuring capabilities and a High Spectral Resolution Lidar (HSRL), which will provide the vertical distribution of the particles. Its polarimeter will be different from APS, in that it will provide measurements in the UV part of the spectrum, as well as a broader swath (~400 km), resulting in a better temporal resolution. Although the spatial and temporal resolution will be an improvement over the APS approach, the measuring accuracy of the imager is expected to be much lower. As highlighted by Mishchenko and Travis, [1997b], the radiometric and polarimetric accuracy of the measurements is of great importance for the stability and uniqueness of the retrieval. Since the polarimeter on ACE mission is still in a configuration stage [Diner et al., 2010], it remains to be seen on what extent this will pose limitations on retrieval accuracy.

1.4. The inversion method as an important component of the aerosol retrieval algorithm

Much attention is given to the information content of the different aerosol retrieval approaches, whereas the importance of the inversion method, used in the corresponding algorithms, is somehow underplayed. This is so, because the vast majority of the inversion problems are solved with the LUT method or the optimal estimation technique, which are used as a panacea, in some cases. As we discuss in detail in chapter 3 though, these methods grow

unwieldy and slow and raise serious convergence issues as the retrieval dimensions are increased, with the inclusion of multispectral, multiangle polarization information. Conversely, the NN approach is able to handle the very large number of variables in the retrieval, without the time and convergence issues of the traditional approaches. However, the NN approaches are not free of major issues and limitations, which we hope to identify and in some sense address.

1.4.1. Comparison of neural networks with traditional inversion methods

The main advantage of the NN method against more conventional approaches is the NN capability to produce real-time retrievals, achievable even for quite large schemes. More specifically, the NNs calculate the inverse function of the retrieval, which applies to all cases, whereas the LUT and the optimal estimator match the aerosol properties to corresponding light measurements for every case separately. Thus, for the NNs, although the calculation of the inverse function may require considerable time, after it is done, makes the retrieval instantaneous, whereas the traditional methods need to reconstruct their "search" scheme for every case, making real-time retrievals for large data scenes very difficult and resource intensive (section 3.1.1).

Furthermore, for such ill-posed problems as the one considered here, the optimal estimator depends heavily on the quality of the first guess, whereas that is not true for the NN (although the first guess certainly helps the NN retrieval [Aires et al., 2001, 2004]) (section 3.2.5). Another disadvantage of the optimal estimator method is that we usually have to make the unavoidable

assumption of constant covariances throughout the parameter space, which makes the retrieval uncertainty estimates somewhat douptful.

1.4.2. Neural network weaknesses

Although we believe that the NN method should be strongly considered as an operational approach for extracting inversion parameters for large scale data sets, like the one considered in this study, its implementation does not come without concerns. The most important issue is the suitable construction of the training dataset (which is used for calculating the inverse function) and the control of its quality. In particular, the calculated inverse function and, for that matter, the NN retrieval, is only relevant within the training dataset space. Thus, in order for the NN to work on real-world cases, it is imperative to make sure that the training dataset takes into account the real-world variability (section 4.3.1.3).

Also, the NNs lack a straightforward way for assessing their output uncertainties (section 3.2.4). Although the NN testing provides an estimate of the output uncertainties, these are only relevant within the testing space, which is not always representative of the real-world cases (chapter 5).

Finally, although the NNs provide real-time retrievals, their training can be quite long. This is unfortunate, since it poses limitations in exploring the NN range of possible realizations for different input/output configurations, training algorithms, architectures and so on.

1.4.3. Data preprocessing with PCA

In any regression scheme, possible redundancies in both the measurement space and the parameter space must be considered, since these issues magnify the ill-poseness of the problem. We try to eliminate these problems using the PCA, which is mostly known as a method for extracting "meaningful" components from a dataset, but it can also be used as a data compression method. This is a very important preprocessing step for our inversion scheme, resulting in the elimination of multicollinearities and the denoising of the data and thus the subsequent increase in performance and robustness of our retrieval (section 3.2.6.1).

The calculated components from PCA are usually a mixture of the original variables. Thus, we need to be cautious against indiscriminate mixing of variables that have different properties (e.g. different physical characteristics). Finally, in order to test the effect of the PCA on the robustness of our retrieval, we examine the NN internal structure by using the NN jacobians (section 3.2.7).

1.4.4. Neural network cascading scheme

The NN retrieval can be further refined by a cascading scheme, with the output from the first NN to be fed into the input of the second NN. This scheme results in an overall better behaving inversion, since the guidance from the first NN seems to suppress particularly erratic behavior in the second NN, especially for the variables which are difficult to retrieve (section 3.2.8.1). Moreover, it can speed up considerably the training of the second NN and, thus, facilitate the exploration of different configurations for it.

Summarizing, the NN technique, as any other technique, along with its advantages has also limitations, which for the most part though, do not affect the quality of the retrieval. The only exception is the NN dependence on the properties of the training dataset, which usually results in narrowing the range of their applicability. One critical example presented in this study, is restricting the content of our training dataset to spherical particles only.

Overall though, we believe that the NNs provide a potentially superior method for handling the multivariate inversion problem of satellite retrieval algorithms, since they are inherently configured to handle the explosion of data sizes to be expected in future retrievals.

Chapter 2

Theoretical background

The remote sensing of aerosol uses the scattered light from a passive light source (e.g. the sun) to infer the aerosol properties. In particular, the modification of the light characteristics, including angular structure and polarization state during the scattering process, provides "indirect" information on the aerosol microphysical structure. These modifications depend strongly on the light wavelength, therefore, sensors which can provide multispectral polarized measurements at different observation angles, are expected to provide the most detailed and accurate information on aerosols. Of course, to properly utilize the complex data sets, mathematical models which invert the top of atmosphere (TOA) return signal for any geometry, wavelength and vertical structure of the atmosphere must be developed. These models, in addition to the fundamental interactions of light with the aerosols themselves, will also account for further interactions with the surrounding molecular atmosphere as well as the interaction with the ocean or land surface.

Clearly, before we attempt to analyze the measurements from any given sensor, it is important to thoroughly understand all the relevant interaction mechanisms thereby constructing a "forward" model, that takes the state description of the atmosphere (i.e aerosol model parameters, observation geometry, ancillary data) and generates the expected

measurement signal vector. In general, the light propagating through a medium, undergoes absorption, emission and/or scattering. In dense media (such as liquids and solids) these processes are quite complicated due to the close proximity of their constituents and their consequent interactions are thereby coherent (i.e. superposition of fields). For the case of scattering, coherent superposition on a microscopic level is manifested macroscopically in the form of reflection and refraction and depends mainly on the frequency, angle of interaction and polarization state of the light in reference to the target plane [Hecht, 2001]. On the other hand, for rarified media (i.e. atmosphere) where the individual light-matter interaction distances are much larger than the wavelength, the scattering process can be described based on a combination of microscopic level incoherent far-field scattering events. In this description, the far-field scattered intensity is a complex but calculable function of the frequency of light relative to the size, as well as the shape and the chemical composition (or more to the point the complex refractive index), of the individual constituents of the medium.

In our study, which considers the retrieval of aerosol properties over the ocean, we must account for the modifications of the VIS and the NIR light, under the following interactions:

1. Absorption and scattering from the atmospheric gases and aerosols.
2. Reflection from the ocean surface.
3. Scattering and absorption from the constituents of the ocean body.

2.1. Absorption in the atmosphere

Light, propagating through the atmosphere, is absorbed by molecular gases and to some extent by aerosols. The selective absorption of the atmospheric molecules in the VIS and the NIR spectrum, gives rise to the characteristic absorption lines (and their aggregation to wider absorption bands) of the transmitted light spectra (Figure 2-1). Absorption in the VIS is due to electronic transitions, whereas in the NIR, it is due to vibrational and combinations of vibrational and rotational transitions. The absorption spectrum features can be very useful in remote sensing, since they provide information about the concentration of the atmospheric gases, along with temperature and pressure profiles of the atmosphere.

However, gaseous absorption constitutes an obstacle for aerosol remote sensing. Therefore, great effort is made in aerosol retrieval channel selection to be far from any significant gas absorption resonances. These low absorption channels are typically identified as so-called spectral “windows”, where the atmosphere is relatively transparent. While many aerosols do not have any significant absorption and mainly scatter light, some aerosols such as biomass burning aerosols, can have significant absorption. However, these aerosols do not absorb as gases, with their absorption being closer to a continuum (as with condensed matter), than to sharp lines or bands. The general atmosphere transmission structure as a function of wavelength can be seen in Figure 2.1. In the spectral domain where aerosol scattering is important, the main resonances to avoid are the water vapor resonances in the NIR and ozone in the UV. On the other hand, we see a degradation of the atmosphere transmission in the VIS

channels which increases with smaller wavelength. This feature is not due to absorption, but due to molecular (Rayleigh) scattering, which has a λ^{-4} power law dependence.

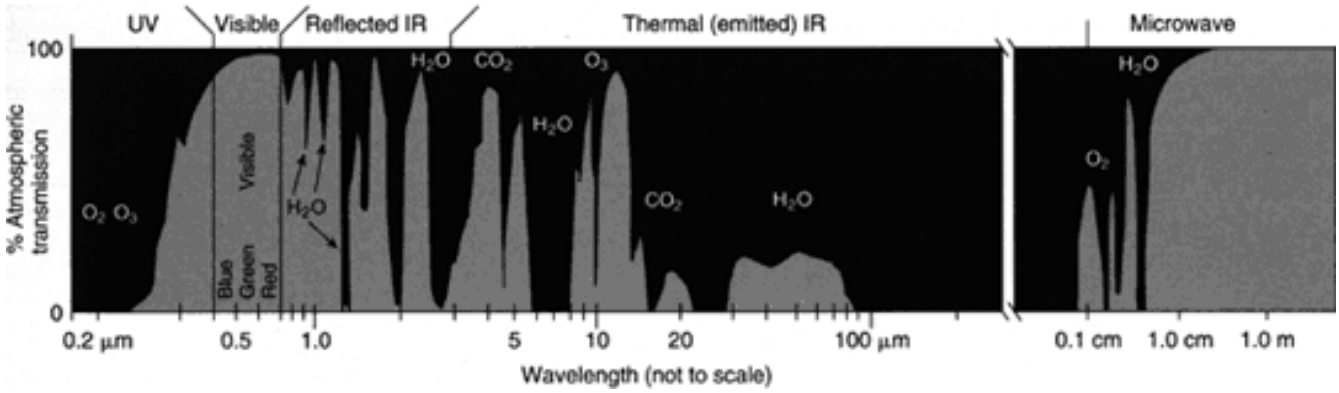

Figure 2-1: Solar transmission of the atmosphere column including spectral windows (source: http://earthobservatory.nasa.gov/Features/RemoteSensing/remote_04.php).

2.2. Scattering in the atmosphere

Scattering is the angular redistribution of the intensity of an incident light beam, together with a possible modification of its polarization state, depending on the angle of the scattered photon. The intensity of scattered light depends critically on the size, shape and refractive index of the target, as well as, on the angle of scattering and the initial polarization state.

To quantify this process, we first must introduce a convenient way of describing the polarization of the beam. In particular, the polarization state expresses the amplitude and phase differences between the orthogonal electric field components. First, we write the electric field as the sum of its components $\vec{E}_x$ and $\vec{E}_y$ along the x- and y- axes on its vibration plane:

$$\vec{E}(\vec{z},t) = \vec{E}_x(\vec{z},t) + \vec{E}_y(\vec{z},t) \qquad (2\text{-}1)$$

where $\vec{z}$ is the position vector along the propagation direction ($\vec{x}$ and $\vec{y}$ are perpendicular to each other and to $\vec{z}$). The incident light is usually considered as a plane wave so that:

$$\vec{E}_x(\vec{z},t) = \vec{x}E_{ox}e^{i(\omega t - k\vec{z} - \delta_x)} \tag{2-2-1}$$

$$\vec{E}_y(\vec{z},t) = \vec{y}E_{oy}e^{i(\omega t - k\vec{z} - \delta_y)} \tag{2-2-2}$$

where k is the wavenumber $\left(k = \frac{2\pi}{\lambda}\right)$. E_{ox} and E_{oy} are the amplitudes of the x- and y- electric field components and δ_x and δ_y are their phases.

Since field quantities such as $\vec{E}_x$ and $\vec{E}_y$ cannot be measured easily by conventional instruments, in order to quantify the complete state of polarization, we use the four so called Stokes parameters, which can be obtained from intensity measurements and are related to $\vec{E}_x$ and $\vec{E}_y$ above as:

$$I = \langle \vec{E}_x\vec{E}_x^* + \vec{E}_y\vec{E}_y^* \rangle = \langle E_{ox}^2 + E_{oy}^2 \rangle \tag{2-3-1}$$

$$Q = \langle \vec{E}_x\vec{E}_x^* - \vec{E}_y\vec{E}_y^* \rangle = \langle E_{ox}^2 - E_{oy}^2 \rangle \tag{2-3-2}$$

$$U = \langle \vec{E}_y\vec{E}_x^* + \vec{E}_x\vec{E}_y^* \rangle = 2\langle E_{ox}E_{oy}cos(\delta_x - \delta_y) \rangle \tag{2-3-3}$$

$$V = i\langle \vec{E}_x\vec{E}_y^* - \vec{E}_y\vec{E}_x^* \rangle = 2\langle E_{ox}E_{oy}sin(\delta_x - \delta_y) \rangle \tag{2-3-4}$$

where "$*$" denotes the conjugate of a complex number and the bracket average is over the time of the measurement, which is much longer than the period of the electromagnetic wave. Here I is the total light intensity, Q and U define the intensity of light that is linearly polarized along the x- or y- axis and along an axis at an angle of ±45° with respect to the y- axis, respectively, while V is the circularly polarized light intensity. The quantity $I_p = \sqrt{Q^2+U^2+V^2}$ is analogous to the intensity of the total polarized light and the quantity $I_{lp} = \sqrt{Q^2+U^2}$, to the intensity of the linearly polarized light. Furthermore, the ratios $DP_p = \frac{I_p}{I}$, $DP_{lp} = \frac{I_{lp}}{I}$, $DP_{cp} = \frac{|V|}{I}$

give the degree of the total, linear and circular polarization, respectively. For 100% polarized light $I^2 = Q^2+U^2 + V^2$, while for partially-polarized light $I^2 \geq Q^2+U^2 + V^2$.

The Stokes parameters are very useful for characterizing the time averaged electric field of an electromagnetic wave and they can be organized as a four component column, the Stokes vector (denoted from now on with a bold $\boldsymbol{I}$).

$$\boldsymbol{I} = \begin{bmatrix} I \\ Q \\ U \\ V \end{bmatrix} \tag{2-4}$$

For unpolarized light , $I = 1,\ Q = U = V = 0$ and the Stokes vector (normalized to Stokes parameter I) is

$$\boldsymbol{I} = \begin{bmatrix} 1 \\ 0 \\ 0 \\ 0 \end{bmatrix} \tag{2-4-1}$$

The unpolarized character of light does not imply that its electric field does not have a given orientation at any specific time, but that it is comprised of a number of electric fields with random polarizations, which have a zero average over the measurement time, leaving the light with no preferred polarization state. Sunlight is a good example of unpolarized light.

A geometric representation of the polarization state using the Stokes parameters is given by the polarization ellipse, which traces the endpoint of the electric field vector. If a and b are the ellipse semimajor and semiminor axes, then:

$$tan\beta = \pm {}^{b}/_{a} \quad \left({}^{-\pi}/_{4} \leq \beta \leq {}^{\pi}/_{4}\right) \tag{2-5}$$

where β is its ellipticity. For $\beta = 0$ the light is linearly polarized, for $\beta < 0$ is left-circularly polarized and for $\beta > 0$ is right-circularly polarized.

Having introduced a means of mathematically quantifying the polarization state, we can consider the angular scattering of a particular light wave and its effect on the incident Stokes vector.

2.2.1. Single scattering approximation

The Stokes vector changes when the light is scattered by the constituents of a medium. The process of scattering is quite involved, especially for dense media whose constituents scatter the external electric field along with the scattered electric field generated from their neighbors. Fortunately, the scattering in atmospheres considered here, is simpler and may be treated as an incoherent process, allowing us to use intensity formulations (i.e. Stokes vector). For a volume element with sufficiently low density, such that its constituents act as discrete scatterers or, in other words, they interact only with the external electric field, a single scattering event only occurs between the solar (incoming) photon and the return photon (single scattering approximation[4]).

The independent scatterers in the volume element generate a new scattered field, which behaves as a spherical wave in the far-field and can be described as:

$$\vec{E}_{sca} = \frac{e^{-ikR+ikz}}{ikR} S(\Theta, \psi) \cdot \vec{E}_{inc} \tag{2-6}$$

where R is the distance of the volume element from the detection point and the 2×2 matrix amplitude matrix [Hovenier et al., 2004]

$$S(\Theta, \psi) = \begin{bmatrix} S_{11}(\Theta, \psi) & S_{12}(\Theta, \psi) \\ S_{21}(\Theta, \psi) & S_{22}(\Theta, \psi) \end{bmatrix} \tag{2-6-1}$$

[4] In reality, instead of the single scattering approximation, the far-field modified uncorrelated single scattering approximation is used, since the forward-scattering interference is neglected [Mishchenko et al, 2006].

depends on the wavelength and direction of the incident light, as well as the size, shape and refractive index of the scatterer, averaged over all its possible orientations. The scattering angle Θ is the angle between the incident and scattered beams and ψ is an azimuth angle measured about the scattering direction. For spherical particles the amplitude matrix is simplified to

$$S(\Theta,\psi) = \begin{bmatrix} S_{11}(\Theta,\psi) & 0 \\ 0 & S_{22}(\Theta,\psi) \end{bmatrix} \quad (2\text{-}6\text{-}2)$$

Using next the Stokes vector formalism, we define the "scattering matrix of the particle" $F^p(\Theta)$ as:

$$\boldsymbol{I}_{sca}^{p} = \frac{1}{k^2R^2} F^p(\Theta) \cdot \boldsymbol{I}_{inc} \quad (2\text{-}7)$$

This formula is defined with respect to the "scattering plane", formed by the incident and the scattered light beams. The $F^p(\Theta)$ matrix is a 4×4 matrix, whose elements are calculated from the amplitude matrix elements (for a more detailed formulation see Hovenier et al., [2004]). The scattering matrix $F(\Theta)$ of the whole volume element, is proportional to the sum of the scattering matrices of its individual particles[5], according to:

$$F(\Theta) = \frac{4\pi}{k^2 k_{sca}} \sum F^p(\Theta) \quad (2\text{-}8)$$

and the Stokes vector of the scattered light from the volume element dV, can be estimated from:

$$\boldsymbol{I}_{sca} = \frac{k_{sca} dV}{4\pi R^2} F(\Theta) \boldsymbol{I}_{inc} \quad (2\text{-}9)$$

where

$$k_{sca} = \frac{\sigma_{sca}}{dV} = \frac{1}{dV} \sum \sigma_{sca,i} \quad (2\text{-}9\text{-}1)$$

[5] For the averaging assumptions of the single scattering approximation to be valid, we consider that the movements of the volume element constituents are random and uncorrelated to each other [Mishchenko et al., 2002].

is the scattering coefficient of the volume element and $\sigma_{sca,i}$ is the scattering cross-section of the scatterer i in the volume, defined as the area containing an incident light energy equal to the energy scattered from the particle.

Similarly, we define the absorption coefficient as $k_{abs} = \frac{1}{dV}\sum \sigma_{abs,i}$ and the total extinction coefficient as:

$$k_{ext} = k_{sca} + k_{abs} = \frac{1}{dV}\sum \sigma_{ext,i} \tag{2-10}$$

The scattering matrix can be much simplified, if the scattering volume is macroscopically isotropic and mirror-symmetric. This is true for mediums containing spherically symmetric and/or randomly oriented non-spherical particles with a plane of symmetry and/or their mirror counterparts in the volume [Mishchenko et al., 2006]. These conditions are generally true for Earth's atmosphere and its scattering matrix takes the following form:

$$F(\Theta) = \begin{bmatrix} a_1(\Theta) & b_1(\Theta) & 0 & 0 \\ b_1(\Theta) & a_2(\Theta) & 0 & 0 \\ 0 & 0 & a_3(\Theta) & b_2(\Theta) \\ 0 & 0 & -b_2(\Theta) & a_4(\Theta) \end{bmatrix} \tag{2-11}$$

In particular, for the special case of a medium containing only spherical particles (as the simulated atmospheric scenes considered in this study), the scattering matrix is simplified even more, with $a_1 = a_2$ and $a_3 = a_4$. The first element, a_1, is the "phase function" and is of special interest, since it describes the angular distribution of the total intensity of the scattered light, when the incident light is unpolarized, as is the case with sunlight.

2.2.1.1. Rayleigh scattering

The formulas for the scattering matrix elements are not simple, since the scattering from particles is a complicated function of their refractive index and of the relationship between their size and the wavelength of the incident light. This relationship is expressed by the "size parameter" x ($x = \frac{2\pi r}{\lambda}$, with r the radius of the particle). In very general terms, the scattered light is generated by the vibration of the electric dipoles and multipoles induced by the incident light field on the particle. Particles much smaller than the wavelength ($x \ll 1$) behave effectively as dipoles, generating a fairly simple scattered field, which is described by Rayleigh scattering. In the atmosphere, the atmospheric gases and smaller aerosols give rise to Rayleigh scattering for the VIS and NIR light, respectively. The scattering matrix in this case takes the following form [Hansen and Travis, 1974]:

(2-12)

$$F(\Theta) = \Delta \begin{bmatrix} \frac{3}{4}\left(1+cos^2(\Theta)\right) & -\frac{3}{4}sin^2(\Theta) & 0 & 0 \\ -\frac{3}{4}sin^2(\Theta) & \frac{3}{4}\left(1+cos^2(\Theta)\right) & 0 & 0 \\ 0 & 0 & \frac{3}{2}cos(\Theta) & 0 \\ 0 & 0 & 0 & \Delta'\frac{3}{2}cos(\Theta) \end{bmatrix} + (1-\Delta)\begin{bmatrix} 1 & 0 & 0 & 0 \\ 0 & 0 & 0 & 0 \\ 0 & 0 & 0 & 0 \\ 0 & 0 & 0 & 0 \end{bmatrix}$$

with $\Delta = \frac{1-\delta}{1+\delta/2}$ and $\Delta' = \frac{1-2\delta}{1-\delta}$, where the depolarization factor δ expresses the deviation from pure isotropic Rayleigh scattering ($\delta = 0$) to more anisotropic cases ($0 < \delta \leq 0.5$). Some indicative values for the main atmospheric gases are $\delta_{N_2} \approx 0.03$, $\delta_{O_2} \approx 0.06$ and $\delta_{CO_2} \approx 0.09$ [Penndorf, 1957].

2.2.1.2. Mie scattering

The scattering from particles with sizes of the order or bigger than the wavelength ($x \sim 1$) is more involved, due to the appearance of vibrating electric and magnetic multipoles within the particles. This complication when the particle size becomes significant in comparison to the wavelength, arises from the fact that the field within the particle is no longer constant, but has a spatial modulation. For spherical particles, as is the case here, Mie theory provides an exact description of the generated scattered field by applying the Maxwell boundary conditions between the incident, the internal and the scattered field at the spherical surface boundary. According to Mie theory, the scattering matrix of a particle is calculated from the elements of its amplitude matrix, as follows (the scattering angle is omitted for simplification) [Van de Hulst, 1957]:

$$F^p = \begin{bmatrix} \frac{S_{11}S_{11}^* + S_{22}S_{22}^*}{2} & \frac{S_{11}S_{11}^* - S_{22}S_{22}^*}{2} & 0 & 0 \\ \frac{S_{11}S_{11}^* - S_{22}S_{22}^*}{2} & \frac{S_{11}S_{11}^* + S_{22}S_{22}^*}{2} & 0 & 0 \\ 0 & 0 & \frac{S_{11}S_{22}^* + S_{22}S_{11}^*}{2} & \frac{i(S_{11}S_{22}^* - S_{22}S_{11}^*)}{2} \\ 0 & 0 & -\frac{i(S_{11}S_{22}^* - S_{22}S_{11}^*)}{2} & \frac{S_{11}S_{22}^* + S_{22}S_{11}^*}{2} \end{bmatrix} \quad (2\text{-}13)$$

with

$$S_{11} = \sum_{n=1}^{\infty} \frac{2n+1}{n(n+1)} [a_n \pi_n + b_n \tau_n] \text{ and } S_{22} = \sum_{n=1}^{\infty} \frac{2n+1}{n(n+1)} [b_n \pi_n + a_n \tau_n] \quad (2\text{-}13\text{-}1)$$

where π_n and τ_n are functions of the scattering angle and the coefficients a_n and b_n are functions of the refractive index and the size parameter of the particle. More specifically, a_1, a_2, a_3, … denote the radiation generated by the induced electric dipoles, quadrapoles, octupoles and so on, respectively. Similarly, b_n denote the radiation generated by the corresponding induced magnetic multipoles in the particle [Hansen and Travis, 1974].

In the atmospheric scenes considered in this study, VIS and NIR light undergoes Mie scattering from spherical aerosols with sizes ranging from 0.1 μm, up to 20 μm. The scattering from non-spherical particles of similar size is much more complex and the resultant numerical techniques are much more time-consuming. Some of the common approximations used for non-spherical particles calculations are the T-matrix method [Mishchenko et al., 1996], the discrete dipole approximation [Purcell and Pennypacker, 1973], the finite difference time domain method [Yee, 1966] and, for bigger particles, the geometrical optics approach (GOA) [Yang and Liou, 1996].

The total and polarized intensity of the scattered light from large spheres ($x \gg 1$), present some distinct features. For the total intensity, we can see primary and secondary rainbows at $\Theta{\sim}150^o$ and $\Theta{\sim}120^o$ respectively, with their actual angular position subject to change with the refractive index of the particles (Figure 2-2). For the polarized light, these features are manifested as steep ridges of positive polarization, resulting from internal reflection of light in the spherical particles (one internal reflection for the primary and two internal reflections for the secondary rainbow) [Hansen and Travis, 1974]. Due to the strong dependence of the rainbows on the geometry of the particles, whenever such features are detected, they are a strong indication of the spherical shape of the particles. Another feature of the scattered light from large particles is the glory at the backscattering direction ($\Theta{\sim}180^o$), which though is independent from the particle shape. These characteristic scattering features are quite pronounced in the region of geometric scattering and they vanish gradually as the size parameter becomes smaller, towards Rayleigh scattering regime. They are present to some

extend in the Mie scattering range, but their formation there, is a more complicated function of the size parameter and the refractive index of the scatterer.

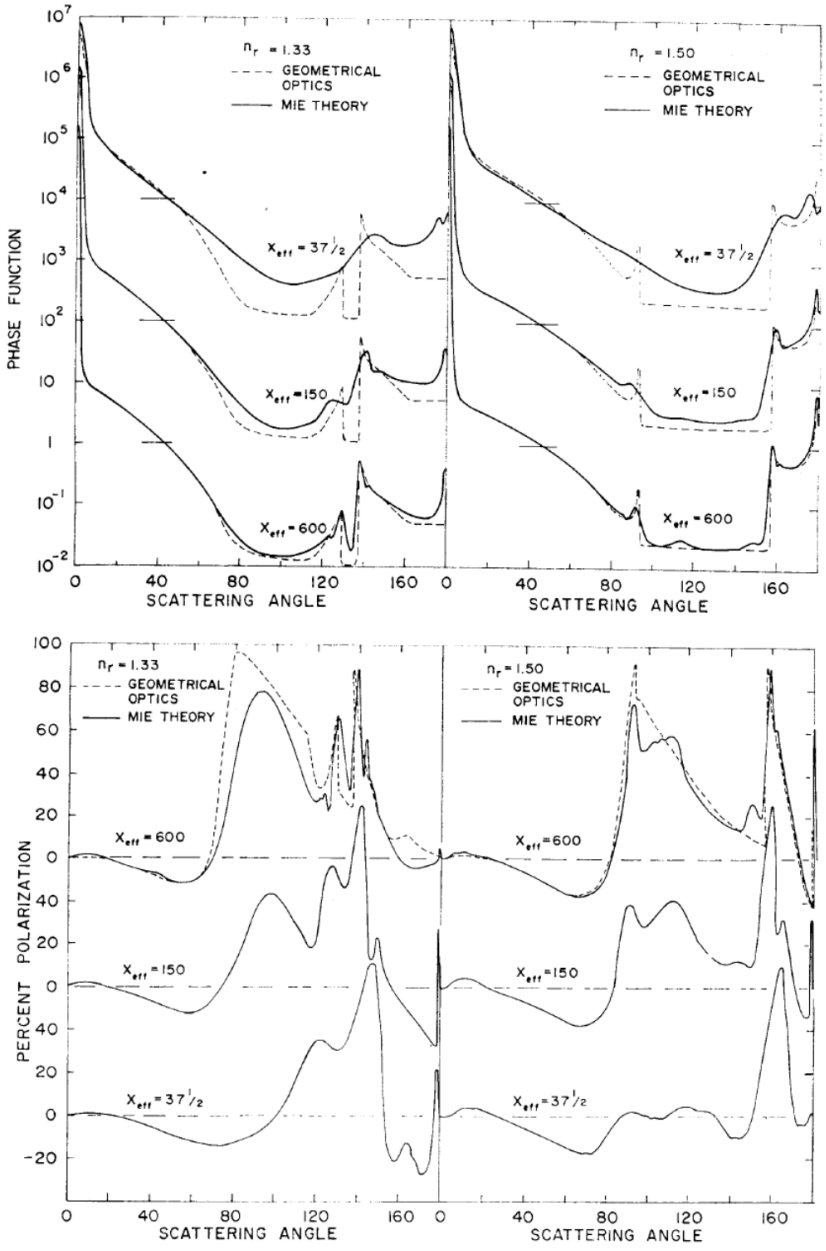

Figure 2-2: The scattering features of the primary and secondary rainbows and the glory in the phase function (first row) and the degree of polarization (second row) of the single-scattered

light from groups of particles of different effective size parameters (see definition in section 4.2.1.) and refractive indices, simulated by Mie theory and geometric optics (source: [Hansen and Travis, 1974]).

When we compare the dependence of the polarized intensity of scattered light on the size parameter and the refractive index of the particles, with the analogous dependence of the total intensity on the same particle characteristics, we see a clear difference in terms of the variability in scattering features. In Figure 2-3a, the total intensity scattered from a volume element, presents much less variability for different size parameters and refractive indices than the degree of linear polarization in Figure 2-3b [Mishchenko and Travis, 1997a]. From this comparison it becomes apparent that total intensity measurements of scattered light, contain much less information for the size and the refractive index of the aerosols, than polarized intensity measurements. It is thus of foremost importance to use, when possible, both total and polarized intensity measurements of light, in order to develop effective aerosol microphysical parameter retrievals.

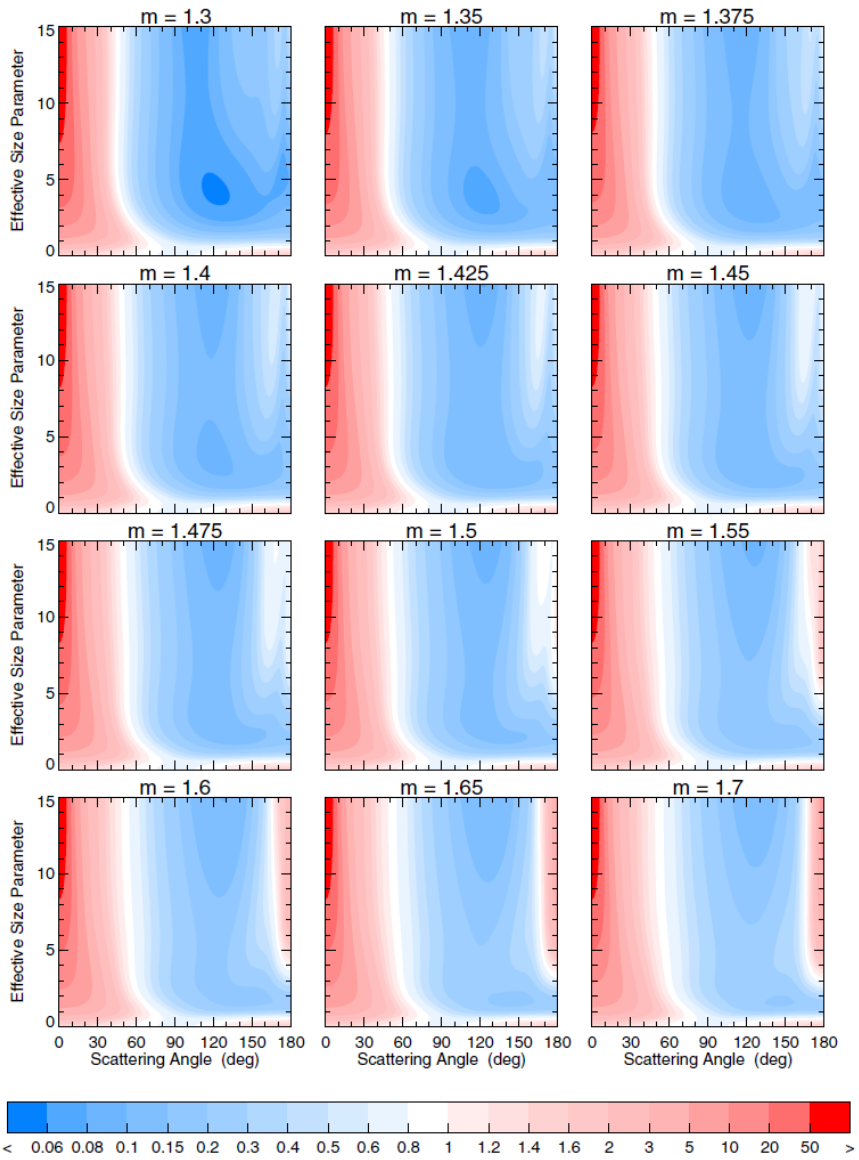

a.

Figure 2-3. The phase function (a) and the degree of linear polarization (b) of single-scattered light from groups of spherical particles of different effective size parameters and refractive indices in the range of 1.3 to 1.7 (source: [Mishchenko and Travis, 1997a]).

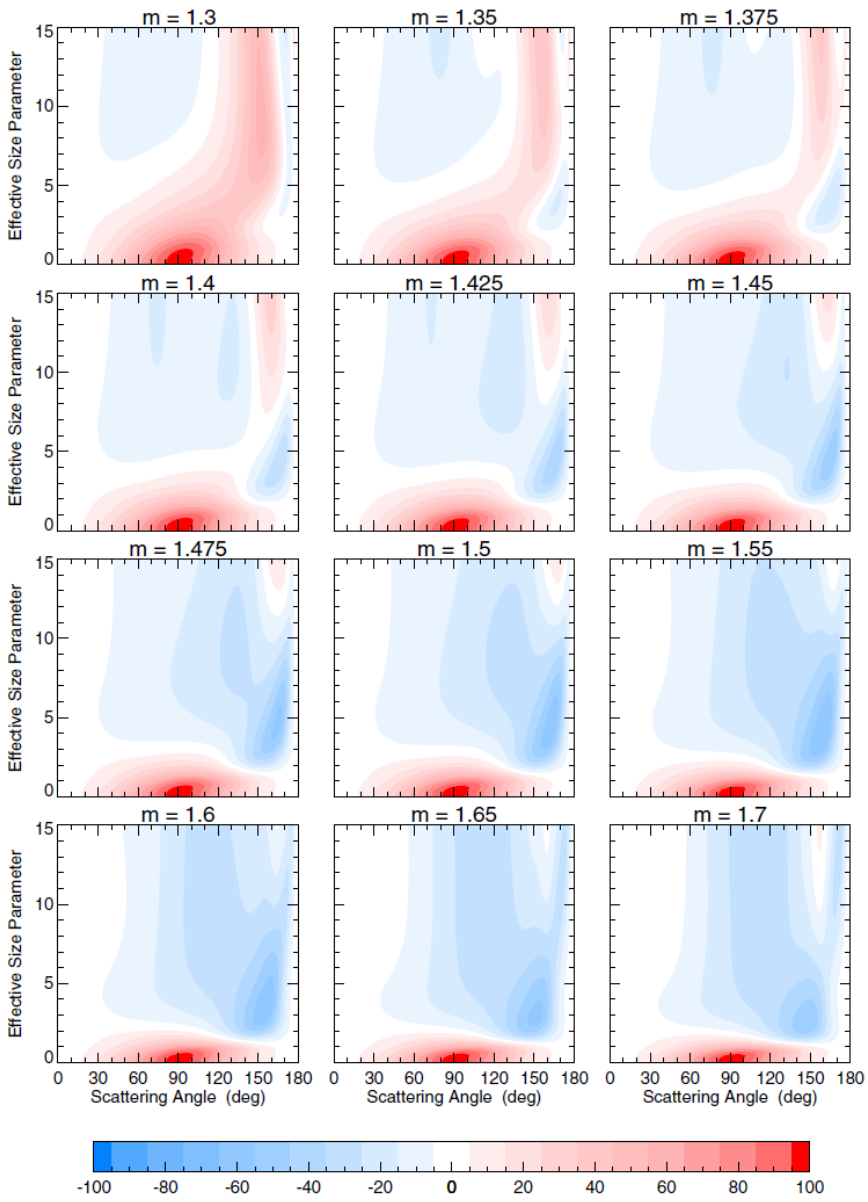

b.

Figure 2-3. (Continued)

2.2.2. Multiple scattering

2.2.2.1. The vector radiative transfer of light in the medium: the adding and doubling method

For many cases, the photons will scatter multiple times and it is clear that to account for such processes, a more sophisticated numerical model is needed than the single single scattering treatment section 2.2.1. Building on the volume element scattering concept, we can formulate the vector radiative transfer of light through the whole atmosphere, taking into account the multiple scattering that occurs in it. An accurate method to calculate the multiple scattering is the so-called *adding and doubling method* [Van de Hulst 1963, 1980, Hansen 1969, 1971a, b, De Haan et al*.,* 1987, Hovenier 1971]. In our study we use the adding and doubling vector radiative transfer code developed from Dr. Brian Cairns, that models the RSP measurements, based on the work of De Haan et al., [1987].

In the adding and doubling method, the atmosphere is comprised of multiple horizontally homogeneous (plane-parallel) layers, each of which can have different aerosol particles. In every layer the light can be scattered multiple times, so the method divides it into very fine sub-layers, which are so optically thin ($\tau \ll 1$), that the light propagating through them undergoes one (single scatter approximation) to two scattering events. The scattering from every homogeneous layer of the atmosphere is the cumulative result of scattering within its individual sub-layers and at the interfaces between them.

Starting with two such optically thin layers in contact, the reflection and transmission matrices for the combined layer they form are calculated as functions of the reflection and transmission matrices of the individual layers. The scattering properties of the layers are easy to calculate analytically, since the incident light experiences one to two scattering events. In the

next step, the same procedure is used to calculate the reflection and transmission matrices of the combined layer from two such double layers in touch. This same procedure is repeated for the combined layer from two four-fold layers in touch, calculated in the previous step, and so on, till the final combined layer coincides with the specific optical depth needed for a given homogenous layers of the atmosphere. After the different individual homogeneous layers are calculated, an adding procedure between distinct homogeneous layers of the atmosphere in contact is implemented. The reflection and transmission properties of the whole atmosphere are calculated, finally, by adding all the homogeneous layers of the atmosphere.

Furthermore, the surface contribution can be included within this scheme by considering the surface as a semi-infinite layer with its own reflection characteristics [Hovenier et al., 2004].

The scattering geometry of the plane-parallel atmosphere is described using the vertical axis z, with its positive direction extended upwards, the angle θ, measured from the positive direction of z and the azimuth angle ϕ, measured clockwise looking towards the positive direction of z (Figure 2-4). Furthermore, to simplify equations, instead of θ we sometimes use $u = -cos(\theta)$ or $\mu = |u|$, with $-\mu$ denoting the upward direction and μ the downward direction. In this geometry, the scattering angle Θ is defined as following:

$$cos(\Theta) = cos(\theta_{view})cos(\theta_{sun}) + sin(\theta_{view})sin(\theta_{sun})cos(\phi_{view} - \phi_{sun}) \qquad (2\text{-}14)$$

where θ_{view} and θ_{sun} are the polar angles and ϕ_{view} and ϕ_{sun} are the azimuthal angles of the sensor and the sun respectively.

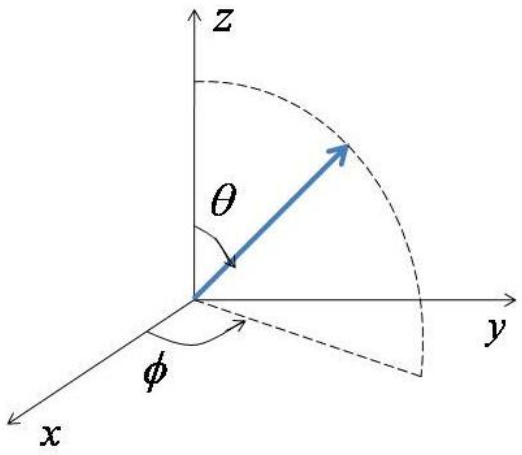

Figure 2-4: The geometry of the plane-parallel atmosphere.

Although the medium is homogeneous horizontally, as discussed above, it can be inhomogeneous along the vertical direction. The vertical variability can be described in terms of z, or in terms of optical depth $\tau(z)$ as:

$$\tau(z) = \int_z^\infty k_{ext}(z')dz' \tag{2-15}$$

where $k_{ext}(z)$ is the extinction coefficient of the medium at height z. The optical depth of the total atmosphere is called "optical thickness b". In what follows, we use $\tau(z)$ instead of z to describe vertical variations. For example, we define the SSA at different optical depths, as the ratio of the extinction of light due to scattering over the total extinction, from the volume element at a certain optical depth $\tau(z)$, i.e. as:

$$\omega(\tau) = \frac{k_{sca}(\tau)}{k_{ext}(\tau)} \rightarrow 0 < \omega(\tau) < 1 \tag{2-16}$$

The SSA is a very important parameter, since it defines how efficient is the aerosol absorption and thus, the energy balance effects due to aerosols.

The single scattering calculation for a volume element in the plane-parallel geometry is done using the phase matrix Z of the volume element, instead of its scattering matrix F. This transformation needs to be made because the scattering matrix assumes that the Stokes vector $\boldsymbol{I}$ is defined with respect to the scattering plane, which changes for each scattering event. The phase matrix on the other hand, assumes that the Stokes vector $\boldsymbol{I}$ is defined with respect to the local meridian planes[6], which remain constant for a beam of light –i.e., these planes do not depend on scattering events: The Stokes vector of the incident light with respect to its local meridian plane, is transformed by the phase matrix to the Stokes vector of the scattered light with respect to its local meridian plane, as follows [Hovenier et al., 2004]:

$$I_{sca}(\tau,\mu,\phi) = \frac{k_{sca}(\tau)}{4\pi} Z(\tau,\mu,\phi,\mu',\phi') I_{inc}(\tau,\mu',\phi') \tag{2-17}$$

where μ', ϕ' define, together with the vertical axis z, the local meridian plane of the incident light and similarly, μ and ϕ define the local meridian plane of the scattered light. The phase matrix is calculated from the scattering matrix from:

$$Z(\tau,\mu,\phi,\mu',\phi') = L(\pi-\sigma_2)F(\Theta)L(-\sigma_1) \tag{2-18}$$

where L is a rotation matrix:

$$L(\pi-a) = L(-a) = \begin{bmatrix} 1 & 0 & 0 & 0 \\ 0 & cos(2a) & -sin(2a) & 0 \\ 0 & sin(2a) & cos(2a) & 0 \\ 0 & 0 & 0 & 1 \end{bmatrix} \tag{2-18-1}$$

and σ_1, σ_2 are the angles between the scattering plane and the local meridian planes of the incident and the scattered light respectively.

The Stokes vector of the scattered light at the TOA, using the reflection matrix of the entire atmosphere R_{atm}, calculated from the adding and doubling method, is:

[6] The planes that contain the light beam and the vertical direction z.

$$\boldsymbol{I}(0,-\mu,\phi) = \frac{1}{\pi}\int_0^1 \mu' d\mu' \int_0^{2\pi} R_{atm}(\mu,\mu',\phi-\phi')\,\boldsymbol{I}(0,\mu',\phi')d\phi' \quad (2\text{-}19)$$

where $\boldsymbol{I}(0,\mu',\phi')$ is the Stokes vector of the incident light at the TOA.

At the bottom of the atmosphere, the Stokes vector of the scattered light, together with the unscattered transmitted light, is:

$$\boldsymbol{I}(b,\mu,\phi) = \frac{1}{\pi}\int_0^1 \mu' d\mu' \int_0^{2\pi} T_{atm}(\mu,\mu',\phi-\phi')\,\boldsymbol{I}(0,\mu',\phi')d\phi' + \; exp\left[{}^{-\tau}/_{\mu}\right]\boldsymbol{I}(0,\mu',\phi') \quad (2\text{-}20)$$

where T_{atm} is the transmission matrix of the atmosphere.

If the initial layers of the adding and doubling scheme are taken to be very optically thin, so as they scatter the light only one, their R and T matrices are calculated as [De Haan et al., 1987]:

$$R(\mu,\mu',\phi-\phi') = \frac{\omega}{4(\mu+\mu')}\left(1 - exp\left(\frac{-b}{\mu}-\frac{b}{\mu'}\right)\right)Z(-\mu,\mu',\phi-\phi') \quad (2\text{-}21)$$

$$T(\mu,\mu',\phi-\phi') = \frac{\omega}{4(\mu-\mu')}\left(exp\left(\frac{-b}{\mu}\right) - exp\left(\frac{-b}{\mu'}\right)\right)Z(\mu,\mu',\phi-\phi') \text{ if } \mu \neq \mu' \quad (2\text{-}22)$$

$$T(\mu,\mu',\phi-\phi') = \frac{\omega\cdot b}{4\mu^2} exp\left(\frac{-b}{\mu}\right)Z(\mu,\mu',\phi-\phi') \text{ if } \mu = \mu' \quad (2\text{-}22\text{-}1)$$

When adding two layers the reflection and transmission matrices of the combined layer are calculated as [De Haan et al., 1987]:

(2-23)

$$R_{comb}(\mu,\mu',\phi-\phi')$$

$$= R'(\mu,\mu',\phi-\phi') + exp\left(\frac{-\tau'}{\mu}\right)U(\tau',\mu,\mu',\phi-\phi')$$

$$+\frac{1}{\pi}\int_0^1 \mu'' d\mu'' \int_0^{2\pi} T'^{*}(\mu,\mu'',\phi-\phi'')\,U(\tau',\mu'',\mu',\phi''-\phi')d\phi''$$

(2-24)

$$T_{comb}(\mu,\mu',\phi-\phi')$$
$$= exp\left(\frac{-\tau'}{\mu'}\right)T''(\mu,\mu',\phi-\phi') + exp\left(\frac{-\tau''}{\mu}\right)D(\tau',\mu,\mu',\phi-\phi')$$
$$+\frac{1}{\pi}\int_0^1 \mu''d\mu'' \int_0^{2\pi} T''(\mu,\mu'',\phi-\phi'')\,D(\tau',\mu'',\mu',\phi''-\phi')d\phi''$$

where the scattering properties of the upper layer are marked with a prime ($'$) and the ones of the lower layer with a double prime ($''$). The matrices U and D describe the "upwards" and "downwards" traveling light, when the layers are illuminated from above. For illumination from bellow they are denoted by U^* and D^*. More detailed formulas of the U, D, U^* and D^* matrices can be found in De Haan et al., [1987].

Although the adding and doubling method can be summarized in a few equations, still the calculations needed to integrate the reflection and transmission matrices over polar and azimuth directions cannot be expressed in closed form. For this reason, we are forced to use numerical methods instead. In the work of De Haan et al., [1987] the integration over azimuth is calculated using a special Fourier decomposition of the corresponding matrices over their azimuth dependence. The Stokes vector of the light at a level of optical thickness τ, is calculated as the sum of Fourier terms m:

$$\boldsymbol{I}(\tau,\mu,\phi) = \sum_{m=0}^{\infty}\left(2-\delta_{m,0}\right)[B^{+m}(\phi)\boldsymbol{I}^{+m}(\tau,\pm\mu) + B^{-m}(\phi)\boldsymbol{I}^{-m}(\tau,\pm\mu)] \qquad (2\text{-}25)$$

where δ is the Kronecker delta, B is the 4×4 diagonal matrix:

$$B^{+m}(\phi) = diag(cos(m\phi), cos(m\phi), sin(m\phi), sin(m\phi),) \qquad (2\text{-}25\text{-}1)$$

$$B^{-m}(\phi) = diag(-sin(m\phi), -sin(m\phi), cos(m\phi), cos(m\phi),) \quad (2\text{-}25\text{-}2)$$

and

$$\boldsymbol{I}^{\pm m}(\tau,\mu) = 2\int_0^1 D^m(\tau,\mu,\mu')\boldsymbol{I}^{\pm m}(0,\mu')\mu' d\mu' + exp\left(\frac{-\tau}{\mu}\right)\boldsymbol{I}^{\pm m}(0,\mu) \quad (2\text{-}25\text{-}3)$$

$$\boldsymbol{I}^{\pm m}(\tau,-\mu) = 2\int_0^1 U^m(\tau,\mu,\mu')\boldsymbol{I}^{\pm m}(0,\mu')\mu' d\mu' \quad (2\text{-}25\text{-}4)$$

The integration over polar angles is approximated by a weighted sum using a Gaussian quadrature formula [Hovenier et al., 2004].

In summary, for fast calculations of the light at any level in the atmosphere, the individual Fourier intensities of the incident light at the TOA are calculated analytically $\boldsymbol{I}^{\pm m}(0,\mu) = \frac{1}{2\pi}\int_0^{2\pi} B^{\pm m}(\phi)\boldsymbol{I}(0,\mu,\phi)\, d\varphi$ for every Fourier term m. Next, the weighted sum for $\boldsymbol{I}^{\pm m}(\tau,\pm\mu)$ is calculated and finally multiplied with $B^{\pm m}(\phi)$ to evaluate $\boldsymbol{I}(\tau,\mu,\phi)$. The calculations can speed up using separate calculations with fewer Fourier terms for the multiple-scattered light compared to the single-scattered light, as well as the twice-scattered light [Hovenier, 1971, Van de Hulst, 1980]. Furthermore, the calculation of D^m, U^m requires the evaluation of the Fourier terms of the initial layer $Z^m(\pm\mu,\mu')$. A full description is provided in De Haan et al., [1987].

2.2 Reflection from the ocean surface

The reflection from the ocean surface is modeled using the Fresnel's formulas. In accounting for wind driven wave structure, the Fresnel reflections are the superposition of the aggregate of reflections from small wave facets, which can be treated locally as flat planes tilted from the

horizontal direction [Mobley, 1994] (Figure 2-5). In our model, we do not take into account the wind direction, thus, the different orientations of the wave facets are modeled with a normal distribution function, with a variance ("mean square slope" (mss)) depending on the wind speed above the surface, as [Cox and Munk, 1954]:

$$mss = 10^{-3}(3 + 5.12v_{wind}) \tag{2-26}$$

where v_{wind} is the wind speed in m/sec.

Since each photon at any moment sees a frozen air-water interface with a complex incident-reflection geometry based on the probability distribution function of the slopes, the calculation of the total and polarized reflectance is essentially applying the Fresnel's formulas for given incident and reflected directions and weighting the result by the probability function of the associated surface slope.

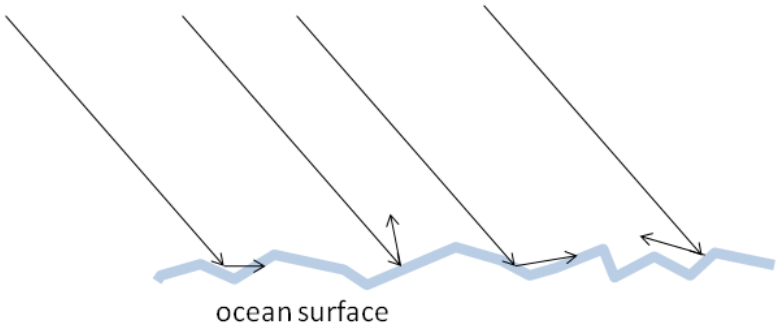

Figure 2-5: Reflectance on the wave facets of the ocean surface.

2.3. Scattering and absorption from the constituents of the ocean body

Further complicating the system, is the fact that some photons penetrate the water interface and scatter off of particles within the water, resulting in what is commonly referred to as water leaving radiance (or reflectance). The radiative transfer code used in this study, considers the reflection from the water body as a simple Lambertian reflectance, and it does not perform the full vector radiative transfer of the light in it. In the future, we plan to use more sophisticated models of the water reflectance such as the ones in the work of Chowdhary et al., [2001, 2002, 2005, 2006].

The optical properties of the open ocean considered here (i.e. "case 1 waters" as defined in Morel and Prieur, [1977]) are commonly modeled taking into account the contribution from water molecules, phytoplankton particles and their by-products. The ratio of downward and upward flux of light just below the ocean surface is given by:

$$R(\lambda) = f\frac{b_b(\lambda)}{a(\lambda)} \tag{2-27}$$

where f depends on the sun position and b_b and a are the ocean body total backscattering coefficient and total absorption coefficient respectively, which express the scattering and absorption from phytoplankton and water molecules [Gordon et al, 1975, Prieur, 1976, Morel and Prieur, 1977].

The spectral total backscattering coefficient $b_b(\lambda)$ is a function of the water backscattering coefficient b_w and the particles backscattering coefficient b_{bp} [Morel and Maritorena, 2001] given by:

$$b_b(\lambda) = 0.5b_w(\lambda) + b_{bp}(\lambda) \tag{2-28}$$

where

$$b_{bp}(\lambda) = \left[0.002 + 0.02\left(0.5 - 0.25log([Chl])\right)\frac{550}{\lambda}\right]\left[b_{p550}([Chl])\right] \quad (2\text{-}28\text{-}1)$$

and

$$b_{p550}([Chl]) = 0.416[Chl]^{0.766} \quad (2\text{-}28\text{-}2)$$

with $[Chl]$ being the chlorophyll concentration. For b_w we use the values provided in Morel and Maritorena, [2001].

Besides the scattering, the water body has natural and component absorption features which enter the model. In particular, the total absorption coefficient a is given by Morel and Maritorena, [2001]:

$$a(\lambda) = a_w(\lambda) + 0.06A_{chl}(\lambda)[Chl]^{0.65} + a_y(\lambda) \quad (2\text{-}29)$$

where

$$a_y(\lambda) = a_y(440)exp\left(-0.014(\lambda - 440)\right) \quad (2\text{-}29\text{-}1)$$

and

$$a_y(440) = 0.2(a_w(440) + 0.06A_{chl}(440)[Chl]^{0.65}) \quad (2\text{-}29\text{-}2)$$

A_{chl} being the particulate absorption factor. For the water absorption coefficient a_w, we use the values provided in Pope and Fry, [1997].

Chapter 3

The inversion algorithm

In any retrieval problem, which extracts underlying model parameters from a given measurement vector, two components must be considered: 1) the *forward model* and 2) the *inversion approach*. The *forward model* is a mathematical (or numerical) estimation of the measurement vector. In our case that is the TOA multispectral angular polarized reflection signal, its calculation based on the physics of light interaction with the medium, given the underlying aerosol properties. Once the forward model is known, the inverse problem provides the aerosol properties, which fit best the measurement vector.

One possibility to perform this inversion would be a brute force comparison of the TOA signals, calculated over a multidimensional database of aerosol properties, consistent with the characteristics of naturally occurring aerosol cases. As discussed in chapter 1, this approach is in fact quite common among the remote sensing community for operational retrievals. In particular, it makes use of precalculated high dimensional LUTs, which are generated before launch, and inversion is performed through a simple search in the LUT, so as to minimize the difference between model and measurement data in a Least Squares manner. Examples of the LUT approach include the AVHRR operational retrieval, presented in chapter 1, which uses a single dimensional LUT for the AOT at the single VIS channel. Due to the lack of sensor

information, it is clear that much a-priori information must be ingested in the retrieval, including the phase function and surface characteristics. Similar considerations occur for more complex sensors, except for the dimensionality of the LUT, which is higher, since the number of aerosol parameters, as well as the measurement vector dimension, are increased. In this case, the linear interpolation between the discrete points of the LUT multidimensional space becomes really slow and the LUT advantage of fast retrieval is no longer valid, setting this approach unsuitable for more complex inversions.

Another possibility is the use of information theoretical approaches, such as the optimal estimator technique[7] [Rodgers, 2000, Dubovik, 2004], which takes into account the a-priori covariance estimates of the signal and the inherent uncertainties of the retrieved parameters. This approach, however, requires extensive computing time, with the inversion process being forced to go through large scale matrix operations on a pixel-to-pixel basis. Even if these operations are fast for every pixel, the total inversion time becomes crucial, when the size of the processed data is very large, as will be the case for the future polarimeter on ACE. As discussed in chapter 1, ACE will include, among other features, a multiangular polarimetric sensor with a broad spectral coverage into the deep blue, SWIR, as well as additional coverage into the UV, to further improve the retrieval capabilities for absorbing aerosols. Most importantly, a cross-track capability (~400 km) would help eliminate the poor swath coverage of the original APS design. Unfortunately though, its measuring accuracy will be much worse

[7] A brief description of this technique is provided in Appendix I. A number of successful applications of the optimal estimator technique on the RSP data can be found in the work of Knobelspiesse, [2010] and Knobelspiesse et al., [2011a, 2011b].

than the one estimated for the APS and that will certainly have a serious effect on the quality of its retrieval.

To account for such possible data explosions, a more time-efficient approach is the NN technique [Haykin 1999], which is specifically designed to handle multi-parameter inversions based on pre-calculated input-output relations. With an inversion algorithm based on such a NN, constructed from a large number of pre-calculated relations between the TOA radiation measurements and the aerosol parameters, real-time inversion becomes cost-efficient, even for datasets as large as the ones from current and future polarimeters. This is one of the main reasons why NN applications are rising in the field of remote sensing for operational retrievals [Doerffer and Schiller, 2008].

3.1.1 Comparison of the global and local approaches

The scattered light observations Y are related, not linearly, to the aerosol characteristics X by:

$$Y = F(X) + \varepsilon \tag{3-1}$$

where F is the non-linear forward model and ε is the measurement noise which is assumed to be unbiased[8].

There are various statistical methods we can use for the inversion of this non-linear equation, being either "localized inversions" or "global inversions". The localized approach provides, for each case separately, the most likely estimation $\hat{X}$ of the aerosol properties for the corresponding measurements Y, through minimizing the distance $D\left(F\left(\hat{X}\right), Y\right)$ between the

[8] This assumption puts stringent requirements on the form of the forward model. In particular, the model should account for the most dominant physical mechanisms and realistic assumptions about the aerosol models used.

measurements Y and the modeling $F(\hat{X})$ of the measurements using the retrieved parameters $\hat{X}$**.** The global approach, on the other hand, constructs a function F_w, equivalent to the inverse function F^{-1}, which can then be applied to all the retrievals. Its optimized parameters "w" are calculated by minimizing a cost function $\int D(\hat{X}, X)P(X, \varepsilon)dXd\varepsilon$ for a number of cases, which constitute the "training dataset" and should adequately represent the real-world variability. In this cost function it is $\hat{X} = F_w(F(X) + \varepsilon)$ and P is the joint probability distribution of the aerosol parameters X and the measurement noise ε. The integration over all parameter states and measurement noise assigns a "global" validity to the optimization of F_w, at least inside the space of the training dataset [Aires et al., 2001]. An example of a localized inversion is the optimal estimator method, whereas the NN approach is a global inversion scheme.

One of the points we should highlight here, as a qualitative difference between the two approaches, is that the local technique finds a solution by minimizing the distance in the observation space (between $F(\hat{X})$ and Y), whereas the global technique finds a solution by minimizing the distance in the parameter space (between $\hat{X}$ and X) [Aires et al., 2001]. Furthermore, the minimization problem in the optimal estimator technique is usually solved considering Gaussian statistics (see Appendix II), whereas this is not necessary for the NN technique. Thus, the NN is able to capitalize on the higher-order statistics of the data, to infer their non-linear relationships.

The calculation of function F_w from the NN is done by training it over a large number of representative (X, Y) pairs. Beyond the training stage, the inversion is fast, since it has only to apply F_w to the scattered light observations, and retrieves the aerosol parameters almost

instantly, making the NNs suitable for real-time retrievals[9]. For the local inversions, a real-time retrieval is unrealistic, since they take much longer and they must be constructed all over again for each observation. Furthermore, the time needed to perform a local inversion increases significantly with the increasing non-linear character of the function F and the number of the variables used. The difficulty of finding a solution, due to poor convergence, and the need of a realistic guess increases too, under these conditions. This is important in our retrieval method, since, after the addition of the polarization measurements along multiple wavelengths and viewing angles, the number of input variables is quite large, and thus problematic to handle with conventional methods.

On the other hand, one may argue that the global dataset needed for the NN training is difficult to put together, since it has to contain the aerosol properties found in the real world, along with a quite accurate model of light measurements, which involves the modeling of the scattered light from particles and the realistic measurement noise from the instrument. If the training dataset misrepresents part of the real-world parameter space or if it contains inaccuracies due to the forward modeling, the NN inversion will not be global and will not work well for every possible case[10].

Furthermore, as mentioned above, the NN inverse function F_w is optimized over the whole space of the training dataset and that possibly involves the compromise of its performance on some parts of the space. This can be tested by examining the characteristics of the output errors at different parts of the testing dataset space. The global character of the training

[9] Real-time retrievals of atmospheric aerosols could be quite useful in case of emergencies, as in volcanic eruptions. A recent example is the 2010 Eyjafjallajökull volcano eruption, which caused a major halt in the air transportations over Europe [Gasteiger et al., 2011].

[10] Actually, the NN has the ability to extrapolate the information of the training dataset and it is possible to function well, outside its space. This is not guaranteed though and needs careful testing to prove.

dataset and the performance of the inverse function are two crucial points in supporting the NN performance and we investigate them further in chapter 4 (section 4.3.2.4).

3.2. The neural network

3.2.1. The neural network architecture

Our NN calculates the inverse function F_w by finding the associations between the light measurements Y (total intensity and linearly polarized intensity of the scattered light taking into consideration the measurement error) and the aerosol properties X. The architecture of the one-hidden layer NN used is shown in Figure 3-1.

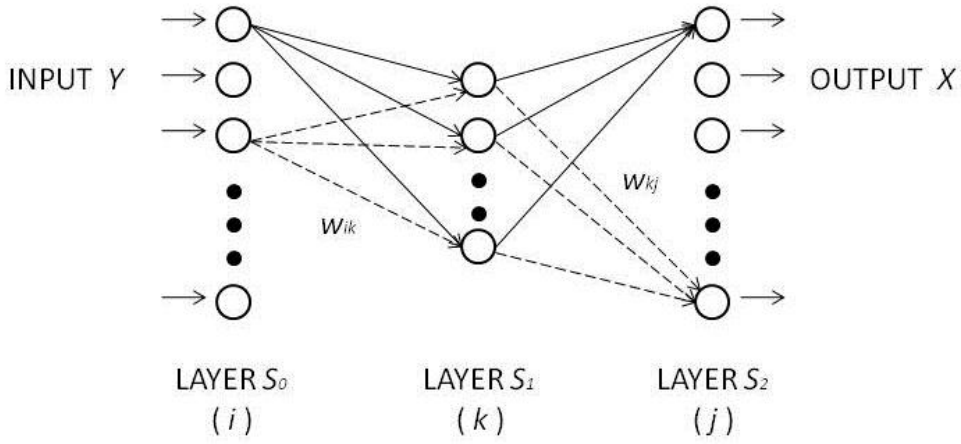

Figure 3-1. One-hidden-layer NN architecture.

We can build a NN with multiple hidden layers, but we choose not to, since more layers make the examination of its internal structure more difficult (for example the examination of the NN

internal structure using its jacobians in section 3.2.7). Furthermore, it is proven that the one-hidden-layer NN is able to model any continuous function [Hornik et al., 1989, Cybenko, 1989], which is suitable for our case.

The first layer S_0 is the input layer, which contains the observations Y. The last layer S_2 is the output layer that generates the aerosol properties X. The hidden layer S_1 contains "nodes" that function as building blocks of the associations between the inputs and the outputs. What comes into every node k is the sum of the weighted inputs plus a bias term $(\sum_i w_{ik}Y_i + b_k)$ and what comes out of it, is the transfer function of this sum. In our NN this transfer function is the hyperbolic tangent sigmoid function $(tanh)$. The NN output X is the weighted sum of the hidden layer node output, augmented by a bias term. More specifically, the output X_j, where j denotes one of the retrieved aerosol properties, is calculated from the equation:

$$X_j = \sum_{k \in S_1} w_{kj} \sigma\left(\sum_{i \in S_o} w_{ik} Y_i + b_k\right) + b_j \quad (3\text{-}2)$$

where σ is the transfer function, w denotes the NN weights and b the NN biases. The weights and biases express the associations between the input and the output. Thus, after the training of the NN, we can retrieve the aerosol parameters by simply applying the above equation on the observations of the total intensity and linearly polarized intensity of light. Therefore, although the time required to build the NN is usually long, after the training is done, the retrieval of aerosol properties from light observations is practically instantaneous.

3.2.2. Neural network training

We train the NN with the "resilient backpropagation algorithm" [Riedmiller and Braun ,1993], which is available from the MATLAB NNs toolbox[11]. The algorithm calculates numerically the weights and biases of the NN, which minimize the total root mean square error (RMSE) $E(w,b)$, given by (3-3), between the NN estimated values and the true values of the aerosol properties in the training dataset:

$$E(w,b) = \frac{1}{2N}\sum_{s=1}^{N}\sum_{j\in S_2} D\left(\hat{X}_j^s, X_j^s\right)^2 \quad (3\text{-}3)$$

where s denotes one of the N samples of the training dataset and D is the Euclidean distance. During the training stage the resilient backpropagation algorithm optimizes the weights and biases accordingly to the sign of the gradient $\frac{\partial E}{\partial w_{ik}}$. For each iteration w_{ik}[12] is increased or decreased by an adaptive step Δw_{ik} as follows:

$$w_{ik}(t+1) = w_{ik}(t) + \Delta w_{ik}(t) \quad (3\text{-}4)$$

with

$$\Delta w_{ik}(t) = \eta_{ik}(t)\cdot \Delta w_{ik}(t-1) \quad (3\text{-}4\text{-}1)$$

where t is the number of the iteration and the product $\eta_{ik}\cdot\Delta w_{ik}$ defines the adaptive step of the particular weight. The step takes an initial value of Δw_{ik}^0, which is increased or decreased in every iteration by η_{ik}, depending on the change of the gradient $\frac{\partial E}{\partial w_{ik}}$ sign. If the sign remains the same, the convergence is in a shallow region and for speed-up purposes the step is

[11] We selected this particular training algorithm among the available ones in the MATLAB NNs toolbox, after testing them all and evaluating their speed and the performance of the NNs they build. The NNs trained with the resilient backpropagation algorithm were found to perform well and have the fastest training of all the others.

[12] The particular weight w_{ik} is used here to represent any of the weights and biases of the NN, since similar formulas apply to all of them.

increased by $\eta_{ik} = 1.2$. If the sign changes, we have a jump of a minimum to the previous step, thus the step is decreased by $\eta_{ik} = -0.5$. The training stops, when $E(w, b)$ reaches a predetermined value, or when there is no more improvement on it. At that point the inverse function, defined by the calculated NN weights and biases (w, b), estimates the aerosol properties of the training dataset with the least possible total RMSE for the particular NN configuration.

3.2.3. Neural network testing

The performance of the constructed NN is evaluated with a testing dataset. This can be comprised of simulated or real data. In our case, our NN was comprehensively tested with simulated measurements (chapter 4), as well as available real measurements from the RSP (chapter 5).

Testing with simulated cases can provide an estimation of the output uncertainties of the NN, since the true values of the aerosol parameters are known. A more thorough discussion about this approach follows in the next section.

3.2.4. Assessing the neural network output uncertainties

A deficiency of the NN retrieval method is the somewhat complicated estimation of the NN output uncertainties. The work of Aires et al., [2004] is a quite successful attempt towards the construction of a method that could provide the NN output uncertainties, but unfortunately it is not as straight-forward and easy to apply to every NN. As a more approximate approach, we resort to estimating the NN output uncertainties from the output uncertainties calculated

during its testing stage. The problem with this approach, though, is its assumption that the testing dataset is representative of the real-world variability. This assumption is never fully true, although we can assess the range of its validity and apply it accordingly (an investigation of the testing dataset compatibility to the real-world cases is presented in chapter 4).

One way to check the validity of the output uncertainties derived from the NN testing (as well as the overall quality of the NN output) is the reproduction of the light measurements from the NN retrieved aerosol properties. This is done operationally on subsets of NN retrieved data, which reproduce the measurements by ingesting them in the forward model. The subsets that reproduce the measurements successfully, within the noise uncertainty, are considered successful retrievals and their uncertainty equals the uncertainty derived by the NN testing. The subsets that fail to do so, are flagged as unsuccessful retrievals. In the same manner, we consider the NN output uncertainty of the RSP data, and of any dataset, to be equal to the output uncertainty derived from the testing dataset, as long as the retrieved values are able to reproduce the light measurements within their estimated uncertainties (chapter 5).

3.2.5. The problem of instability of the inversion –use of a-priori information

Non-linear ill-posed problems, such as the one we study here, can become quite unstable, making the use of a-priori information especially important for stabilizing the retrieval process and constraining the solutions within a physical meaningful range. This a-priori information can be ingested in the NN in the form of a first guess, as in the work of Aires et al., [2001, 2004]. Such a first guess can be made, based on climatological values, from a mean estimate of experimentally obtained aerosol properties or even by their crude estimation from a less-

sophisticated algorithm. However, one of the advantages of the NN approach is that this is not absolutely necessary. In particular, in our algorithm we do not use a first guess per se, but we take into account the physical properties of aerosols by constructing the training dataset in accordance to their real-world variability, using aerosol climatologies.

3.2.6. The problem of multicollinearities in the inversion scheme

"Multicollinearities" is the term used to describe the correlations among the input or the output variables in a regression scheme [Gelman et al., 1995]. This is the case with our NN too, where the input variables and some of the output variables are strongly correlated. The multicollinearities of the input and the output inhibit our NN performance, because of information overlap in the measurement and aerosol property spaces, respectively, which results in phenomena of competing NN weights between the correlated variables. Such competition inhibits the predictive ability of the corresponding measurements and results in less accurate and less robust evaluation of the NN outputs [Aires et al., 2004]. In order to avoid the multicollinearities effect, we need to preprocess our input and output, so as to eliminate the strong correlations between the variables.

3.2.6.1. Preprocessing with PCA

For the elimination of the multicollinearities in the input and output variables we perform the PCA[10] and reduce the redundancy to acceptable levels. The result is the transformation of the

[10] The PCA is mainly known as a method for extracting "meaningful" components from a dataset, although here we use its less known application of data compressing [Jolliffe, 2002]. For the first case, it assumes linearity, orthogonallity and maximum variance explained by successive components in the dataset. These assumptions are

variables to their Principal Components (PCs), which retain the information of the original variables, but are orthogonal and thus uncorrelated. After transforming the input and output to their uncorrelated PCs, only a small number of them are retained and the rest are discarded. This is crucial since the independent information content of a measurement can be reliably obtained only in the "directions" of the largest PCs. The smaller PCs, in fact, cannot be separated from noise components or from redundant information. Thus, by discarding the low order PCs, along with the data compression, we effectively provide a denoising operation to our input. This does not come without a cost, as it introduces a bias and decreases the resolution of our retrieval [Jolliffe, 2002]. Although, for the system sizes we are considering, the gain in the robustness of the NN is by far more important though.

Transforming the original dataset to its PCs involves also some mixing of the original variables, since every PC usually represents parts of more than one projected variables from the original dataset. The original variables, though, can be physically different (for example the total intensity variables versus the linearly polarized intensity variables in the input and the spectral AOT versus the spectral SSA in the output). Furthermore, the input variables may have different predictive capabilities for different aerosol properties (for example, the short wavelength intensities are more sensitive to the fine mode properties and the longer wavelength intensities to the coarse mode properties). In both cases, the mixing of the

---

quite restrictive (especially for physical systems). The components extracted by datasets with more general characteristics (non-linearity, correlations between the variables) are closer to a mixture of the components of the dataset [Aires et al., 2002]. On the contrary, for the second case, the PCA, as a data compressing technique, does not need to assume linearity or orthogonallity and so on, since the mixing of the variables in the PCs is not a concern here (at least to the point that we do not have mixing of physically different variables –see further discussion in section 4.3.2.1).

variables in the input and output PCs can potentially introduce difficulties for our regression scheme in finding the physical associations between the input and output PCs. With that in mind, we divide the original variables into different groups and perform the PCA to each of them separately. The calculated PCs from the different groups are not necessarily uncorrelated, but our tests showed that some degree of correlation between the PCs of the input or the output is preferable over the undiscriminating mixing.

More specifically, we divide the input variables into four groups; the total intensity measurements at 412, 470 and 555 nm, the total intensity measurements at 865, 1590 and 2250 nm, the linearly polarized intensity measurements at 412, 470 and 555 nm and the linearly polarized intensity measurements at 865, 1590 and 2250 nm. The distinction between the shorter and the longer wavelengths is done on the basis of their dependence on the fine and coarse mode aerosol properties, respectively, as mentioned above. We perform the PCA separately for the variables of the four groups. For the output variables we form three groups; the first group contains the fine and coarse mode AOT at 412, 470, 555, 865, 1590 and 2250 nm, the second group contains the fine and coarse mode SSA at the same wavelengths and the third group contains the rest of the output variables, which are uncorrelated (fine and coarse mode effective radius, effective variance, real and imaginary refractive indices and number density). Since the third group variables are not correlated, we do not need to preprocess them and we perform the PCA, separately, on the AOT and SSA groups only.

The number of retained PCs is decided based on the basis of the following two criteria: 1) the percentage of the explained total variance [Jolliffe 2002] and 2) the performance of the resulting NN. For the second criterion, we evaluate the performance of many NNs, with

different combinations of PC numbers in the formed groups. Based on these tests, the retained optimal PCs, enough to explain the noise-free dataset variance and result to a well-performing NN, are 100 PCs for the input variables and 17 PCs for the AOT and SSA output variables (see details in chapter 4).

3.2.7. Neural network jacobians

The NNs are usually considered more or less as black boxes, due to their complex internal structure. It is thus important to describe, at least to some degree, the internal associations they use to produce the output. The NN jacobians are the first derivatives of the output with respect to the input and they provide a first-level description of the NN non-linear regression, in the same way the regression coefficients of a linear regression do[13]. For the one-hidden-layer NN considered in this study, we can easily calculate the analytic expression of the jacobians from equation 3-2, as:

$$\frac{\partial X_j}{\partial Y_i} = \sum_{k\epsilon S_1} w_{ik} w_{kj} \sigma'\left(\sum_{i\epsilon S_0} w_{ik} Y_i + b_k\right) \quad (3\text{-}5)$$

Moreover, we can use the jacobians to assess the retrieval robustness, since a NN, performing a robust mapping of the input to the output, has well-defined associations (and therefore jacobians) between the input and the output. Conversely, highly variable jacobians are a sign of poor robustness of the NN [Aires et al., 2004].

An example of this method is shown in Figure 3-2: The first column contains the histograms of the jacobians for a NN with unprocessed input, whereas the second column contains the

[13] Unlike the linear regression coefficients, the NN jacobians are case-dependent, due to the non-linear character of the NN regression.

jacobians of a NN with PCA-processed input. More specifically, the histograms contain the averages over 1000 testing dataset cases of the fine mode effective radius (first row) and the fine mode number density (second row) jacobians, with respect to all the linearly polarized intensity variables used in the retrieval, over different wavelengths and viewing angles. Similar histograms apply to the rest of the NN jacobians.

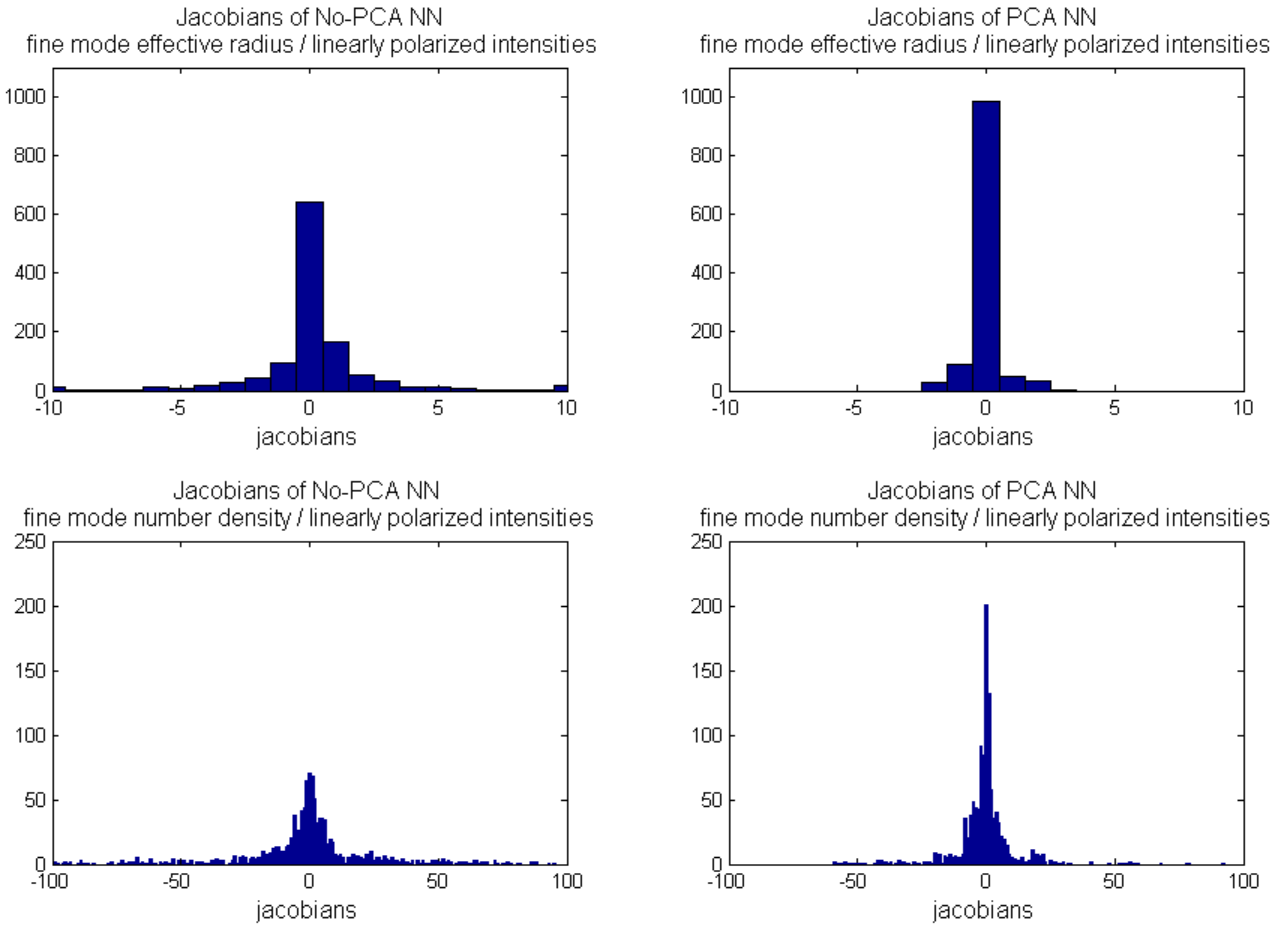

Figure 3-2. The histograms of the averaged jacobians from 1000 testing dataset cases. The first row contains the fine mode effective radius jacobians with respect to all linearly polarized intensity variables and the second row the fine mode number density jacobians with respect to

all linearly polarized intensity variables, for a NN with no preprocessed input (first column) and a NN with PCA-processed input (second column).

It is clear that for the first NN the jacobians are more variable, showing that, due to the multicollinearities in the input, the associations between the input and the output are not well defined and the NN retrieval not robust enough. On the other hand, for the second NN, the PCA reduces the multicollinearities problem, the internal structure is more well-defined and the NN jacobians are less variable.

3.2.8. Exploring different NN retrieval schemes

In order to decide on the most effective NN scheme for retrieving the aerosol properties, we explored a number of different NNs, mainly with different combinations for their input variables, as described below and summarized in Table 3-1. Furthermore, we also explored the use of cascading NNs, where the output of the first NN, together with the measurement vector, is fed into the input of the second NN.

Table 3-1. Different NN retrieval schemes explored.

	INPUT	
	NN 1	NN 2
retrieval #1	total intensity AND linearly polarized intensity measurements	-None-
retrieval #2	**total intensity AND linearly polarized intensity measurements**	**- total intensity AND linearly polarized intensity measurements** **- aerosol properties output from NN 1**
retrieval #3	total intensity measurements	- total intensity measurements - aerosol properties output from NN 1
retrieval #4	total intensity AND linearly polarized intensity measurements	- total intensity measurements - aerosol properties output from NN 1

Table 3-2 compares the performances of the retrieval schemes in Table 3-1, based on the mean fractional RMSE[14] and the R-square of their testing. The highlighted parameters in Table 3-2 denote the most important aerosol parameters for our retrieval, as those reported in section 4.1.1.

As shown below and in chapter 4, we believe that the most effective retrieval scheme is retrieval #2 (highlighted in Table 3-1), which is a cascading scheme of two NNs combining total and linearly polarized intensity measurements for estimating the aerosol properties. On the other hand, the least effective is retrieval #3, which uses only the total intensity measurements, without taking into account the polarization information.

[14] The fractional RMSE is defined here as the RMSE of the retrieved values in a specific part of the range, divided by the corresponding mean. The mean fractional RMSE averages the fractional RMSEs over the whole range.

Table 3-2. The explored retrieval schemes performance.

			mean fractional RMSE x 100				R-square			
			retr. #1	retr. #2	retr. #3	retr. #4	retr. #1	retr. #2	retr. #3	retr. #4
fine mode	**effective radius**		**5.5**	**4.6**	**7.9**	**4.8**	**0.96**	**0.97**	**0.9**	**0.97**
	effective variance		**13.1**	**11.7**	**19.7**	**12.4**	**0.81**	**0.84**	**0.56**	**0.82**
	number density		19.6	16.9	29.5	18.2	0.91	0.93	0.81	0.92
	AOT at 555 nm		**6.4**	**6**	**8.6**	**6.2**	**0.99**	**0.99**	**0.96**	**0.99**
	SSA at 555 nm		**3**	**2.8**	**4.1**	**2.8**	**0.73**	**0.75**	**0.56**	**0.75**
	real refractive index		**1.6**	**1.4**	**3.4**	**1.6**	**0.89**	**0.92**	**0.55**	**0.9**
	imaginary refractive index	m_a	112	75.3	70.7	52.5	0.38	0.48	0.35	0.59
		m_b	110	53.4	84.1	50.4	0.45	0.29	0.44	0.77[15]
coarse mode	**effective radius**		**7.8**	**7.1**	**13.4**	**7.7**	**0.92**	**0.93**	**0.77**	**0.92**
	effective variance		**9.3**	**9**	**11.8**	**9.4**	**0.72**	**0.75**	**0.57**	**0.72**
	number density		23.6	21.7	30.9	22.2	0.84	0.86	0.72	0.85
	AOT at 555 nm		**9**	**8.1**	**15.3**	**8.8**	**0.98**	**0.98**	**0.94**	**0.98**
	SSA at 555 nm		**2.5**	**2.5**	**4**	**2.5**	**0.62**	**0.65**	**0.25**	**0.62**
	real refractive index		**0.4**	**0.4**	**1**	**0.5**	**0.96**	**0.97**	**0.79**	**0.95**
	imaginary refractive index	m_a	74.7	89	71.5	65.3	0.28	0.73	0.2	0.35
		m_b	141.1	116.3	96.2	75.3	0.27	0.31	0.17	0.52

[15] Retrieval method #4, which uses the total and linearly polarized intensities as input for the first NN (as retrieval #2) but only the total intensity for the second NN (see discussion below), have a quite similar performance with retrieval #2 and performs moderately better for the imaginary refractive index. This may seem strange at first, but it is justified by the more compact structure of retrieval #4 second NN (smaller number of input variables), which results to a more stabilized regression environment for retrieving this quite unstable variable, compared to retrieval #2.

3.2.8.1. Refinement of the NN output using a cascading scheme with two NNs

Using a cascading scheme of two identical NNs[16], which passes the output from the first NN to the input of the second NN, combined with the assimilation of the original measurement vector, we achieve an overall more accurate retrieval of the aerosol properties. In particular, the performance increases for all aerosol properties, mainly due to suppressing any erratic behaviors in the second NN. This is more obvious for the imaginary refractive index, which is the most unstable parameter in the retrieval. In Figure 3-3 we show the performance of the first NN (or retrieval #1 in Table 3-1) on the fine mode real refractive index and on the m_a parameter of fine mode imaginary refractive index (see definition in section 4.2.2) and we compare them with the respective performances from the cascading scheme of the two NNs (retrieval #2 in Table 3-1). Although for the bulk part the performances of the two retrieval schemes are similar, we note that with the cascading scheme the (limited but present) erratic behavior of the m_a parameter is suppressed in the second NN. The already successfully retrieved real refractive index is not greatly affected from the second NN.

[16] This scheme is <u>not</u> equivalent to a two-hidden-layers NN.

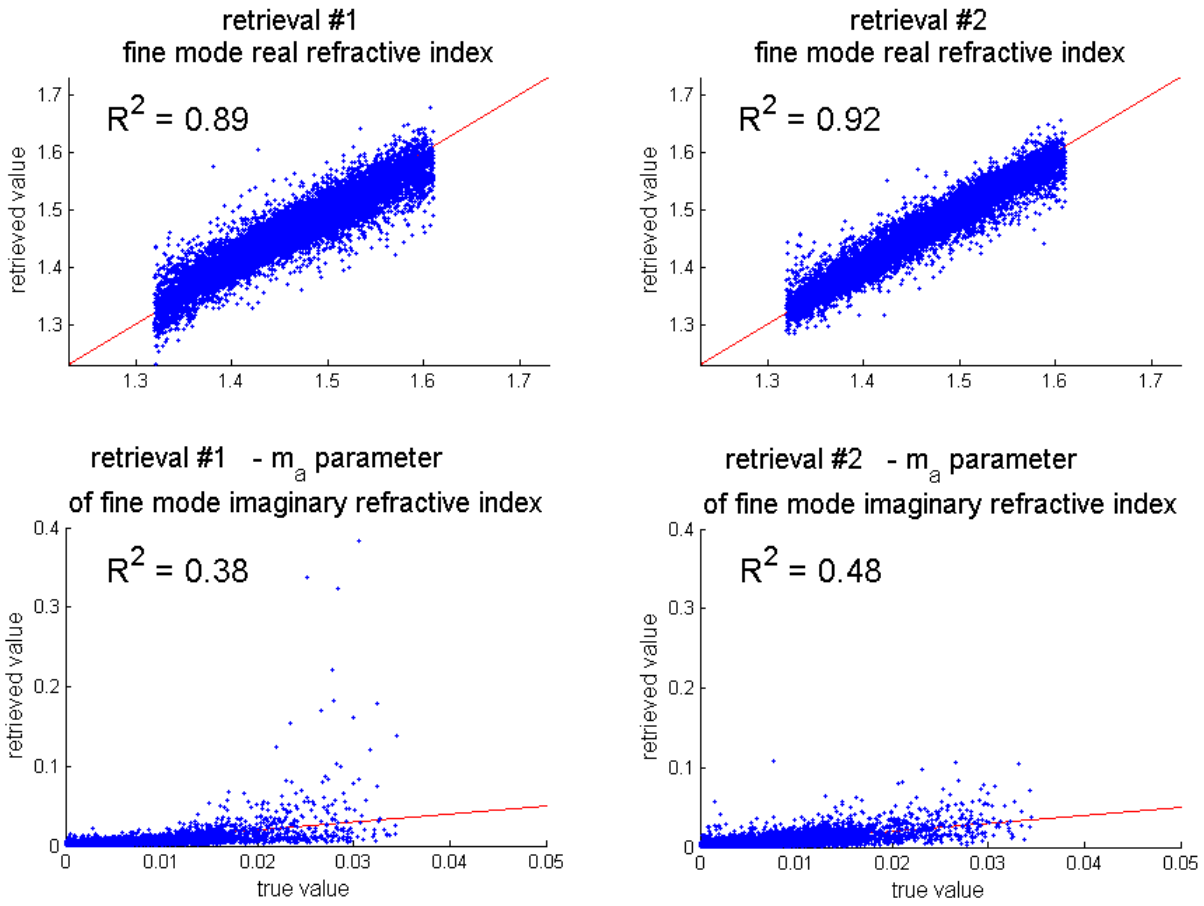

Figure 3-3. Comparison of retrieval #1 performance (first column) with retrieval #2 performance (second column), on fine mode real refractive index and m_a parameter of the fine mode imaginary refractive index.

3.2.8.1. Exploring different combinations of input variables

In order to prove the better performance of the retrieval, when polarization information is included, we compared the performances of two retrieval approaches, one using only total intensity measurements (retrieval #3 in Table 3-1) and one combining total intensity and linearly polarized intensity measurements (retrieval #2 in Table 3-1). The results shown in

Figure 3-4 advocate in favor of the polarization-including retrieval. Specifically, the total intensity-only NN is able to retrieve the AOT, but does not have the necessary information to accurately retrieve the aerosol real refractive index, SSA and effective radius. With the inclusion of polarization measurements in the retrieval, the aerosol properties estimation is far more accurate.

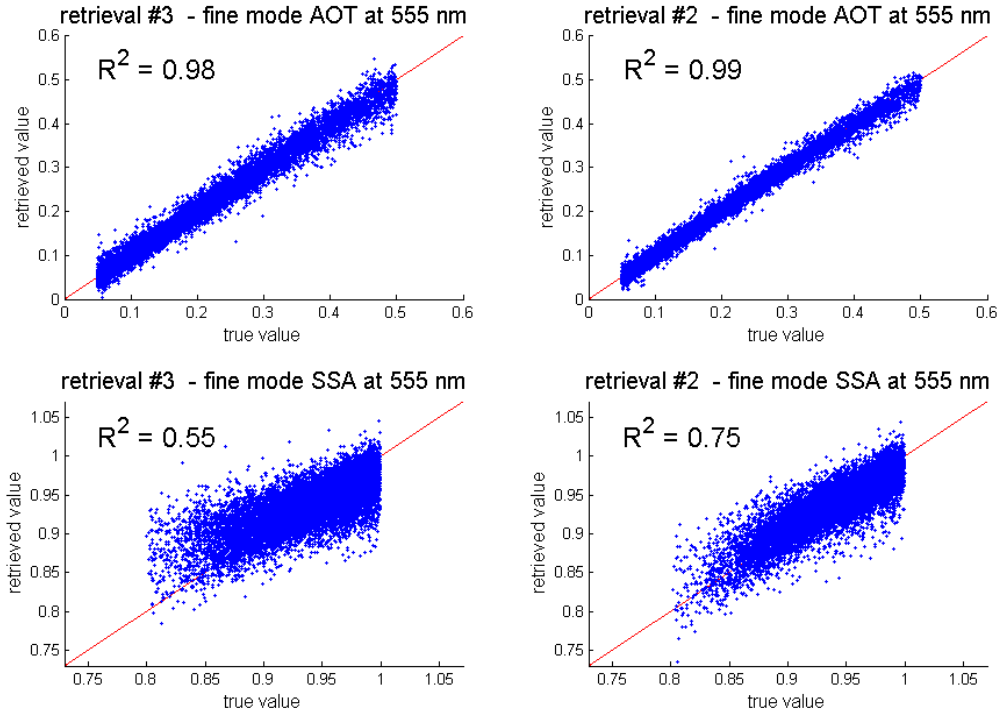

Figure 3-4. Comparison of retrieval #3 performance (first column) with retrieval #2 performance (second column), on fine mode AOT at 555 nm, fine mode SSA at 555 nm, fine mode real refractive index and fine mode effective radius.

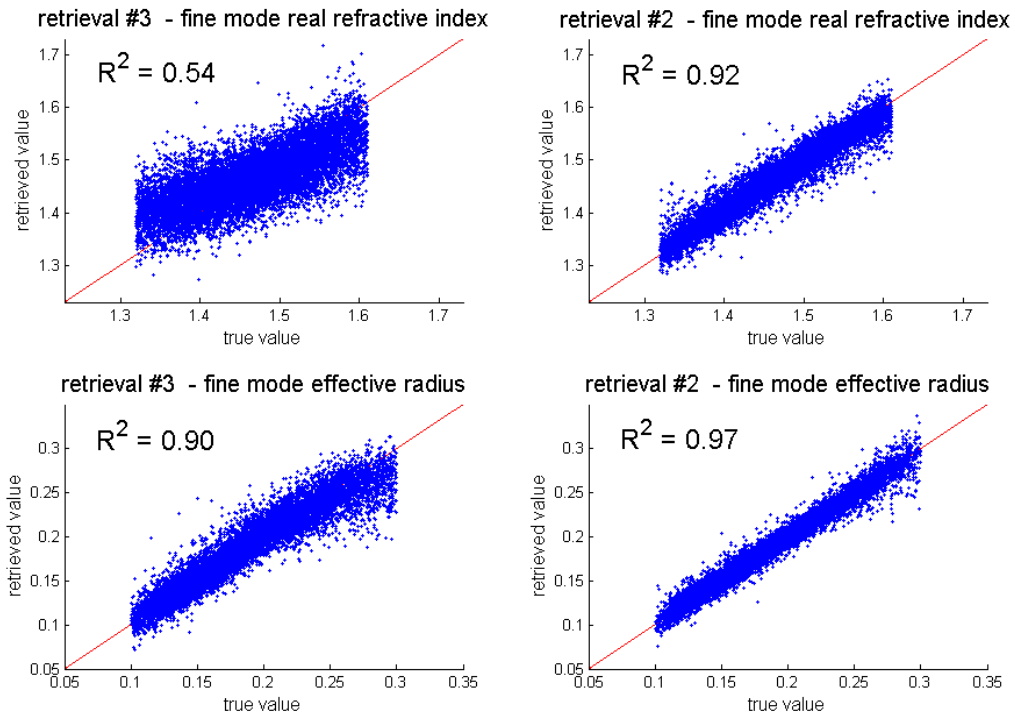

Figure 3-4. (Continued)

An interesting combination, for reasons that will be more apparent in chapter 5, is the retrieval #4 in Table 3-1. It is also comprised from two NNs, with the first NN using the combination of total intensity and linearly polarized intensity measurements and the second NN using only the total intensity measurements along with the output from the first NN. Figure 3-5 shows a comparison between the performances of retrieval #4 and retrieval #2. As discussed above, the total intensity-only retrievals are not able to retrieve most of the aerosol properties accurately enough, whereas in Figure 3-5 we see that, by including good a-priori information, this changes. The fact that total intensity-only retrievals are heavily dependent on the quality of a-priori assumptions is also highlighted in the work of Mishchenko and Travis,

[1997a, b]. In our case the “a-priori assumptions” are the outputs of the first NN, which uses the combination of total intensity and linearly polarized intensity measurements. Due to the inclusion of polarization information, the output is really close to the true values of the aerosol properties.

This example may seem redundant, but its importance will become more apparent in chapter 5, where retrieval #4 is applied on a non-spherical particles case. It is shown there that retrieving non-spherical particle properties with spherical-shape, total intensity-only algorithms, including good a-priori information, can fool us into plausible results, which are not necessarily true. We will further show, that only with the inclusion of polarization measurements (mainly in the longer wavelengths) we can actually identify the mistake. We consider the case of retrieval #4 very important, since good a-priori assumptions in total intensity-only retrieval algorithms, built for retrieving spherical particle properties, are widely used as a panacea for “successful” retrievals.

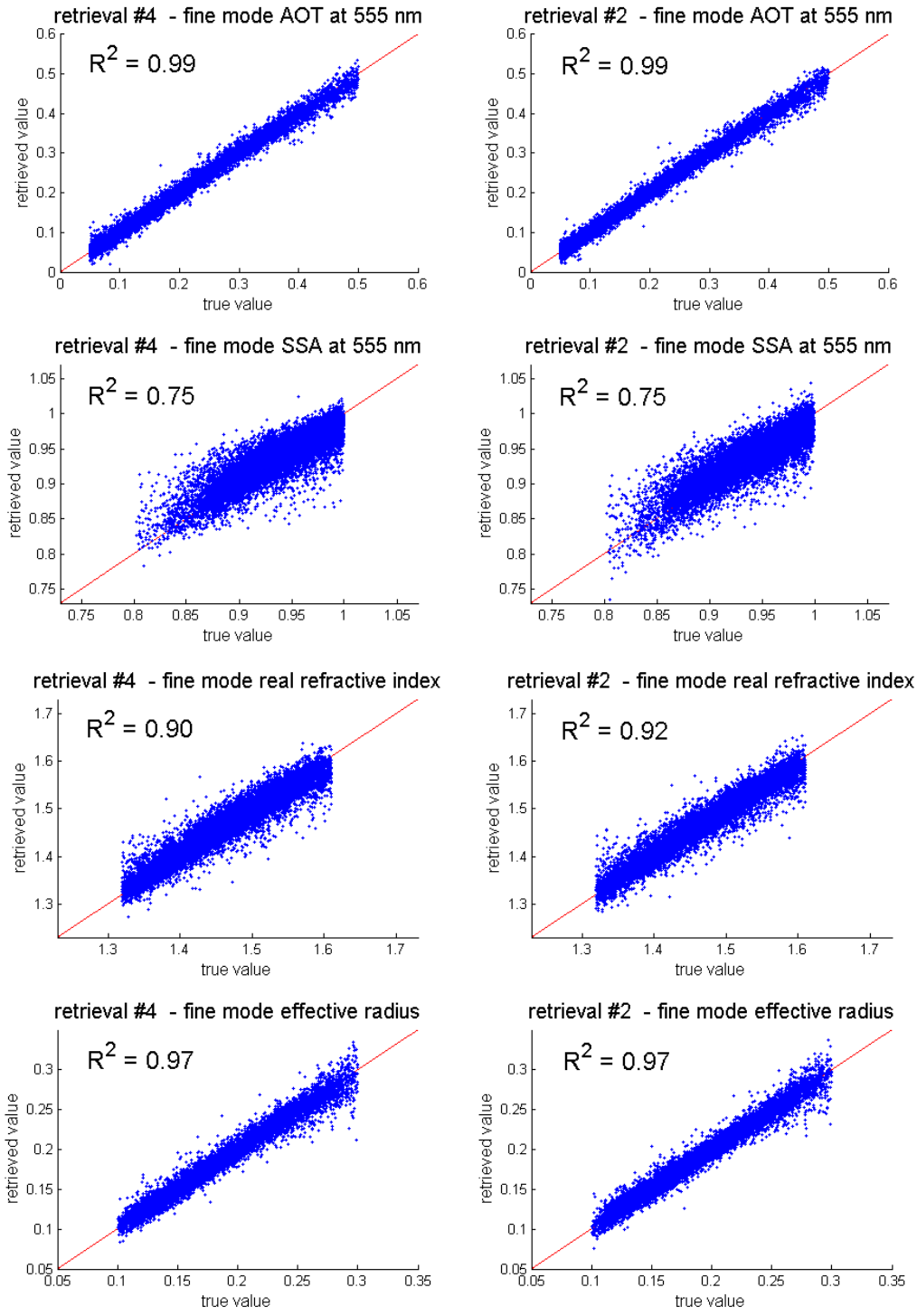

Figure 3-5. Comparison of retrieval #4 performance (first column) with retrieval #2 performance (second column), on fine mode AOT at 555 nm, fine mode SSA at 555 nm, fine mode real refractive index and fine mode effective radius.

Chapter 4

The construction of the retrieval algorithm

In the previous chapter we presented different retrieval scheme options and, from the comparison of their performances, it became apparent that the inclusion of polarization is necessary for the success of our aerosol retrieval algorithm. In this chapter we describe in detail the most effective approach, "retrieval #2" (see Table 3.1), a cascading configuration of two NNs, which combines the multispectral, multiangle total and linearly polarized intensity measurements from RSP and retrieves successfully enough the aerosol properties.

We start first with the general retrieval objectives, which set the accuracy aerosol property requirements, and we continue next with the description of the individual parts of the constructed algorithm. At the end of the chapter we present the retrieval performance on simulated cases, focusing mainly on retrieval approach #2. The retrieval approach #1, #3 and #4, are not described in detail, since their general construction is quite similar to retrieval #2. Nevertheless, we include their testing on simulated cases in Appendix III, in order to better interpret the performance improvement observed.

4.1. Retrieval objectives

4.1.1. Accuracy requirements of the retrieved aerosol parameters for their use in atmospheric and climate studies

As discussed in chapter 1, the global monitoring of atmospheric aerosols is done predominantly for the accurate description of their direct and indirect effects on the climate, providing at the same time valuable information on the physical and chemical properties of the atmosphere. To achieve this aim, the aerosol properties must be retrieved with a sufficient accuracy [Mishchenko et al., 2004]. For example, a significant change in the aerosol forcing of 0.25 W/m^2 (compared to the anticipated change in the GHG forcing of 1 W/m^2 in the next ~20 years [Hansen et al., 1995]), corresponds to a change in the global mean AOT of 0.01, setting the accuracy requirement of the retrieved AOT to 0.01.

As discussed in length in chapter 1 in length, the quantification of the aerosol direct effect requires first the accurate estimation of the SSA, which provides the sign of the forcing, as well as the AOT and phase function, which determine the magnitude of the forcing [Hansen et al., 1997]. The spectral AOT can be retrieved directly from light measurements or can be calculated from the retrieved microphysical properties of the aerosols, i.e. their size distribution, spectral refractive index and number density. The spectral SSA and the spectral phase function are usually by-products of the retrieved microphysical properties, as well.

As for the aerosol indirect effect, it depends on their number concentration and their droplet-nucleation efficiency, which is a function of their size and hygroscopicity. The hygroscopicity can be inferred from the refractive index of the particles [Tang and Munkelwitz, 1996]. Also, the

size and refractive index help the classification of the particles to anthropogenic and natural, giving us valuable information about their sources, which is of great help for shaping effective environmental policies.

The science objectives of the aerosol retrievals, reported in Mishchenko et al, [2004], are feasible through *synergetic algorithms*, which utilize the capabilities of *both active and passive satellite instruments*. In Mishchenko et al., [2007] the *passive satellite instrument retrieval requirements* are reported, which are less stringent, since they amount only for a part only of the synergetic retrieval. A passive remote sensing polarimeter, such as APS, is expected to provide, independently for fine and coarse modes, the spectral AOT, the spectral SSA, the spectral real part of refractive index, the effective radius, the effective variance of the size distribution and the shape of the particles, with uncertainties shown in Table 4-1. However, the polarimeter on the future ACE mission will have much lower measuring accuracies and its retrieval capabilities will be probably worse than what reported in Table 4-1.

4.1.2. Accuracy goals of the retrieved parameters from the constructed algorithm

We consider that the retrieval requirements reported in [Mishchenko et al., 2007] should be the target accuracy for our RSP retrieval, since the objectives of passive remote sensing are met by the RSP specifications. The retrieved aerosol parameters from our algorithm (see discussion about their characteristics in following section) and their associate uncertainties, based on the expected capabilities of the polarized multispectral, multiangle RSP measurements, are shown in Table 4-1.

Table 4-1. The retrieved microphysical and optical aerosol properties, along with their accuracy goals (source: [Mishchenko et al., 2007]).

Retrieved aerosol parameters (independently for the fine and the coarse modes)	**Uncertainty goals reported in Mishchenko et al., [2007]**	**Uncertainty goals of our algorithm**
Spectral AOT	0.02 over ocean 0.04 over land	0.02
Effective radius of the size distribution	10%	10%
Effective variance of the size distribution	40%	40%
Real refractive index (spectrally constant)[17]	0.02	0.02
Spectral imaginary refractive index	Not given	Not given
Spectral SSA	0.03	0.03
Number density	Not given	Not given
Particle shape	N/A	Not retrieved

4.2. Characteristics of the retrieved aerosol properties

Our algorithm retrieves, independently for the fine and coarse modes, the column AOT and SSA at 412, 470, 555, 865, 1590 and 2250 nm, the spectral refractive index, the effective radius and the effective variance of the size distribution, as well as the number density. We assume that only the imaginary part of the refractive index varies with light wavelength, which

[17] In Mishchenko et al., [2007] the spectral real refractive index is reported.

expresses the absorbing character of the material, while the real part remains constant throughout the considered part of the spectrum. The shape of the particles is not retrieved, since we consider only scenes with spherical particles. We realize though that this assumption makes our algorithm ill-suited to non-spherical particle retrievals [Dubovik et al., 2006] and we therefore plan to ingest non-spherical particle retrieval capabilities in a future version of it (see discussion in chapter 5 and 6).

In the following we give a description of the particle microphysical properties retrieved from our algorithm.

4.2.1. Size distribution

The size distribution of the particles, after classifyind them in the fine and coarse groups, is modelled using the parameters of a bimodal log-normal distribution: $N(r) = n_f(r) + n_c(r)$, where $n_f(r)$ is the log-normal size distribution of the fine mode and $n_c(r)$ is the log-normal size distribution of the coarse mode [Hansen and Travis, 1974]. Any log-normal size distribution can be written as:

$$n(r) = \frac{1}{\sqrt{2\pi}\sigma_g}\frac{1}{r} exp\left(\frac{-(lnr-lnr_g)^2}{2\sigma_g^2}\right) \quad (4\text{-}1)$$

with $lnr_g = \int_0^\infty lnrn(r)\,dr$ and $\sigma_g^2 = \int_0^\infty (lnr - lnr_g)n(r)\,dr$, where r_g is the geometric mean radius and σ_g is the distribution width. Instead of geometric mean radius and width we retrieve the effective radius and the effective variance of the corresponding modes, which are defined for each mode by:

$$r_{eff} = \frac{\int_{rmin}^{rmax} \pi r^3 n(r) dr}{\int_{rmin}^{rmax} \pi r^2 n(r) dr} \quad (4\text{-}2)$$

$$v_{eff} = \frac{\int_{rmin}^{rmax}(r-r_{eff})^2 \pi r^2 n(r) dr}{\int_{rmin}^{rmax} \pi r^2 n(r) dr} \quad (4\text{-}3)$$

For the log-normal distribution the above formulas can be approximated with [Hansen and Travis, 1974]:

$$r_{eff} \approx r_g \left(1 + \sigma_g\right)^{5/2} \quad (4\text{-}4)$$

$$v_{eff} \approx exp\left(\sigma_g^2\right) - 1 \quad (4\text{-}5)$$

The effective radius and effective variance are preferred over the geometric mean radius and width of the size distribution, since they are less dependent on the particular type of the distribution, allowing in this way the somewhat arbitrary choice of its type in the modeling of the optical properties. This is supported from the findings of [Hansen and Travis, 1974], who showed that different types of size distributions, having different r_g and σ_g but the same r_{eff} and v_{eff}, present similar scattering properties, whereas the opposite is not true.

4.2.2. Refractive index

The real refractive index is taken as constant for the part of the spectrum considered here. The spectral variation of the imaginary refractive index is modeled using two parameters, m_a and m_b, as follows:

$$Im\left(m(\lambda)\right) = m_a + m_b \cdot (\lambda + 0.445)^{-10} \quad (4\text{-}6)$$

where λ is expressed in microns. This model refers to the spectral variation of organic carbon aerosol absorption used in Knobelspiesse et al. [2011a], based on the work of Bergstrom et al. [2010]. The spectral variation of the aerosol imaginary refractive index has not been studied extensively and so there are no definite formulas for its modeling. In the work of Knobelspiesse

et al. [2011a] a comparison is not given of the used model with other models in the literature for particles containing organic carbon, as shown in Figure 4-1. We use the particular model to account for the organic carbon in the aerosols from the INTEX-B/MILAGRO campaign, which we use to test our algorithm (chapter 5). Although the model does not represent all the possible spectral variations of the imaginary refractive index, it is used here as a test case, since there is no better available. Due to these limitations, for 1/3 of our simulations we consider that the imaginary refractive index is spectrally constant, with $m_b = 0$.

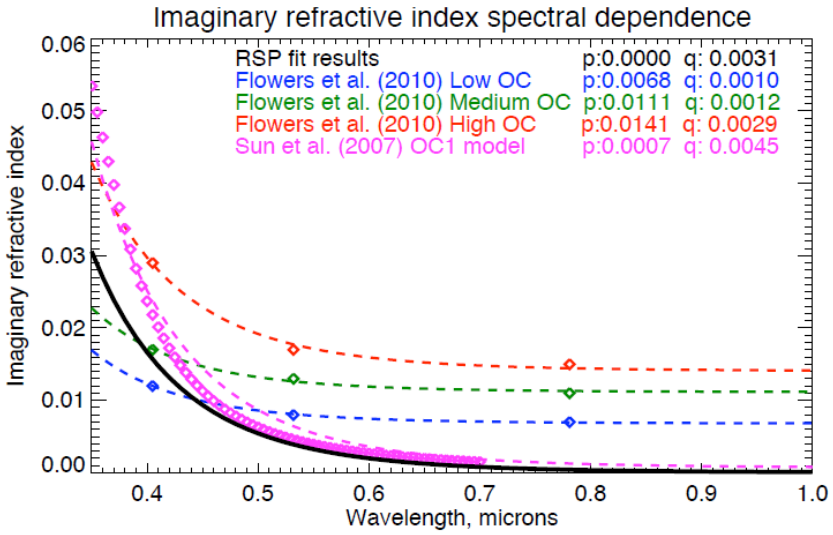

Figure 4-1. Comparison of the imaginary refractive index spectral dependence model used in Knobelspiesse et al., [2011a] (black curve) with other models in the literature for particles containing organic carbon (source: [Knobelspiesse et al., 2011a]).

4.3. Construction of the retrieval algorithm

A schematic of the constructed algorithm components is shown in Figure 4-2. The following is a detailed presentation of their characteristics.

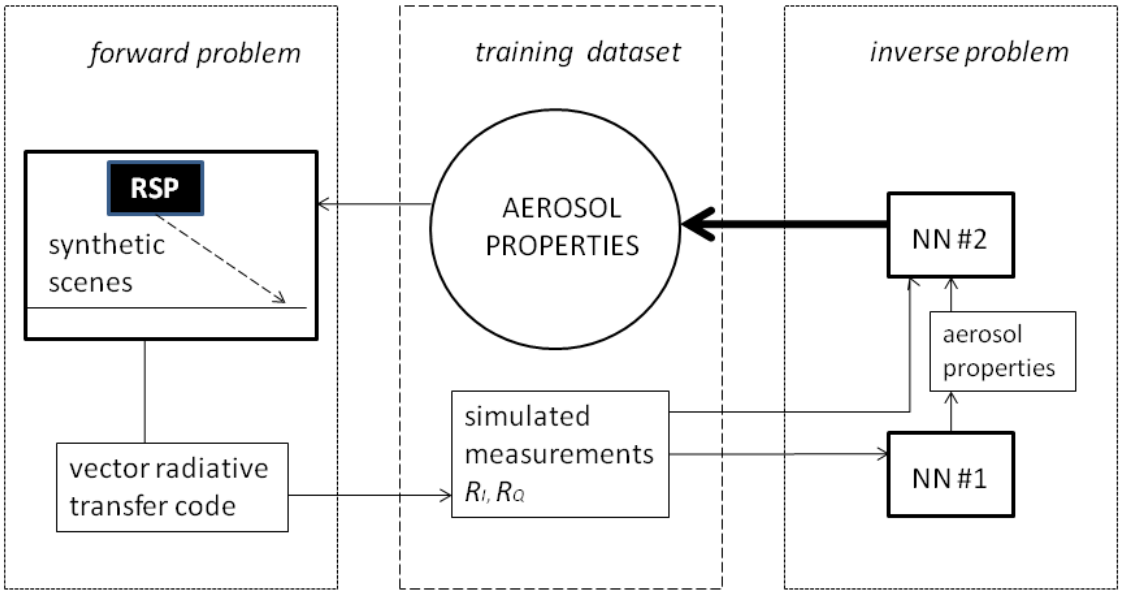

Figure 4-2. The components of the constructed retrieval algorithm.

4.3.1. Simulations

We train our NN with a simulated dataset, which we try to make as representative of the real world as possible, for the algorithm to be applicable on real world cases. Our training dataset consists of the multispectral, multiangle total intensity and linearly polarized intensity of light, simulated as if they were measured above atmosphere/ocean synthetic scenes by the RSP, with properties taken from various climatologies [Dubovik et al., 2002, Smirnov et al., 2002]. Using the aerosols, gases and surface properties of the synthetic scenes, we calculate the total

intensity and linearly polarized intensity of the scattered light at the aircraft level, using the adding and doubling vector radiative transfer code [De Haan et al., 1987], designed by Dr. Brian Cairns to model the RSP measurements. The realistic noise of the RSP instrument is also taken into account (section 4.3.1.2).

4.3.1.1. Synthetic scene characteristics

A schematic of the synthetic scenes used for the simulations is shown in Figure 4-3. We generate the synthetic scene properties randomly and independently from each other. The distributions of the values used for all the properties, along with their units, are shown in Table 4-2 and 4-3.

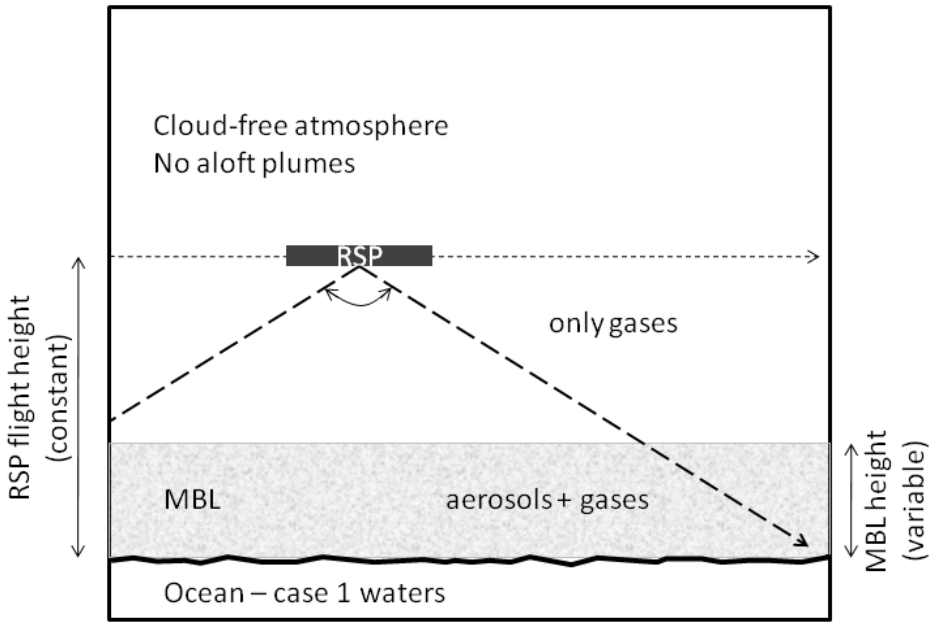

Figure 4-3. Schematic of the synthetic scenes used in the simulations.

We consider a simple plane-parallel atmosphere without clouds or aloft plumes, with all the aerosols concentrated in a homogeneous marine boundary layer (MBL) of variable height from 200 m to 2000 m [Zeng et al., 2004]. The surface is taken to be the open ocean (case 1 waters [Morel and Prieur, 1977]), with chlorophyll concentration in the range of 0.06-2.0 mg/m^3, wind speed of 2-8 m/sec and no dissolved organic matter[18].

We also take into account the absorption from water vapor, ozone and nitrogen dioxide. These gases are homogeneously distributed in the atmosphere below the aircraft, with concentrations in the range of 1.5-4.5 cm/atm, 50-350 Db and 1-30 ppb, respectively. These values are indicative and do not cover the whole range of worldwide gas concentrations.

The aerosol properties come from AERONET dataset (Level 2 Almucantar Inversion Products), the information provided in Dubovik et al., [2002], Smirnov et al., [2002] and suggestions by Dr. Jacek Chowdhary. In particular, we used the global AERONET dataset to derive the types of the aerosol property natural distributions (by constructing the respective histograms from the whole dataset) and the other sources to infer the corresponding distribution parameters (mean, width and range). The aerosol properties have the characteristics of "oceanic" and "mixed" type aerosols [Dubovik et al., 2002]. We included mixed aerosols along with oceanic aerosols, since the RSP measurements above the ocean are usually performed in close proximity to the land, where mixed aerosols can be present in the MBL.

Unfortunately, the AERONET dataset is not very representative of the oceanic aerosols, since its sensors network is situated mainly on the land, with very few stations on the ocean. In the study of Smirnov et al. [2002] the data come from ships in the ocean and they are sparse. For

[18] The chlorophyll and wind speed values are suggested by Dr. Jacek Chowdhary.

these reasons, we consider that the oceanic aerosol properties in both climatologies are only indicative, but nevertheless, their mean values are close to the mean values of the true distributions. We thus construct the oceanic aerosol distributions to be broader than those indicated in the climatologies.

The multivariate distributions, which contain the values of oceanic and mixed aerosol properties, overlap in some regions of the parameter space and, for simplification reasons, we group them into the "oceanic and mixed" group, with characteristics shown in Table 4-2. This simplification results in points in the parameter space, which do not belong to either individual groups and may even be unrealistic. On the other hand though, as discussed above for the oceanic aerosols, the distributions in the climatologies are indicative and they are not necessarily all-inclusive of the real world variability. In any case, even if this simplification introduces some unrealistic combinations of aerosol parameters in our training dataset, it is not that important, as long as the real variability is included as well, and the constructed NN performs well.

4.3.1.2. The characteristics of the simulated RSP measurements

The total intensity and linearly polarized intensity measurements are simulated for six VIS and NIR channels of the RSP instrument (412, 470, 555, 865, 1590 and 2250 nm) [Cairns et al., 1999] in reflectance units. Also, we approximate the linearly polarized intensity as $I_{lp} = Q$ (instead of $I_{lp} = \sqrt{Q^2 + U^2}$), since the measurements we use are close to the principal plane, where $U \sim 0$.

For the scattering geometry of the simulated measurements of our training dataset, we choose the difference in the azimuth angles between the sun and the RSP to be in the range of -

10^o to $+10^o$. We decided on this configuration, because a scan along the principal plane contains the most of the scattering angles, therefore providing the most information for the scattering properties of the aerosols. Furthermore, the measurements close to the scattering plane are less contaminated by the polarized water leaving radiance [Chowdhary et al. 2002, 2005]. However, this is not going to be the case for the polarimeters on future satellite platforms, where more out-of-plane configurations will be realized.

Furthermore, the sun zenith angle is in the range of 20^o to 45^o and the viewing angles of the RSP scan are from -70^o to 35^o (angles between $+35^o$ and $+70^o$ are vignetted by the aircraft hull). The height, where the RSP measurements are performed, is set at 4000 m. Although these values are based on the characteristics of the INTEX-B/MILAGRO campaign data (chapter 5), we do not consider them to pose any restrictions on the capabilities of our algorithm.

The RSP instrument noise is modeled using the formulas of Waquet et al. [2009] as white noise with width defined as:

$$\varepsilon_{I_i} = \sqrt{10^{-7} cos(\theta_o) R_{Ii} + \left(\frac{\Delta R_{Ii}}{R_{Ii}} \cdot R_{Ii}\right)^2} \tag{4-7}$$

$$\varepsilon_{Q_i} = \sqrt{10^{-7} cos(\theta_o) R_{Qi} + \left(\frac{\Delta R_{Qi}}{R_{Qi}} \cdot R_{Qi}\right)^2 + \left(0.001\left[R_{Ii} + \left|R_{Qi}\right|\right]\right)^2} \tag{4-8}$$

where ε_I is the width of the total intensity measurement noise, taking into account the shot noise (first component) and the calibration noise (second component). ε_Q is the width of the linearly polarized intensity measurement noise, which takes into account the above two sources of noise as well, but also the noise due to the polarimetric uncertainty (third component). R_I and R_Q denote the total intensity and linearly polarized intensity, respectively, in reflectance units, i denotes the measurement at a specific viewing angle and wavelength, θ_o

is the sun zenith angle, and $\frac{\Delta R}{R}$ is the relative calibration uncertainty. Although in Waquet et al, [2009] the calibration uncertainty is taken to be fixed to 3% for all wavelengths, this was not the case for the measurements performed during the INTEX-B/MILAGRO campaign, where the relative calibration uncertainty is[19] 3.4%, 2.6%, 3%, 2.8%, 3% and 3% for the corresponding RSP measurements at 412, 470, 555, 865, 1590 and 2250 nm.

[19] The values are provided by Dr. Brian Cairns.

Table 4-2. The distributions of the aerosol microphysical properties used for the simulations.

				min-max	distribution type	distribution mean	distribution width
oceanic and mixed aerosol properties	lognormal bimodal size distribution parameters		fine mode effective radius (μm)	0.1-0.3	lognormal	0.2	0.1
			fine mode effective variance	0.1-0.3	lognormal	0.18	0.1
			fine mode number density (number of particles/m^2)	0.01-10	lognormal	7	8
			coarse mode effective radius (μm)	1-3	lognormal	1.8	1.2
			coarse mode effective variance	1-2	lognormal	1.4	0.7
			coarse mode number density (number of particles/m2)	0.01-0.1	lognormal	0.04	0.04
	real refractive index		fine mode	1.33-1.6	normal	1.46	0.1
			coarse mode	1.3-1.41	normal	1.36	0.04
	imaginary refractive index	m_a	fine mode	0-0.03	lognormal	0.07	0.09
			coarse mode	0-0.006	lognormal	0.007	0.008
		m_b	fine mode	0-0.03	lognormal	0.07	0.09
			coarse mode	0-0.006	lognormal	0.007	0.008

Table 4-3. The surface characteristics, gases concentrations and the aircraft measurement geometries, used for the simulations.

		min-max	distribution type
ocean properties (case 1 waters)	wind speed (m/sec)	2-8	uniform
	chlorophyll concentration (mg/m^3)	0.06-2	uniform
atmospheric gas concentrations	water vapor (cm/atm)	1.5-4.5	uniform
	ozone (Db)	50-350	uniform
	nitrogen dioxide (ppb)	1-30	uniform
MBL height (m)		200-2000	uniform
geometry of the measurement	sun zenith angle (degrees)	20^o-50^o	uniform
	viewing angles (degrees)	197 angles from -70^o to $+35^o$	none (fixed values)
	difference in azimuth between the sun and the RSP (degrees)	-10^o - $+10^o$	uniform
	RSP height (m)	4000	none (fixed value)

4.3.1.3. Is the training dataset representative of the real-world cases?

It is apparent that the training dataset is not representative of all the real-world cases. In our opinion, its main deficiency is the assumption of the spherical particle shape. Although this is a quite common assumption for oceanic aerosols, it is gradually challenged by findings of non-spherical oceanic coarse mode particles, with the advance of more sophisticated retrieval

algorithms, which infer the particle shape, utilizing polarization information [Chowdhary et al., 2011]. Furthermore, the assumption of no-aloft plumes, the inadequate modeling of the refractive index and the restriction of the measurements geometry close to the principal plane, narrow the general character of the training dataset and, subsequently, the general applicability of our retrieval algorithm.

On the other hand though, as shown in the last section of this chapter, our retrieval is quite successful for the real-world cases, which are represented accurately in the training dataset. Subsequently, this work is closer to a proof of concept, than to a complete retrieval algorithm ready to be applied on any case, and it is in our future goals to extend its applicability by, ingesting the non-spherical character of the particles in our simulations (see discussion in chapter 6).

4.3.2. The neural network

As described in chapter 3, retrieval #2 uses two NNs in a cascading configuration and combines the multispectral, multiangle total and linearly polarized intensity measurements from RSP to retrieve the aerosol properties. A schematic is shown in Figure 4-4.

The first NN output, used as input in the second NN, designates an area in the parameter space, where the true value lies, in order to guide the search of the second NN towards the right direction. In this way, the learning process of the second NN becomes much faster, and its retrieval more robust, since any erratic behavior in it is suppressed. This was also shown in chapter 3, Figure 3-3, for the retrieved real refractive index and m_a parameter of the fine mode imaginary refractive index.

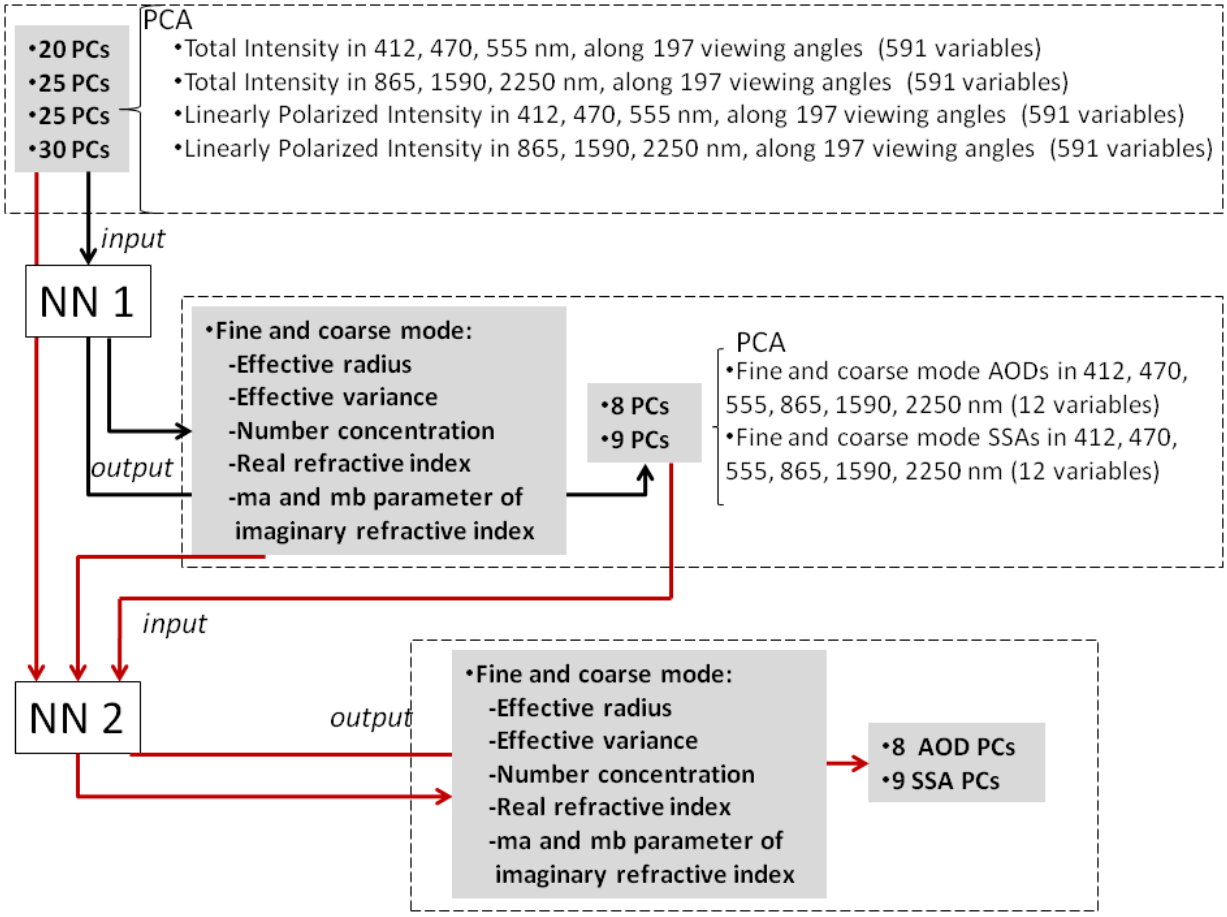

Figure 4-4. Retrieval #2 inversion scheme.

The training and testing of the first NN are similar to the ones of the second NN (with the same training and testing datasets used and same preprocess of the input with the PCA method). The total number of the simulated cases are ~26000. From those we randomly choose 60% (~15000 cases) for training and 40% (~11000 cases) for testing of the NNs. We consider the particular cases sufficient for the effective training and testing of the NNs, since

we achieve similar NN performances with fewer cases, but we use 15000 cases as a safer approach.

4.3.2.1. The preprocessing of the input with the PCA

The original input variables are the total intensity and the linearly polarized intensity of light in the six RSP wavelengths (412, 470, 555, 865, 1590 and 2250 nm), along 197 viewing angles of the RSP scan (from -70^o to 35^o)[20]. That amounts to a total of 2364 variables, a number quite large for a regression scheme to handle. Furthermore, the strong multicollinearities in the input variables inhibit the performance and the robustness of our inversion, as discussed in detail in chapter 3. In order to correct for these multicollinearities and to reduce the number of the input variables, we need to compress the input with the PCA method.

We performed the PCA separately for the total intensity measurements at 412, 470 and 555 nm (591 variables), for the total intensity measurements at 865, 1590 and 2250 nm (591 variables), for the linearly polarized measurements at 412, 470 and 555 nm (591 variables) and for the linearly polarized intensity measurements at 865, 1590 and 2250 nm (591 variables), in order to avoid any mixing of the physically different groups, as discussed in chapter 3. We also performed an additional PCA on the spectral AOT (12 variables) and on the spectral SSA (12 variables) of the output. The rest of the output variables are uncorrelated and do not need any preprocessing. The input also includes the output variables from the first NN, which are preprocessed in a similar way as the output of the second NN. Before the transformation of the

[20] The original RSP scan contains 152 viewing angles, whose actual values change for different scans. Thus, before they are used as input in our inversion scheme, the real measurements need to be interpolated to the fixed viewing angles used in our algorithm. With 197 angles we make sure that the fixed viewing angles will not be much different from the actual viewing angles of the RSP measurements and the angular scattering features of the measurements will be preserved.

input variables to their PCs, we need to standardize them by subtracting their mean and dividing them with their standard deviation as follows:

$$R_i' = \frac{R_i - mean(R_i)}{std(R_i)} \quad \text{or} \quad X_j' = \frac{X_j - mean(X_j)}{std(X_j)} \tag{4-9}$$

where R_i is the total intensity or the linearly polarized intensity in reflectance units, with i denoting the wavelength and the viewing angle of the corresponding measurement and X is one of the AOT or SSA variables.

PCA transforms the input and output into their PCs, which are orthogonal, with each of them expressing as much variability of the original dataset as possible. Thus, the 591 multispectral, multiangle variables of each group of the total intensity or the linearly polarized intensity are transformed into 591 PCs, the 12 AOT variables into 12 PCs and the 12 SSA variables into 12 PCs too. The first of these PCs express most of the variance of the original variables, whereas the last PCs contain mainly redundant information and/or noise. Thus, only few of the first PCs are used as input in the NN, with the discarded ones considered as not containing any valuable information for the inversion. In this way, along with the multicollinearities of the input, we eliminate part of its noise. In Figure 4-5 we show the denoising effect of PCA by comparing the denoised linearly polarized intensity measurements at 2250 nm after the PCA, with the corresponding noisy measurements, as well as the original noise-free measurements. We use the linearly polarized intensity in the 2250 nm channel to show how well the retained PCs reproduce the noise-free data, even for a difficult case, since the longer-wavelength linearly polarized intensity measurements have distinctive angular features, which are not smoothed out by the PCA. The denoised measurements are overall quite close to the original noise-free data.

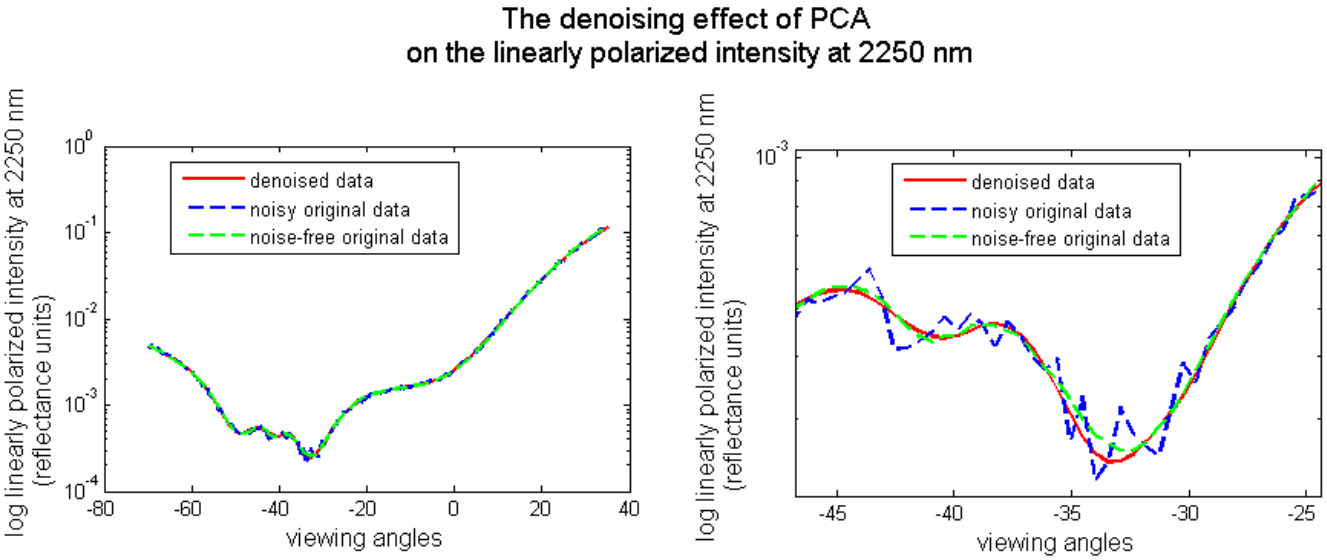

Figure 4-5. The denoising effect of PCA on the linearly polarized intensity at 2250 nm. (The right plot is a magnification of the left plot.)

4.3.2.1.1. Selection of the retained principal components

Unfortunately, it is difficult to assess the cut-off point between the PCs to be retained and the ones PCs to be discarded, since there are no universally applicable rules for its estimation, but it depends mainly on the particular characteristics of the scheme [Jolliffe, 2002]. One of the standard rules states that the retained PCs must include all the true variability of the dataset. This implies that, if the noise level of the dataset is ε% of the total variance, we should keep at least the first PCs that express the 100 – ε% of the total variance.

For the output variables $\varepsilon = 0$ and the retained PCs should express 100% of the original variables variance. For the input variables though, the PCs selection is not as straight forward.

Although we cannot retrieve anything from the noise, we know intuitively that some noise or redundancy gives some short of "flexibility" to the mapping process of our inversion, which is always useful. Moreover, as mentioned by Aires et al., [2004], retaining more PCs than necessary (up to a point) should not significantly affect the NN performance, except for making its training longer.

In order to effectively combine all the above issues, we follow a more practical approach for selecting the retained input PCs. We trained many NNs with different combinations of retained PCs for the groups of the total intensity and the linearly polarized intensity variables, and we evaluated their performance. At the same time we also checked, whether the retained PCs express at least the noise-free variance of the original measurements. The results of this exploration show that, for our retrieval scheme, the best performing NNs use more PCs than the ones, which include only the noise-free variance. Furthermore, if we use more PCs, the performance of the NN does not change, up to a point. Also, the sensitivity to the included noise seems to affect some of the retrieved aerosol parameters more than some others.

An example of the effect on the NN performance in retrieving the coarse mode effective radius, with different numbers of retained PCs, is shown in Figure 4-6. In particular, the x axis is the total intensity at 412, 470 and 555 nm PCs, the y axis is the linearly polarized intensity at 865, 1590 and 2250 nm PCs and the z axis is the R-square of the regression fit. For better visualization, the numbers of the retained PCs of total intensity at 865, 1590 and 2250 nm and of linearly polarized intensity at 412, 470 and 555 nm are held constant to 20 and 25, respectively. A similar plot for the m_b parameter of fine mode imaginary refractive index is shown in Figure 4-7. As seen in the figures, different combinations of retained PCs affect the

retrieval of m_b parameter more than the retrieval of effective radius. This is expected, since the m_b parameter retrieval is more demanding and, thus, more affected by the retained noise in the system. Studying similar plots for all retrieved parameters from the NN, we determined that an optimal combination of retained PCs for our scheme is 20 PCs of the total intensity at 412, 470 and 555 nm, 25 PCs of the total intensity at 865, 1590 and 2250 nm, 25 PCs of the linearly polarized intensity at 412, 470 and 555 nm, 30 PCs of the linearly polarized intensity at 865, 1590 and 2250 nm, 8 PCs of spectral AOT and 9 PCs of spectral SSA.

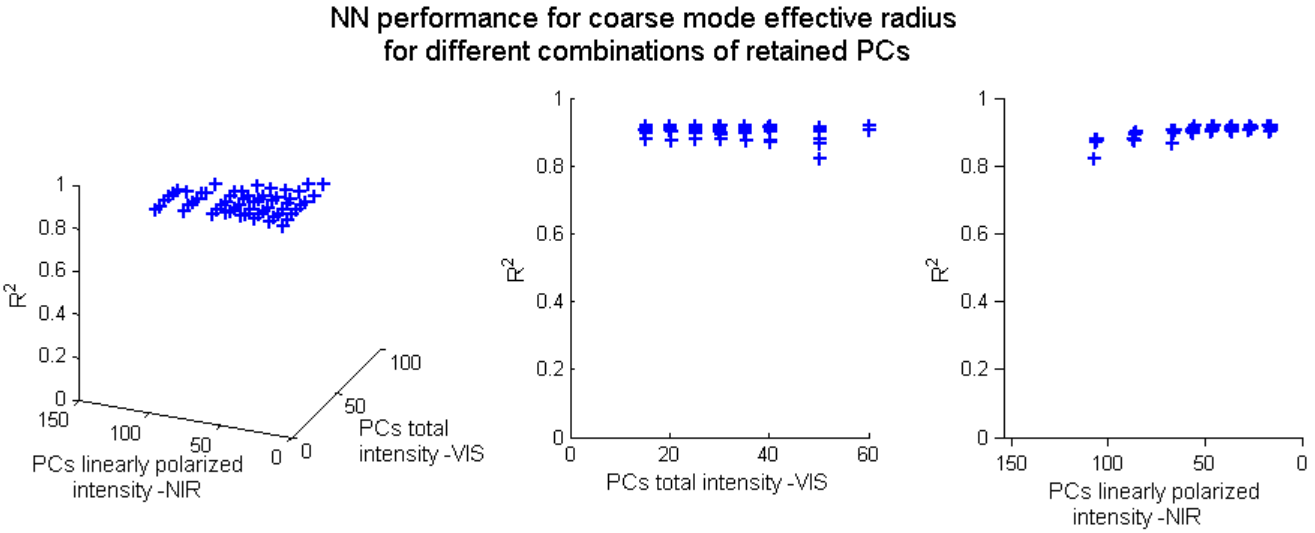

Figure 4-6. The NN performance (R-square) for the coarse mode effective radius, for different combinations of retained PCs. The retained PCs of total intensities at 412, 470 and 555 nm ("total intensity –VIS") are plotted on the x axis and the retained PCs of linearly polarized intensities at 865, 1590 and 2250 nm ("linearly polarized intensity –NIR"), are plotted on y axis . The retained PCs of total intensities at 865, 1590 and 2250 nm and of linearly polarized intensities at 412, 470 and 555 nm, are 20 and 25, respectively.

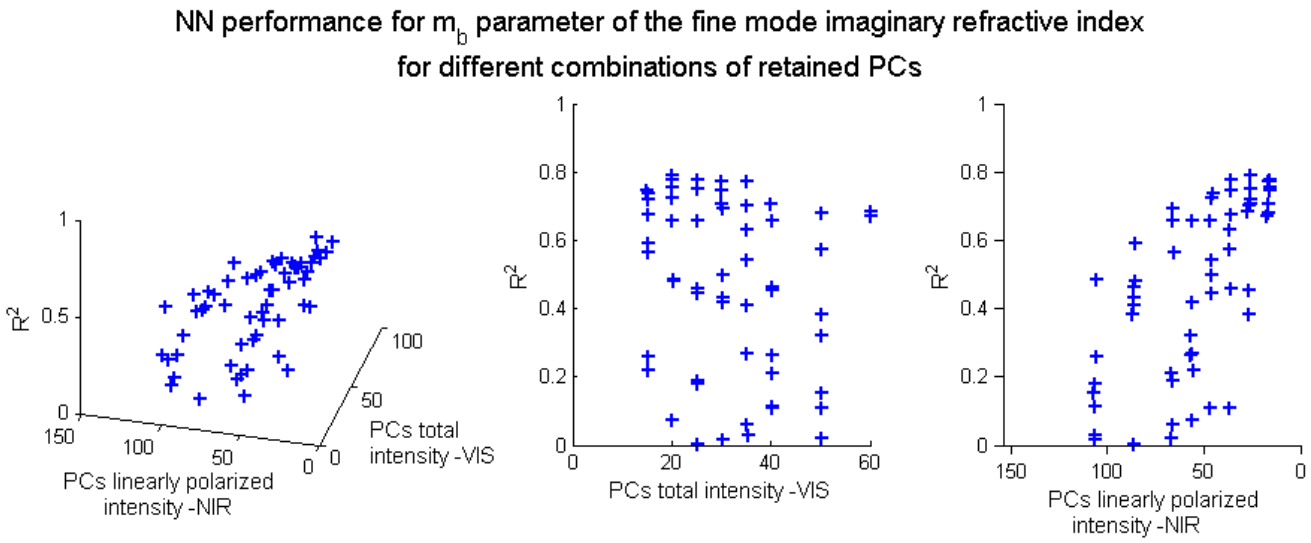

Figure 4-7. As for Figure 4-6, for the m_b parameter of fine mode imaginary refractive index.

4.3.2.2. The neural network architecture

In order to decide on the number of nodes in the hidden layer of our one-hidden-layer NN, we performed several tests which showed that a sufficient number of nodes is the number of input variables in the NN. However, since our tests were not extensive, this conclusion is not a definite one and needs further investigation.

4.3.2.3. The training of the neural network

Before using the input and output variables to train the NN, we need to standardize them as follows:

$$PC_k' = \frac{PC_k - mean(PC_k)}{std(PC_k)} \quad \text{or} \quad X_j' = \frac{X_j - mean(X_j)}{std(X_j)} \tag{4-10}$$

where PC_k is a principal component in the groups of the total intensity or the linearly polarized intensity of the input, or of the AOT or SSA of the output and k is its order (first, second, etc.). X_j is any of the output unprocessed variables.

The training of the second NN required 50000 iterations, lasted ~16 hours and resulted in a total MSE of 0.18, as shown in Figure 4-8. Although it is not shown here, the training is much faster than the training of the first NN, since it is guided from the first NN output. In Figure 4-9 we show, as an example, the training performance of fine mode real refractive index.

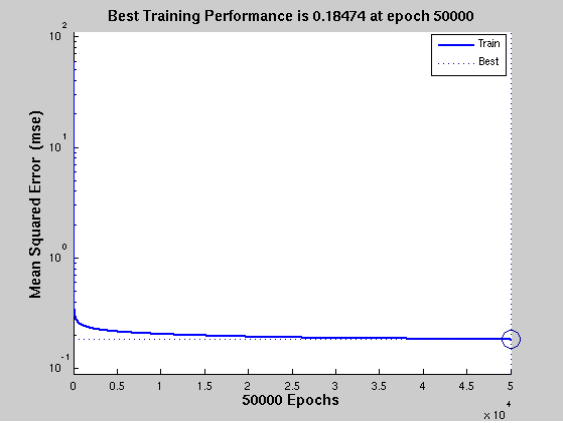

Figure 4-8. The NN training performance.

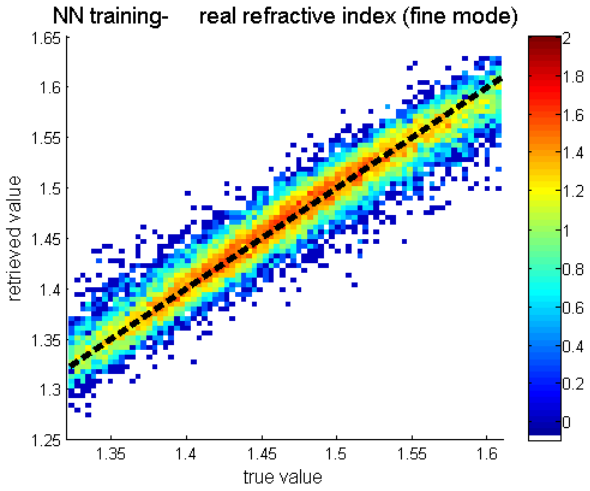

Figure 4-9. NN training performance for fine mode real refractive index. The plot is the log-density scatter plot of true versus retrieved values. The black dashed line is the 1-1 line

4.3.2.4. Testing the neural network with simulated data

A comparison of the testing performance for retrievals #1, #2, #3 and #4 is shown in Table 4-4, at the end of this section. The retrieval #2 NN performance, for the simulated testing dataset, is shown in Figure 4-10 for the fine and coarse effective radius and the fine mode refractive index, in Figure 4-11 for the fine mode AOT at 412 and 555 nm and in Figure 4-12 for the fine mode SSA at 412 and 555 nm. The testing performance for all retrieved aerosol properties, is included in Appendix III. In particular, the first plot in every row is the log-density scatter plot, of true versus retrieved values. The black dashed line is the 1-1 line. The second plot shows the fractional RMSE of the retrieval, multiplied by 100, along the considered range of the true values. The third plot shows the percentage of the testing cases that fall within one standard deviation of the specified uncertainty in Mishchenko et al., [2007] (black circles) and two

standard deviations (red crosses). Considering the retrieval uncertainty to be normally distributed[21], the uncertainty goal is reached, if the one-standard deviation percentage exceeds 66%. A more stringent requirement is for the two-standard deviations percentage to exceeds 99%.

The fractional RMSE plot provides valuable information for the retrieval performance in different parts of the parameter space. For most of retrieved parameters the performance is, as expected, better in the densely populated areas, where the NN training weights more heavily, and worse close to the minimum and maximum cut-off points of the space.

Furthermore, from the third plot, we see that the retrieved aerosol microphysical properties (Figure 4-10) fulfill the reported accuracy requirements. The only exception is the spectral SSA (Figure 4-12), which is retrieved successfully though at 555 nm and the fine mode AOT at 412 nm, for values larger than 0.5 (Figure 4-11).

[21] This assumption is generally true, as can be inferred from the density scatter plots of the retrieved parameters.

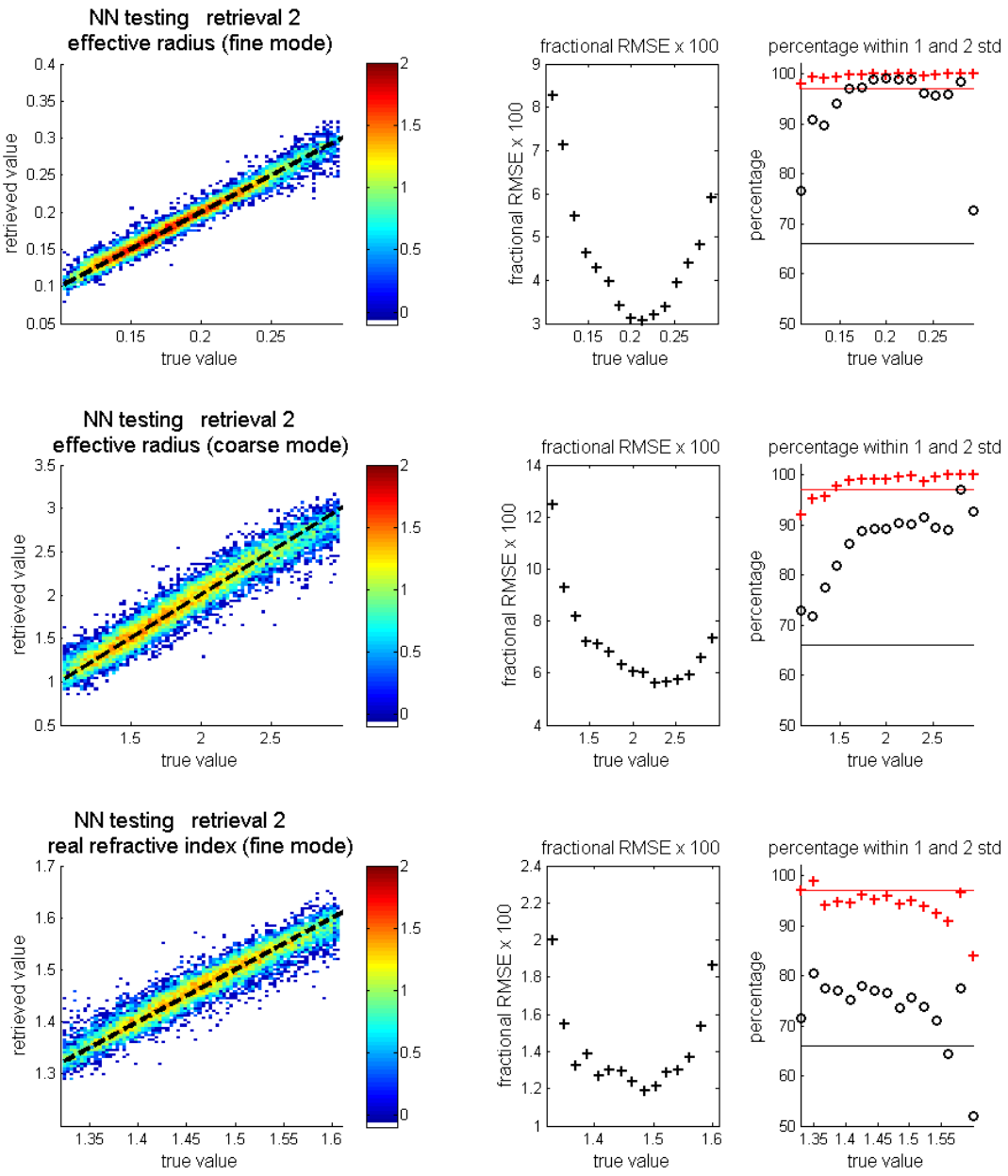

Figure 4-10. Retrieval #2 NN testing performance, for fine and coarse effective radius and fine mode real refractive index. In every row, the first plot is the log-density scatter plot of true versus retrieved values. The black dashed line is the 1-1 line and the color bar denotes the log number of testing cases. The second plot shows the fractional retrieval RMSE along the considered range, multiplied by 100. The third plot shows the percentage of the testing cases that fall within one standard deviation (black circles), or two standard deviations (red crosses)

of the required uncertainty. The uncertainty goal is reached if the one-standard deviation percentage is larger than 66% (black line) and the two-standard deviations percentage is larger than 99% (red line).

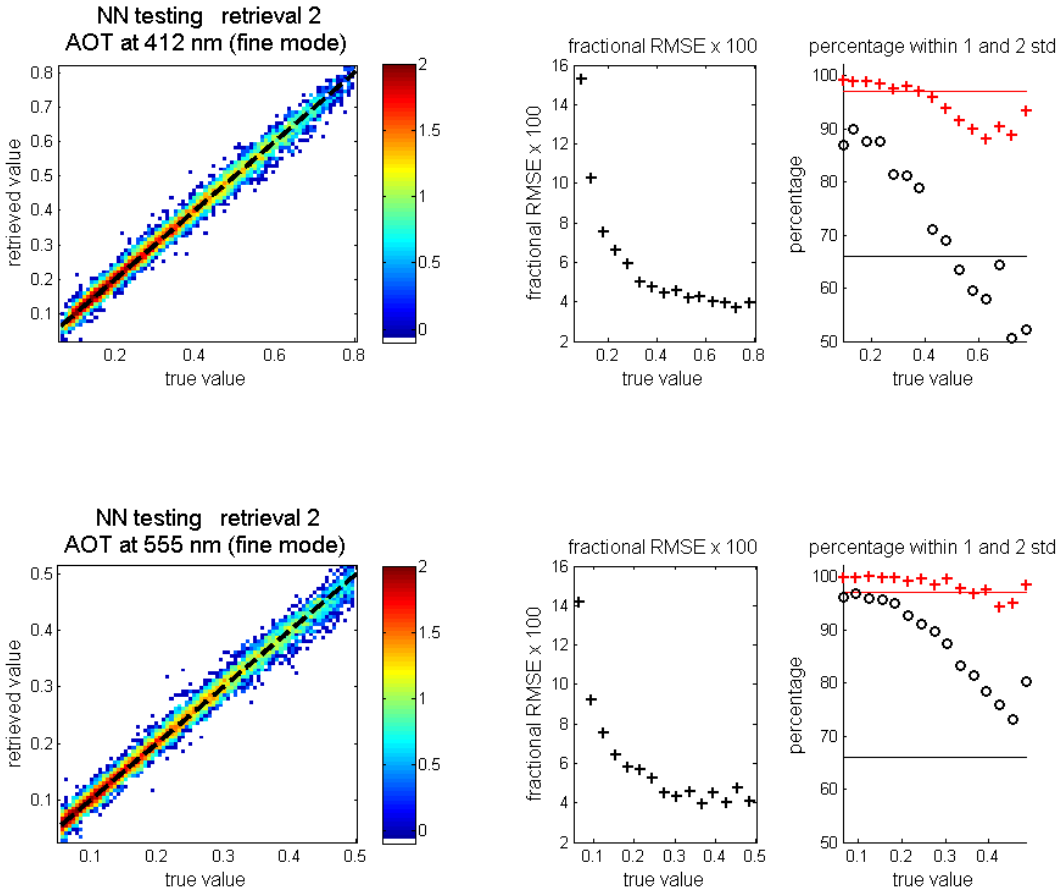

Figure 4-11. The same as for Figure 4-10, for the fine mode AOT in 412 and 555 nm.

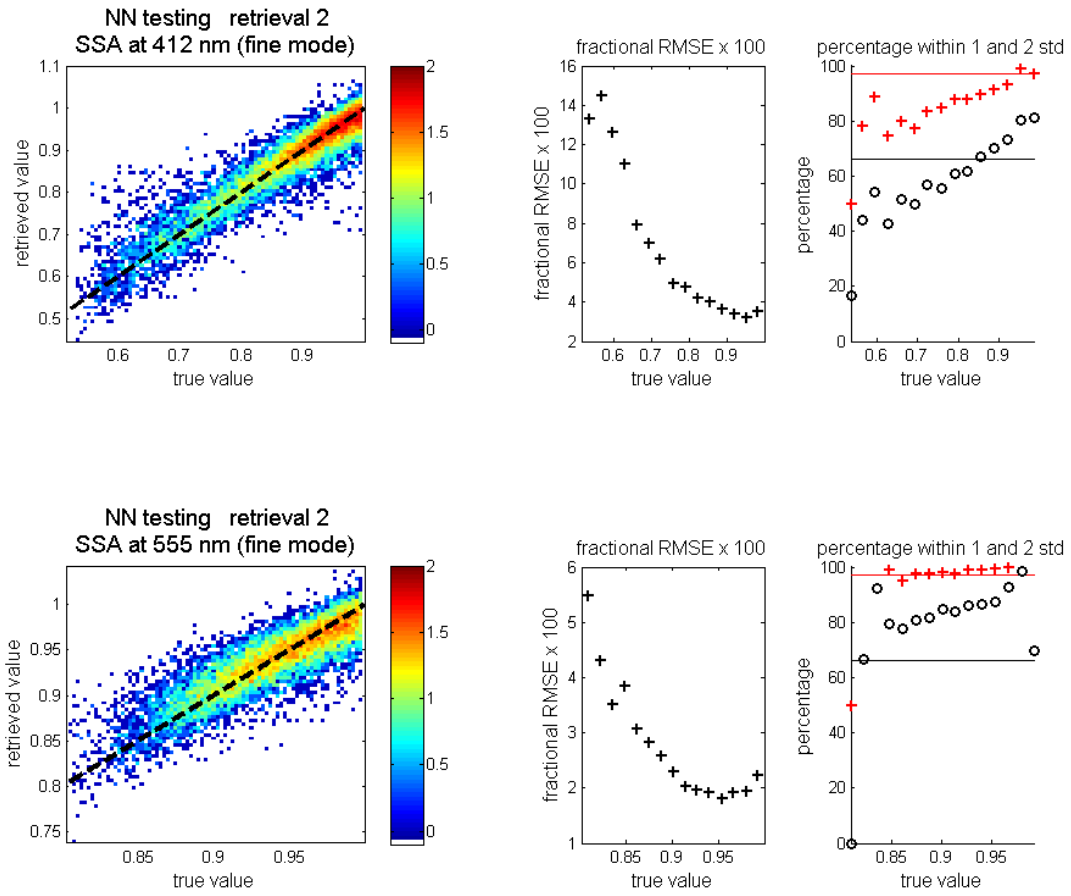

Figure 4-12. The same as for Figure 4-10, for the fine mode SSA in 412 and 555 nm.

The testing performance for retrieval #3 is also included in Appendix III. Table 4-4 shows the comparison of retrieval approach #1, #2, #3 and #4, based on their testing mean fractional RMSE and their mean percentage falling within one standard deviation and two standard deviations of the required uncertainty.

Table 4-4. Comparison of the explored retrieval approaches.

			retrieval #1			retrieval #2		
			mean fractional RMSE x 100	mean % within 1 std	mean % within 2 std	mean fractional RMSE x 100	mean % within 1 std	mean % within 2 std
fine mode	effective radius		5.5	92	99	4.6	93	100
	effective variance		13.1	92	100	11.7	99	100
	number density		19.6	-	-	16.9	-	-
	AOT at 555 nm		6.4	83	98	6	88	98
	SSA at 555 nm		3	70	97	2.8	78	95
	real refractive index		1.6	60	83	1.4	73	94
	imaginary refractive index	m_a	112	-	-	75.3	-	-
		m_b	110	-	-	53.4	-	-
coarse mode	effective radius		7.8	78	94	7.1	87	98
	effective variance		9.3	100	100	9	100	100
	number density		23.6	-	-	21.7	-	-
	AOT at 555 nm		9	98	100	8.1	99	100
	SSA at 555 nm		2.5	77	94	2.5	88	99
	real refractive index		0.4	99	100	0.4	98	100
	imaginary refractive index	m_a	74.7	-	-	89	-	-
		m_b	141.1	-	-	116.3	-	-

Table 4-4. (Continued)

			retrieval #3			retrieval #4		
			mean fractional RMSE x 100	mean % within 1 std	mean % within 2 std	mean fractional RMSE x 100	mean % within 1 std	mean % within 2 std
fine mode	effective radius		7.9	84	98	4.8	94	100
	effective variance		19.7	91	100	12.4	99	100
	number density		29.5			18.2		
	AOT at 555 nm		8.6	75	94	6.2	86	99
	SSA at 555 nm		4.1	70	89	2.8	88	99
	real refractive index		3.4	32	56	1.6	71	94
	imaginary refractive index	m_a	70.7	-	-	52.5	-	-
		m_b	84.1	-	-	50.4	-	-
coarse mode	effective radius		13.4	60	88	7.7	84	98
	effective variance		11.8	100	100	9.4	100	100
	number density		30.9	-	-	22.2	-	-
	AOT at 555 nm		15.3	89	100	8.8	97	100
	SSA at 555 nm		4	70	97	2.5	83	100
	real refractive index		1	83	97	0.5	99	100
	imaginary refractive index	m_a	71.5	-	-	65.3	-	-
		m_b	96.2	-	-	75.3	-	-

Chapter 5

Testing the constructed algorithm on RSP measurements from the INTEX-B/MILAGRO campaign

5.1. Data description

The RSP measurements used in this study were conducted during the Megacity Initiative: Local and Global Research Observations (MILAGRO) campaign, over the Mexico City metropolitan area during March of 2006. The objective of the MILAGRO campaign was to record the emissions from Mexico City, one of the largest megacities in the world, and analyze their impact regionally as well as globally [Molina et al., 2010]. The RSP was deployed on the J-31 aircraft during the Intercontinental Chemical Transport Experiment-B (INTEX-B) field campaign of MILAGRO, which focused on the characterization of transcontinental/ intercontinental transport of gases and aerosols and their impact on the climate. Figure 5-1 shows the geographic extent of the INTEX-B campaign, along with the other campaigns conducted during MILAGRO.

Figure 5-1. The geographic coverage of MILAGRO campaigns. The INTEX-B campaign took place in the "large" blue color area of the map (source: [Molina et al., 2010]).

The J-31 aircraft payload, together with the RSP (Figure 5-2), included the Ames Airborne Tracking Sun-photometer (AATS), the Solar Spectral Flux Radiometer (SSFR), the Cloud Absorption Radiometer (CAR) and other sensors, which provided positioning, orientation and meteorological information during the flights. Table 5-1 lists the instruments on board, with a brief description of their data products [Molina et al., 2010].

Figure 5-2. The RSP mounted on the J-31 aircraft during the INTEX-B/MILAGRO campaign (source: [Russell et al., 2007]).

Table 5-1. Instruments on board the J-31 aircraft during the INTEX-B/MILAGRO campaign (source: [Molina et al., 2010]).

Instrument Name	Data Products
Research Scanning Polarimeter (RSP)	Polarized radiance, aerosol, cloud and Earth surface properties
Ames Airborne Tracking Sunphotometer (AATS)	Aerosol optical depth and extinction, water vapor column and profile
Solar Spectral Flux Radiometer (SSFR)	Solar spectral flux
Cloud Absorption Radiometer (CAR)	Radiance, aerosol, cloud and Earth surface properties
Navigation, Meteorology, and Data Acquisition System (NavMet)	Pressure, temperature, humidity
Position and Orientation System (POS)	Aircraft position and orientation

It is against this data set that we tested our algorithm on two RSP images, files #22 and #51, acquired on the first and second flight of J-31 aircraft on March 10th (Figure 5-3). The RSP file #22 and #51 flight characteristics (sun zenith angle θ_o, difference in azimuth angles $\Delta\phi$ and time of the measurements), are shown in Table 5-2. For the selection of the particular scenes, we explored the atmospheric vertical profile of the aerosol scattering ratio at 532 nm and the aerosol depolarization ratio at 532 nm from the High Spectral Resolution Lidar (HSRL) data (section 5.1.3). Furthermore, for validating our retrieval results, we used the AATS AOT data (section 5.4) and the retrieved values for RSP file #53 and #55, reported in Chowdhary et al., [2011][22].

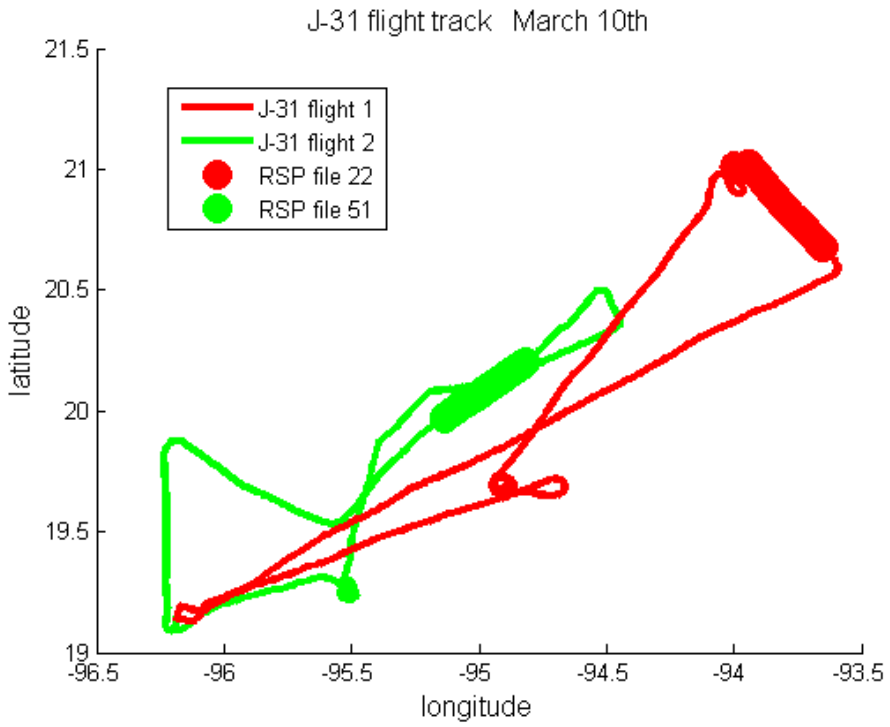

Figure 5-3. The J-31 aircraft flights on March 10th. The RSP file #22 (red) was acquired during the first flight and the RSP file #51 (green) was acquired during the second flight.

[22]The measurements of RSP file #53 and #55 were performed during the second flight, as for RSP file #51, which we use to test our retrieval.

Table 5-2. RSP file #22 and #51 flight characteristics.

	sun zenith angle (θ_o) range (degrees)	difference in azimuth ($\Delta\phi$) angles range (degrees)	time (UTC)
RSP file #22	31 - 32.4	0.78 - 11	17 - 17.13
RSP file #51	38.7 - 39.6	-12.7 - 0.26	20.55 - 20.66

5.1.1. The RSP instrument

The RSP instrument measures the I, Q and U Stokes light parameters in the following bands in the VIS and NIR : 412 (30), 470 (20), 555(20), 672 (20), 865 (20), 960 (20), 1590 (60), 1880 (90) and 2250 (120) nm, where the values in parenthesis express the full width at half maximum bandpass [Cairns et al., 1999]. The measurements of I, Q and U are performed simultaneously for all wavelengths, using paired telescopes that measure the linearly polarized components of intensity along the 0° and 90° axis and along the 45° and 135° axis. Furthermore, each scan acquires measurements at 152 angles over the angular range of ±70° from nadir.

The RSP measures the normalized radiances:

$$i = \frac{I\pi}{F_o} \quad q = \frac{Q\pi}{F_o} \quad u = \frac{U\pi}{F_o} \tag{5-1}$$

where F_o is the solar constant in $^{W}/_{m^2\mu m}$. Before using them as input in our retrieval, we transform them in reflectance units, as follows:

$$R_I = \frac{i \cdot r_o^2}{cos(\theta_o)} \qquad R_Q = \frac{q \cdot r_o^2}{cos(\theta_o)} \qquad R_U = \frac{u \cdot r_o^2}{cos(\theta_o)} \tag{5-2}$$

where θ_o is the solar zenith angle and r_o is the solar distance in AU, with both values provided in the RSP files.

Furthermore, the position and the orientation information of the particular flights, recorded with the POS instrument onboard the J-31 aircraft, are also provided in the RSP files. The available information includes the date and time, the longitude and latitude coordinates of the track, the flight height, the solar zenith angle, along with the aircraft pitch, roll and heading angles (Figure 5-4). These angles are measured with some uncertainty, which propagates into the uncertainty of the measurement geometry and affects the accuracy of the retrieval. The largest errors in the retrieval are caused from the uncertainty in the pitch angle, which results in misplacement of the viewing angles in the scan [Knobelspiesse et al., 2011a]. As described in section 5.3.1, we correct for this effect, using as a steady point of reference the sun glint angular position of the degree of linear polarization at 2250 nm.

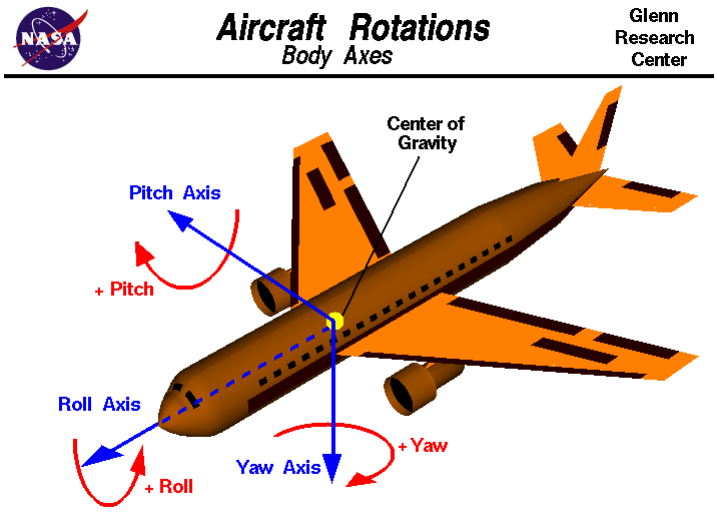

Figure 5-4. The pitch, roll and yaw angles of the aircraft orientation (source: Glenn Research Center –NASA).

In our retrieval we use the I and Q[23] measurements, i.e. the total intensity and the linearly polarized intensity of light, in the six RSP spectral bands: 412, 470, 555, 865, 1590 and 2250 nm, in conformity with the NN construction. The measurements of the 960 and 1880 nm bands are contaminated by water vapor absorption and are used mainly for estimating the water vapor content and identify any cirrus clouds in the scene. Also, the 672 nm band is sensitive to chlorophyll fluorescence [Chowdhary et al., 2005] and is not used in our retrieval.

Furthermore, the RSP measurements used as input in our algorithm, were averaged over 20 consecutive scans (see section 5.3.2). Finally, before ingesting the averaged measurements in our retrieval, we interpolate their values at the 152 RSP viewing angles, so as to match the 197 viewing angles used in our algorithm.

5.1.2. The AATS instrument

The AATS instrument measures the transmission of the direct solar beam through the atmosphere and calculates the total column AOT in 14 wavelengths (from 354 nm to 2139 nm) [Redemann et al., 2009].

[23] As discussed in chapter 4, we use Q instead of $\sqrt{Q^2 + U^2}$, as a proxy for the linearly polarized intensity of light, since the measurements considered here are performed close to the principal plane.

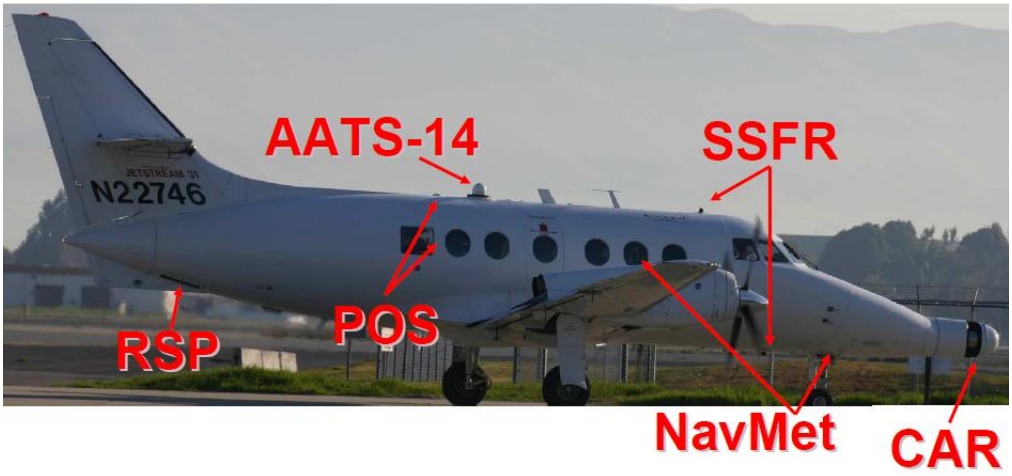

Figure 5-5. The instruments locations on the J-31 aircraft during the INTEX-B/MILAGRO campaign (source: [Russell et al., 2007]).

The AATS is located at the top of the J-31 aircraft and measures the AOT above it, whereas the RSP is located at the bottom and measures the AOT below the aircraft (Figure 5-5). Thus, in order to validate the retrieved AOT from the RSP measurements at the high-altitude flights, we have to use the AATS data from the low-altitude flights. Since the RSP and the AATS AOT data are not collocated, there is always the possibility to be different, since the AOT can vary even for close-by measurements. We estimate this variation from the spatial variation in AOT, measured with the AATS along the track and we assign it as the AATS AOT uncertainty, along with the uncertainty reported for the AATS AOT data. The selected segments for the estimation of the AATS AOT spatial variability are shown in Figures 5-6 and 5-7, for RSP file #22 and #51, respectively. Furthermore, the AATS AOT from the low-altitude flights does not take into account the aerosols between the low-altitude and the ocean surface, but we do not consider that the particular aerosol load is substantial, since the aircraft flies at an altitude of ~50 – 60

m. In summary, although we do not have collocated RSP and AATS measurements for the total spectral AOT, we can perform a comparison between their values, taking into account their spatial variability.

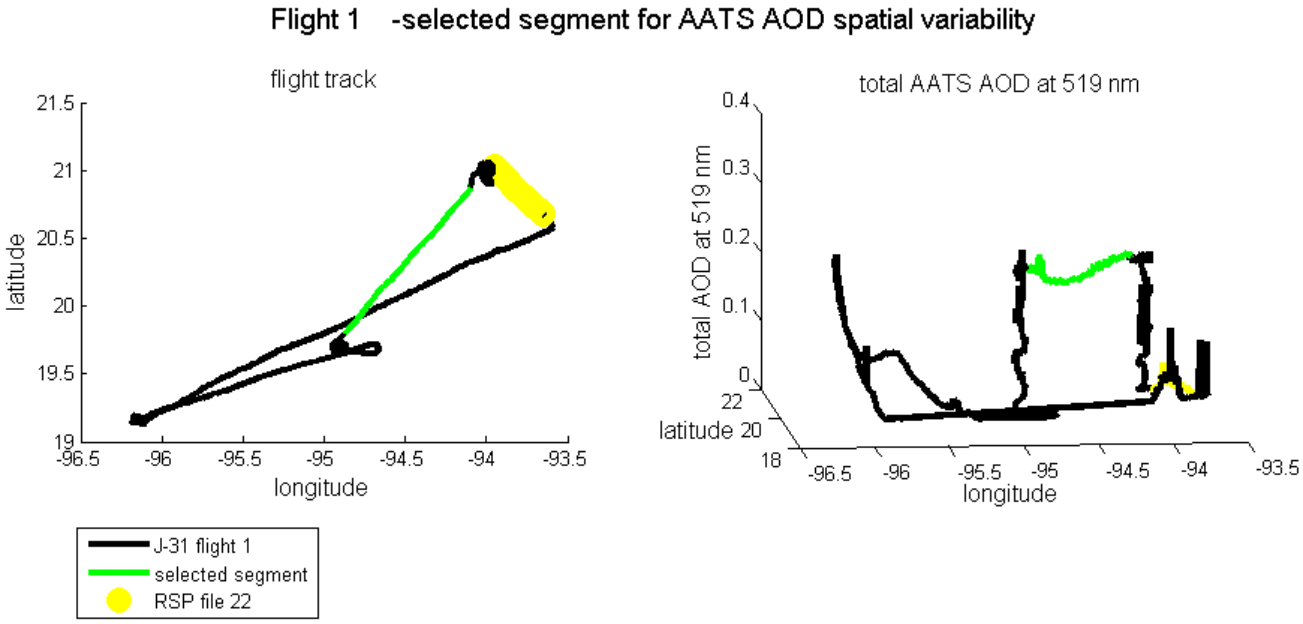

Figure 5-6. Selected segment for the estimation of the AATS AOT spatial variability, for flight 1 (RSP file #22).

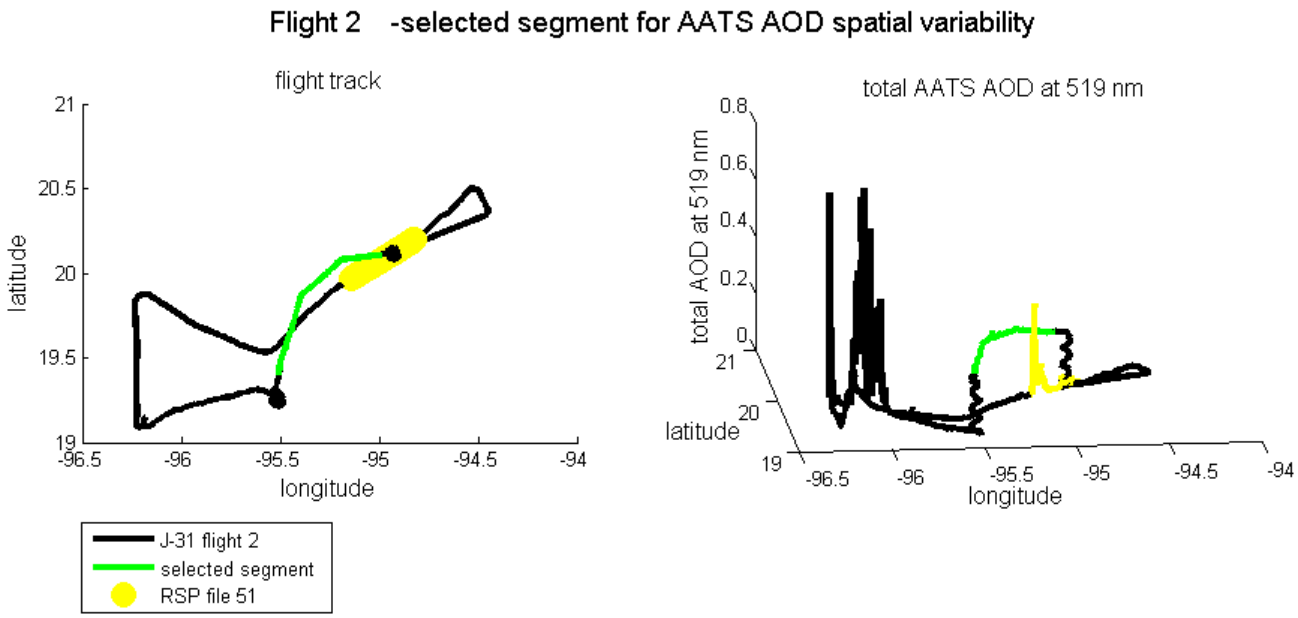

Figure 5-7. The same as Figure 5-6, for flight 2 (RSP file #51).

5.1.3. The HSRL instrument

During the INTEX-B/MILAGRO campaign, the HSRL instrument was mounted on the NASA LaRC King Air B-200 aircraft and measured the aerosol backscatter and depolarization at 532 and 1064 nm and the aerosol extinction at 532 nm. From these measurements we can infer the aerosol scattering ratio R_{532} and the aerosol depolarization ratio δ_{a532} at 532 nm, as follows [Hair et al., 2008]:

$$R_{532} = \frac{\beta_{m532}+\beta_{a532}}{\beta_{m532}} \tag{5-3}$$

$$\delta_{a532} = \frac{\beta_{a532}^{\perp}}{\beta_{a532}^{\parallel}} \tag{5-4}$$

where β_{a532} is the aerosol backscatter coefficient at 532 nm, $\beta_{a532}^{\perp}$ and $\beta_{a532}^{\parallel}$ are its components for the vertical and parallel polarized light, respectively, and β_{m532} is the molecular backscatter coefficient at 532 nm.

The aerosol scattering ratio is a measure of the aerosol abundance in the scene. We use it to identify the MBL height and the existence of aloft plumes and/or clouds. The aerosol depolarization ratio provides information about the shape of the particles in the scene. In particular, as shown in Omar et al., [2009], we consider that the "upper limit" of the aerosol depolarization ratio for spherical particles is 0.05, with larger values indicating the existence of non-spherical particles.

5.2. Selection of the scenes

Our algorithm is designed to retrieve the properties of spherical particles in cloud-free, aloft-plumes-free atmospheres above the open ocean. Thus, in order to test its performance, we need to find RSP measurements performed above scenes with similar characteristics. Using the HSRL data we identify the 10th of March 2006, as the day that satisfies most closely these requirements.

On March 10th the J-31 aircraft performed two flights, from which we acquire the #22 and #51 RSP files, respectively (Figure 5-8). During the first flight, the aircraft was synchronized with the NASA LaRC King Air B-200 aircraft, carrying on board the HSRL instrument. Unfortunately, there are no HSRL data for the second flight, which took place ~3 hours later (the time difference is shown in Figure 5-8). Nevertheless, we note that the general characteristics of the scene vertical distribution, inferred by the HSRL data, remained the same for the second flight, since the time interval is not that long.

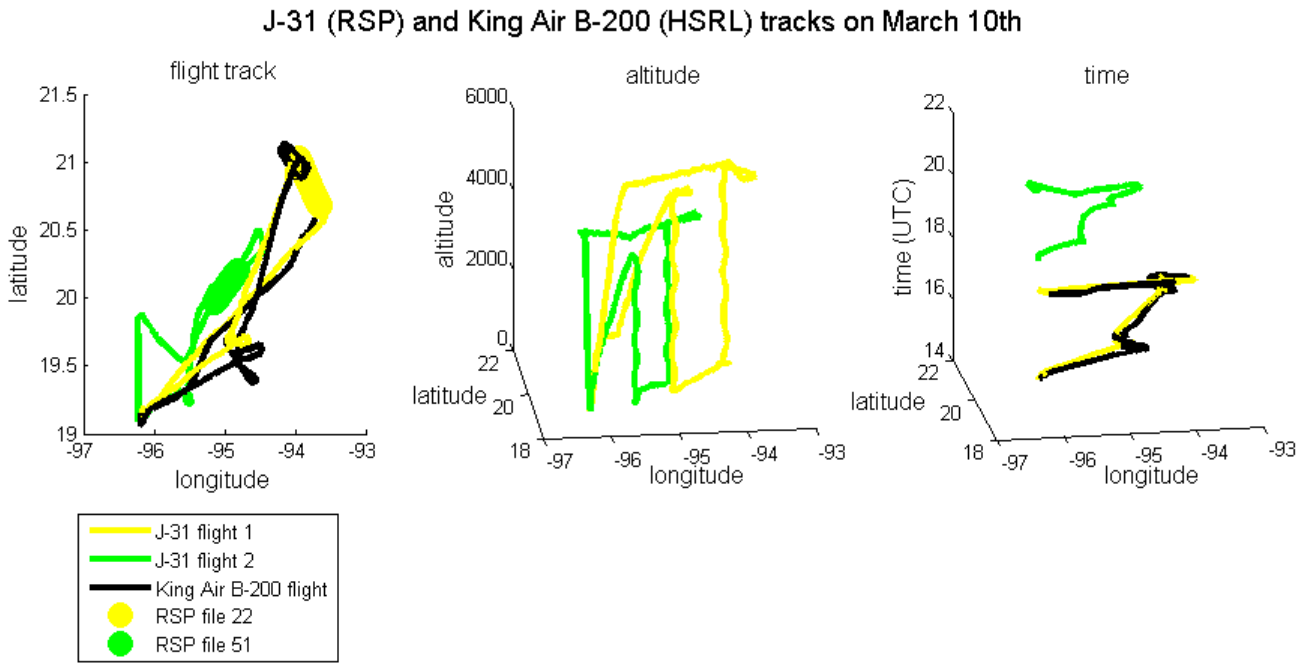

Figure 5-8. The J-31 aircraft flight track, altitude and time (yellow and green, for first and second flight respectively), along with the RSP file #22 (yellow) and #51 (green) and the NASA LaRC King Air B-200 aircraft flight track (black), on March 10th.

The aerosol scattering ratio at 532 nm (Figure 5-9 –plotted here as $(R_{532}-1)$ though) shows a well-formed MBL at ~500 m (with $(R_{532}-1)\approx 5$), no clouds and no aloft plumes, with only a quite thin layer of aerosols (with $(R_{532}-1)\approx 1$) extending up to 4 km. From the aerosol depolarization ratio at 532 nm (Figure 5-10) we see that the MBL contains spherical particles ($\delta_{a532}<0.05$), whereas the thin layer above contains non-spherical particles as well ($\delta_{a532}\leq 0.15$). Although our retrieval algorithm is not designed to handle non-spherical particles, the particular scene we are using is the most suitable one in the MILAGRO campaign.

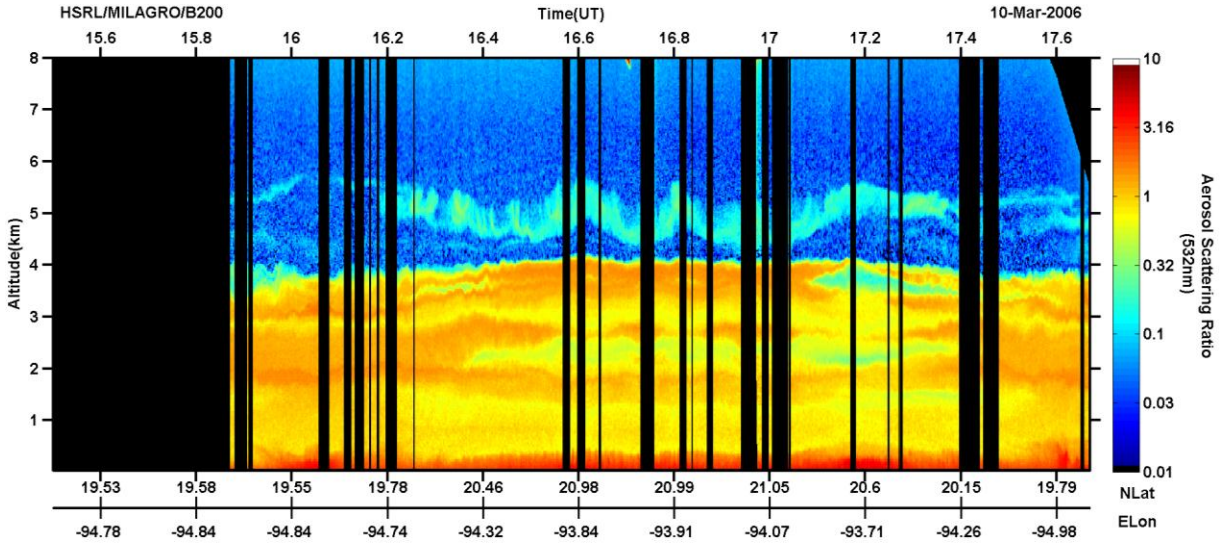

Figure 5-9. The aerosol scattering ratio at 532 nm $(R_{532} - 1)$ measured by the HSRL on March 10th, during the INTEX-B/MILAGRO campaign (source: NASA Langley Research Center (LaRC)).

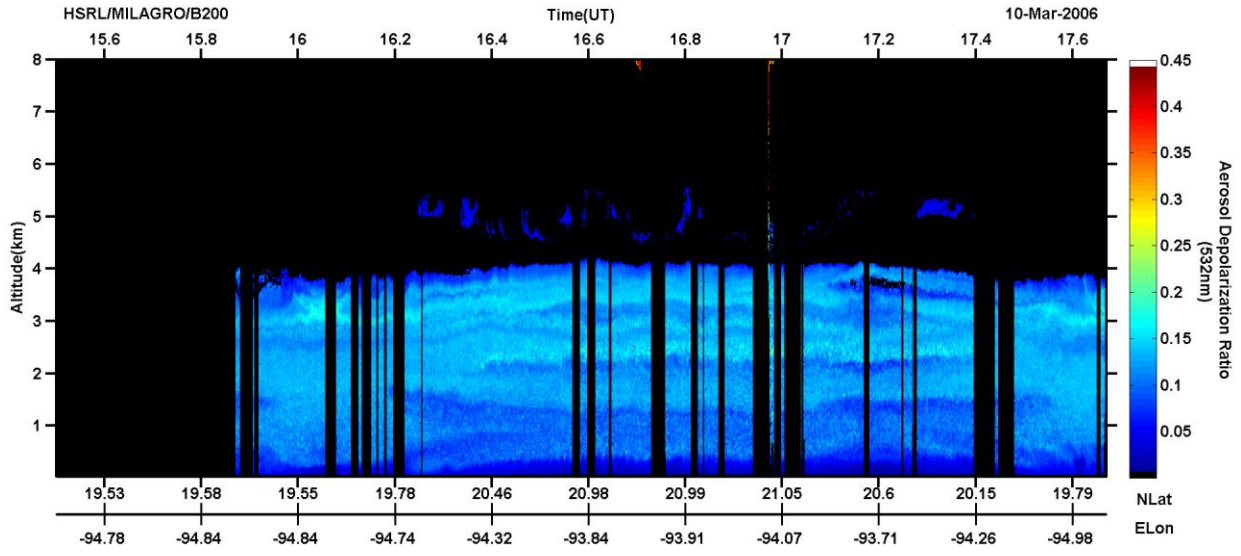

Figure 5-10. The aerosol depolarization ratio at 532 nm (δ_{532}) measured by the HSRL on March 10th, during the INTEX-B/MILAGRO campaign (source: NASA Langley Research Center (LaRC)).

5.3. RSP data

5.3.1. Correction for the pitch angle of the aircraft

Before using the RSP measurements as input in our retrieval algorithm, we have to correct them for misalignments due to the aircraft pitch angle. Corrections for the aircraft heading, yaw and roll angles also need to be applied, but they are not performed in this study. In any case though, for small heading, yaw and roll angles, the effect of the pitch angle is the most important for our retrieval, as mentioned above.

We correct for the pitch angle effect (the uncertainty in the viewing angles of the measurement), using the position of the sun glint as a steady reference of the real viewing angles[24]. The degree of linear polarization at 2250 nm and close to the sun glint is not greatly affected by aerosol scattering. We simulate the degree of linear polarization at 2250 nm for an aerosol-free scene and we compare it with the real measurements. The difference in the position of the sun glint for the two spectra is approximately the correction we need to apply to the real data to eliminate the pitch angle effect. The measurements in file #51 are corrected by $\sim 1.5^{o}$ (Figure 5-11), whereas for file #22 no correction was necessary.

[24] This method was proposed by Dr. Jacek Chowdhary.

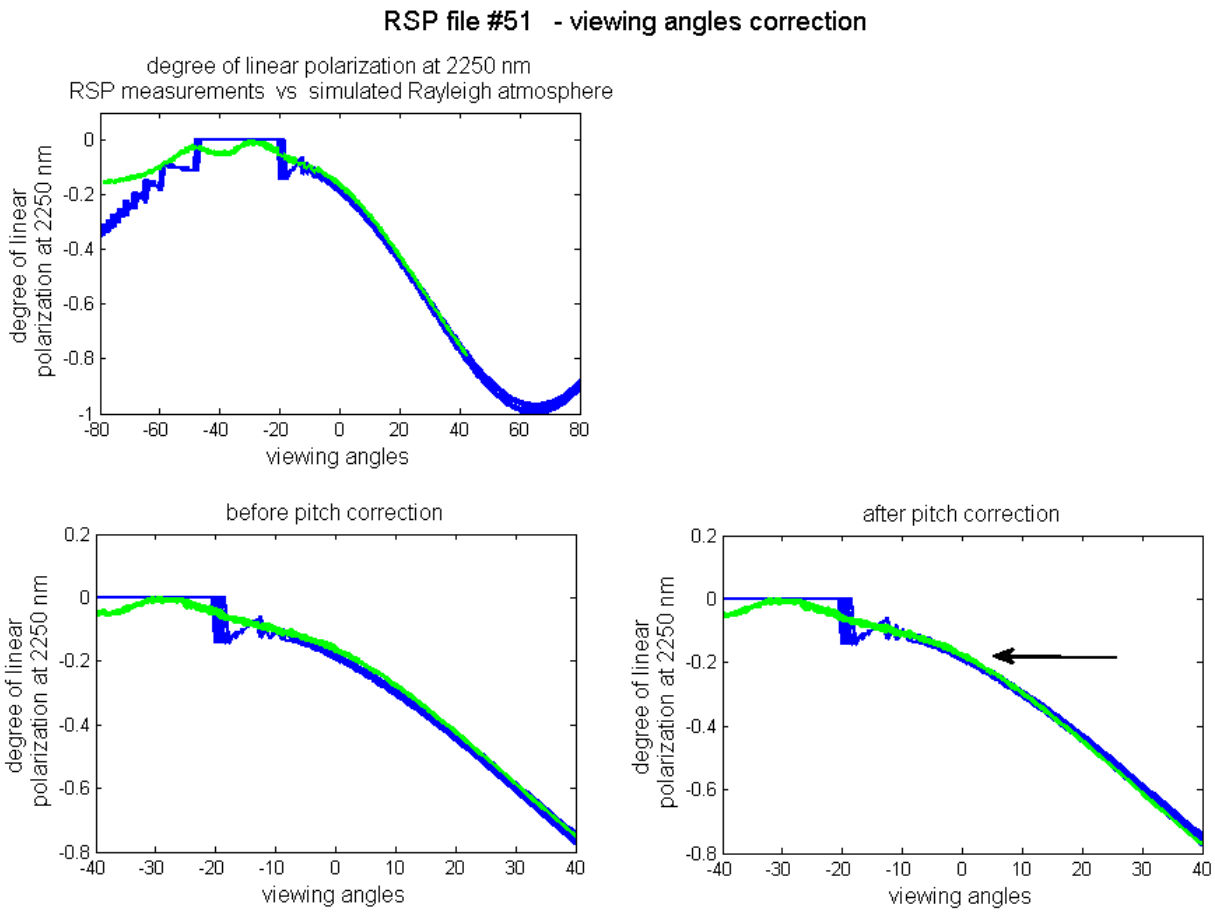

Figure 5-11. Viewing angles correction for pitch angle effect. The green line indicates the RSP measurements, whereas the blue line indicates the simulated measurements.

5.3.2. Selection of the measurements

The RSP files #22 and #51, from the first and second flights, are shown in Figure 5-3 and their characteristics are given in Table 5-2. We selected the particular files based on the following criteria:

- The measurements are performed close to the principal plane. The difference between the azimuth angle of the sun and the azimuth angle of the RSP is in the range of -10^{o} to +10^{o}.
- The pitch and roll angles of the aircraft are as close as possible to zero.

In Figure 5-12 we plot the difference in azimuth, the pitch and the roll angles of file #22 scans used. A similar plot for file #51 is shown in Figure 5-13.

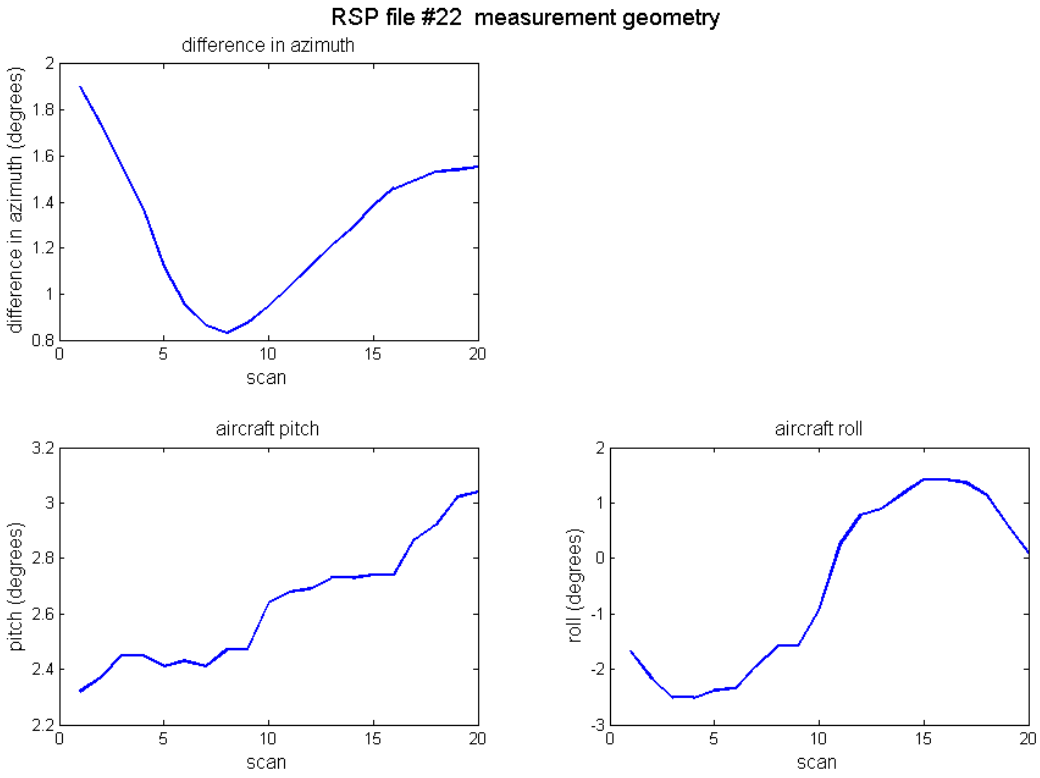

Figure 5-12. The measurement geometry of the scans used from RSP file #22. The difference in azimuth, the pitch and roll angles.

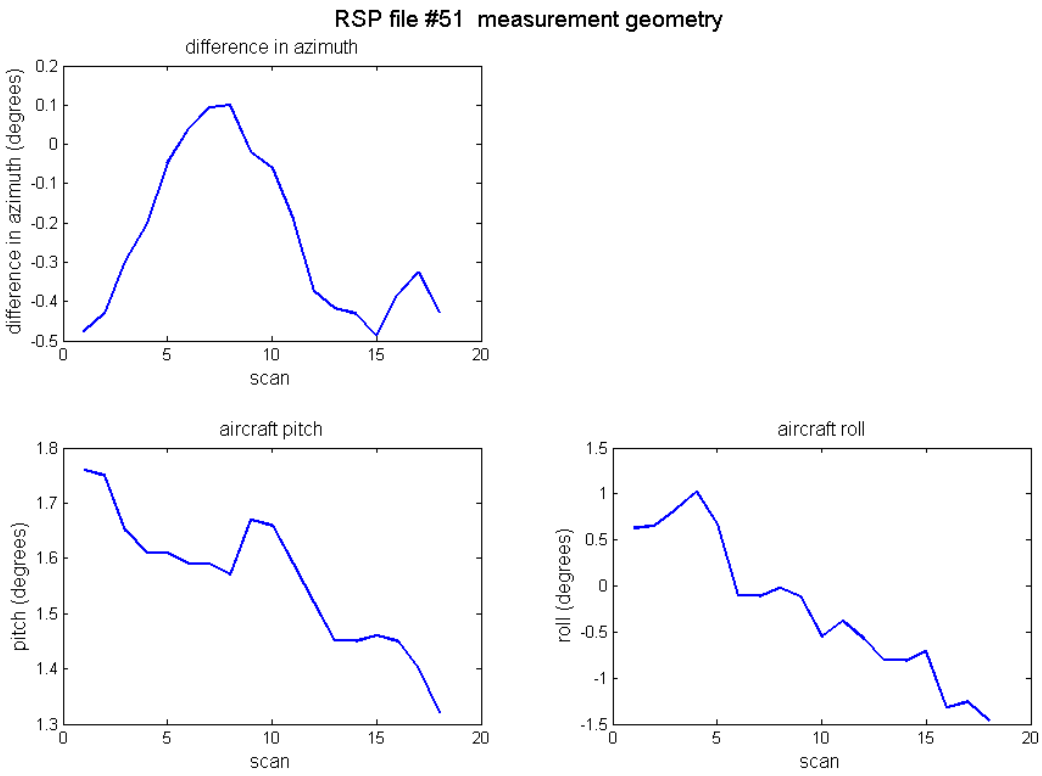

Figure 5-13. Same as Figure 5-12, for RSP file #51.

5.4. Aerosol properties retrieval

We retrieved the aerosol properties of the selected scenes using the retrieval approach #1, #2, #3 and #4. Table 5-3 and 5-4 show the retrieved values[25] for the RSP file #22 and #51, respectively, and compares them with the ones retrieved by Chowdhary et al. [2011] from the RSP files #53 and #55 for the same day.

[25] AOT and SSA values are provided only for 555 and 2250 nm.

Table 5-3. Retrieved aerosol properties from RSP file #22, applying retrieval approaches #1, #2, #3 and #4, and retrieved properties from RSP file #53 and #55, from Chowdhary et al. [2011].

		RSP file #22				RSP file #53 and #55
		retr. #1	retr. #2	retr. #3	retr. #4	Chowdhary et al., [2011]
effective radius	fine mode	0.17	0.11	0.14	0.1	**0.15**
	coarse mode	1.6	1.6	2	1.31	**2**
effective variance	fine mode	0.16	0.21	0.16	0.32	**0.1**
	coarse mode	1.6	1.55	1.5	1.42	**1**
number concentration	fine mode	4.15	9.68	9.57	23.23	**-**
	coarse mode	0.08	0.12	0.11	0.12	**-**
real refractive index	fine mode	1.37	1.41	1.38	1.42	**1.40 - 1.46**
	coarse mode	1.36	1.35	1.23	1.33	**1.39 - 1.45**
m_a parameter of imaginary refractive index	fine mode	0	0	0.0001	0.0002	**-**
	coarse mode	0.18	0.07	0.0008	0.005	**-**
m_b parameter of imaginary refractive index	fine mode	0.037	0.0001	0.63	0.0001	**-**
	coarse mode	0.025	0.0002	0.0001	0.003	**-**
AOT 555 nm	fine mode	0.18	0.13	0.14	0.16	**0.15**
	coarse mode	0.09	0.09	0.12	0.13	**0.08**
SSA 555 nm	fine mode	1	1	0.77	1	**0.94**
	coarse mode	0.7	0.76	0.95	0.8	**1**

Table 5-4. The same as Table 5-3, for RSP file #51.

		RSP file #51				RSP file #53 and #55
		retr. #1	retr. #2	retr. #3	retr. #4	Chowdhary et al., [2011]
effective radius	fine mode	0.11	0.12	0.14	0.12	**0.15**
	coarse mode	2.4	2.1	1.55	2	**2**
effective variance	fine mode	0.28	0.19	0.18	0.18	**0.1**
	coarse mode	1.96	2.42	1.34	2	**1**
number concentration	fine mode	12.23	5.44	8.83	6.82	**-**
	coarse mode	0.05	0.14	0.08	0.06	**-**
real refractive index	fine mode	1.58	1.54	1.36	1.5	**1.40 - 1.46**
	coarse mode	1.36	1.39	1.32	1.36	**1.39 - 1.45**
m_a parameter of imaginary refractive index	fine mode	0.0025	0.0004	0	0.005	**-**
	coarse mode	0.0002	0.0001	0.003	0.001	**-**
m_b parameter of imaginary refractive index	fine mode	0	0.0002	0.12	0	**-**
	coarse mode	0.074	0.006	0	0.007	**-**
AOT 555 nm	fine mode	0.19	0.09	0.18	0.14	**0.15**
	coarse mode	0.07	0.07	0.1	0.08	**0.08**
SSA 555 nm	fine mode	0.97	1	0.86	0.95	**0.94**
	coarse mode	0.92	0.93	0.9	0.86	**1**

In order to verify our results we first feed them into the forward model and check how well they reproduce the RSP measurements.

In trying to assess the performance, it is clear that the retrievals #2 and #4 seem to provide the best matchups against the estimates of Chowdhary et al. [2011], which actually take into account the non-spherical shape of the particles in the scene. Furthermore, we see in general that we retrieve the fine mode properties relatively better than the coarse mode properties, which seems reasonable, since the coarse mode particles are the non-spherical ones. In addition, our retrieval of file #51 seems to be closer to Chowdhary et al. [2011] retrieval, which is also reasonable since they were acquired during the same flight.

In addition, from the retrieved microphysical distributions, we can calculate the total spectral AOT in the RSP bands. The retrieved aerosol properties are validated by plotting the AOT calculated using their values ("reconstructed AOT"), against the AOT from the AATS measurements. Small differences between the AATS and RSP wavelengths exist but can be properly interpolated for our purposes.

Figures 5-14 and 5-15 show the AOT plots of the retrievals #1, #2, #3 and #4 for the #22 and #51 RSP files, respectively. In the plots, along with the reconstructed total spectral AOT from the retrieved aerosol properties (full blue circles), we also include the total spectral AOT, which is directly retrieved from the corresponding measurements (open red circles). Their uncertainties are set equal to 0.02, which is the required accuracy of retrieved AOT [Mishchenko et al., 2007]. Remember that the uncertainties derived from the NN testing do not apply in these cases, since they involve non-spherical particles. The AATS total spectral AOT

(black curve) is plotted also, along with its uncertainty, which includes the reported uncertainty of the AATS data and its spatial uncertainty, as described in section 5.1.2.

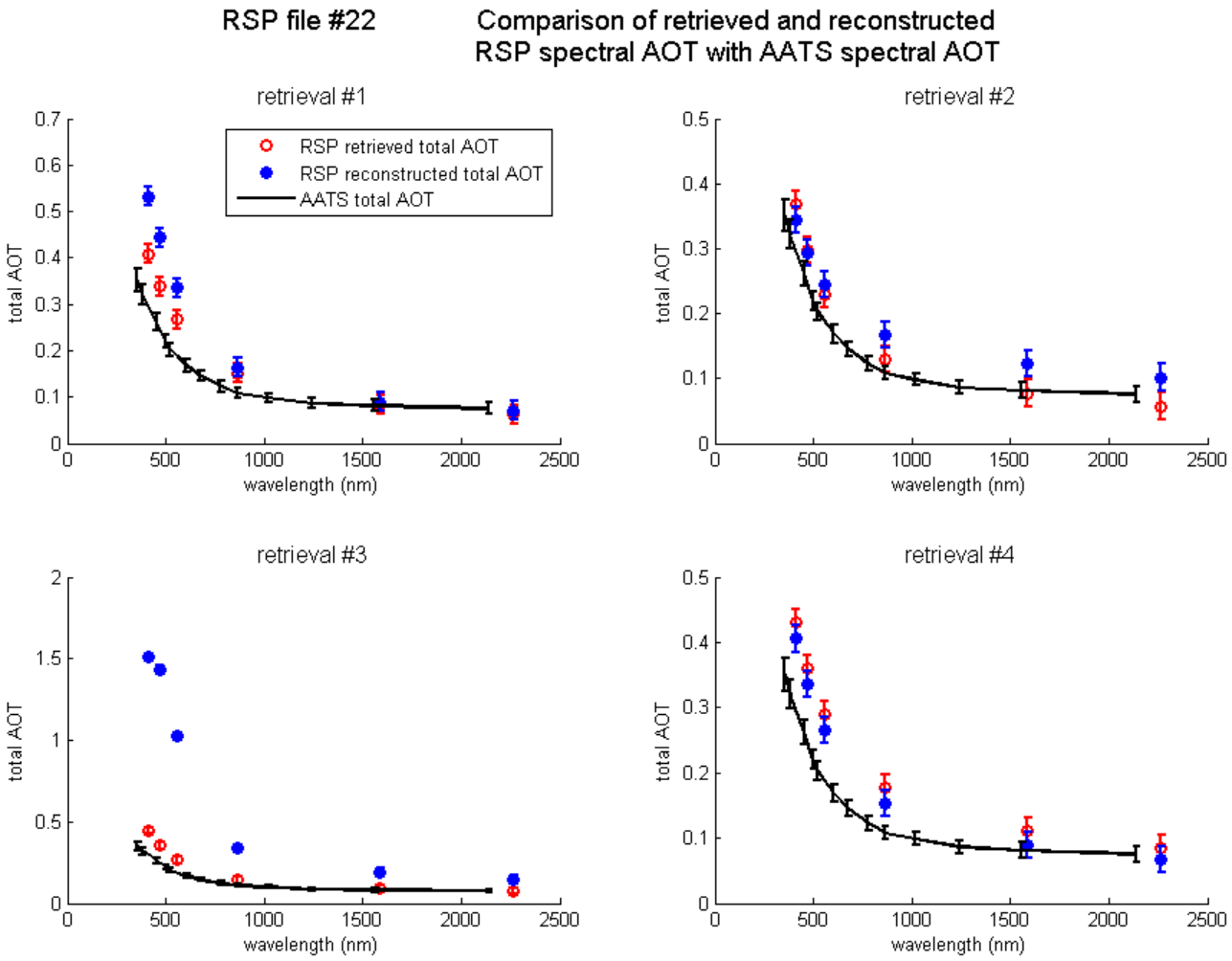

Figure 5-14. Comparison of AATS total spectral AOT (black curve), with retrieved (open red circles) and reconstructed (filled blue circles) total spectral AOT from retrievals #1, #2, #3 and #4, for RSP file #22.

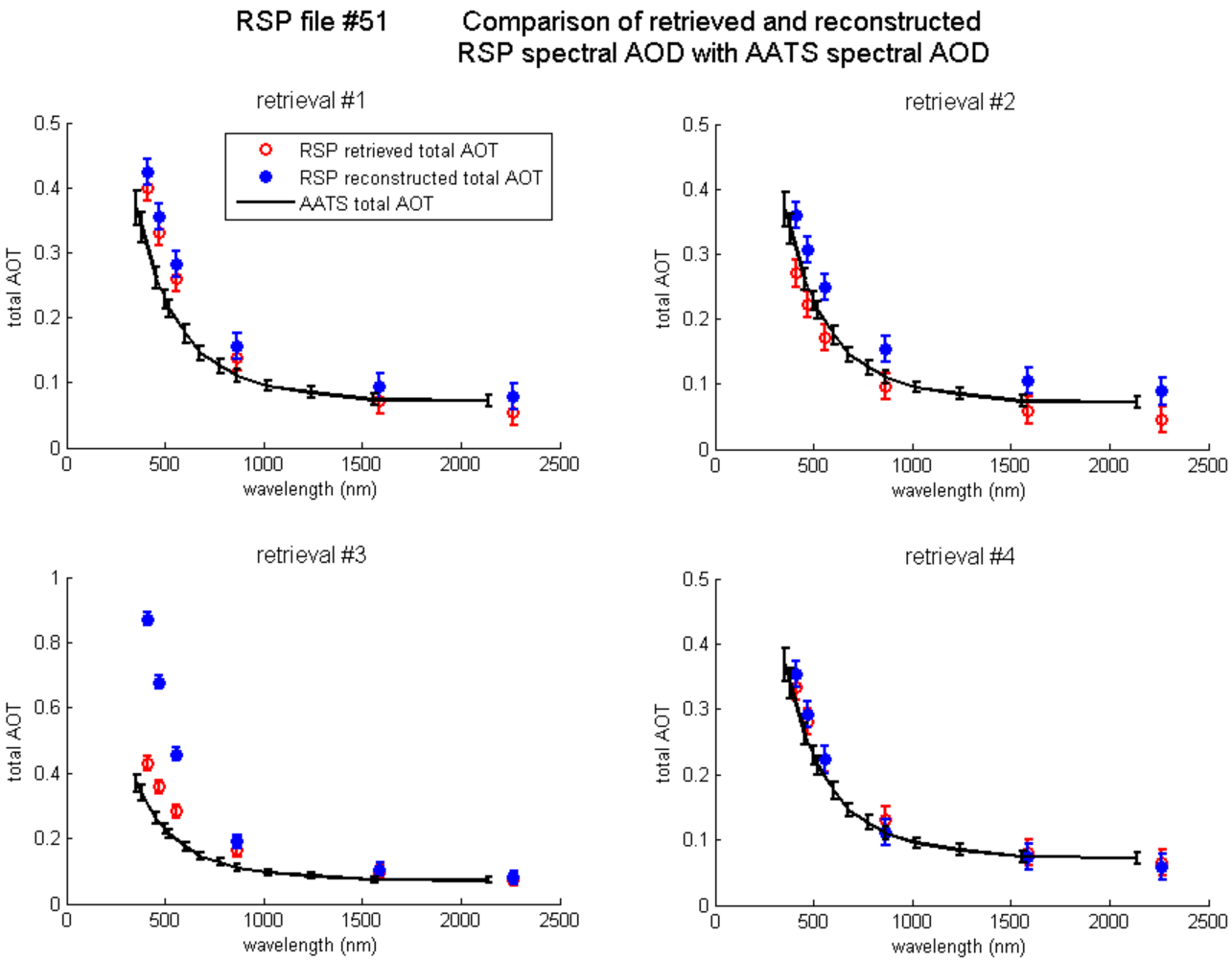

Figure 5-15. Same as Figure 5-14, for RSP file #51.

It is obvious from the results in Figure 5-14 and 5-15, that retrieval #3, which uses only total intensity measurements, fails the validation test. That was more or less expected, since the total intensity measurements do not contain all the necessary information for accurately retrieving the aerosol properties, as it was mentioned also in chapters 3 and 4. Furthermore, for both cases, retrieval #1 performs worse than retrieval #2, highlighting the importance of the second NN in the cascading scheme of retrieval #2.

Figures 5-16 and 5-17 show the fit of total and linearly polarized intensity measurements at 555 and 2250 nm from RSP files #22 and #51, with the respective reconstructed measurements using the retrieved aerosol properties from retrieval #2 and #4. (The fit for the measurements in all RSP bands is included in Appendix IV).

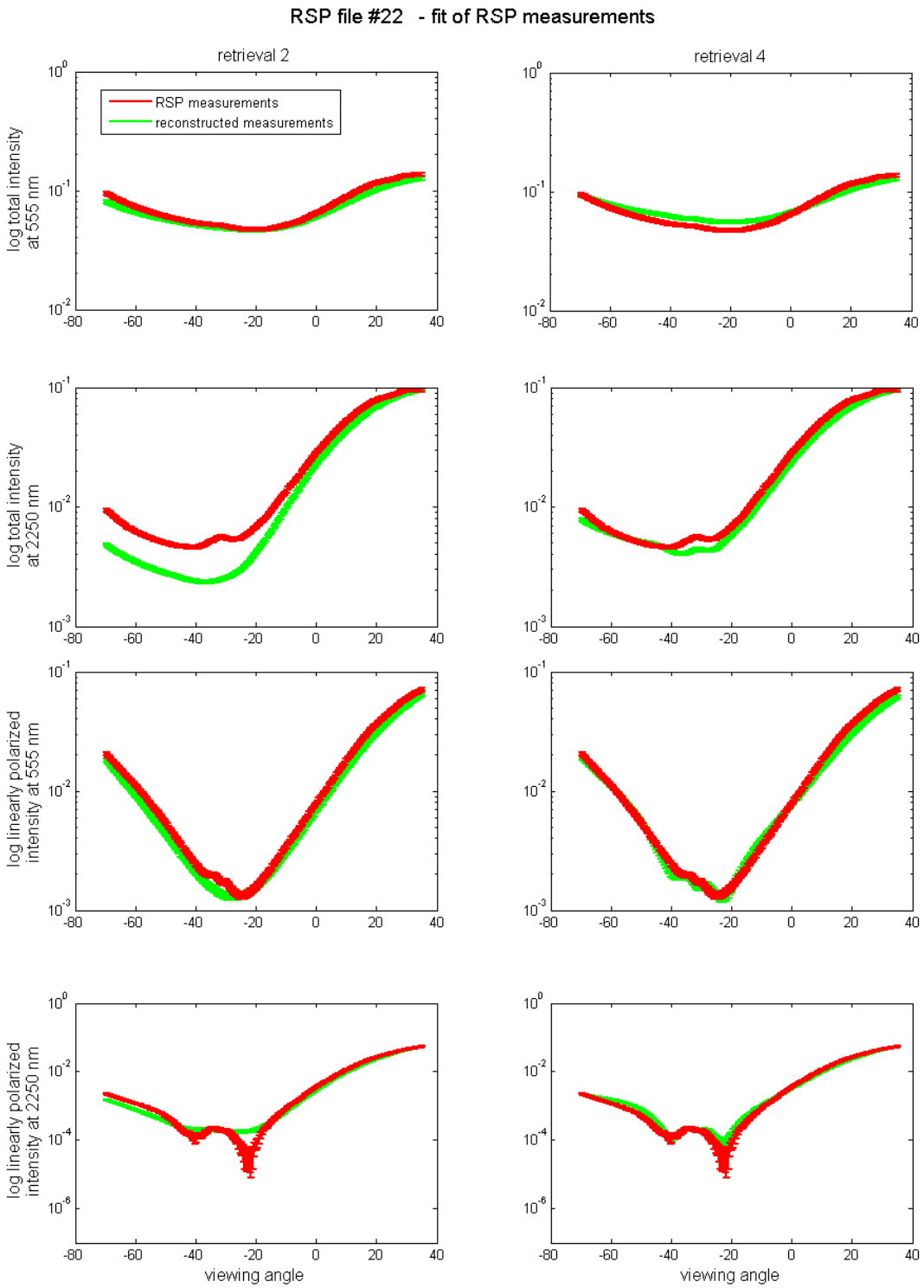

Figure 5-16. Fit of the total and linearly polarized intensity measurements of RSP file #22, with reconstructed measurements using the retrieved aerosol properties from retrieval #2 and #4.

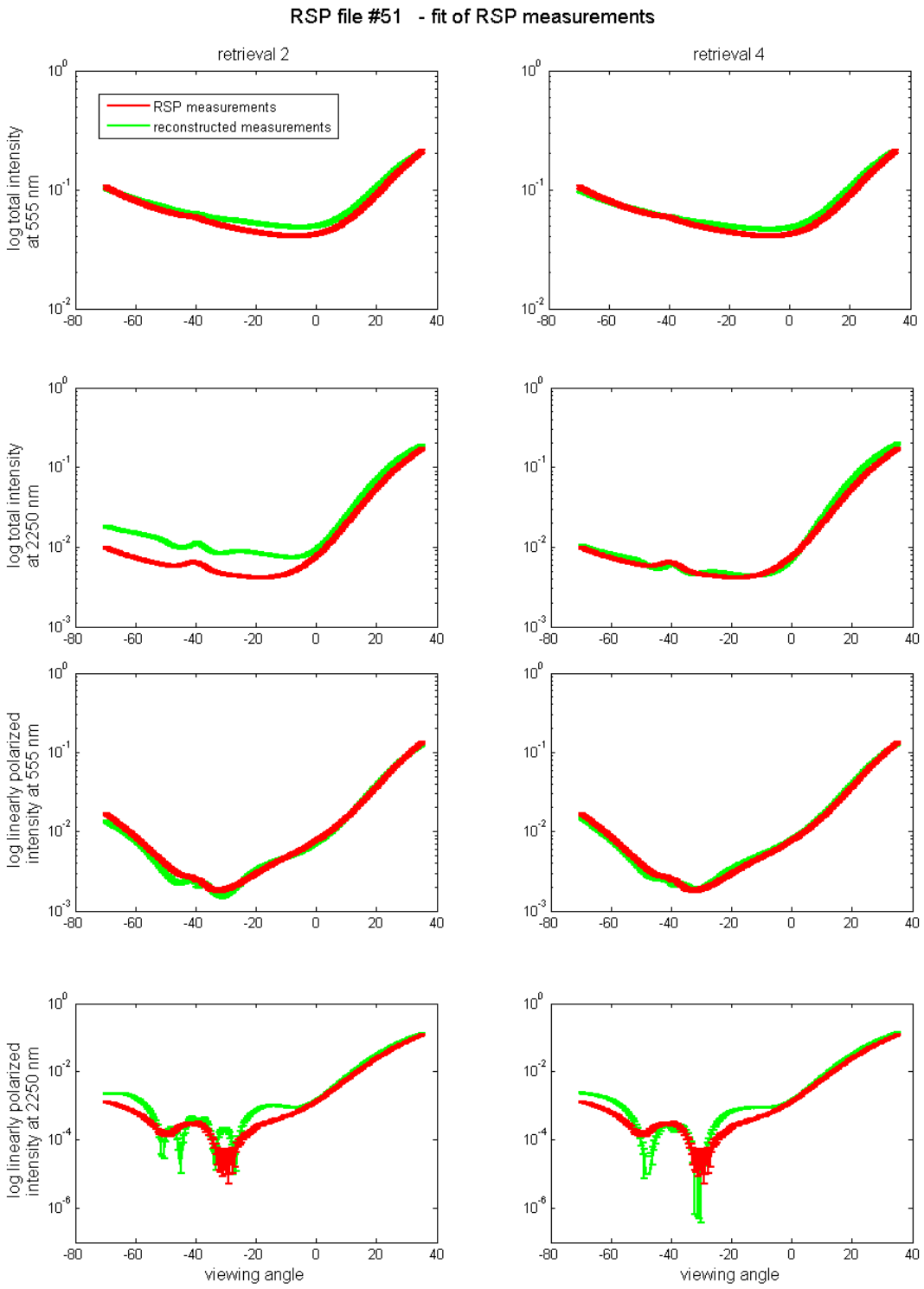

Figure 5-17. Same as Figure 5-16, for RSP file #51.

The results in Figures 5-14, 5-15, 5-16 and 5-17 show that retrieval #2 fails both tests. This can be attributed to the presence of non-spherical coarse mode particles, which generate much flatter scattering features in comparison to the spherical particles [Dubovik et al., 2006], especially for the linearly polarized scattered light in longer wavelengths. The angular features shown in the reconstructed linearly polarized measurements at 865, 1590 and 2250 nm (and to a lesser degree in the total intensity measurements at 1590 and 2250 nm) are due to the rainbow features, characteristic for the spherical particles scattering, as described in chapter 2. It is thus obvious in this case that retrieval #2 is not able to provide an accurate estimation of the aerosol properties, since it is not trained to fit the flatter scattering features of the linearly polarized light generated by the non-spherical particles in the scene.

Interestingly, that does not affect retrieval #4, since it fits only the total intensity measurements, where these features are not as prominent. For file #51, the reconstructed total spectral AOT is quite close to the AATS total spectral AOT. Moreover, the retrieved properties reproduce successfully the total intensity RSP measurements in all RSP bands and they even reproduce the linearly polarized RSP measurements at 412, 470 and 555 nm. They fail to reproduce the linearly polarized measurements at 865, 1590 and 2250 nm, but even in this case, the fit is much better than the fit from retrieval #2. For file #22, the retrieved aerosol properties do not match the total intensity measurements (although they are quite close and reproduce successfully the linearly polarized measurements, even at the longer wavelengths) and they fail to match the AATS total spectral AOT.

As discussed in chapter 3, retrieval #4 is a typical example of the widely accepted, but nevertheless mistaken notion, that total intensity-only retrieval algorithms, which consider

spherical particles and use good a-priori information, are able to accurately retrieve the aerosol properties. As shown here, this is not true, at least for cases involving non-spherical particles. For cases as the RSP file #22, the limitations of the retrieval are shown in the poor fit of the total intensity measurements. For cases, such as the RSP file #51 though, without the linearly polarized measurements in the longer wavelengths, the mistake can not be identified easily, since the total intensity measurements and the linearly polarized measurements in short wavelengths are reproduced successfully.

In summary, by applying the different retrieval schemes on real RSP data, it becomes apparent that the total intensity-only algorithms, without good a-priori information, are not able to retrieve the aerosol properties accurately enough. Even with good a-priori estimates though, the final retrieval using total intensity-only algorithms built to retrieve spherical particle properties, is not successful for the case of non-spherical particles, although it seems to accurately retrieve the spectral extinction profile. Furthermore, retrievals combining total and linearly polarized intensities from spherical particle aerosols, are not successful in retrieving non-spherical particle properties either, but at least, the linearly polarized intensity measurements at longer wavelengths can be used as a tool to assess the quality of their results. Overall, the test of our algorithm with real data highlighted the necessity of its training with non-spherical particle cases, which is in our future plans, as discussed further in the next chapter.

Chapter 6

Discussion and future work

The test of our retrieval on real RSP data, highlighted its weakness on handling non-spherical particle cases. Although the assumption of spherical particle shape we use is quite common for oceanic aerosol retrievals, it obviously needs to be revaluated for more realistic estimates of the aerosol properties above the ocean. Based on this realization, we plan for the near future to ingest non-spherical particle retrieval capabilities in our algorithm.

6.1. Future work: Non-spherical particle retrieval

The forward modeling of non-spherical particle scattering is much more complicated and time costly than the spherical case (Mie theory). As discussed in chapter 2, some of the available methods are the T-matrix method [Mishchenko et al., 1996], the geometrical optics approach [Yang and Liou, 1996], numerical methods, such as the discrete dipole approximation [Purcell and Pennypacker, 1973], and the finite difference time domain technique [Yee, 1966]. The T-matrix method is an exact solution of the electromagnetic field scattering from spheroids, which are the simplest non-spherical particles. The other methods can handle particles of any

shape, but the required calculation time is so large, that, on a practical level, they cannot be used for most cases. Although the range of applicability of the T-matrix method is not clearly defined yet, its value is proven in reproducing the flattening of the phase function for desert dust [Mishchenko et al., 1997c] and it is by far faster than the other methods.

Due mainly to time-cost concerns, in our future retrieval work we plan to use the T-matrix method, and therefore the scattering features of spheroids, in order to model the scattering from non-spherical particles in the scene. In particular, for this scheme we will consider a new size distribution, with the fine mode containing only spherical particles and the coarse mode containing a mixture of spherical particles and spheroids[26]. We will model the coarse mode size distribution using five parameters: the effective radius[27], the effective variance, the number density and, to account for the mixture of spherical and non spherical modes, a volume mixing fraction η, as well as an aspect ratio[28] ε of the spheroids. Of course, this aspect ratio will not be constant, but a distribution, and will be specified by the distribution lower moments. However, such complexities should not be applied from start, but a gradual approach, ramping up in complexity, should be followed. Specifically, a simple first approach will consider an equi-probable aspect ratio distribution for spheroids of any size. Afterwards, we will have to decide on a more realistic type of aspect ratio distribution, with particular mean values and widths, which will change for different cases.

[26] The coarse mode particles considered in our algorithm are not very large (the maximum effective size parameter is $\sim$30), thus, they are well inside the range of applicability of T-matrix method, as shown in Dubovik et al., [2006].
[27] The radius of the spheroid volume-equivalent or surface-equivalent sphere.
[28] The ratio of semi-major to semi-minor axis lengths.

Finally, we will extend the range of applicability of our algorithm to different measurement geometries, evaluating different models for the spectral variation of the refractive index, and will test our algorithm on more real-world cases.

6.2. Conclusions

Summarizing, the main incentive of our work was the need for an effective aerosol retrieval, which utilizes to the fullest the available information of polarization measurements from future sensors on satellite platforms, together with the realization that the conventional inversion tools are not designed to optimally handle the high dimensionality of the problem. Although the particular satellite datasets are not available yet, the RSP data used in this work are a good proxy for what is expected, in principal at least, from future missions. In this sense, we highlighted the importance of the inclusion of polarization measurements, in order to increase the available information content of the retrieval and show the importance of the NN inversion method on the speed and the wide applicability of the aerosol retrieval. Improving this approach further and accounting for non-spherical particle cases, we expect its merit to become obvious on a practical level, as well.

Regarding the performance of the NN approach on real RSP data, we first note that the retrieval of the spectral extinction profiles, when using the polarization – polarization cascade scheme or the polarization – intensity cascade scheme, were surprisingly close to the AATS

column extinction measurements. This agreement is somewhat surprising at first glance, since the current version of our retrieval is not trained to estimate non-spherical particle properties and, thus, we would not expect it to retrieve them accurately from the measurements of the INTEX-B/MILAGRO campaign.

The different schemes we used provided an insightful view about two crucial points of the nature of the retrieval problem. First, they highlighted the importance of utilizing the information content of the polarization measurements (retrieval #2 in Table 3-1), showing at the same time the serious deficiencies of the total-intensity only approach (retrieval #3 in Table 3-1). Second, they underlined the danger of using retrieval schemes, which are not sensitive enough to the aerosol properties of the aerosols (retrieval #4 in Table 3-1), since they may sometimes lead to plausible results of certain aerosol properties (spectral extinction values, for example), but do not necessarily provide true estimates of other microphysical properties. As we showed in chapter 5, without polarization information, it is not only difficult to get a good estimate of the aerosol properties, but, even more importantly, it is also difficult to test the quality of the retrieval. In fact, the inability of the spherical model to reproduce the fine structure of the linear polarized signal, especially in the longer wavelengths, makes it clear that, even when the retrieval seems accurate for spectral extinction data, errors are present and a true non-spherical treatment is needed.

6.2.1. Approach advantages

We showed first that, for the simple simulated scenes considered, the NN approach is quite successful, since it retrieves all the aerosol properties with the required accuracies, except –the

difficult to retrieve- SSA in some wavelengths. This implies that as long as the training dataset is suitably representative, the parameter retrieval accuracies are sufficient for climate forcing studies. However, we must emphasize that, contrary to the common notion, which considers the NNs as black boxes, this outcome is a product of extensive exploration of their dynamic capabilities for different input/output combinations, architectures, training algorithms, as well as the exploration of the NN cascading configuration and the incorporation in the scheme of the data preprocess with the PCA.

In particular, we demonstrated the added value of using a cascading scheme, in improving the performance for difficult to retrieve aerosol properties, such as the imaginary refractive index of the particles. The overall performance is not substantially enhanced for most parameters, but nevertheless, yet reduction in retrieval outliers was observed. It is expected that such post conditioning will become more critical in the case of more ill-posed problems, such as the non-spherical problem.

Furthermore, the guided training of the second NN in the cascading scheme is much faster than the unguided training of the first NN, allowing for easier exploration of the second NN configuration alternatives.

The PCA preprocessing of the retrieval data facilitates greatly the NN calculation of the input/output associations, helping achieving a more accurate and robust retrieval. The PCA effect was tested by examining the internal structure of the resulting NN, using the variability of its jacobians, as a measure of the NN robustness.

Finally, we should not forget the main NN advantage, which is the real time inversion. As discussed extensively in chapters 1 and 3, a real-time retrieval is extremely difficult using

traditional approaches, especially when considering high dimensionality datasets, as the multispectral, multiangle polarimetric data used in this study. On the contrary, the calculated inversion function from the NN provides instantaneous retrievals, even for quite large datasets.

6.2.2. Approach weaknesses

The main weakness of the NN retrieval is its dependence on the training dataset and the extensive work it is required for making sure it covers (most of) the real world variability or, if this is no true, to assess its limits. For our retrieval, the main limiting factor was the assumption of the spherical shape of the particles. Including in our future work the non-spherical particle properties, we expect to see a great improvement on the quality of the training dataset and the subsequent improvement on the performance of our retrieval on real-world cases.

Another NN weak point is the lack of a direct method to calculate its output errors. We hope to handle this in a more efficient way in the future, by incorporating in our retrieval the work presented in Aires et al., [2004]. Until then, the output errors are estimated in a more approximate way, based solely on the NN testing output errors.

Finally, we point out the need to explore all sources of variability of the model, which were assumed, but not counted within the output parameter set. For example, while we included wind variability in the training set, we did not extract wind speed as an output. This has the effect of forcing hidden variabilities onto different retrieval parameters. Exploring possible biases requires a major effort and should be addressed in the future.

Overall, we believe that we demonstrated the potential of the NN method towards the construction of an operational retrieval for the future polarimetric datasets, assessing, at the same time, possible weaknesses and how these should be handled. Although our retrieval does not have the capability of retrieving non-spherical particles, and for that reason it does not perform well on the real RSP data from INTEX-B/MILAGRO campaign, it demonstrates a strong potential for the simulated spherical cases, giving us incentive to continue on a more realistic approach, using the experience gained so far, and handle the bigger complexity of a non-spherical particle retrieval algorithm.

Appendix I

Aerosol classes

- Mineral dust
- Marine aerosols (sea salt)
- Sulphate aerosols
- Biomass burning aerosols
- Nitrate aerosols
- Organic carbon aerosols from fossil fuels
- Black carbon aerosols from fossil fuels
- Natural organic carbon aerosols
- Aerosols from dimethyl sulphide
- Aerosols from iodine compounds

1.1.1. Mineral dust

As mentioned above, mineral dust aerosols can be natural or anthropogenic and they are mainly of coarse size. Their formation depends predominantly on the wind, as well as on meteorological and climatological conditions and on agricultural and industrial practices. They are usually absorbing particles, with a composition depending on the source soil. Unfortunately, their direct effect is not well quantified, since their microphysical properties cannot be

retrieved with the necessary accuracy from algorithms that do not take into account their non-spherical shape.

1.1.2. Marine aerosols (sea salt)

The marine aerosols consist mainly from sea salt. Their generation depends on the wind above the ocean surface, as well as on the atmospheric stability and other meteorological and environmental factors of the atmosphere and the ocean. They reflect the incoming sunlight and affect the formation of the clouds above the ocean and their precipitation, having a negative forcing on the climate.

1.1.3. Sulphate aerosols

Sulphates are anthropogenic aerosols, consisting mainly from sulphuric acid, which is created from fossil fuel burning SO_2 emissions. They are also a product of biomass burning or they are emitted naturally from volcanoes or phytoplankton in the ocean. They are reflecting aerosols, at least in the Visible (VIS) part of the spectrum, and present a small absorption in the Near-Infrared (NIR) part. They usually form composite particles with organic substances or mineral dust and nitrate aerosols. The composite particles have optical properties closer to the ones of the mixture than to the sulphates.

1.1.4. Biomass burning aerosols

The biomass burning aerosols are created from forest or grassland fires. Their composition depends on the combustion products and is usually a mixture of black carbon, organic carbon

and inorganic constituents, such as nitrate and sulphate. They are mainly fine mode aerosols and they can be absorbing or reflecting, depending on their composition, which possibly changes as they age.

1.1.5. Nitrate aerosols

Nitrate aerosols are anthropogenic aerosols, formed in highly industrialized areas from NO_x emissions. They mainly reflect the incoming sunlight.

1.1.6. Organic carbon aerosols from fossil fuels

These aerosols are a complex mixture of emitted carbonic compounds from fossil fuel and biofuel burning. They are also formed as a secondary product of organic gases condensation. The organic carbon aerosols are not absorbing by themselves, but they take part in composite particles, which can be either absorbing or reflecting.

1.1.7. Black carbon aerosols from fossil fuels

Black carbon aerosols are formed from incomplete combustion of fossil fuels or biomass burning and they are mostly of anthropogenic origin. They are highly absorbing particles.

1.1.8. Natural organic carbon aerosols

The natural organic carbon aerosols are directly emitted in the atmosphere from biogenic organic material or volatile organic compounds (VOCs) in the ground or the ocean. Their emission is dependent on climatological conditions.

1.1.9. Aerosols from dimethyl sulphide

Dimethyl sulphide (DMS) is produced from the phytoplankton in the ocean and depends on its surface concentration and the wind speed.

1.1.10. Aerosols from iodine compounds

Aerosols from iodine compounds are released in coastal environments, mainly from macroalgae.

Appendix II

The optimal estimator technique

According to the Bayesian approach [Rodgers 2000, Dubovik 2004], we find the most probable state $\hat{X}$ by maximizing the conditional probability distribution function of X for given observations of I (total intensity) and Q (linearly polarized intensity)

$$P\left(F_I(X), F_Q(X)\middle|I, Q\right) = P(F_I(X)|I)P\left(F_Q(X)\middle|Q\right) \sim$$

$$\sim exp\left(-\frac{1}{2}\left[\left(I - F_I(X)\right)^T S_I^{-1}\left(I - F_I(X)\right) + \left(Q - F_Q(X)\right)^T S_Q^{-1}\left(Q - F_Q(X)\right)\right]\right)$$

where $F_I(X)$, $F_Q(X)$ are the total intensity and linearly polarized intensity measurements as calculated from the forward problem for aerosol parameters X**,** and S_I, S_Q are the measurement error covariance matrices for the total intensity and linearly polarized intensity, respectively.

For the derivation of this formula we assume that the probabilities $(F_I(X)|I)$, $P\left(F_Q(X)\middle|Q\right)$ are independent and the PDFs of the errors $I - F_I(X)$, $Q - F_Q(X)$ are Gaussian.

The most probable state for X is the one that satisfies the maximization of the conditional probability:

$$\nabla_X\left(-2lnP\left(F_I(X), F_Q(X)\middle|I, Q\right)\right) = 0 \implies$$

$$\implies K_I^T(X)S_I^{-1}\left(I - F_I(X)\right) + K_Q^T(X)S_Q^{-1}\left(Q - F_Q(X)\right) = 0$$

where $K_I(X) = \nabla_X F_I(X)$, $K_Q(X) = \nabla_X F_Q(X)$ are the Jacobian matrices of the forward problem F with respect to X.

In the case of available a-priori information the equation takes the following form:

$$K_I^T(X)S_I^{-1}\big(I - F_I(X)\big) + K_Q^T(X)S_Q^{-1}\left(Q - F_Q(X)\right) + S_a^{-1}(X - X_a) = 0$$

where X_a is the mean value of the a-priori information for X and S_a is the a-priori covariance matrix.

The traditional ways to solve this equation are the Newton and the Newton-Gauss approximations. These methods do not converge to a solution for many practical applications, so what is usually used is their modification, the Levenberg-Marquardt method:

$$X_{i+1} = X_i + \left[\left(\big(K_I(X_i)\big)^T S_I^{-1}K_I(X_i) + \left(K_Q(X_i)\right)^T S_Q^{-1}K_Q(X_i) + S_a^{-1}\right)(1 + \gamma_i I)\right]^{-1} \times$$

$$\times \left[\big(K_I(X_i)\big)^T S_I^{-1}\big(I - F_I(X_i)\big) + \left(K_Q(X_i)\right)^T S_Q^{-1}\left(Q - F_Q(X_i)\right) + S_a^{-1}(X_i - X_a)\right]$$

where γ_i is modified at each step in order to minimize the value of $\nabla_X\big(-2lnP(\dots)\big)$. By this way, the Levenberg-Marquardt method oscillates between the Newton-Gauss method (for $\gamma_i \to 0$, the step size is large) and the steepest descent method (for $\gamma_i \to \infty$, the step size $\to 0$).

Appendix III

Testing retrievals #1, #2, #3 and #4 on simulated data

In every figure, the first plot is the log-density scatter plot of true versus retrieved values. The black dashed line is the 1-1 line. The second plot shows the fractional retrieval RMSE along the considered range, multiplied by 100. The third plot shows the percentage of the testing cases that fall within one standard deviation (black circles), or two standard deviations (red crosses) of the required uncertainty. The uncertainty goal is reached if the one-standard deviation percentage is larger than 66% (black line) and the two-standard deviations percentage is larger than 99% (red line).

Retrieval #1

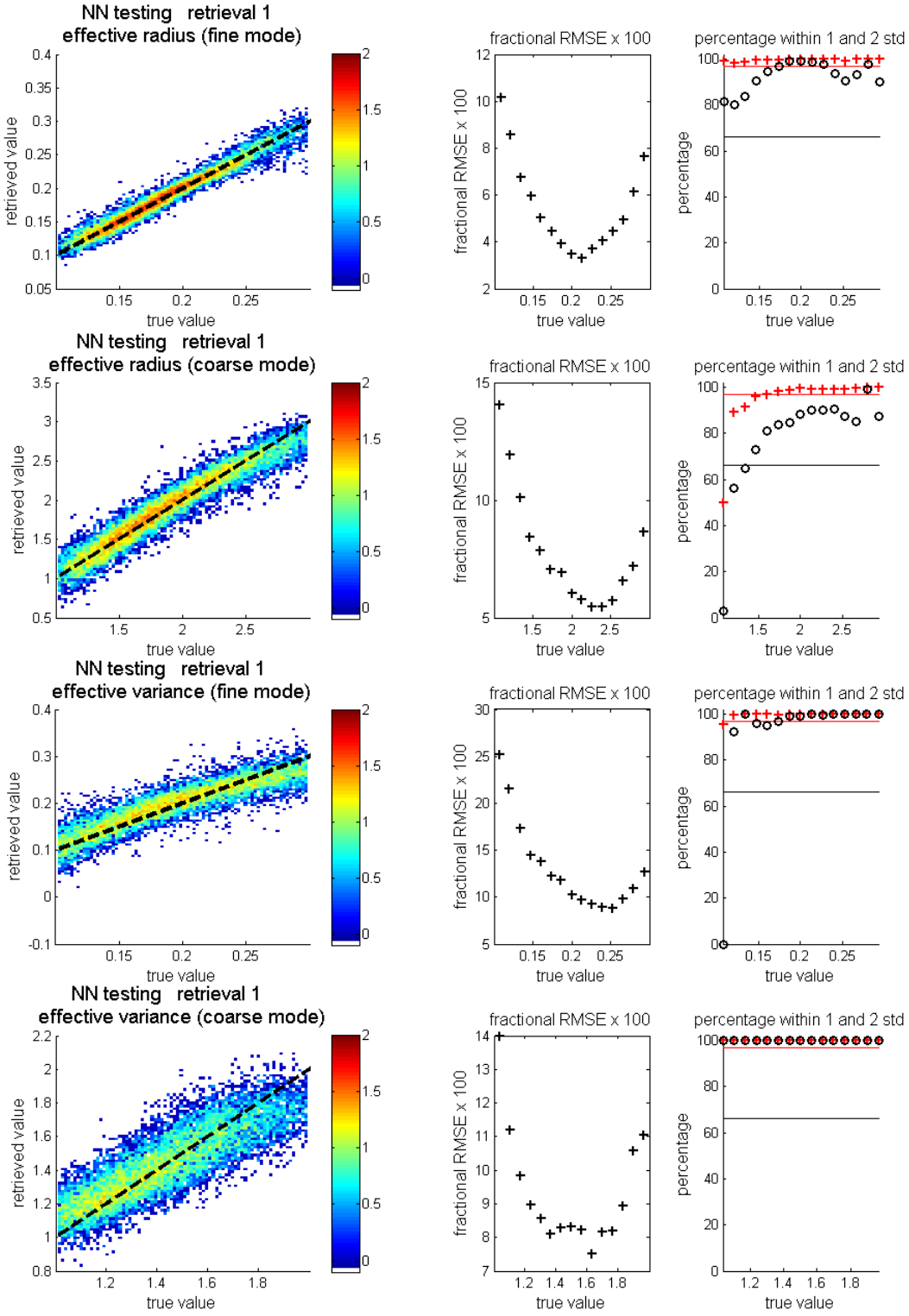
NN testing retrieval 1
effective radius (fine mode)
retrieved value
true value
fractional RMSE x 100
fractional RMSE x 100
true value
percentage within 1 and 2 std
percentage
true value
NN testing retrieval 1
effective radius (coarse mode)
retrieved value
true value
fractional RMSE x 100
fractional RMSE x 100
true value
percentage within 1 and 2 std
percentage
true value
NN testing retrieval 1
effective variance (fine mode)
retrieved value
true value
fractional RMSE x 100
fractional RMSE x 100
true value
percentage within 1 and 2 std
percentage
true value
NN testing retrieval 1
effective variance (coarse mode)
retrieved value
true value
fractional RMSE x 100
fractional RMSE x 100
true value
percentage within 1 and 2 std
percentage
true value

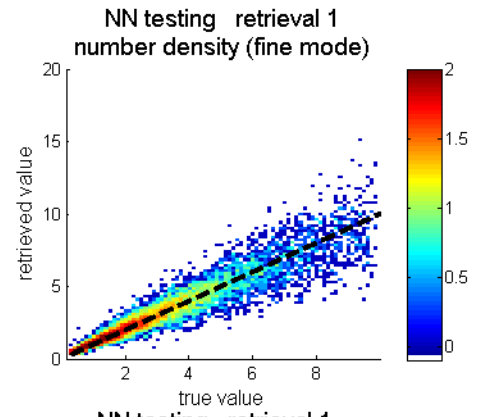
NN testing retrieval 1
number density (fine mode)
retrieved value
true value

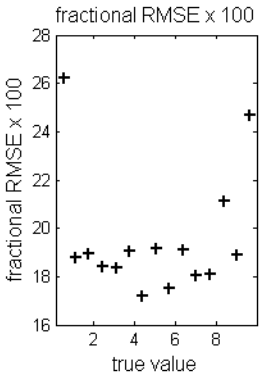
fractional RMSE x 100
fractional RMSE x 100
true value

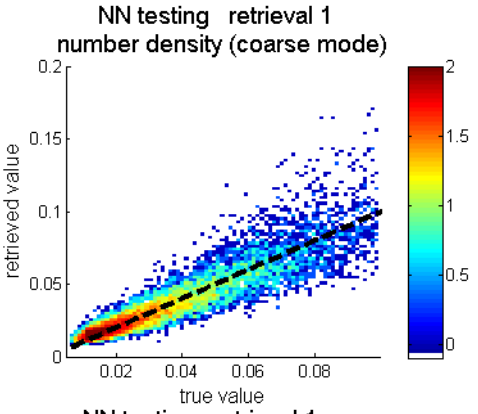
NN testing retrieval 1
number density (coarse mode)
retrieved value
true value

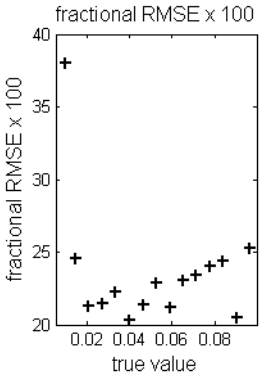
fractional RMSE x 100
fractional RMSE x 100
true value

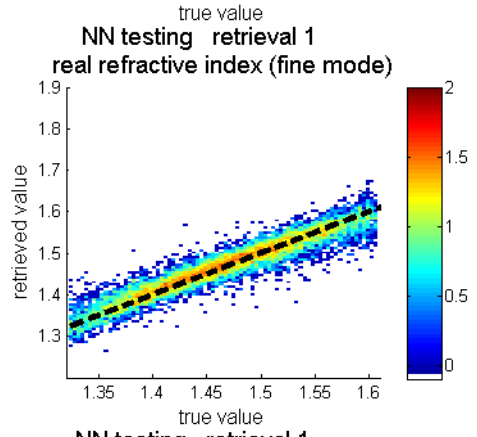
NN testing retrieval 1
real refractive index (fine mode)
retrieved value
true value

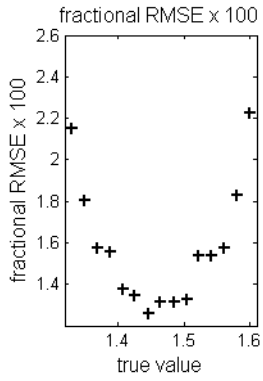
fractional RMSE x 100
fractional RMSE x 100
true value

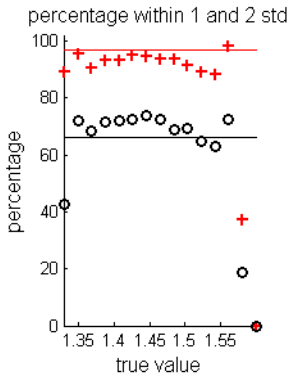
percentage within 1 and 2 std
percentage
true value

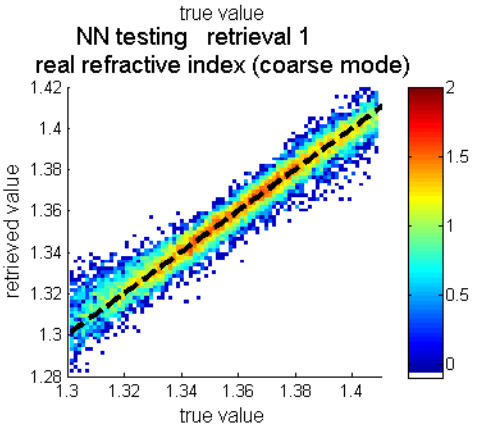
NN testing retrieval 1
real refractive index (coarse mode)
retrieved value
true value

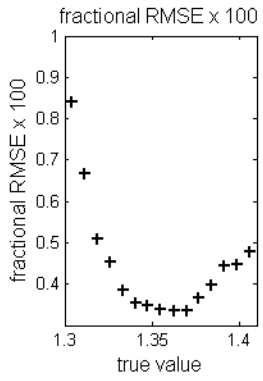
fractional RMSE x 100
fractional RMSE x 100
true value

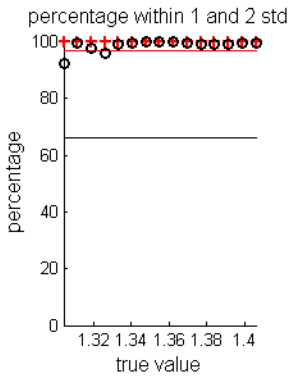
percentage within 1 and 2 std
percentage
true value

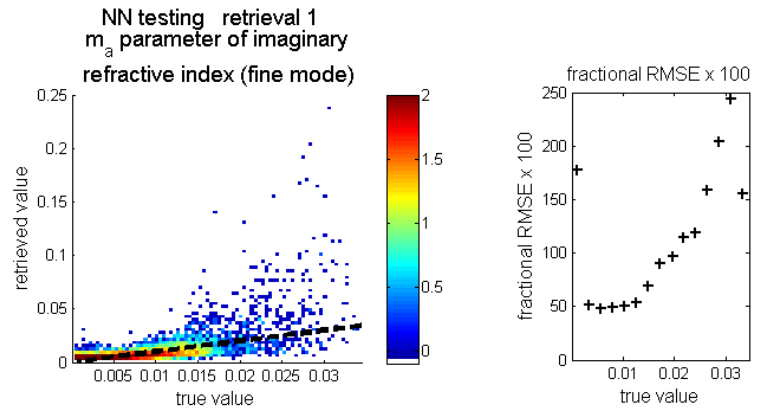
NN testing retrieval 1
m_a parameter of imaginary
refractive index (fine mode)
retrieved value
true value
fractional RMSE x 100
fractional RMSE x 100
true value

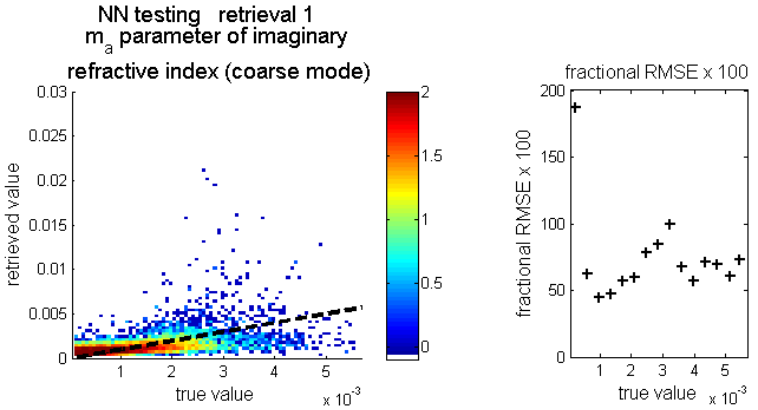
NN testing retrieval 1
m_a parameter of imaginary
refractive index (coarse mode)
retrieved value
true value
x 10^-3
fractional RMSE x 100
fractional RMSE x 100
true value
x 10^-3

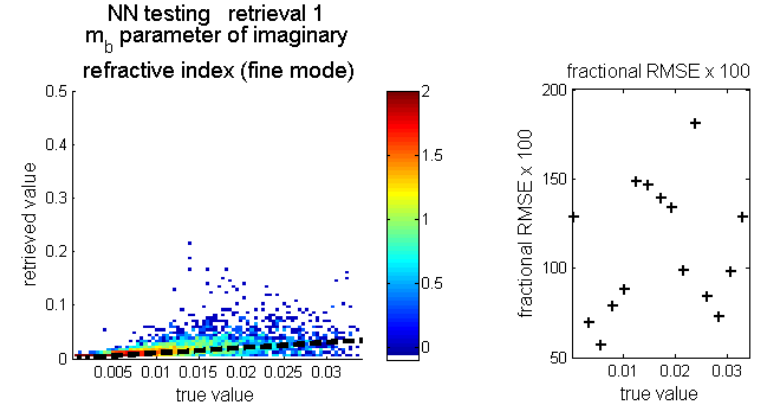
NN testing retrieval 1
m_b parameter of imaginary
refractive index (fine mode)
retrieved value
true value
fractional RMSE x 100
fractional RMSE x 100
true value

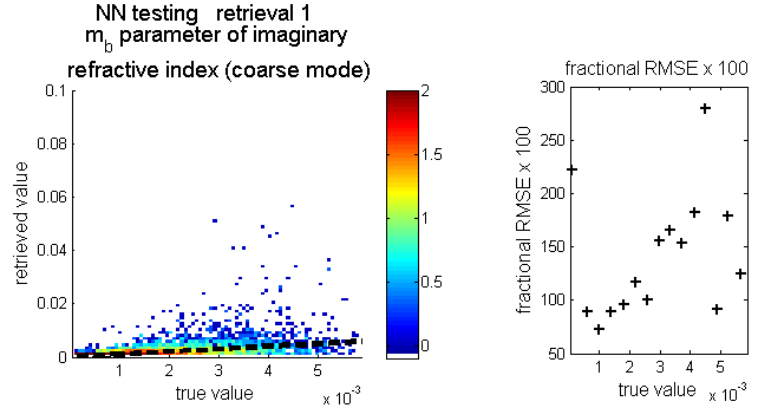
NN testing retrieval 1
m_b parameter of imaginary
refractive index (coarse mode)
retrieved value
true value
x 10^-3
fractional RMSE x 100
fractional RMSE x 100
true value
x 10^-3

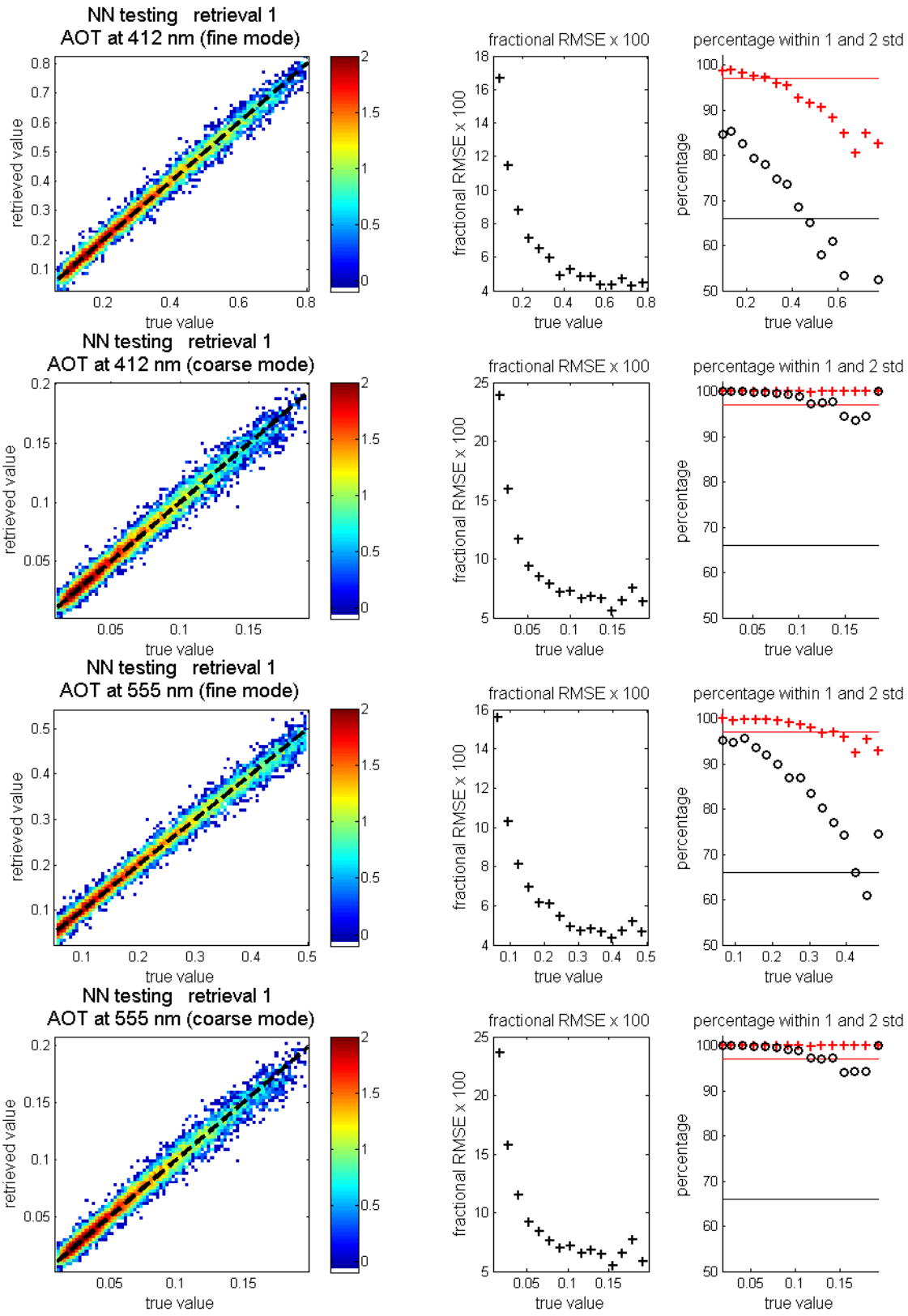
NN testing retrieval 1
AOT at 412 nm (fine mode)
retrieved value
true value
fractional RMSE x 100
true value
percentage within 1 and 2 std
percentage
true value
NN testing retrieval 1
AOT at 412 nm (coarse mode)
retrieved value
true value
fractional RMSE x 100
true value
percentage within 1 and 2 std
percentage
true value
NN testing retrieval 1
AOT at 555 nm (fine mode)
retrieved value
true value
fractional RMSE x 100
true value
percentage within 1 and 2 std
percentage
true value
NN testing retrieval 1
AOT at 555 nm (coarse mode)
retrieved value
true value
fractional RMSE x 100
true value
percentage within 1 and 2 std
percentage
true value

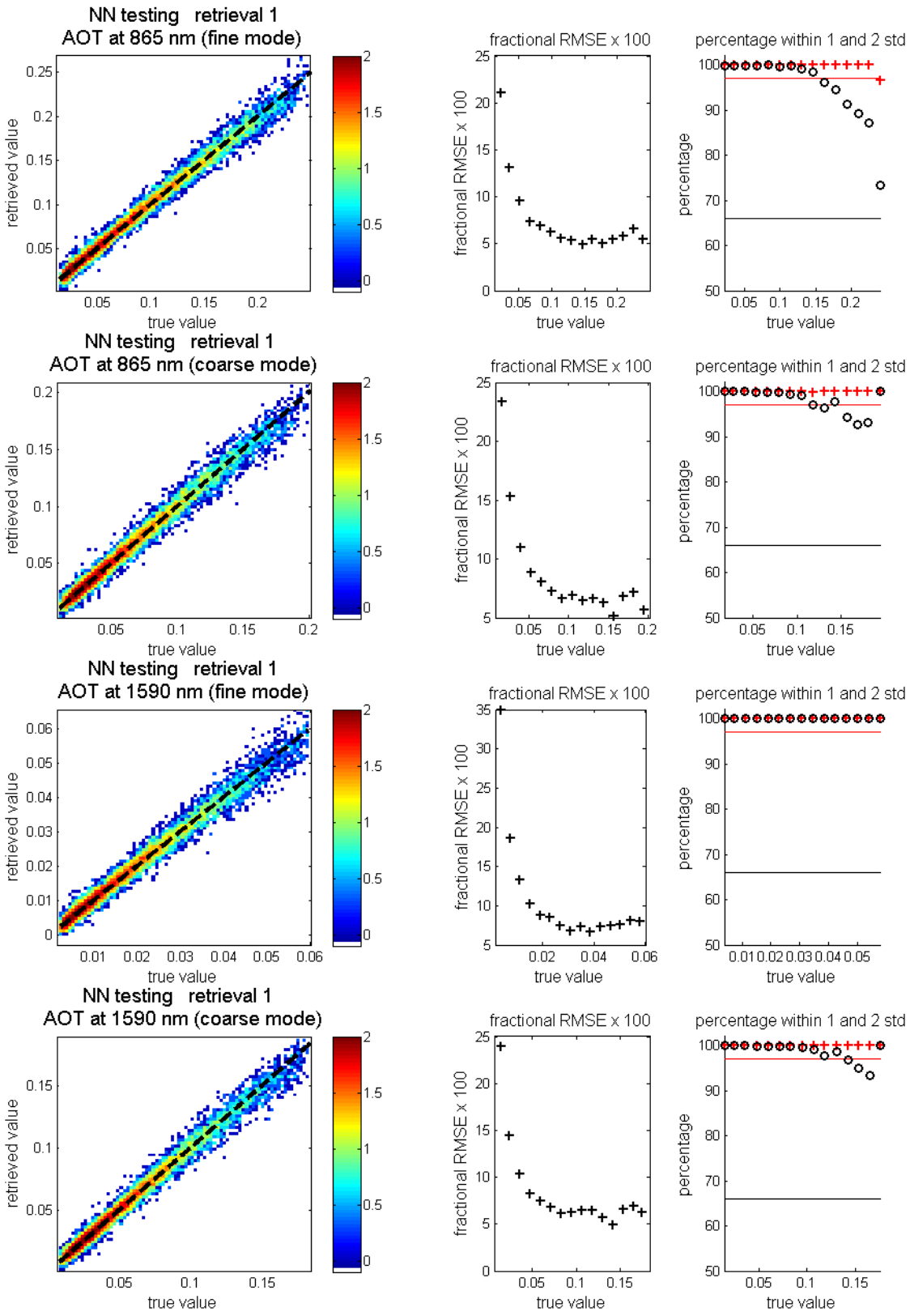
NN testing retrieval 1
AOT at 865 nm (fine mode)
retrieved value
true value
fractional RMSE x 100
fractional RMSE x 100
true value
percentage within 1 and 2 std
percentage
true value
NN testing retrieval 1
AOT at 865 nm (coarse mode)
retrieved value
true value
fractional RMSE x 100
fractional RMSE x 100
true value
percentage within 1 and 2 std
percentage
true value
NN testing retrieval 1
AOT at 1590 nm (fine mode)
retrieved value
true value
fractional RMSE x 100
fractional RMSE x 100
true value
percentage within 1 and 2 std
percentage
true value
NN testing retrieval 1
AOT at 1590 nm (coarse mode)
retrieved value
true value
fractional RMSE x 100
fractional RMSE x 100
true value
percentage within 1 and 2 std
percentage
true value

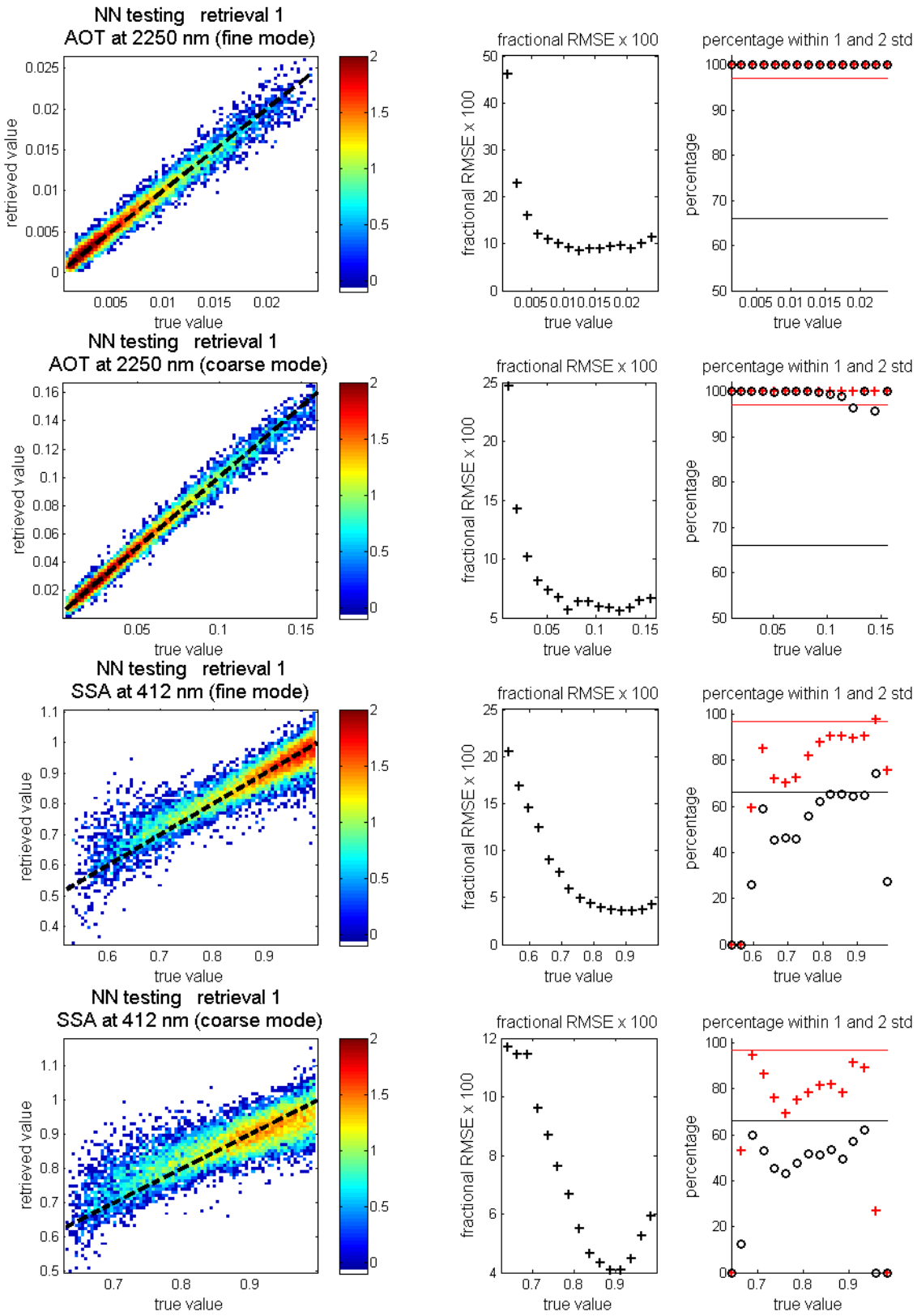
NN testing retrieval 1
AOT at 2250 nm (fine mode)
retrieved value
true value
fractional RMSE x 100
fractional RMSE x 100
true value
percentage within 1 and 2 std
percentage
true value
NN testing retrieval 1
AOT at 2250 nm (coarse mode)
retrieved value
true value
fractional RMSE x 100
fractional RMSE x 100
true value
percentage within 1 and 2 std
percentage
true value
NN testing retrieval 1
SSA at 412 nm (fine mode)
retrieved value
true value
fractional RMSE x 100
fractional RMSE x 100
true value
percentage within 1 and 2 std
percentage
true value
NN testing retrieval 1
SSA at 412 nm (coarse mode)
retrieved value
true value
fractional RMSE x 100
fractional RMSE x 100
true value
percentage within 1 and 2 std
percentage
true value

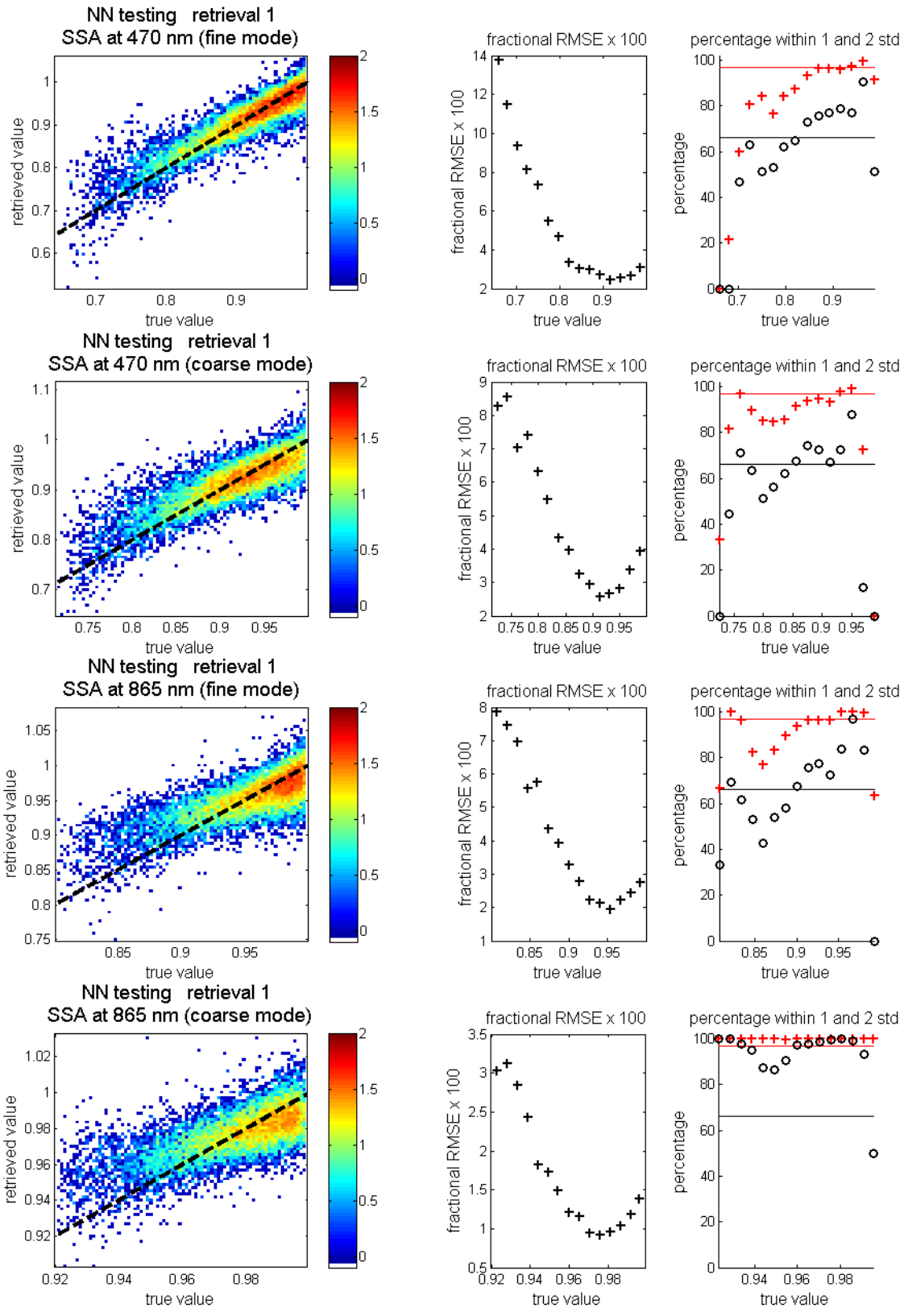
NN testing retrieval 1
SSA at 470 nm (fine mode)
retrieved value
true value
fractional RMSE x 100
fractional RMSE x 100
true value
percentage within 1 and 2 std
percentage
true value
NN testing retrieval 1
SSA at 470 nm (coarse mode)
retrieved value
true value
fractional RMSE x 100
fractional RMSE x 100
true value
percentage within 1 and 2 std
percentage
true value
NN testing retrieval 1
SSA at 865 nm (fine mode)
retrieved value
true value
fractional RMSE x 100
fractional RMSE x 100
true value
percentage within 1 and 2 std
percentage
true value
NN testing retrieval 1
SSA at 865 nm (coarse mode)
retrieved value
true value
fractional RMSE x 100
fractional RMSE x 100
true value
percentage within 1 and 2 std
percentage
true value

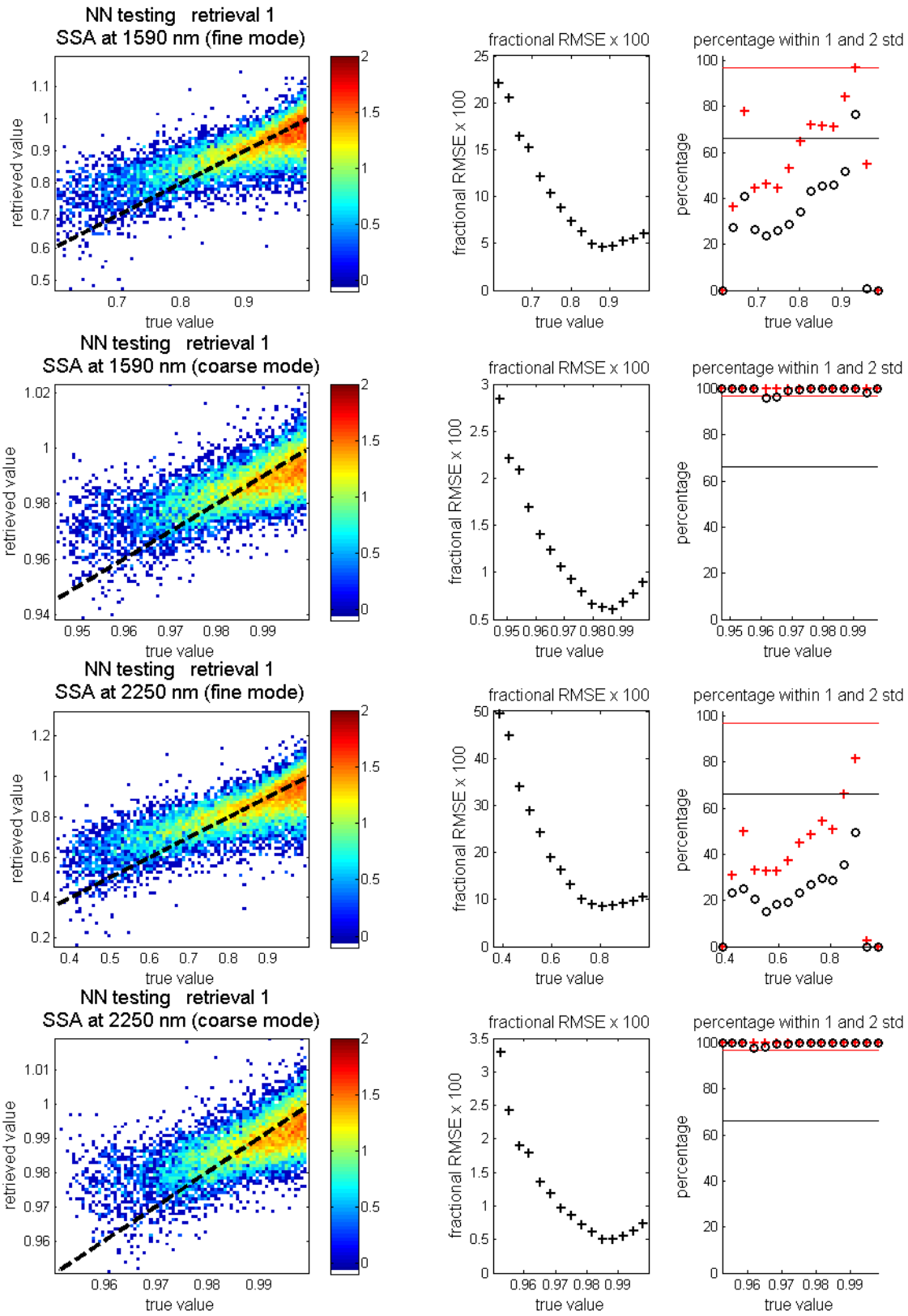
NN testing retrieval 1
SSA at 1590 nm (fine mode)
retrieved value
true value
fractional RMSE x 100
fractional RMSE x 100
true value
percentage within 1 and 2 std
percentage
true value
NN testing retrieval 1
SSA at 1590 nm (coarse mode)
retrieved value
true value
fractional RMSE x 100
fractional RMSE x 100
true value
percentage within 1 and 2 std
percentage
true value
NN testing retrieval 1
SSA at 2250 nm (fine mode)
retrieved value
true value
fractional RMSE x 100
fractional RMSE x 100
true value
percentage within 1 and 2 std
percentage
true value
NN testing retrieval 1
SSA at 2250 nm (coarse mode)
retrieved value
true value
fractional RMSE x 100
fractional RMSE x 100
true value
percentage within 1 and 2 std
percentage
true value

Retrieval #2

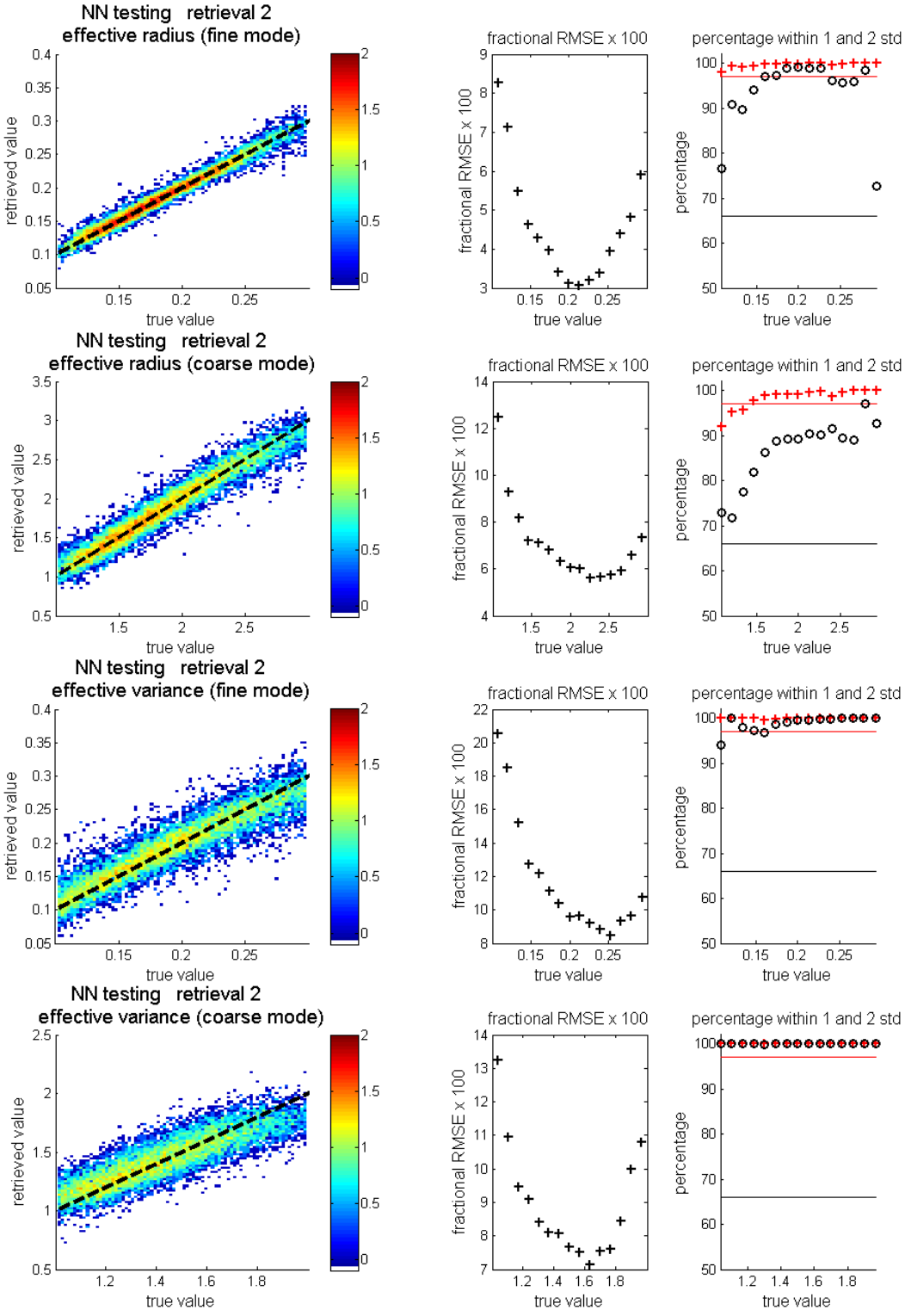
NN testing retrieval 2
effective radius (fine mode)
retrieved value
true value
fractional RMSE x 100
true value
percentage within 1 and 2 std
percentage
true value
NN testing retrieval 2
effective radius (coarse mode)
retrieved value
true value
fractional RMSE x 100
true value
percentage within 1 and 2 std
percentage
true value
NN testing retrieval 2
effective variance (fine mode)
retrieved value
true value
fractional RMSE x 100
true value
percentage within 1 and 2 std
percentage
true value
NN testing retrieval 2
effective variance (coarse mode)
retrieved value
true value
fractional RMSE x 100
true value
percentage within 1 and 2 std
percentage
true value

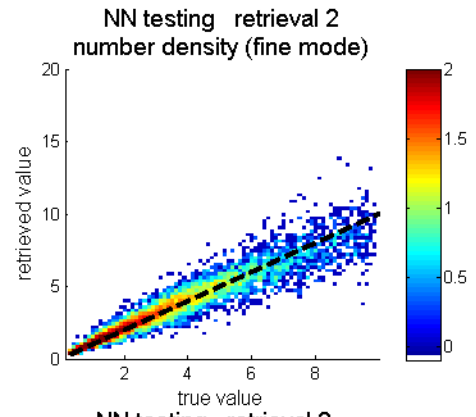
NN testing retrieval 2
number density (fine mode)
retrieved value
true value

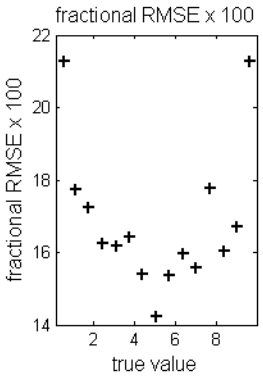
fractional RMSE x 100
fractional RMSE x 100
true value

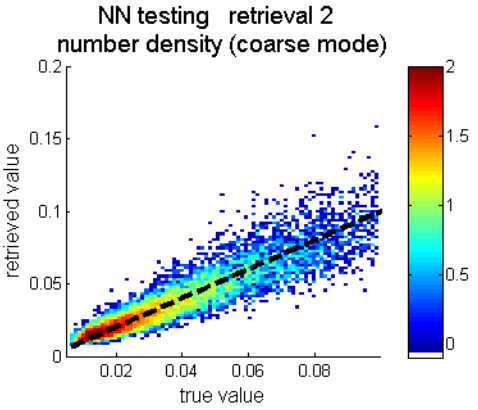
NN testing retrieval 2
number density (coarse mode)
retrieved value
true value

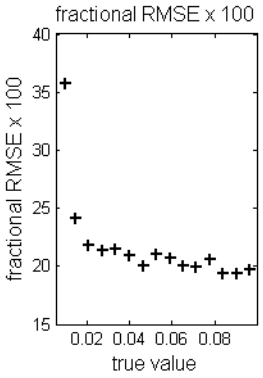
fractional RMSE x 100
fractional RMSE x 100
true value

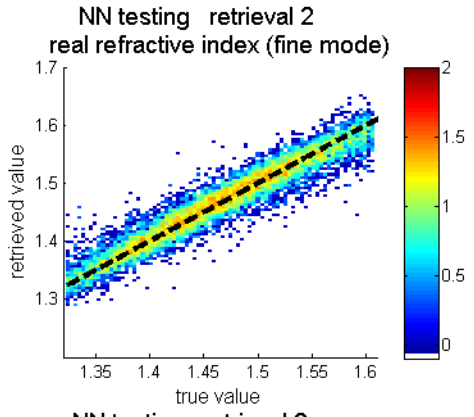
NN testing retrieval 2
real refractive index (fine mode)
retrieved value
true value

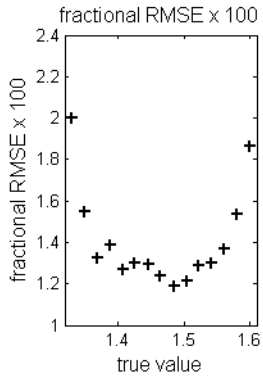
fractional RMSE x 100
fractional RMSE x 100
true value

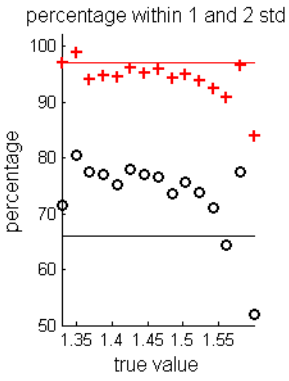
percentage within 1 and 2 std
percentage
true value

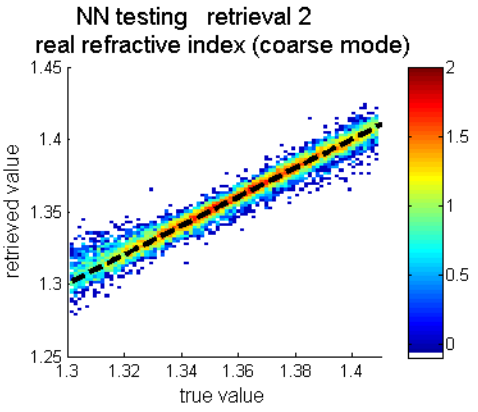
NN testing retrieval 2
real refractive index (coarse mode)
retrieved value
true value

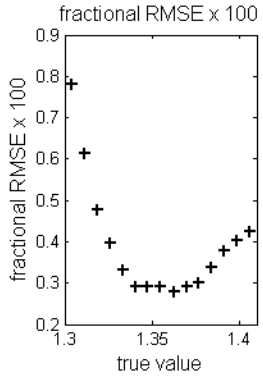
fractional RMSE x 100
fractional RMSE x 100
true value

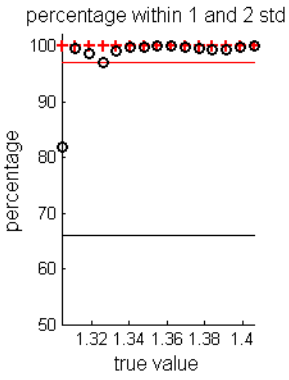
percentage within 1 and 2 std
percentage
true value

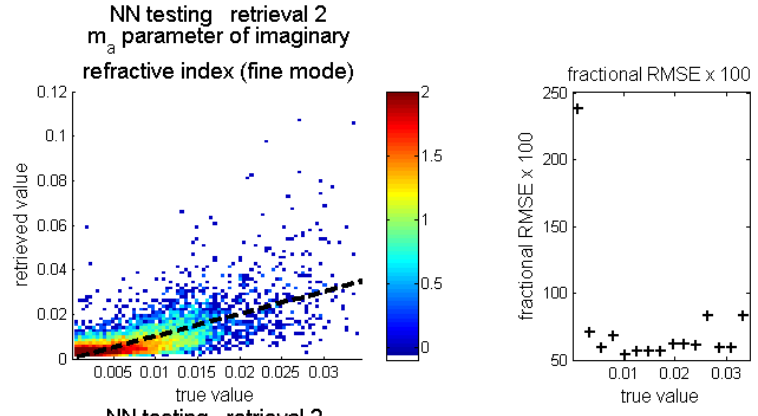
NN testing retrieval 2
m_a parameter of imaginary
refractive index (fine mode)
retrieved value
true value
fractional RMSE x 100
fractional RMSE x 100
true value

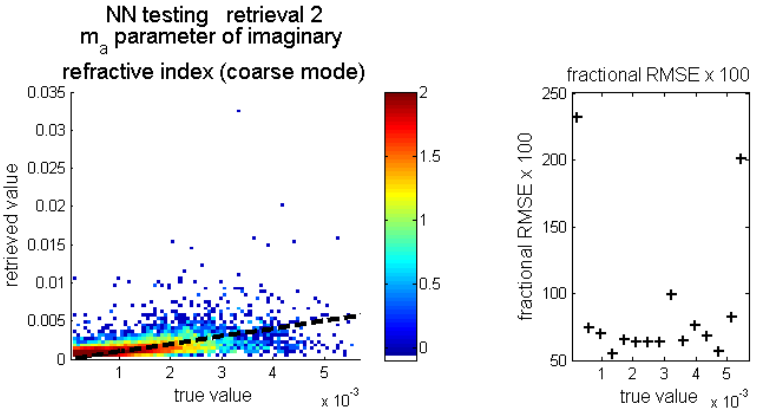
NN testing retrieval 2
m_a parameter of imaginary
refractive index (coarse mode)
retrieved value
true value
x 10^-3
fractional RMSE x 100
fractional RMSE x 100
true value
x 10^-3

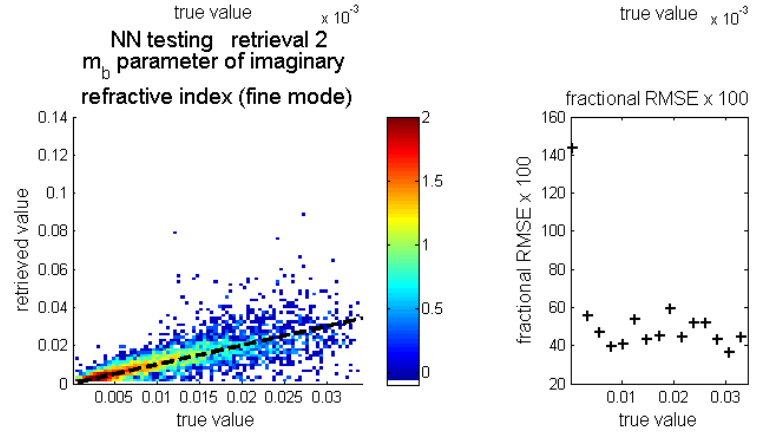
NN testing retrieval 2
m_b parameter of imaginary
refractive index (fine mode)
retrieved value
true value
fractional RMSE x 100
fractional RMSE x 100
true value

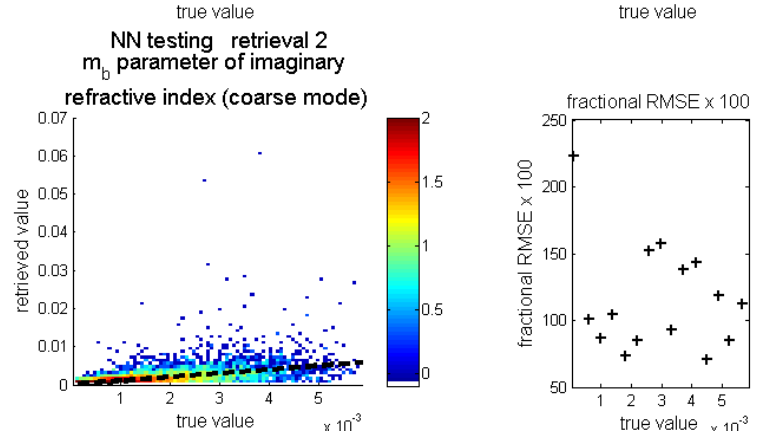
NN testing retrieval 2
m_b parameter of imaginary
refractive index (coarse mode)
retrieved value
true value
fractional RMSE x 100
fractional RMSE x 100
true value

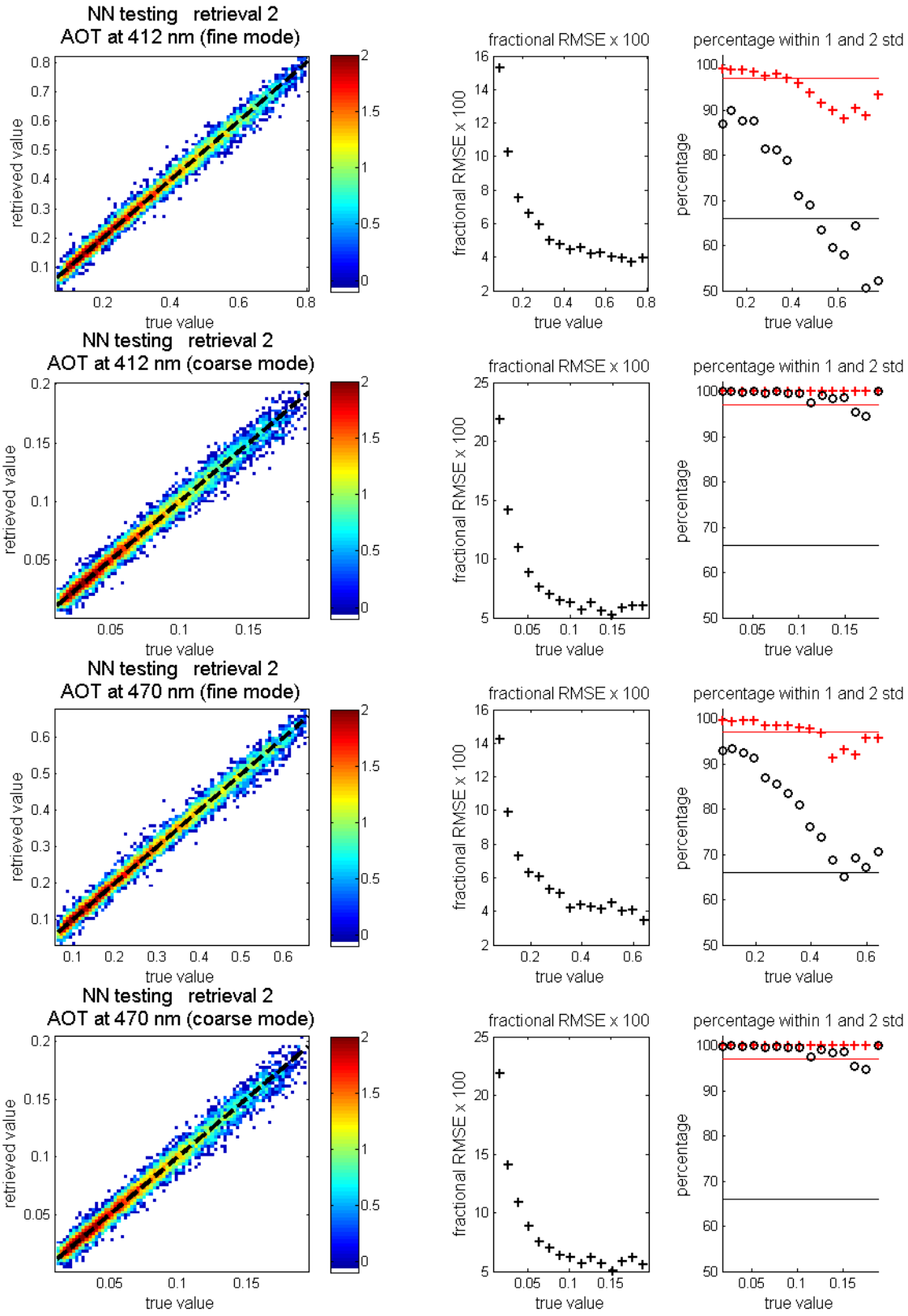
NN testing retrieval 2
AOT at 412 nm (fine mode)
retrieved value
true value
fractional RMSE x 100
fractional RMSE x 100
true value
percentage within 1 and 2 std
percentage
true value
NN testing retrieval 2
AOT at 412 nm (coarse mode)
retrieved value
true value
fractional RMSE x 100
fractional RMSE x 100
true value
percentage within 1 and 2 std
percentage
true value
NN testing retrieval 2
AOT at 470 nm (fine mode)
retrieved value
true value
fractional RMSE x 100
fractional RMSE x 100
true value
percentage within 1 and 2 std
percentage
true value
NN testing retrieval 2
AOT at 470 nm (coarse mode)
retrieved value
true value
fractional RMSE x 100
fractional RMSE x 100
true value
percentage within 1 and 2 std
percentage
true value

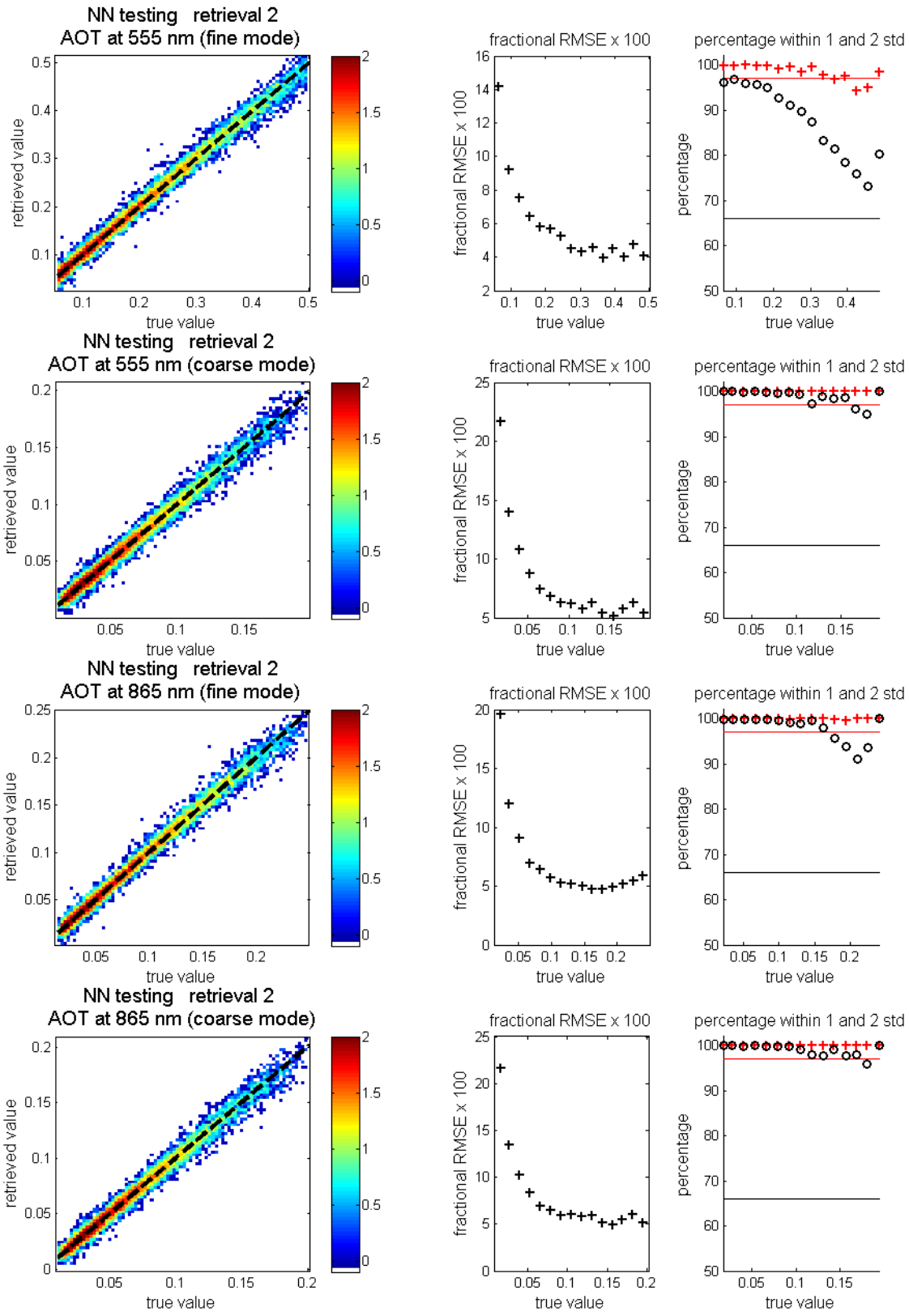
NN testing retrieval 2
AOT at 555 nm (fine mode)
retrieved value
true value
fractional RMSE x 100
fractional RMSE x 100
true value
percentage within 1 and 2 std
percentage
true value
NN testing retrieval 2
AOT at 555 nm (coarse mode)
retrieved value
true value
fractional RMSE x 100
fractional RMSE x 100
true value
percentage within 1 and 2 std
percentage
true value
NN testing retrieval 2
AOT at 865 nm (fine mode)
retrieved value
true value
fractional RMSE x 100
fractional RMSE x 100
true value
percentage within 1 and 2 std
percentage
true value
NN testing retrieval 2
AOT at 865 nm (coarse mode)
retrieved value
true value
fractional RMSE x 100
fractional RMSE x 100
true value
percentage within 1 and 2 std
percentage
true value

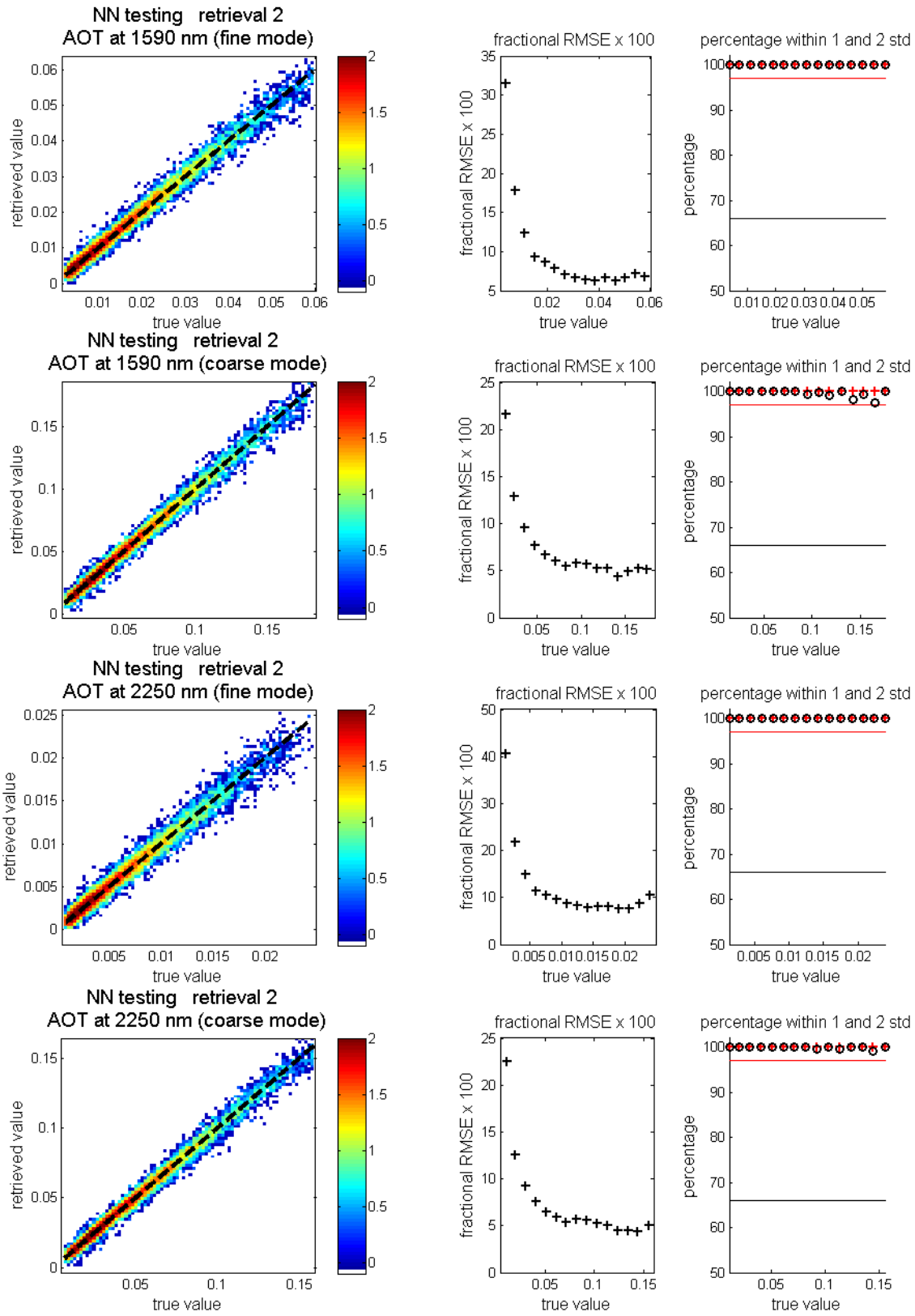
NN testing retrieval 2
AOT at 1590 nm (fine mode)
retrieved value
true value
fractional RMSE x 100
fractional RMSE x 100
true value
percentage within 1 and 2 std
percentage
true value
NN testing retrieval 2
AOT at 1590 nm (coarse mode)
retrieved value
true value
fractional RMSE x 100
fractional RMSE x 100
true value
percentage within 1 and 2 std
percentage
true value
NN testing retrieval 2
AOT at 2250 nm (fine mode)
retrieved value
true value
fractional RMSE x 100
fractional RMSE x 100
true value
percentage within 1 and 2 std
percentage
true value
NN testing retrieval 2
AOT at 2250 nm (coarse mode)
retrieved value
true value
fractional RMSE x 100
fractional RMSE x 100
true value
percentage within 1 and 2 std
percentage
true value

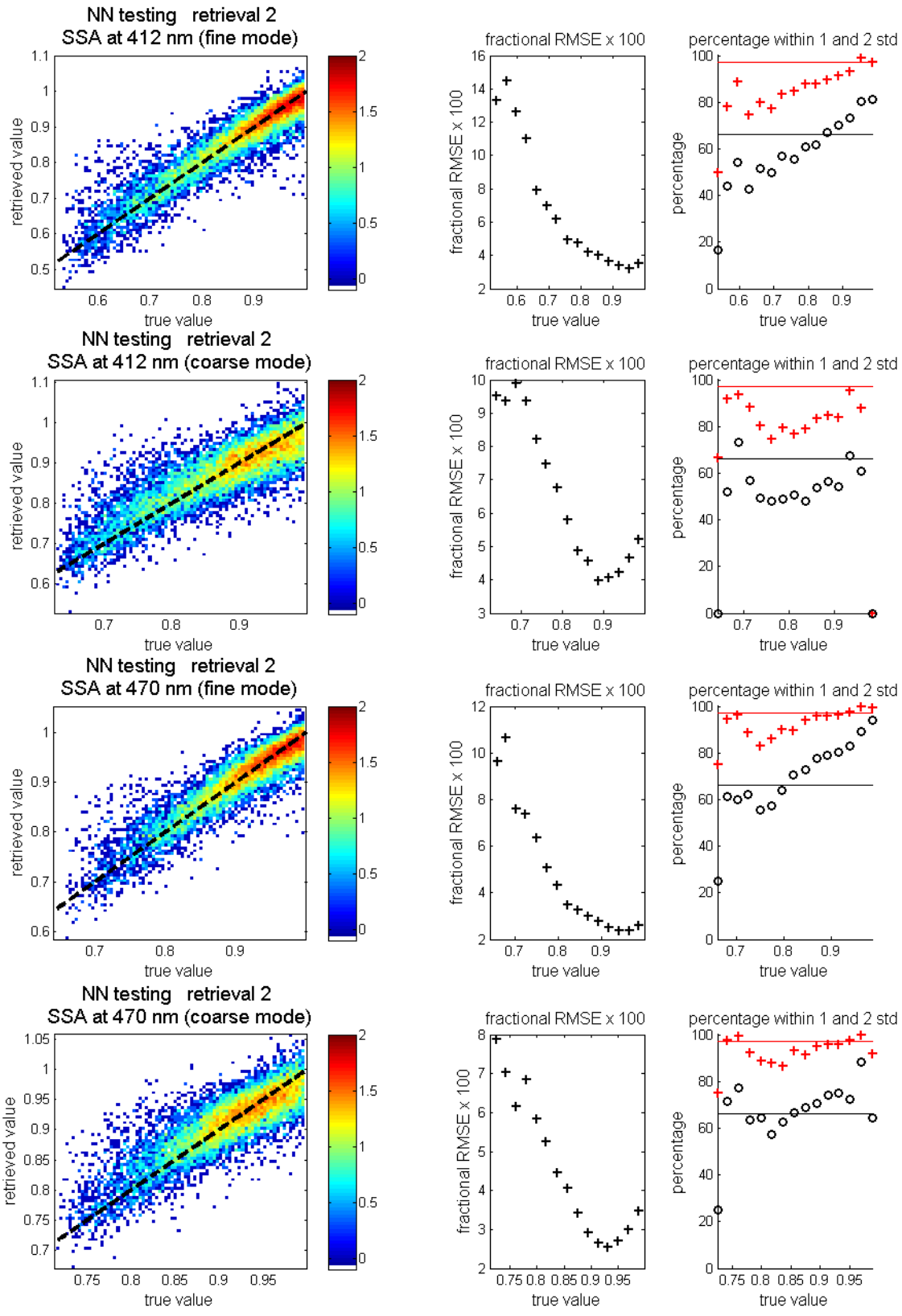
NN testing retrieval 2
SSA at 412 nm (fine mode)
retrieved value
true value
fractional RMSE x 100
fractional RMSE x 100
true value
percentage within 1 and 2 std
percentage
true value
NN testing retrieval 2
SSA at 412 nm (coarse mode)
retrieved value
true value
fractional RMSE x 100
fractional RMSE x 100
true value
percentage within 1 and 2 std
percentage
true value
NN testing retrieval 2
SSA at 470 nm (fine mode)
retrieved value
true value
fractional RMSE x 100
fractional RMSE x 100
true value
percentage within 1 and 2 std
percentage
true value
NN testing retrieval 2
SSA at 470 nm (coarse mode)
retrieved value
true value
fractional RMSE x 100
fractional RMSE x 100
true value
percentage within 1 and 2 std
percentage
true value

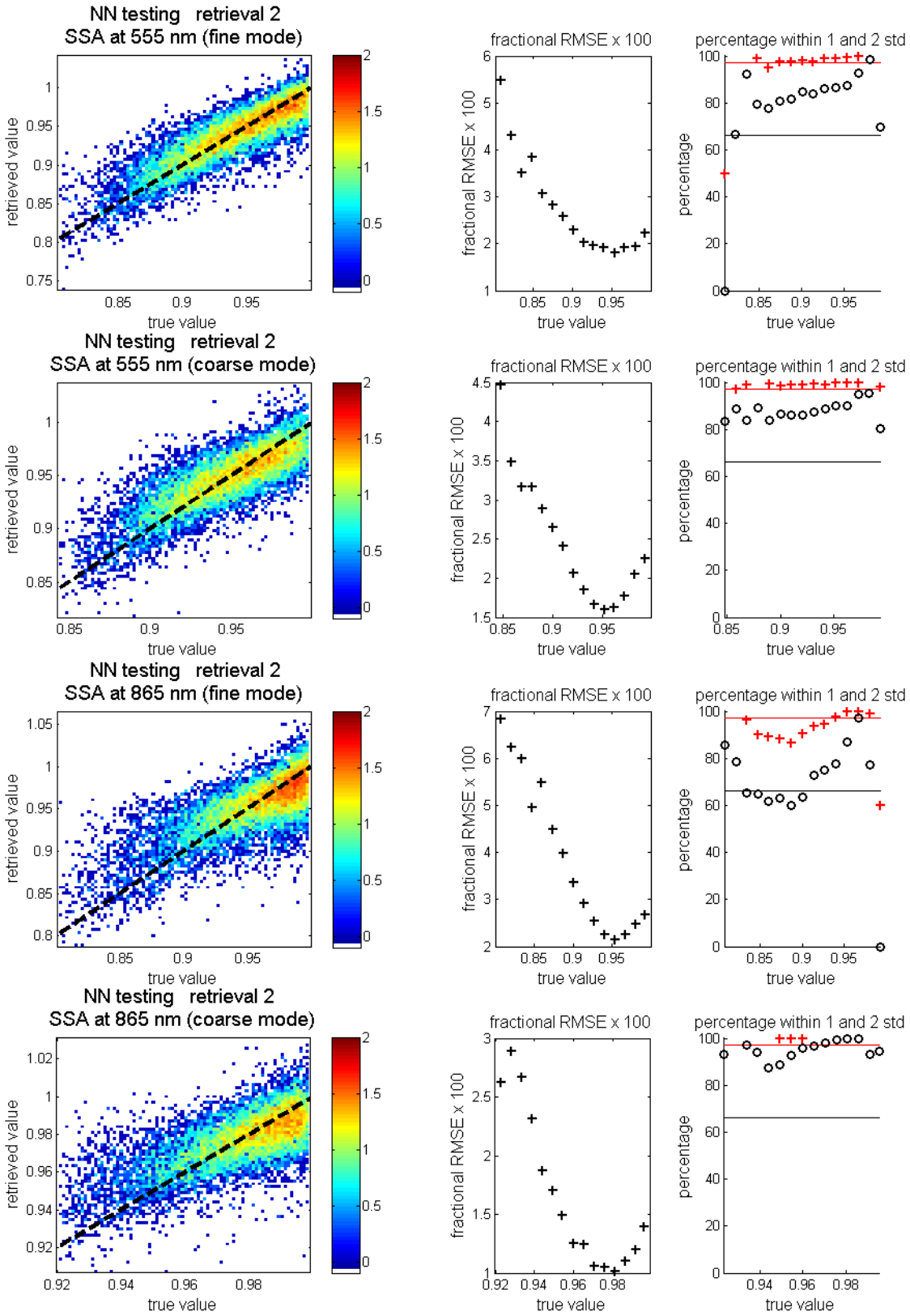
NN testing retrieval 2
SSA at 555 nm (fine mode)
retrieved value
true value
fractional RMSE x 100
fractional RMSE x 100
true value
percentage within 1 and 2 std
percentage
true value
NN testing retrieval 2
SSA at 555 nm (coarse mode)
retrieved value
true value
fractional RMSE x 100
fractional RMSE x 100
true value
percentage within 1 and 2 std
percentage
true value
NN testing retrieval 2
SSA at 865 nm (fine mode)
retrieved value
true value
fractional RMSE x 100
fractional RMSE x 100
true value
percentage within 1 and 2 std
percentage
true value
NN testing retrieval 2
SSA at 865 nm (coarse mode)
retrieved value
true value
fractional RMSE x 100
fractional RMSE x 100
true value
percentage within 1 and 2 std
percentage
true value

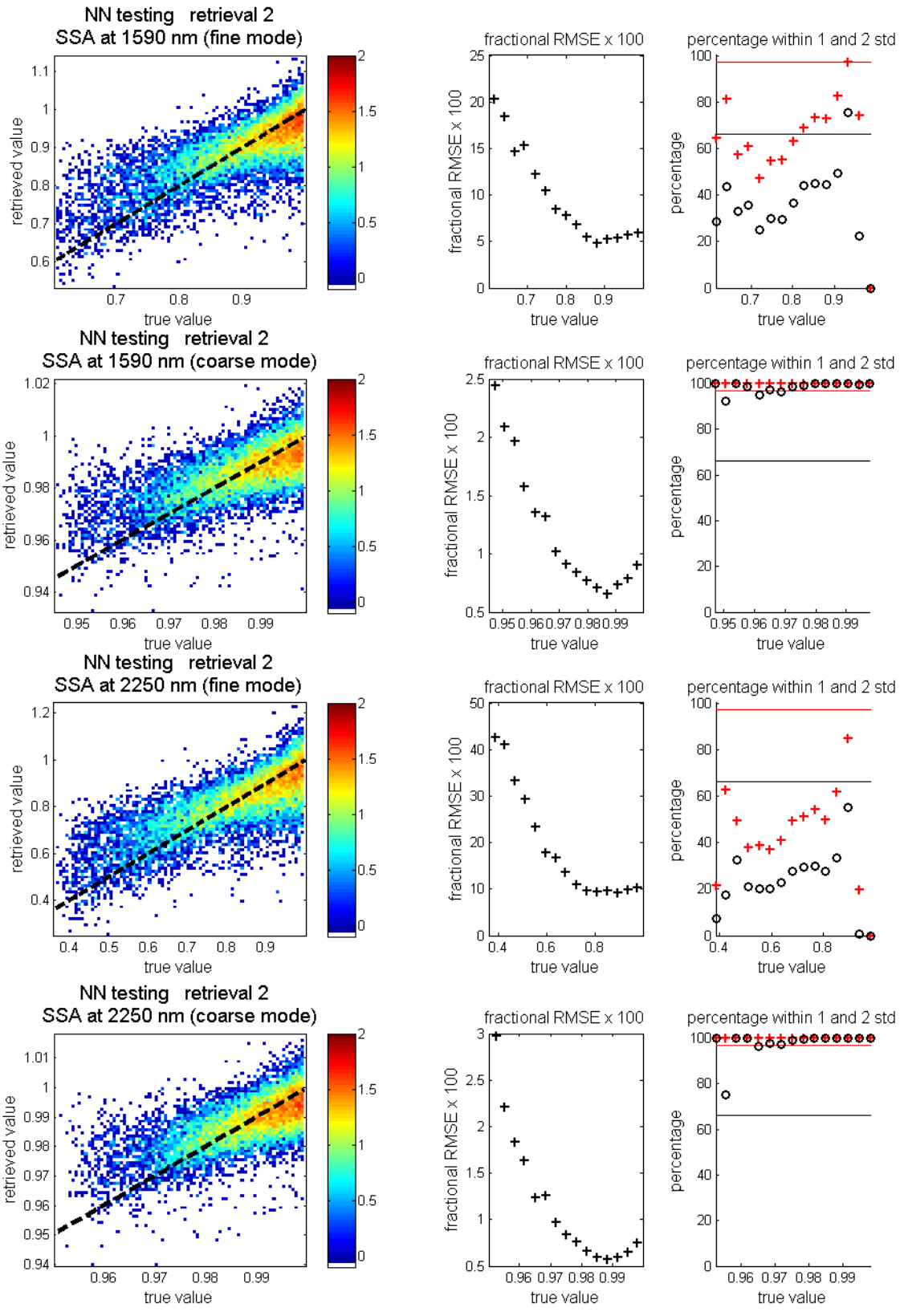
NN testing retrieval 2
SSA at 1590 nm (fine mode)
retrieved value
true value
fractional RMSE x 100
fractional RMSE x 100
true value
percentage within 1 and 2 std
percentage
true value
NN testing retrieval 2
SSA at 1590 nm (coarse mode)
retrieved value
true value
fractional RMSE x 100
fractional RMSE x 100
true value
percentage within 1 and 2 std
percentage
true value
NN testing retrieval 2
SSA at 2250 nm (fine mode)
retrieved value
true value
fractional RMSE x 100
fractional RMSE x 100
true value
percentage within 1 and 2 std
percentage
true value
NN testing retrieval 2
SSA at 2250 nm (coarse mode)
retrieved value
true value
fractional RMSE x 100
fractional RMSE x 100
true value
percentage within 1 and 2 std
percentage
true value

Retrieval #3

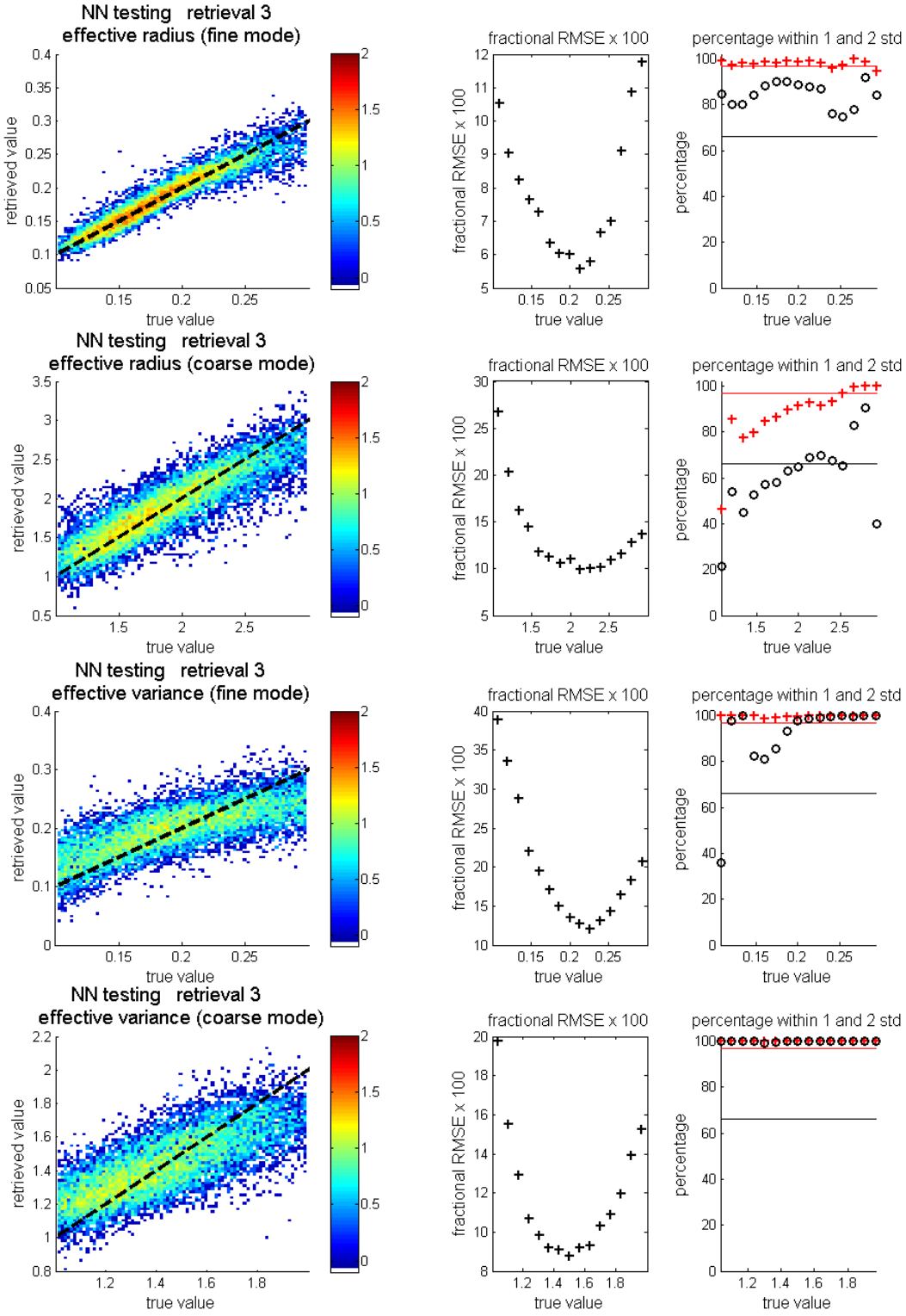
NN testing retrieval 3
effective radius (fine mode)
retrieved value
true value
fractional RMSE x 100
true value
percentage within 1 and 2 std
percentage
true value
NN testing retrieval 3
effective radius (coarse mode)
retrieved value
true value
fractional RMSE x 100
true value
percentage within 1 and 2 std
percentage
true value
NN testing retrieval 3
effective variance (fine mode)
retrieved value
true value
fractional RMSE x 100
true value
percentage within 1 and 2 std
percentage
true value
NN testing retrieval 3
effective variance (coarse mode)
retrieved value
true value
fractional RMSE x 100
true value
percentage within 1 and 2 std
percentage
true value

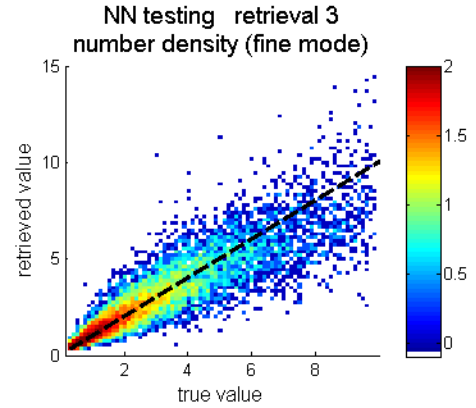
NN testing retrieval 3
number density (fine mode)
retrieved value
true value

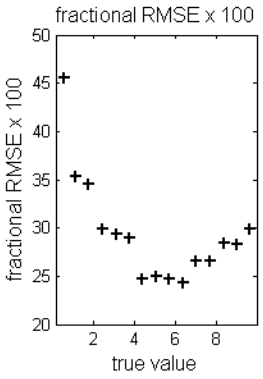
fractional RMSE x 100
fractional RMSE x 100
true value

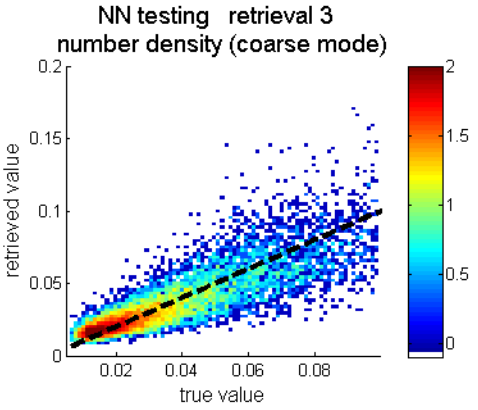
NN testing retrieval 3
number density (coarse mode)
retrieved value
true value

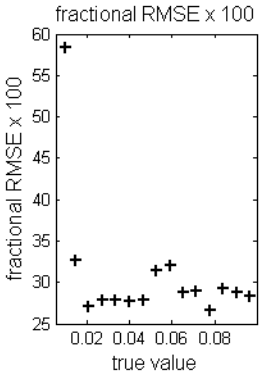
fractional RMSE x 100
fractional RMSE x 100
true value

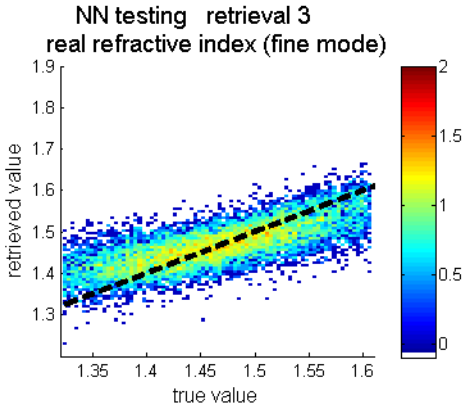
NN testing retrieval 3
real refractive index (fine mode)
retrieved value
true value

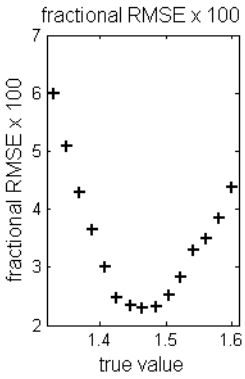
fractional RMSE x 100
fractional RMSE x 100
true value

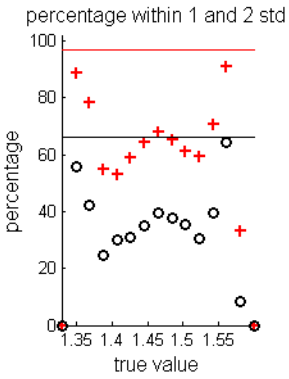
percentage within 1 and 2 std
percentage
true value

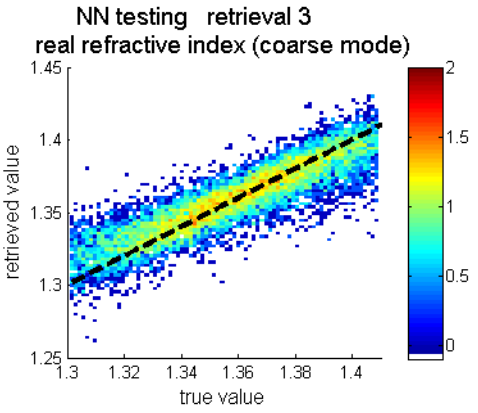
NN testing retrieval 3
real refractive index (coarse mode)
retrieved value
true value

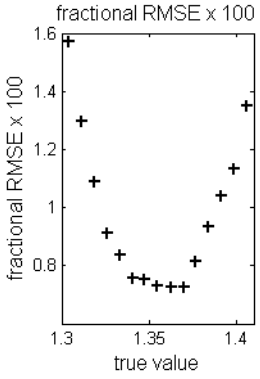
fractional RMSE x 100
fractional RMSE x 100
true value

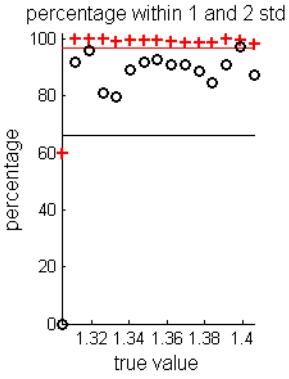
percentage within 1 and 2 std
percentage
true value

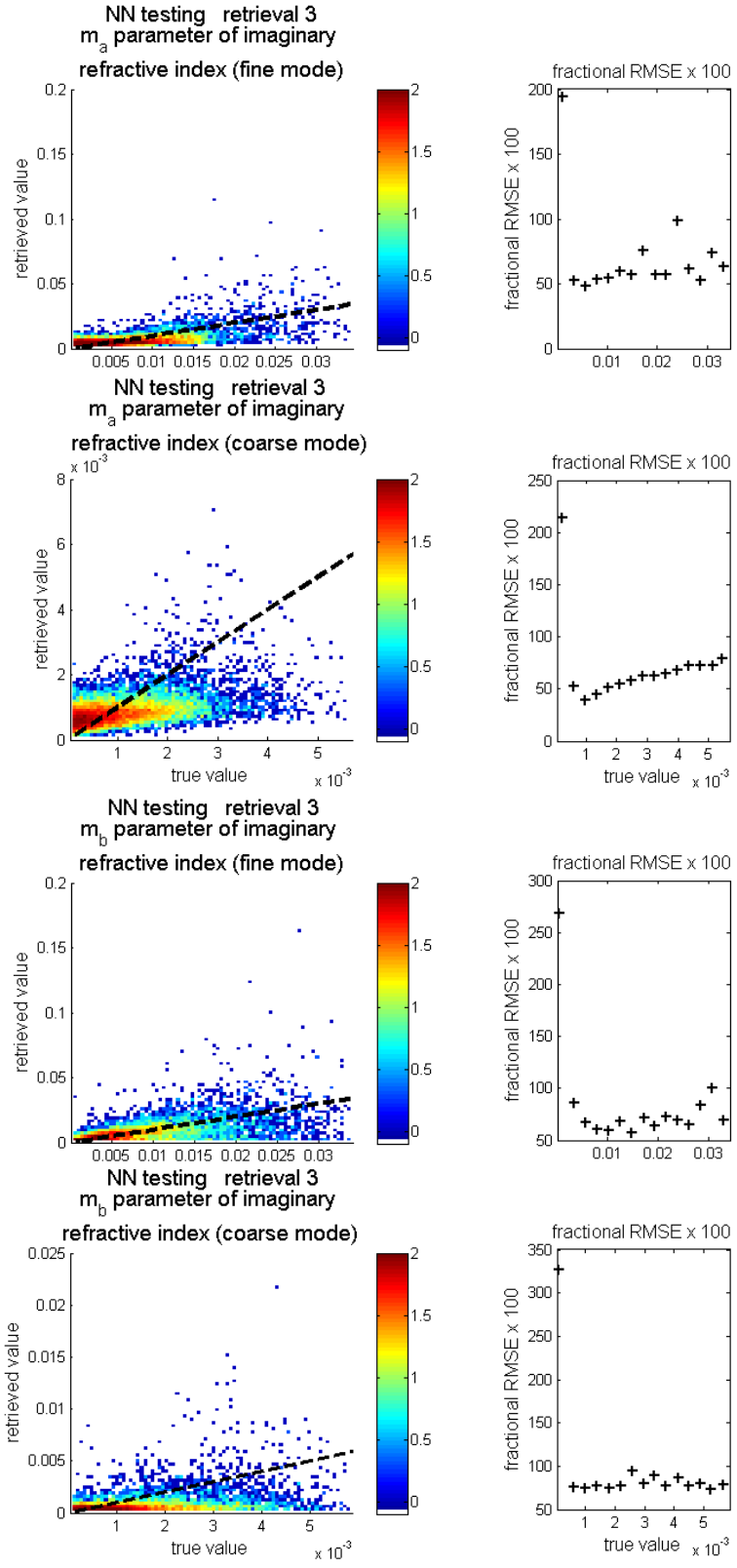
NN testing retrieval 3
m_a parameter of imaginary
refractive index (fine mode)
retrieved value
fractional RMSE x 100
NN testing retrieval 3
m_a parameter of imaginary
refractive index (coarse mode)
x 10^-3
retrieved value
true value
x 10^-3
fractional RMSE x 100
NN testing retrieval 3
m_b parameter of imaginary
refractive index (fine mode)
retrieved value
fractional RMSE x 100
NN testing retrieval 3
m_b parameter of imaginary
refractive index (coarse mode)
retrieved value
true value
x 10^-3
fractional RMSE x 100

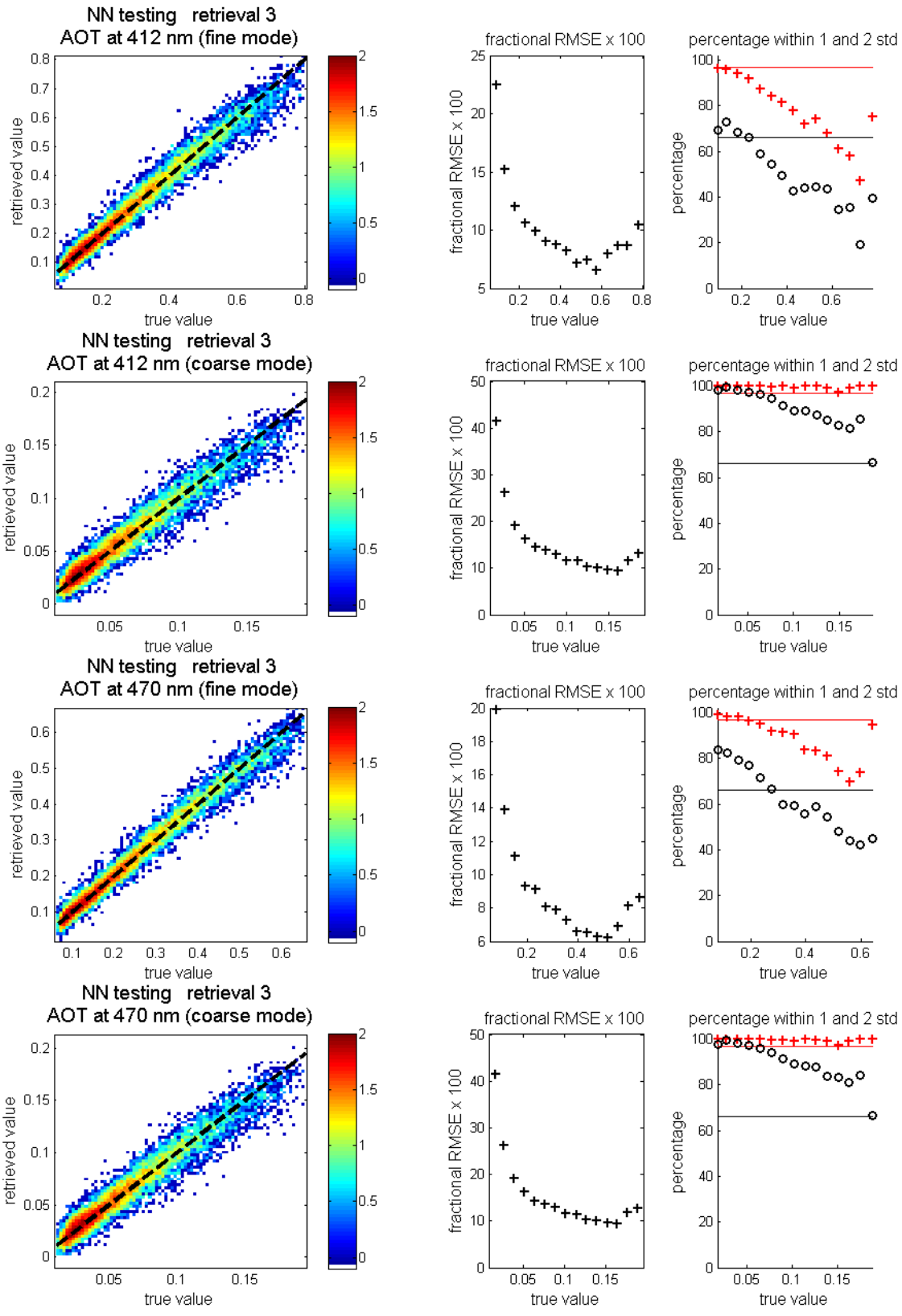
NN testing retrieval 3
AOT at 412 nm (fine mode)
retrieved value
true value
fractional RMSE x 100
fractional RMSE x 100
true value
percentage within 1 and 2 std
percentage
true value
NN testing retrieval 3
AOT at 412 nm (coarse mode)
retrieved value
true value
fractional RMSE x 100
fractional RMSE x 100
true value
percentage within 1 and 2 std
percentage
true value
NN testing retrieval 3
AOT at 470 nm (fine mode)
retrieved value
true value
fractional RMSE x 100
fractional RMSE x 100
true value
percentage within 1 and 2 std
percentage
true value
NN testing retrieval 3
AOT at 470 nm (coarse mode)
retrieved value
true value
fractional RMSE x 100
fractional RMSE x 100
true value
percentage within 1 and 2 std
percentage
true value

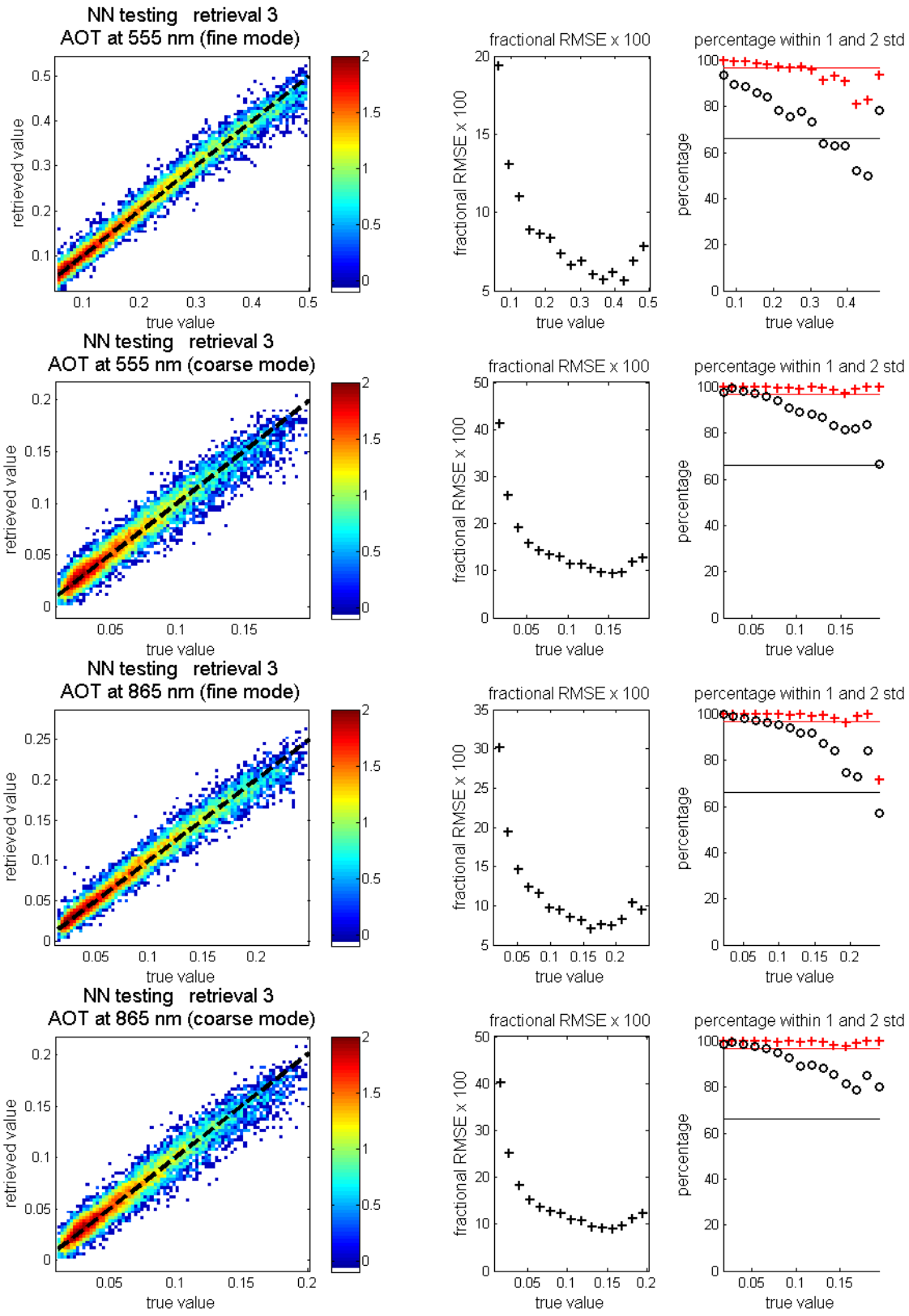
NN testing retrieval 3
AOT at 555 nm (fine mode)
retrieved value
true value
fractional RMSE x 100
fractional RMSE x 100
true value
percentage within 1 and 2 std
percentage
true value
NN testing retrieval 3
AOT at 555 nm (coarse mode)
retrieved value
true value
fractional RMSE x 100
fractional RMSE x 100
true value
percentage within 1 and 2 std
percentage
true value
NN testing retrieval 3
AOT at 865 nm (fine mode)
retrieved value
true value
fractional RMSE x 100
fractional RMSE x 100
true value
percentage within 1 and 2 std
percentage
true value
NN testing retrieval 3
AOT at 865 nm (coarse mode)
retrieved value
true value
fractional RMSE x 100
fractional RMSE x 100
true value
percentage within 1 and 2 std
percentage
true value

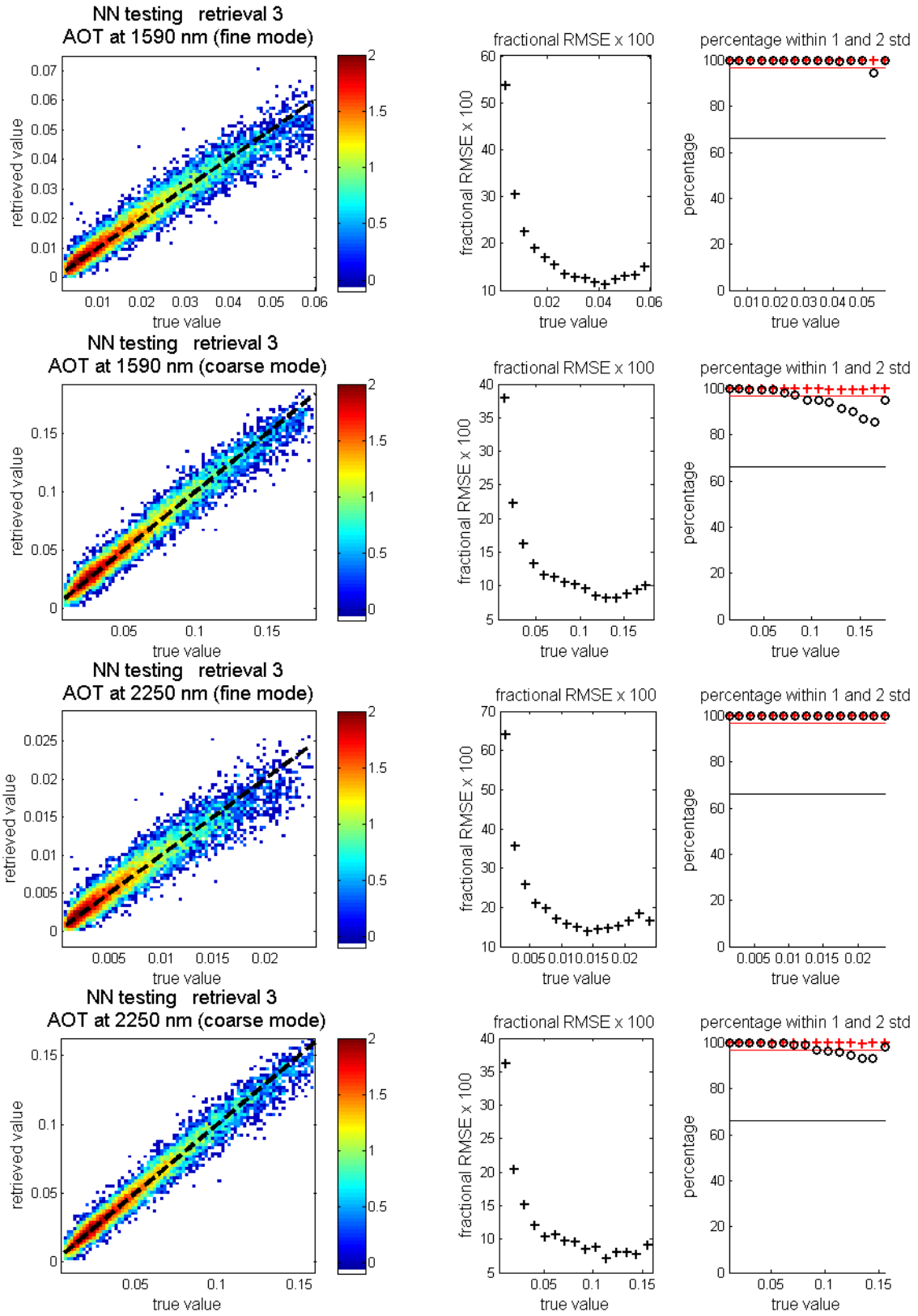
NN testing retrieval 3
AOT at 1590 nm (fine mode)
retrieved value
true value
fractional RMSE x 100
fractional RMSE x 100
true value
percentage within 1 and 2 std
percentage
true value
NN testing retrieval 3
AOT at 1590 nm (coarse mode)
retrieved value
true value
fractional RMSE x 100
fractional RMSE x 100
true value
percentage within 1 and 2 std
percentage
true value
NN testing retrieval 3
AOT at 2250 nm (fine mode)
retrieved value
true value
fractional RMSE x 100
fractional RMSE x 100
true value
percentage within 1 and 2 std
percentage
true value
NN testing retrieval 3
AOT at 2250 nm (coarse mode)
retrieved value
true value
fractional RMSE x 100
fractional RMSE x 100
true value
percentage within 1 and 2 std
percentage
true value

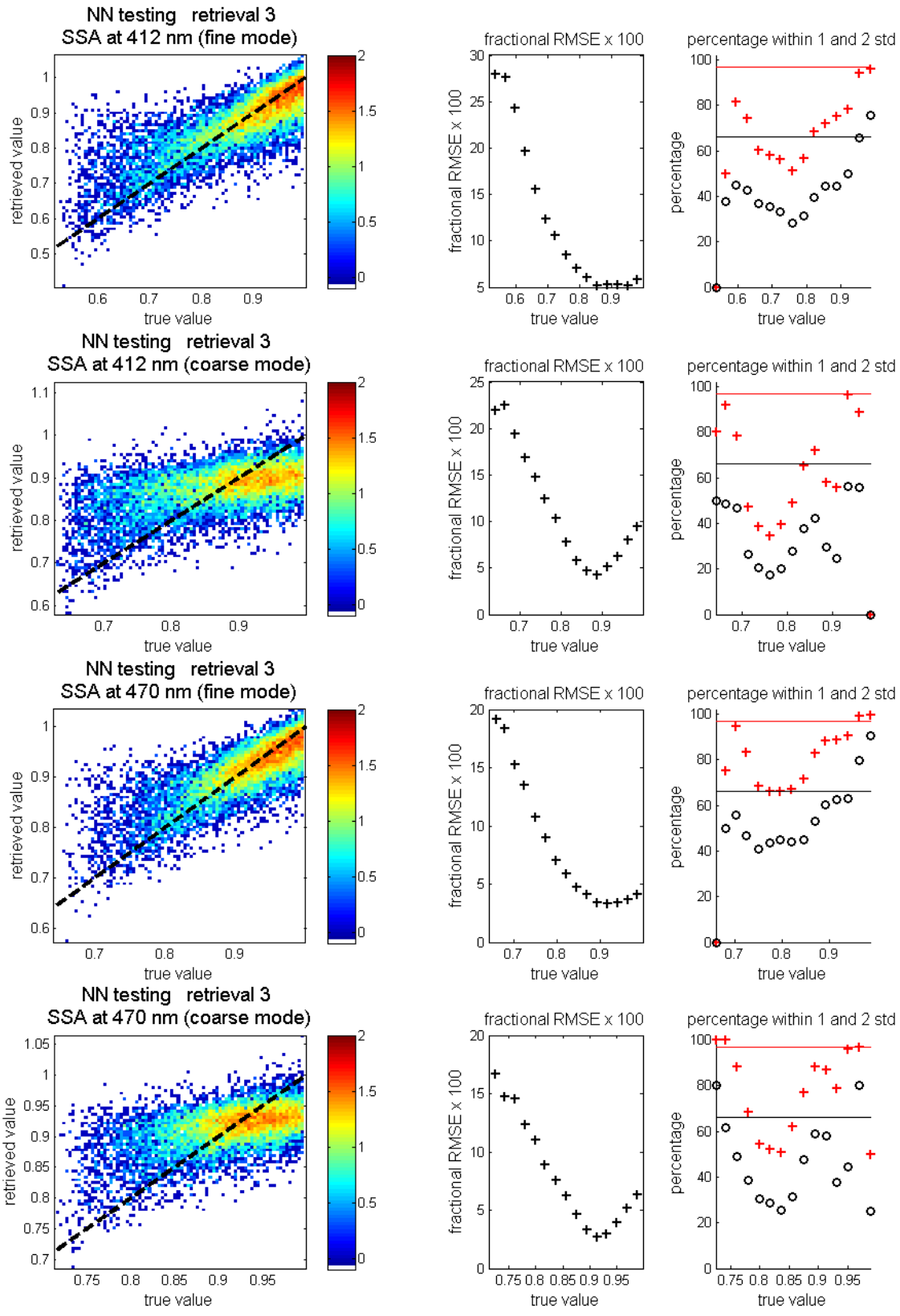
NN testing retrieval 3
SSA at 412 nm (fine mode)
retrieved value
true value
fractional RMSE x 100
fractional RMSE x 100
true value
percentage within 1 and 2 std
percentage
true value
NN testing retrieval 3
SSA at 412 nm (coarse mode)
retrieved value
true value
fractional RMSE x 100
fractional RMSE x 100
true value
percentage within 1 and 2 std
percentage
true value
NN testing retrieval 3
SSA at 470 nm (fine mode)
retrieved value
true value
fractional RMSE x 100
fractional RMSE x 100
true value
percentage within 1 and 2 std
percentage
true value
NN testing retrieval 3
SSA at 470 nm (coarse mode)
retrieved value
true value
fractional RMSE x 100
fractional RMSE x 100
true value
percentage within 1 and 2 std
percentage
true value

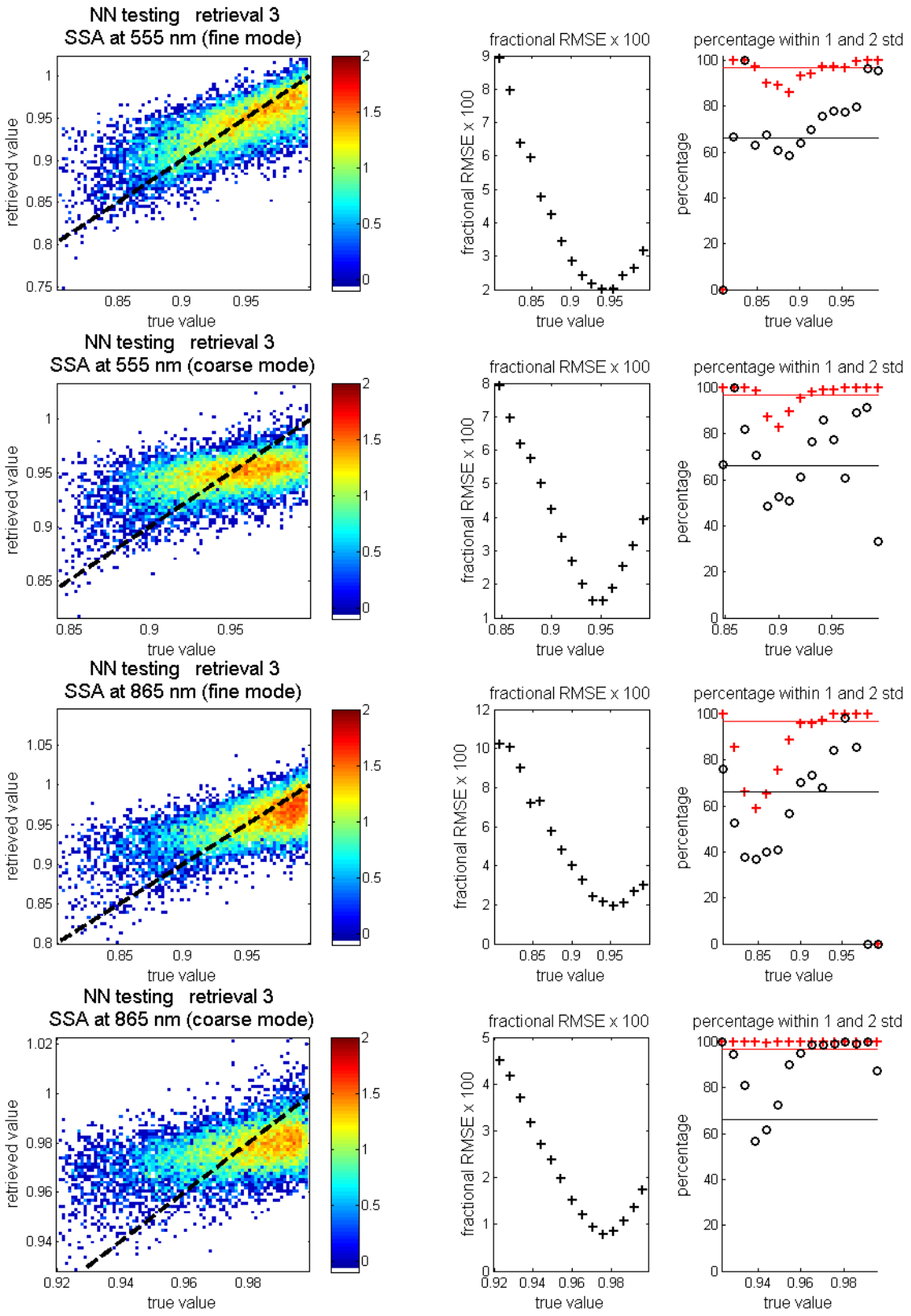
NN testing retrieval 3
SSA at 555 nm (fine mode)
retrieved value
true value
fractional RMSE x 100
fractional RMSE x 100
true value
percentage within 1 and 2 std
percentage
true value
NN testing retrieval 3
SSA at 555 nm (coarse mode)
retrieved value
true value
fractional RMSE x 100
fractional RMSE x 100
true value
percentage within 1 and 2 std
percentage
true value
NN testing retrieval 3
SSA at 865 nm (fine mode)
retrieved value
true value
fractional RMSE x 100
fractional RMSE x 100
true value
percentage within 1 and 2 std
percentage
true value
NN testing retrieval 3
SSA at 865 nm (coarse mode)
retrieved value
true value
fractional RMSE x 100
fractional RMSE x 100
true value
percentage within 1 and 2 std
percentage
true value

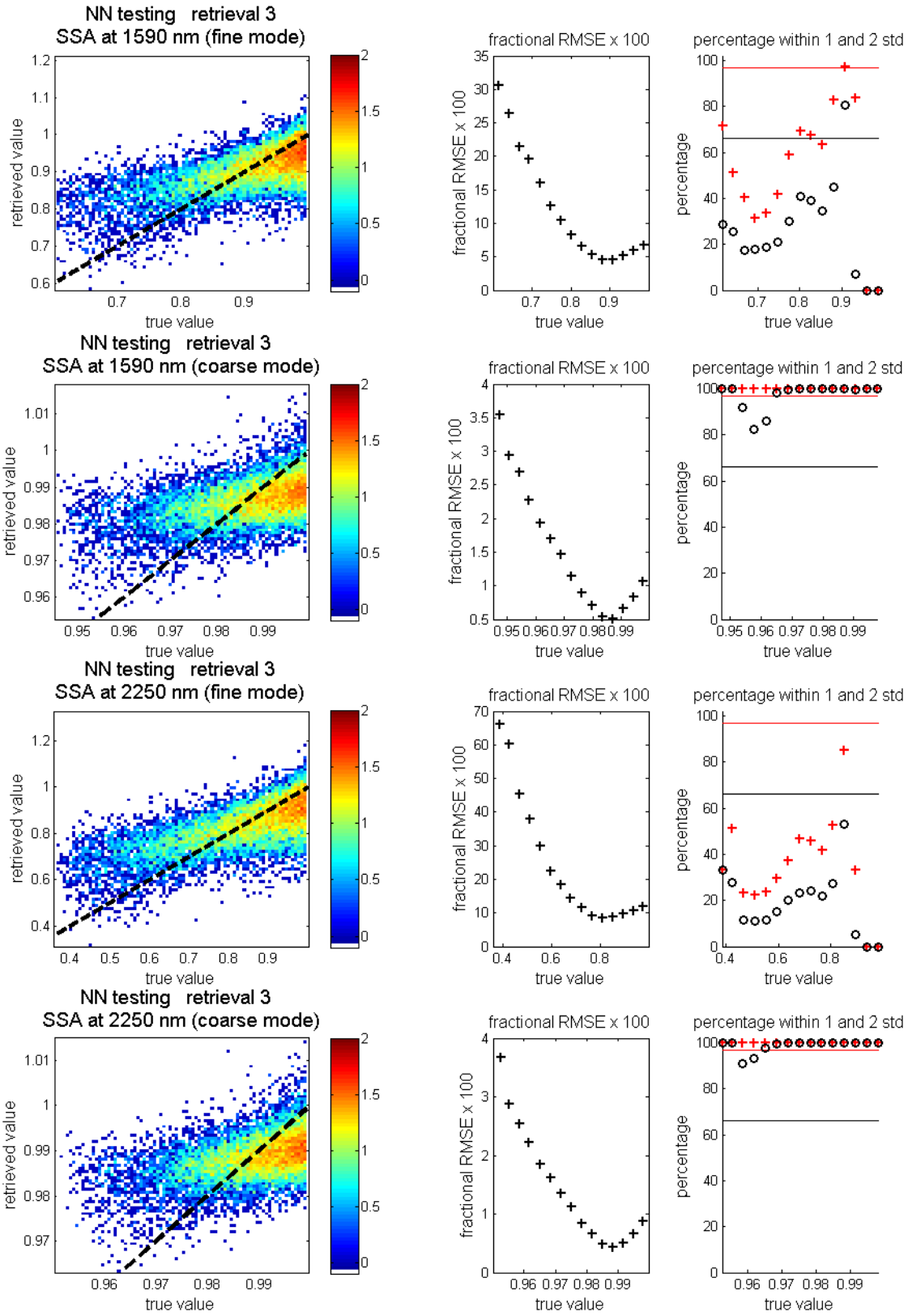
NN testing retrieval 3
SSA at 1590 nm (fine mode)
retrieved value
true value
fractional RMSE x 100
fractional RMSE x 100
true value
percentage within 1 and 2 std
percentage
true value
NN testing retrieval 3
SSA at 1590 nm (coarse mode)
retrieved value
true value
fractional RMSE x 100
fractional RMSE x 100
true value
percentage within 1 and 2 std
percentage
true value
NN testing retrieval 3
SSA at 2250 nm (fine mode)
retrieved value
true value
fractional RMSE x 100
fractional RMSE x 100
true value
percentage within 1 and 2 std
percentage
true value
NN testing retrieval 3
SSA at 2250 nm (coarse mode)
retrieved value
true value
fractional RMSE x 100
fractional RMSE x 100
true value
percentage within 1 and 2 std
percentage
true value

Retrieval #4

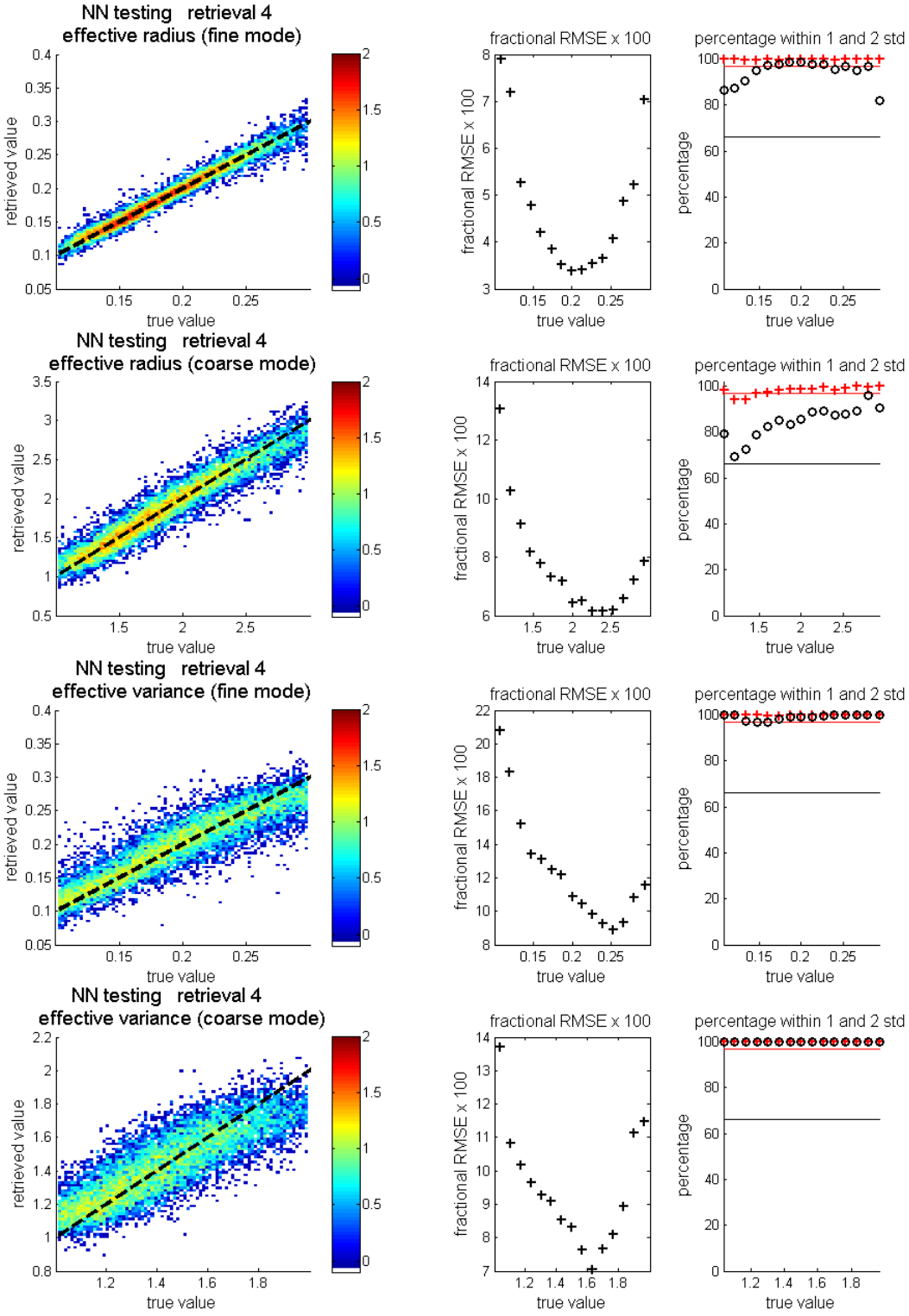
NN testing retrieval 4
effective radius (fine mode)
retrieved value
true value
fractional RMSE x 100
true value
percentage within 1 and 2 std
percentage
true value
NN testing retrieval 4
effective radius (coarse mode)
retrieved value
true value
fractional RMSE x 100
true value
percentage within 1 and 2 std
percentage
true value
NN testing retrieval 4
effective variance (fine mode)
retrieved value
true value
fractional RMSE x 100
true value
percentage within 1 and 2 std
percentage
true value
NN testing retrieval 4
effective variance (coarse mode)
retrieved value
true value
fractional RMSE x 100
true value
percentage within 1 and 2 std
percentage
true value

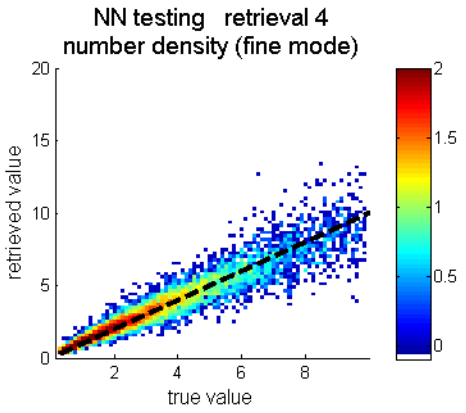
NN testing retrieval 4
number density (fine mode)
retrieved value
true value

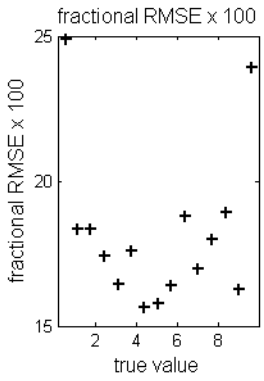
fractional RMSE x 100
fractional RMSE x 100
true value

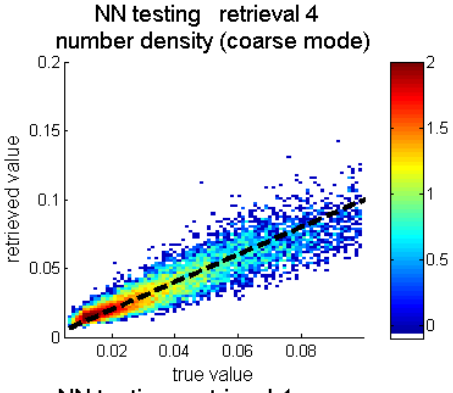
NN testing retrieval 4
number density (coarse mode)
retrieved value
true value

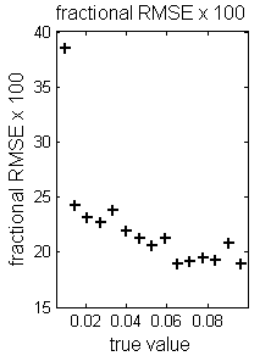
fractional RMSE x 100
fractional RMSE x 100
true value

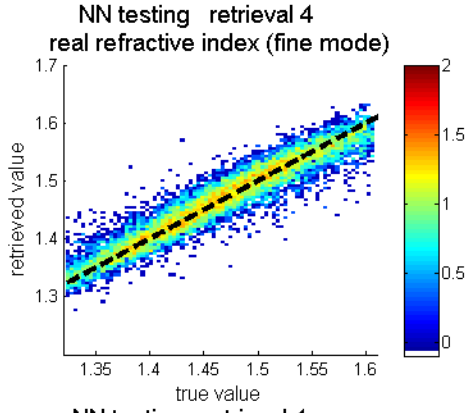
NN testing retrieval 4
real refractive index (fine mode)
retrieved value
true value

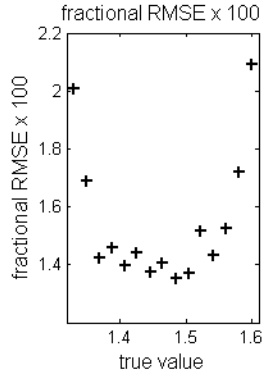
fractional RMSE x 100
fractional RMSE x 100
true value

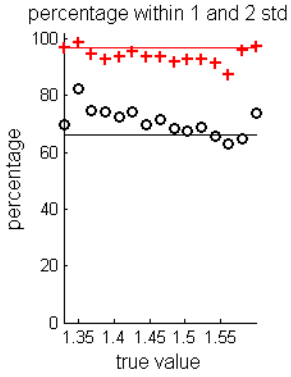
percentage within 1 and 2 std
percentage
true value

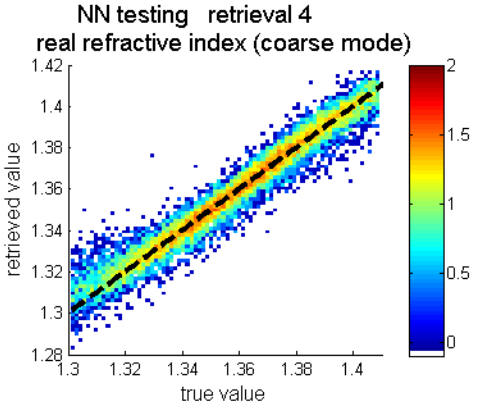
NN testing retrieval 4
real refractive index (coarse mode)
retrieved value
true value

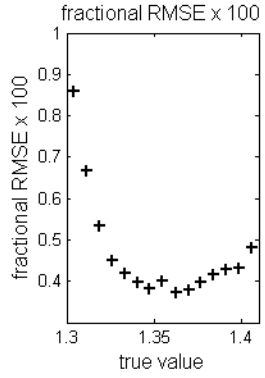
fractional RMSE x 100
fractional RMSE x 100
true value

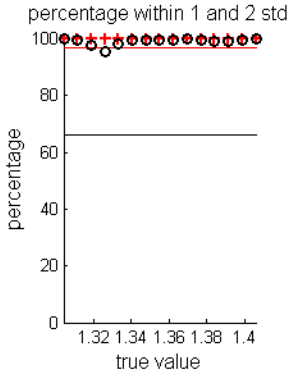
percentage within 1 and 2 std
percentage
true value

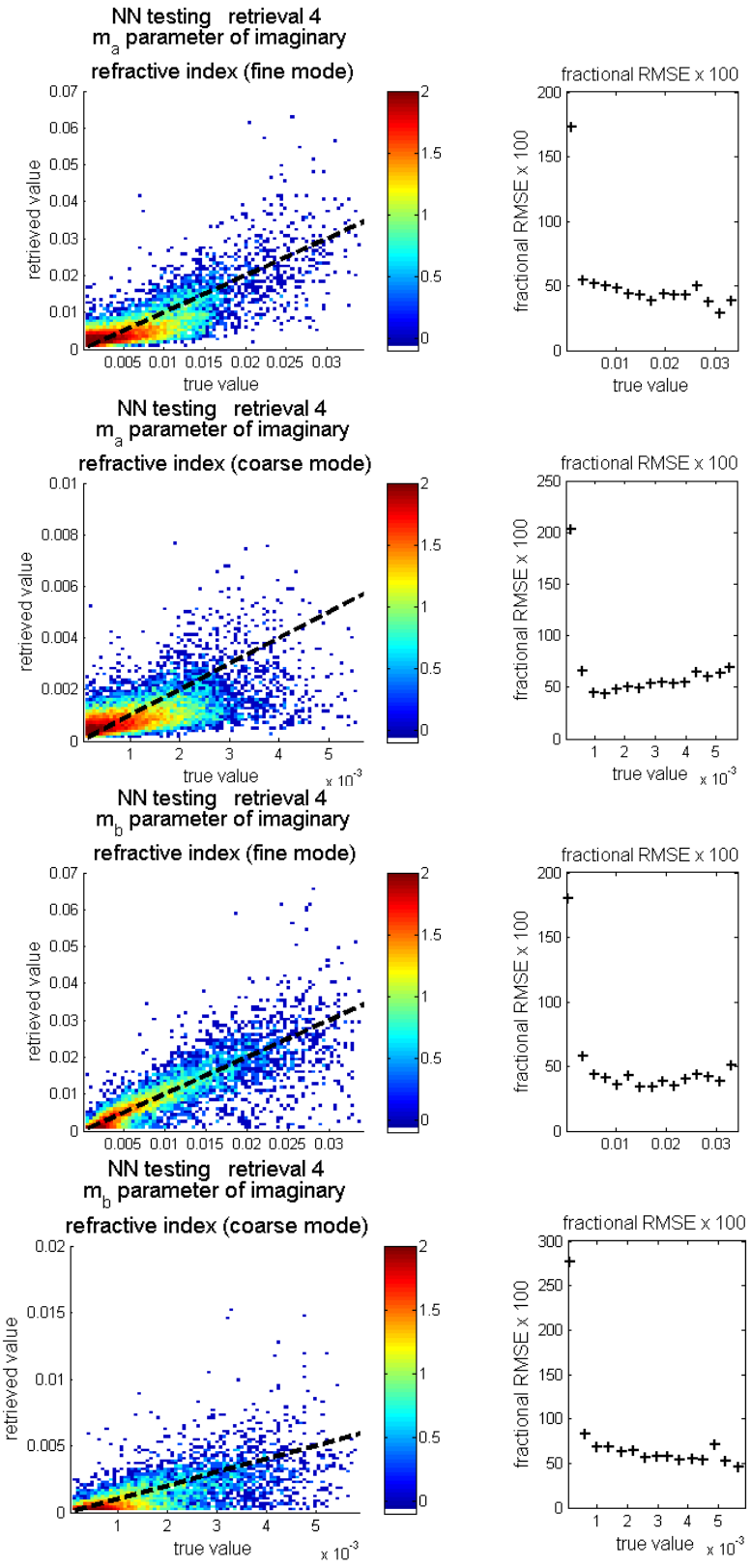
NN testing retrieval 4
m_a parameter of imaginary
refractive index (fine mode)
retrieved value
true value
fractional RMSE x 100
fractional RMSE x 100
true value
NN testing retrieval 4
m_a parameter of imaginary
refractive index (coarse mode)
retrieved value
true value
x 10^-3
fractional RMSE x 100
fractional RMSE x 100
true value
x 10^-3
NN testing retrieval 4
m_b parameter of imaginary
refractive index (fine mode)
retrieved value
fractional RMSE x 100
fractional RMSE x 100
NN testing retrieval 4
m_b parameter of imaginary
refractive index (coarse mode)
retrieved value
true value
x 10^-3
fractional RMSE x 100
fractional RMSE x 100
true value
x 10^-3

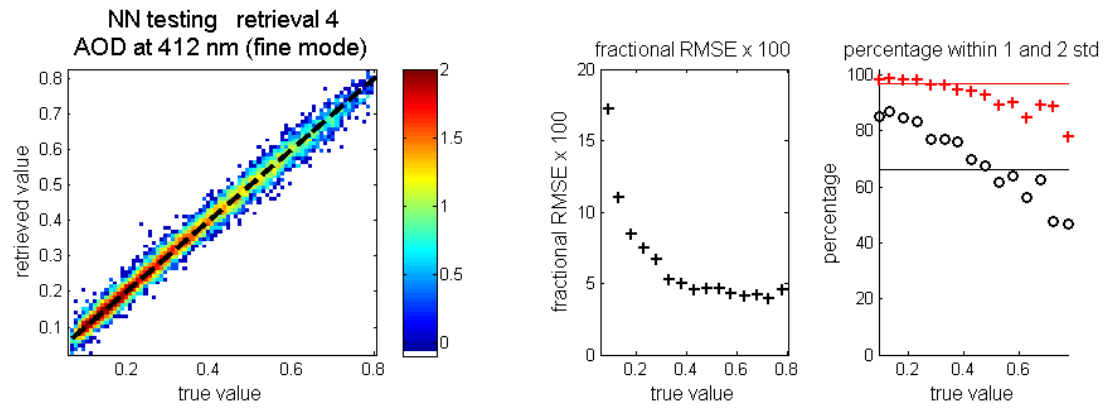
NN testing retrieval 4
AOD at 412 nm (fine mode)
retrieved value
true value
fractional RMSE x 100
fractional RMSE x 100
true value
percentage within 1 and 2 std
percentage
true value

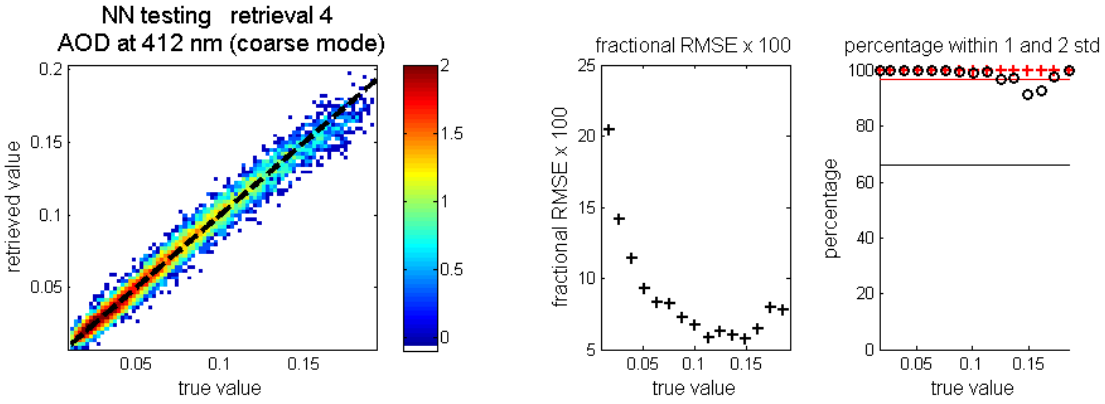
NN testing retrieval 4
AOD at 412 nm (coarse mode)
retrieved value
true value
fractional RMSE x 100
fractional RMSE x 100
true value
percentage within 1 and 2 std
percentage
true value

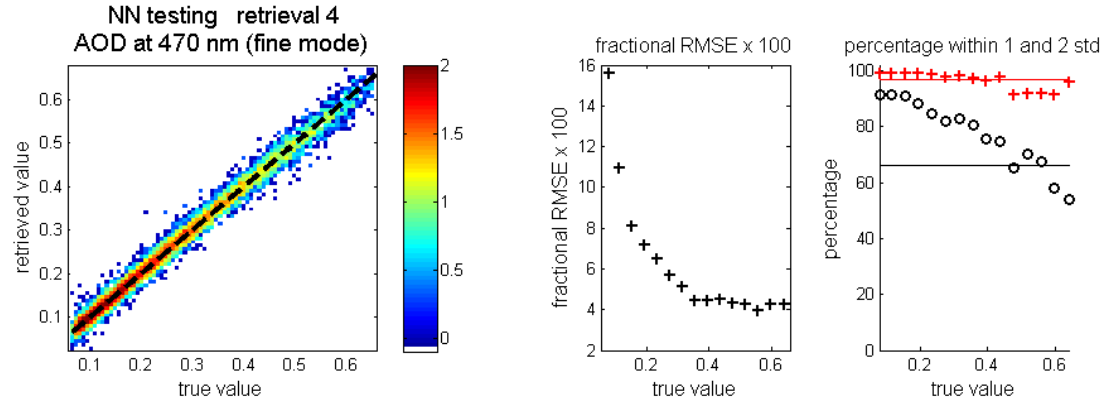
NN testing retrieval 4
AOD at 470 nm (fine mode)
retrieved value
true value
fractional RMSE x 100
fractional RMSE x 100
true value
percentage within 1 and 2 std
percentage
true value

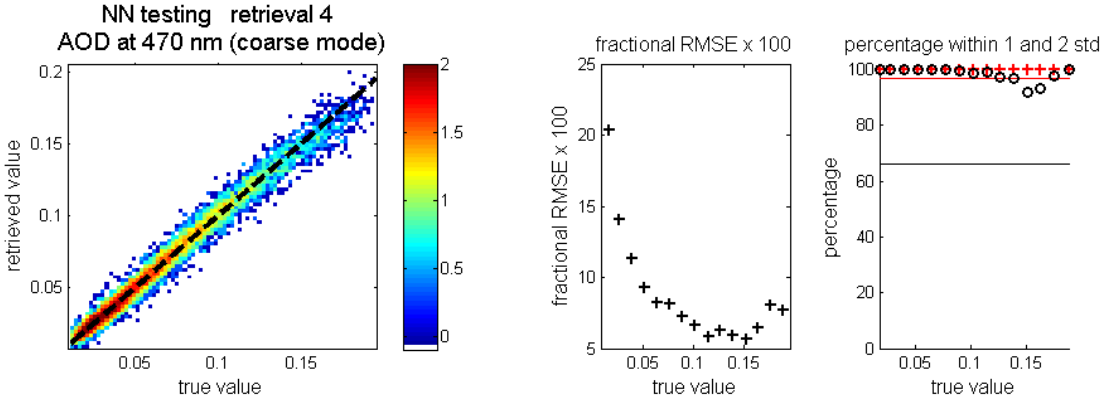
NN testing retrieval 4
AOD at 470 nm (coarse mode)
retrieved value
true value
fractional RMSE x 100
fractional RMSE x 100
true value
percentage within 1 and 2 std
percentage
true value

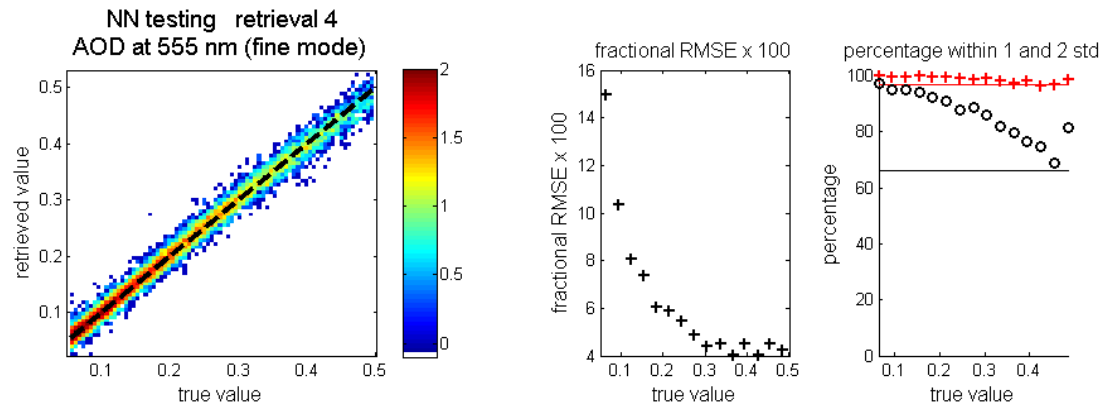
NN testing retrieval 4
AOD at 555 nm (fine mode)
retrieved value
true value
fractional RMSE x 100
fractional RMSE x 100
true value
percentage within 1 and 2 std
percentage
true value

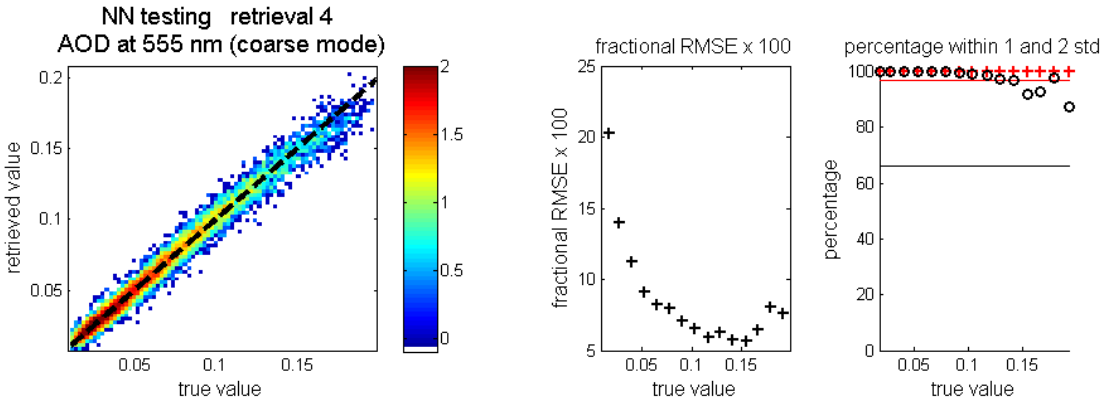
NN testing retrieval 4
AOD at 555 nm (coarse mode)
retrieved value
true value
fractional RMSE x 100
fractional RMSE x 100
true value
percentage within 1 and 2 std
percentage
true value

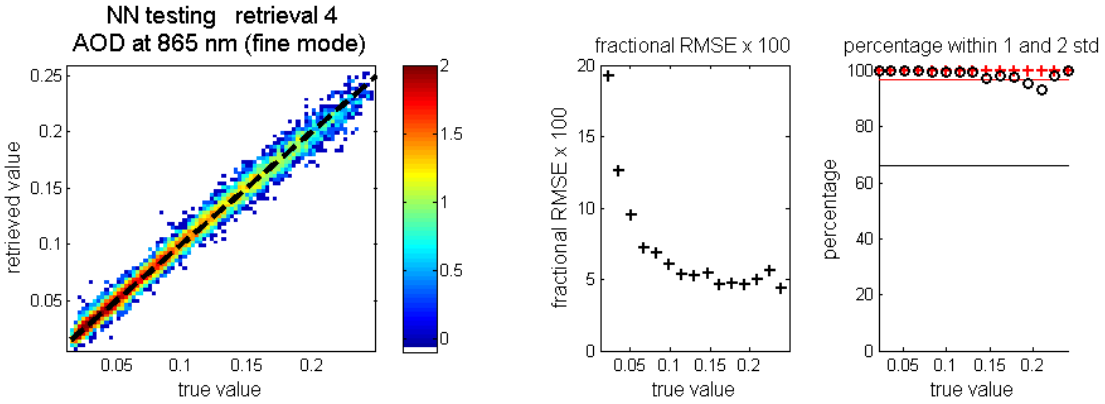
NN testing retrieval 4
AOD at 865 nm (fine mode)
retrieved value
true value
fractional RMSE x 100
fractional RMSE x 100
true value
percentage within 1 and 2 std
percentage
true value

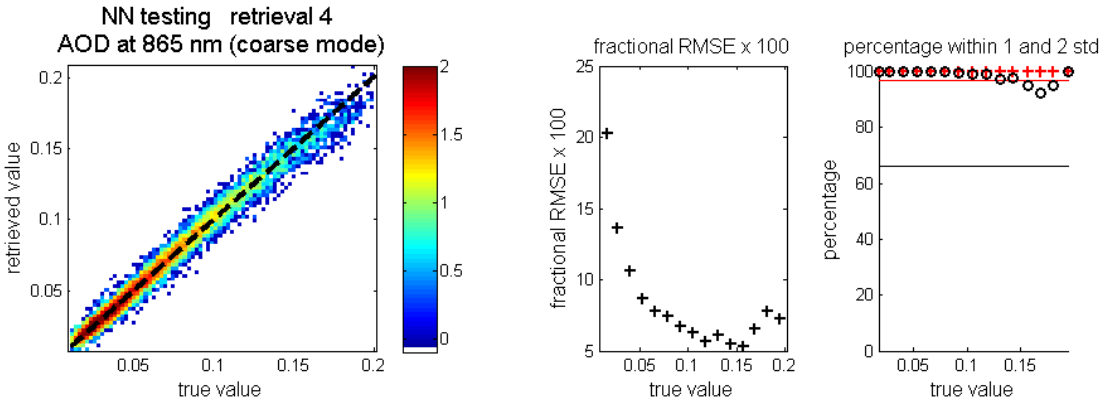
NN testing retrieval 4
AOD at 865 nm (coarse mode)
retrieved value
true value
fractional RMSE x 100
fractional RMSE x 100
true value
percentage within 1 and 2 std
percentage
true value

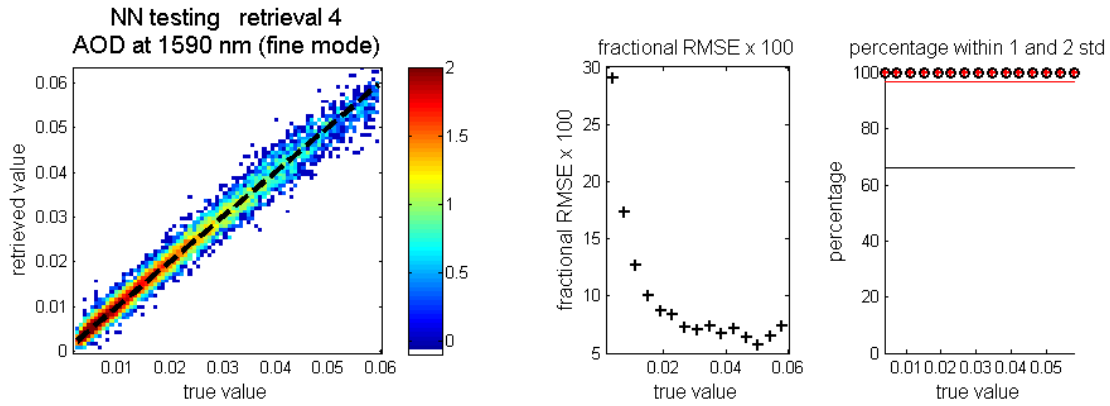
NN testing retrieval 4
AOD at 1590 nm (fine mode)
retrieved value
true value
fractional RMSE x 100
fractional RMSE x 100
true value
percentage within 1 and 2 std
percentage
true value

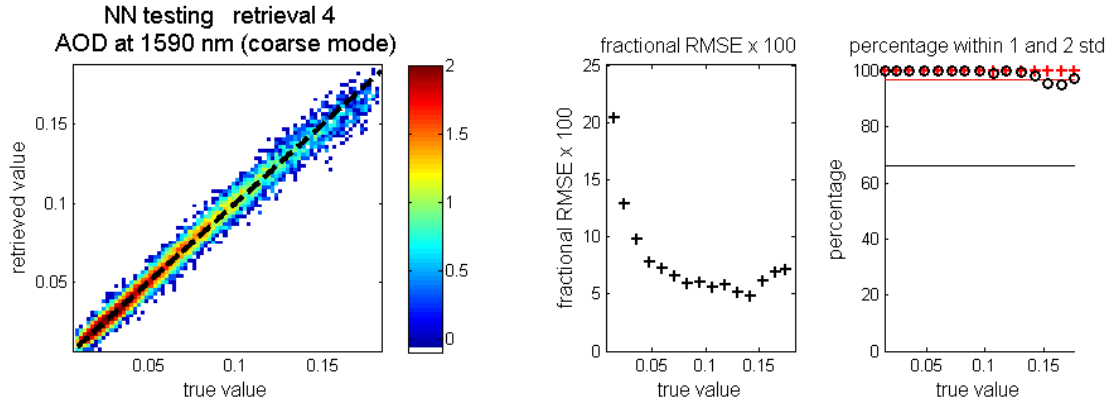
NN testing retrieval 4
AOD at 1590 nm (coarse mode)
retrieved value
true value
fractional RMSE x 100
fractional RMSE x 100
true value
percentage within 1 and 2 std
percentage
true value

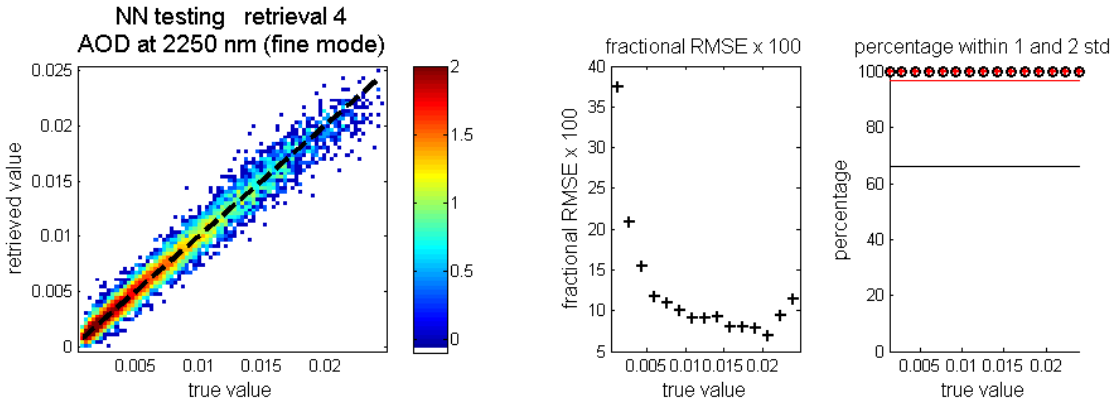
NN testing retrieval 4
AOD at 2250 nm (fine mode)
retrieved value
true value
fractional RMSE x 100
fractional RMSE x 100
true value
percentage within 1 and 2 std
percentage
true value

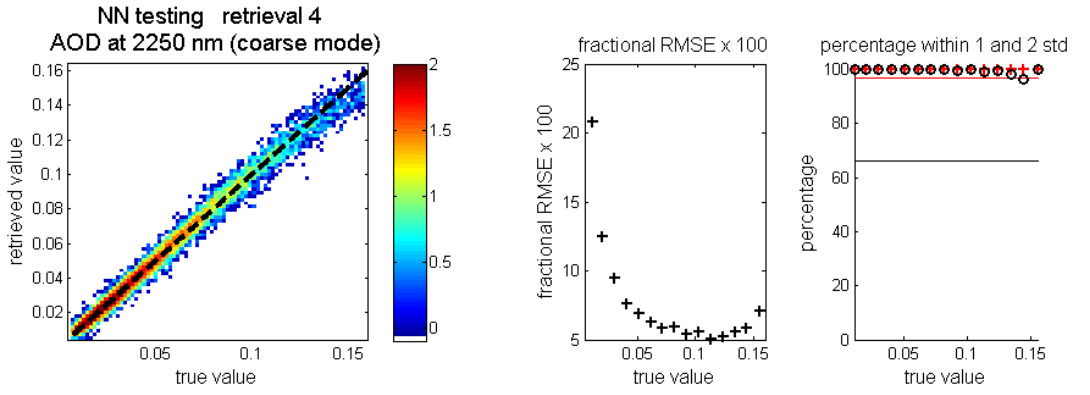
NN testing retrieval 4
AOD at 2250 nm (coarse mode)
retrieved value
true value
fractional RMSE x 100
fractional RMSE x 100
true value
percentage within 1 and 2 std
percentage
true value

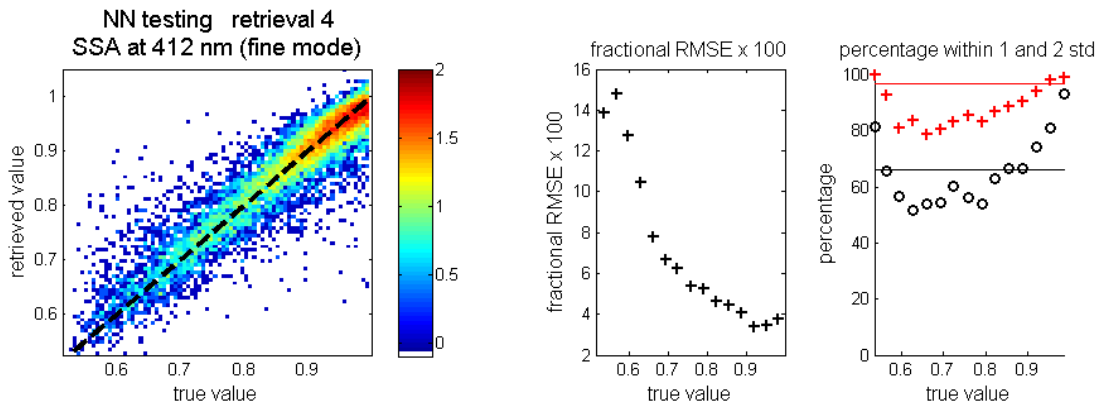
NN testing retrieval 4
SSA at 412 nm (fine mode)
retrieved value
true value
fractional RMSE x 100
fractional RMSE x 100
true value
percentage within 1 and 2 std
percentage
true value

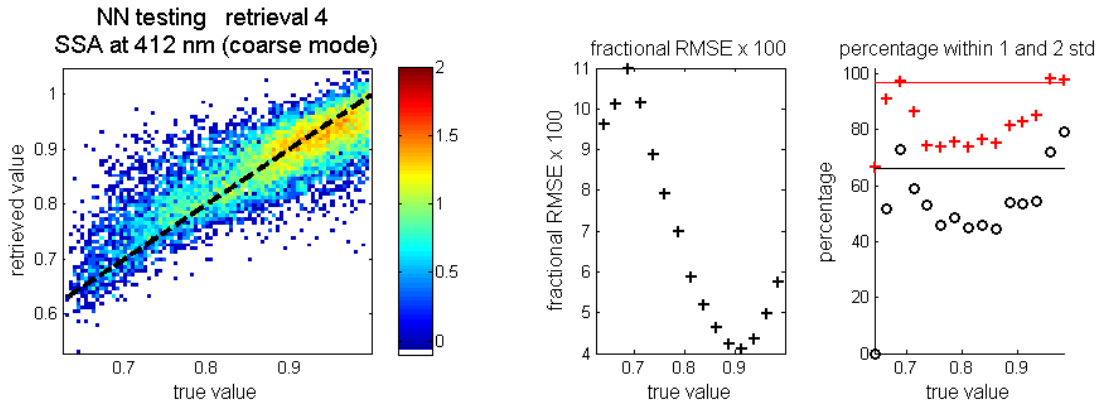
NN testing retrieval 4
SSA at 412 nm (coarse mode)
retrieved value
true value
fractional RMSE x 100
fractional RMSE x 100
true value
percentage within 1 and 2 std
percentage
true value

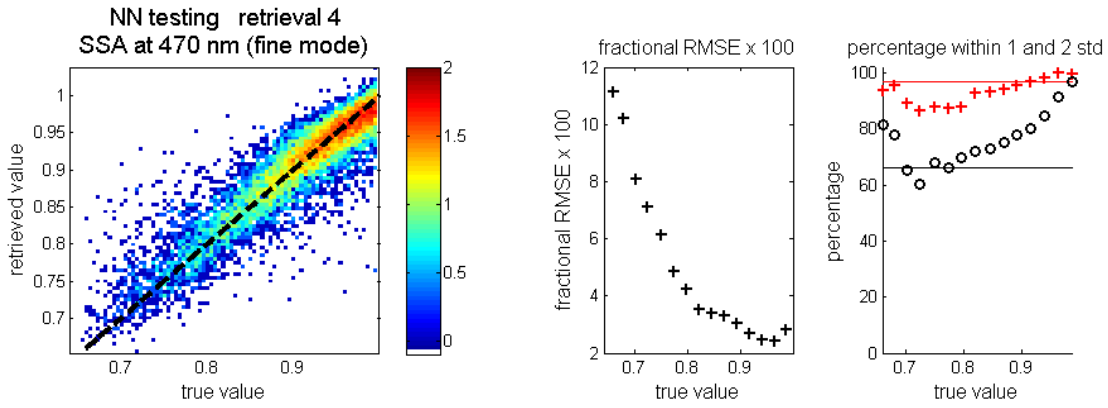
NN testing retrieval 4
SSA at 470 nm (fine mode)
retrieved value
true value
fractional RMSE x 100
fractional RMSE x 100
true value
percentage within 1 and 2 std
percentage
true value

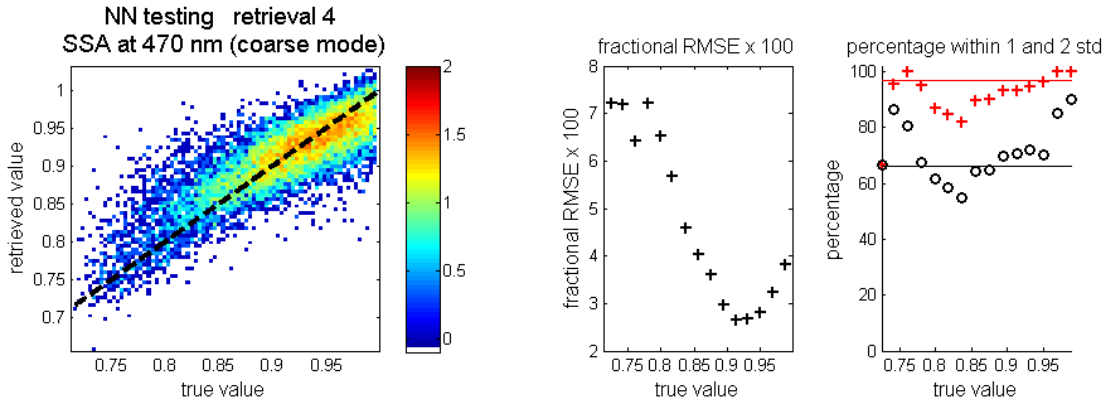
NN testing retrieval 4
SSA at 470 nm (coarse mode)
retrieved value
true value
fractional RMSE x 100
fractional RMSE x 100
true value
percentage within 1 and 2 std
percentage
true value

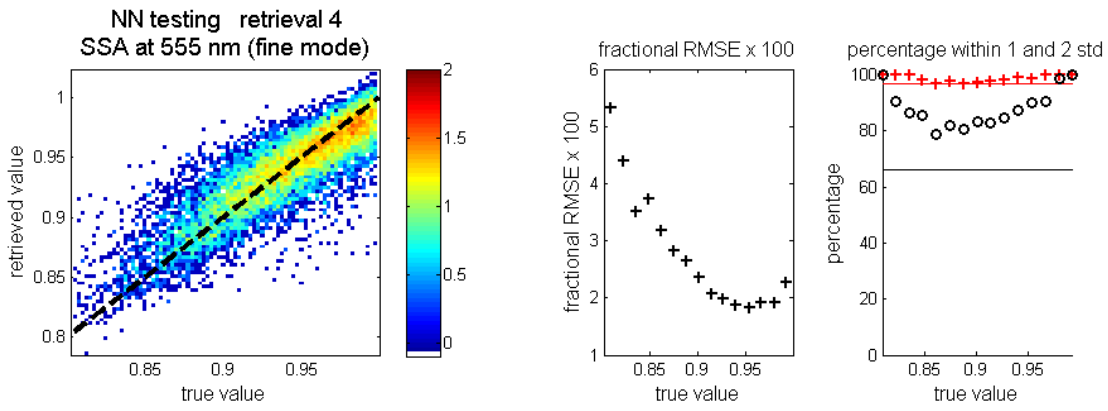
NN testing retrieval 4
SSA at 555 nm (fine mode)
retrieved value
true value
fractional RMSE x 100
fractional RMSE x 100
true value
percentage within 1 and 2 std
percentage
true value

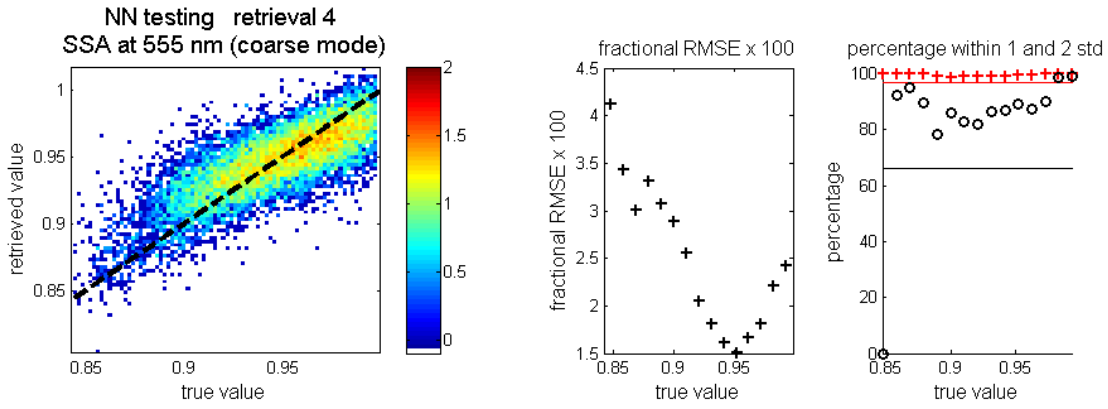
NN testing retrieval 4
SSA at 555 nm (coarse mode)
retrieved value
true value
fractional RMSE x 100
fractional RMSE x 100
true value
percentage within 1 and 2 std
percentage
true value

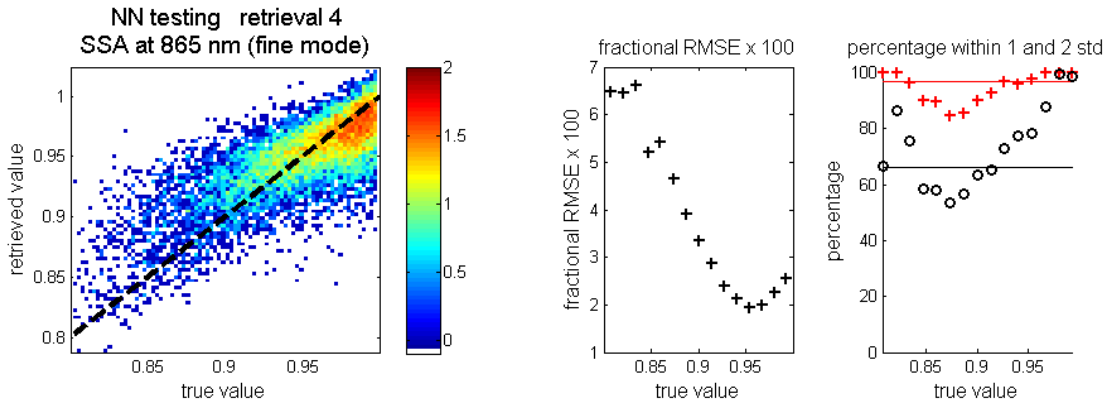
NN testing retrieval 4
SSA at 865 nm (fine mode)
retrieved value
true value
fractional RMSE x 100
fractional RMSE x 100
true value
percentage within 1 and 2 std
percentage
true value

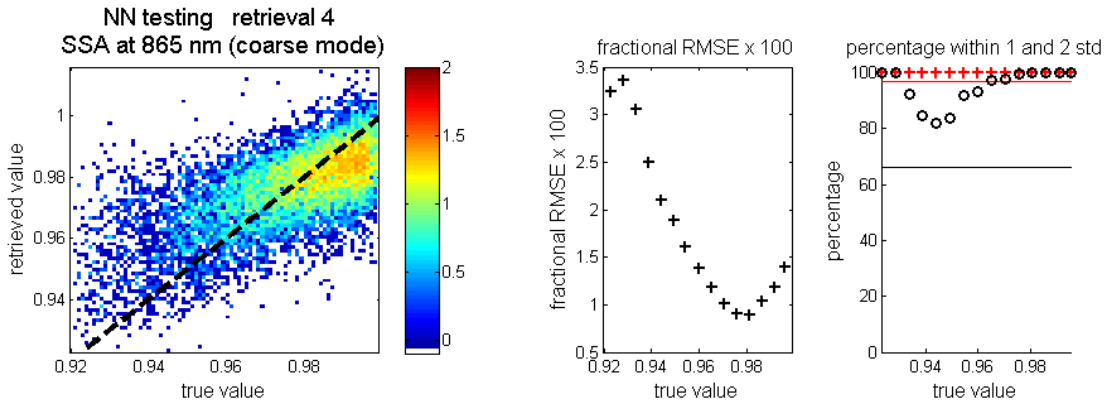
NN testing retrieval 4
SSA at 865 nm (coarse mode)
retrieved value
true value
fractional RMSE x 100
fractional RMSE x 100
true value
percentage within 1 and 2 std
percentage
true value

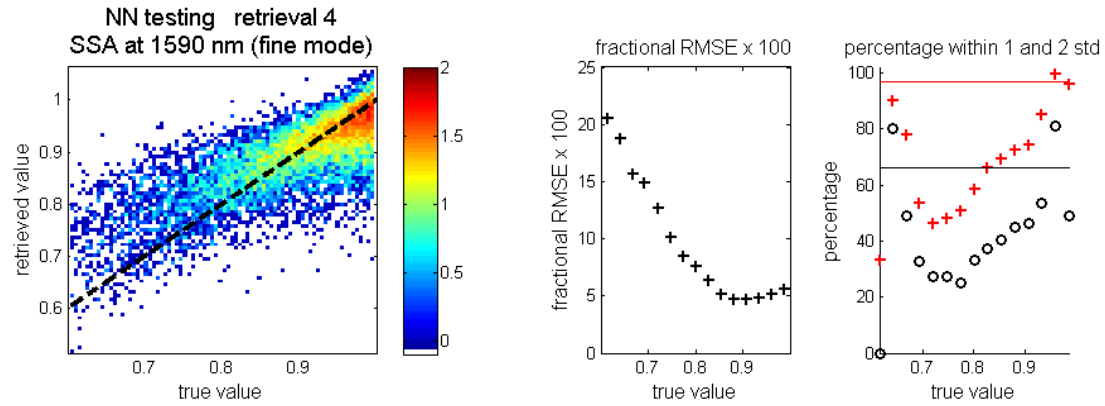
NN testing retrieval 4
SSA at 1590 nm (fine mode)
retrieved value
true value
fractional RMSE x 100
fractional RMSE x 100
true value
percentage within 1 and 2 std
percentage
true value

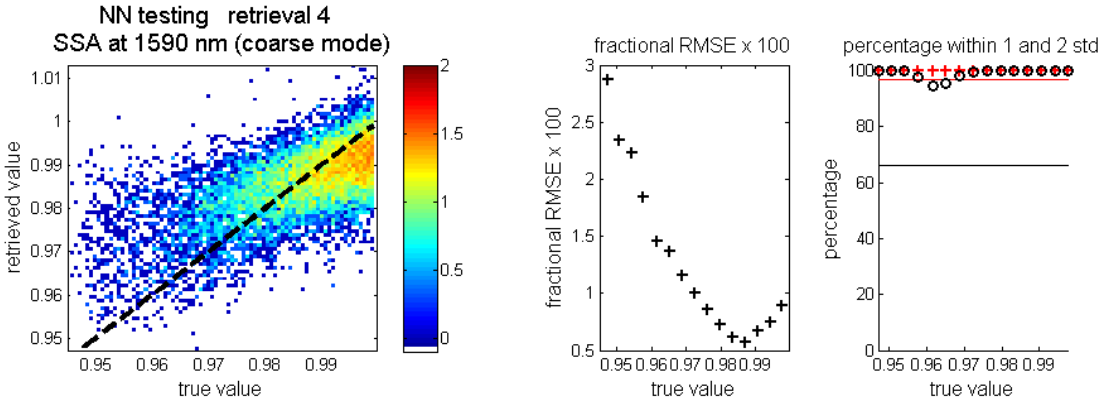
NN testing retrieval 4
SSA at 1590 nm (coarse mode)
retrieved value
true value
fractional RMSE x 100
fractional RMSE x 100
true value
percentage within 1 and 2 std
percentage
true value

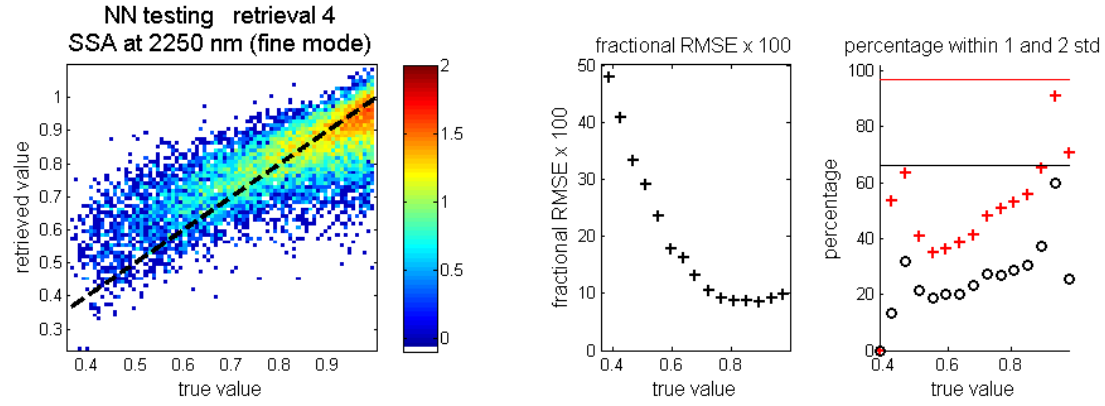
NN testing retrieval 4
SSA at 2250 nm (fine mode)
retrieved value
true value
fractional RMSE x 100
fractional RMSE x 100
true value
percentage within 1 and 2 std
percentage
true value

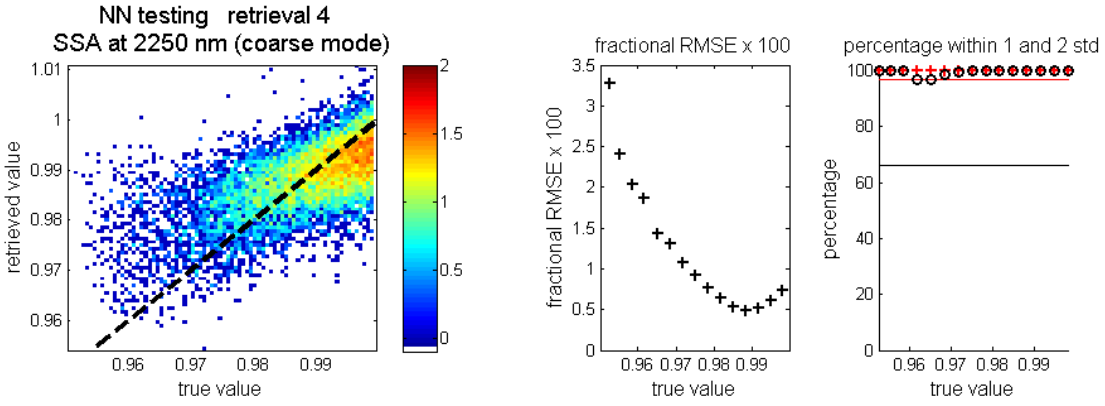
NN testing retrieval 4
SSA at 2250 nm (coarse mode)
retrieved value
true value
fractional RMSE x 100
fractional RMSE x 100
true value
percentage within 1 and 2 std
percentage
true value

Appendix IV

Testing retrievals #2 and #4 on RSP files #22 and #51 from the INTEX-B/MILAGRO campaign

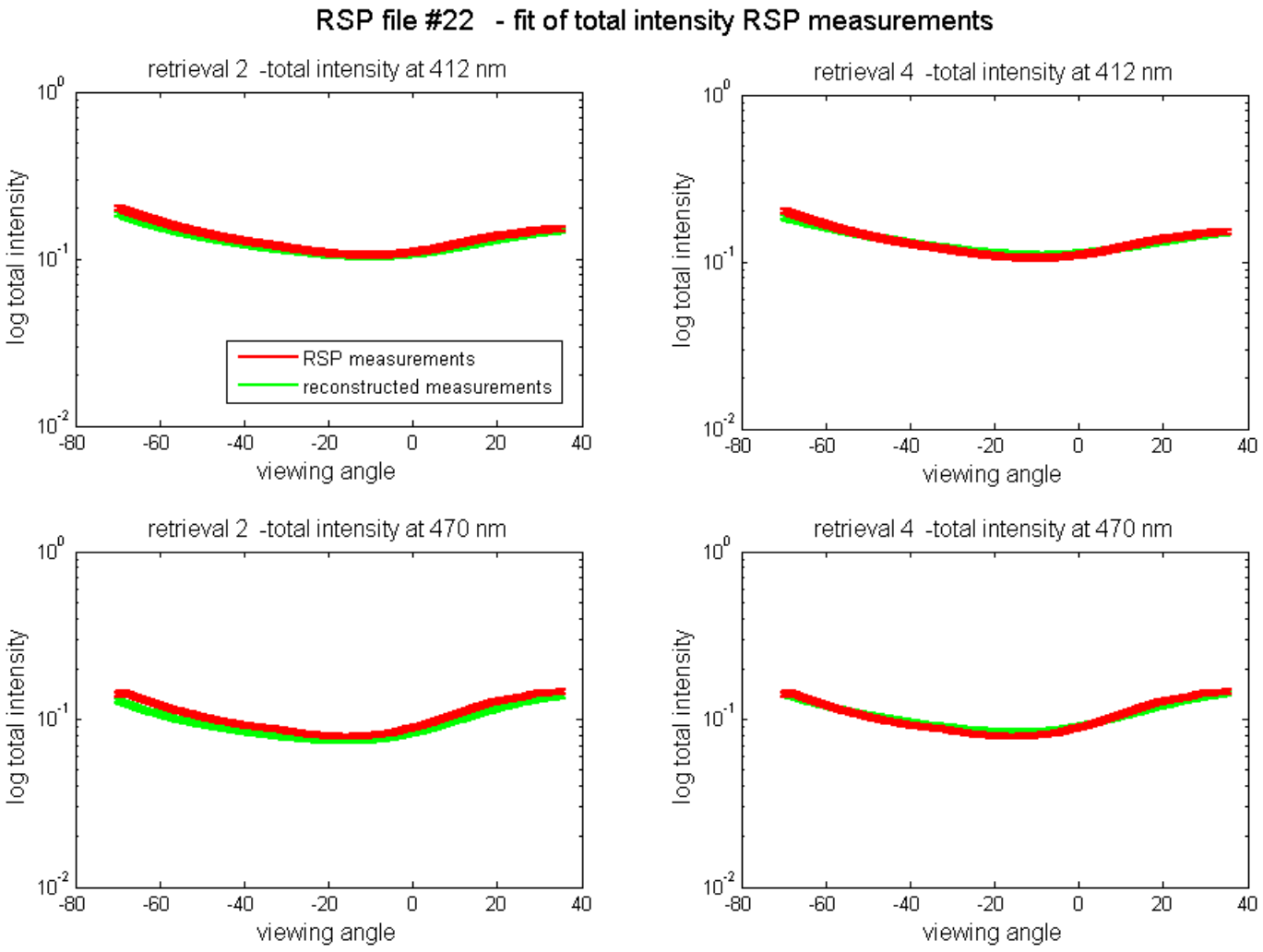

RSP file #22 - fit of total intensity RSP measurements (continue)

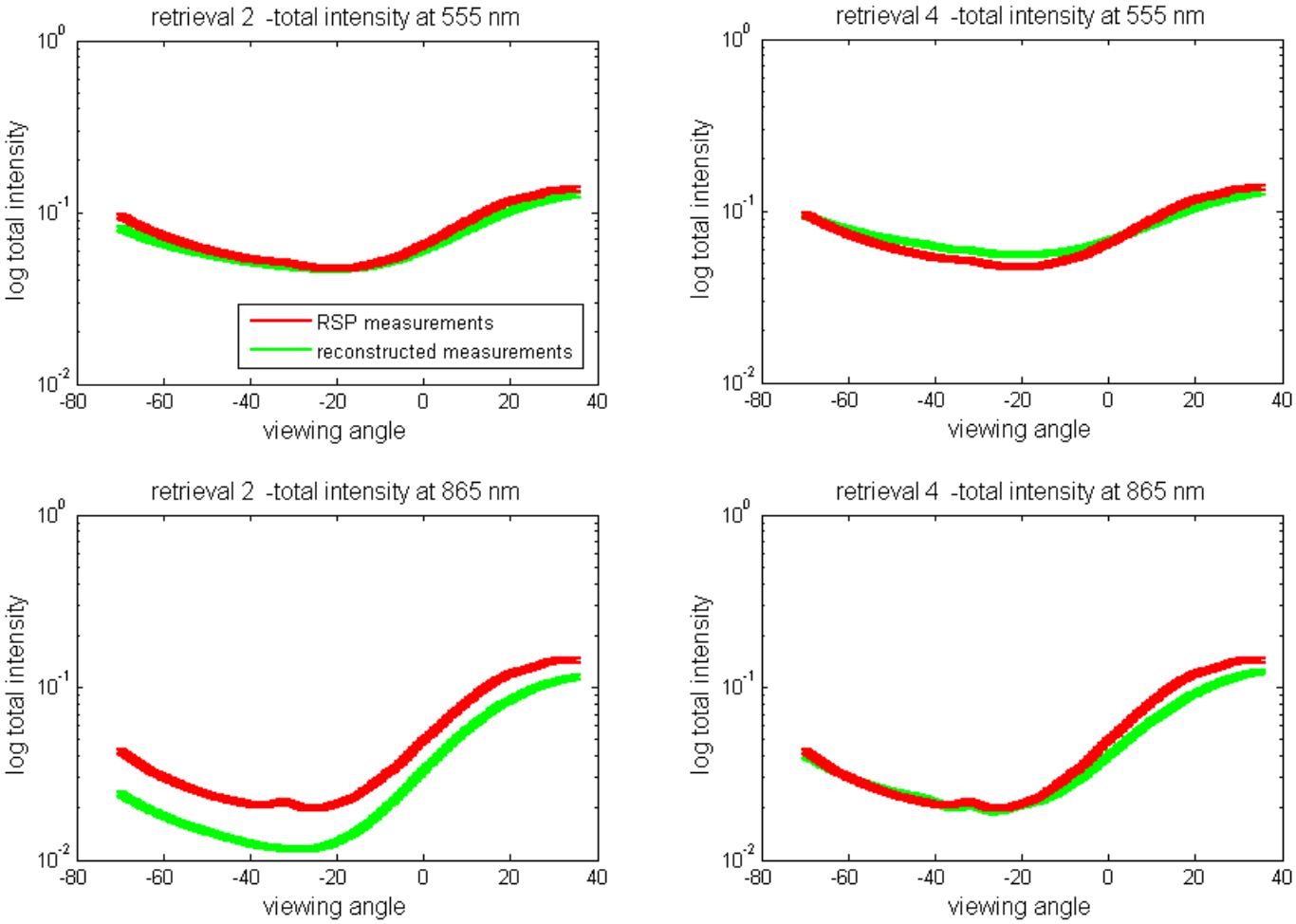

RSP file #22 - fit of total intensity RSP measurements (continue)

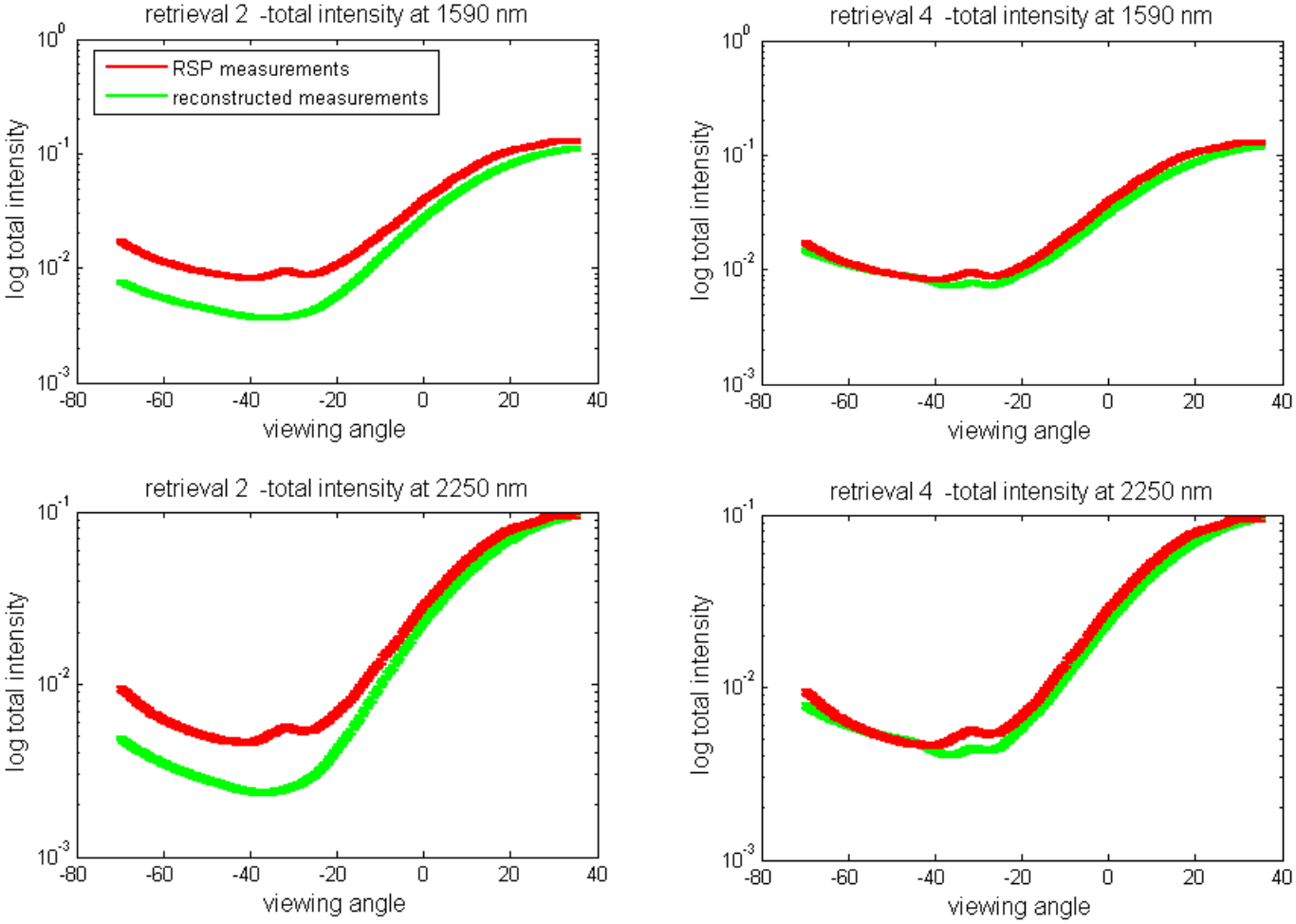

RSP file #22 - fit of linearly polarized intensity RSP measurements

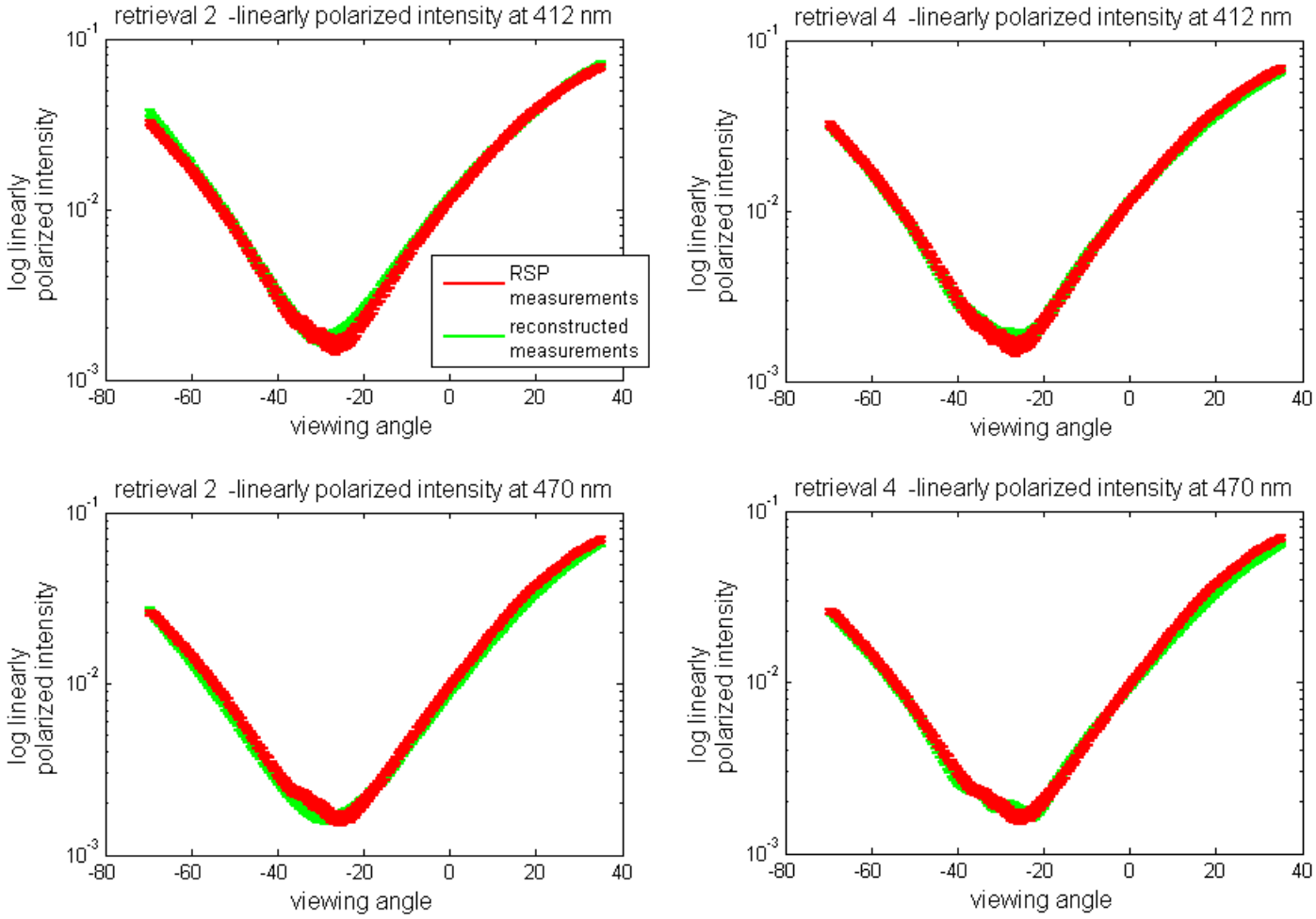

RSP file #22 - fit of linearly polarized intensity RSP measurements (continue)

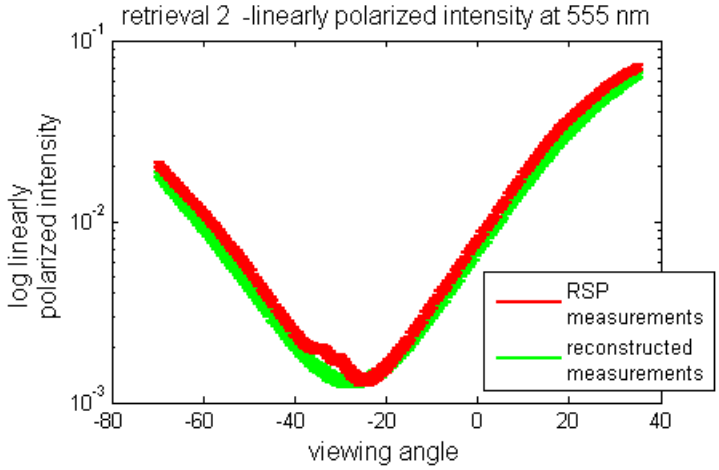

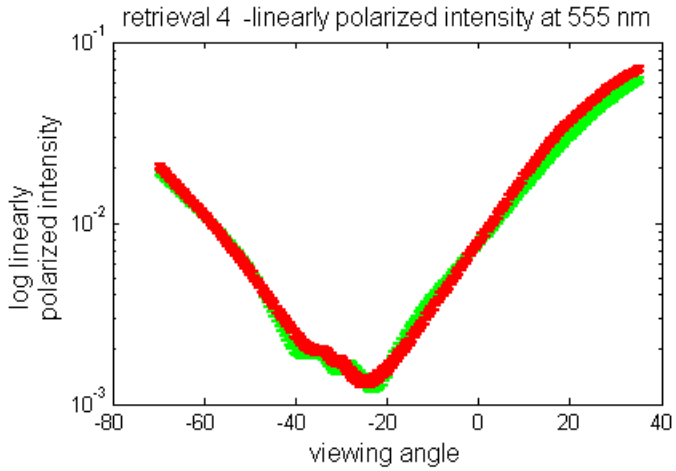

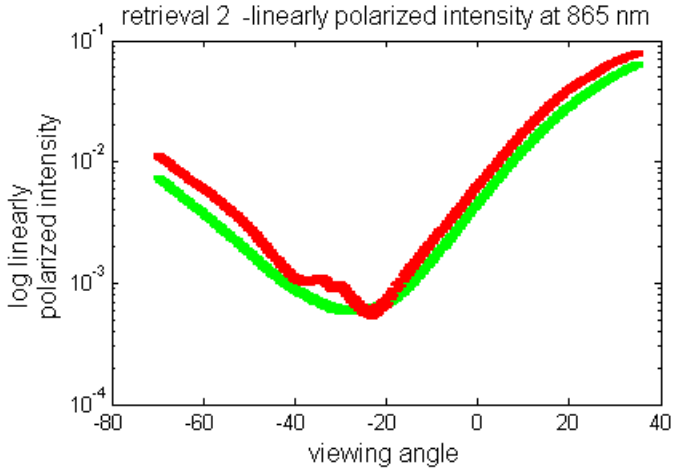

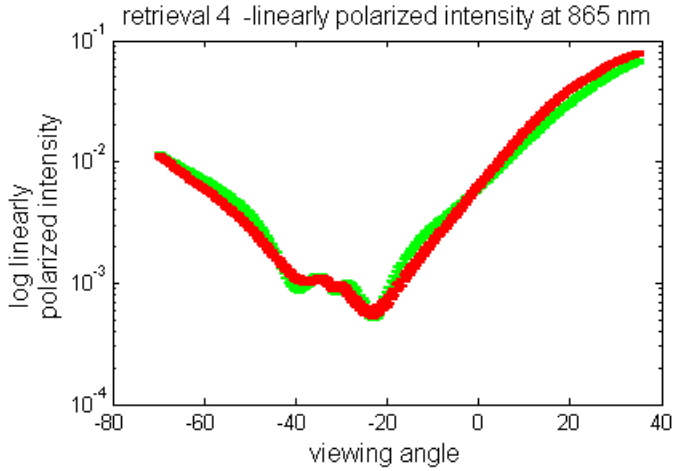

RSP file #22 - fit of linearly polarized intensity RSP measurements (continue)

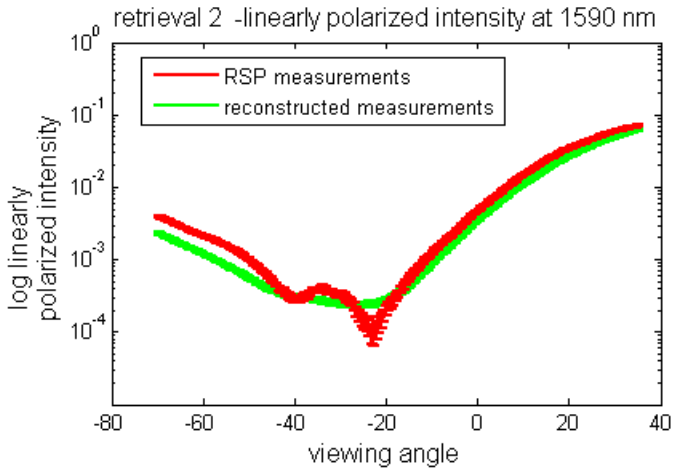

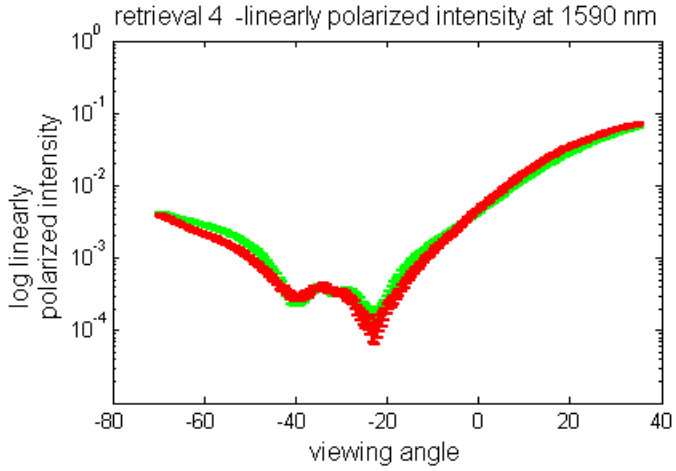

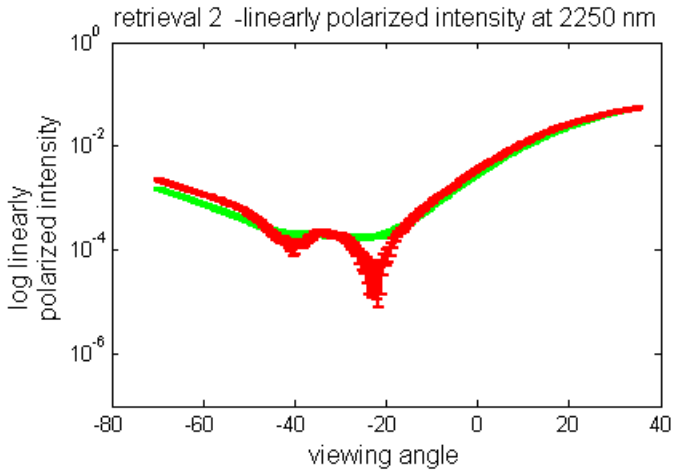

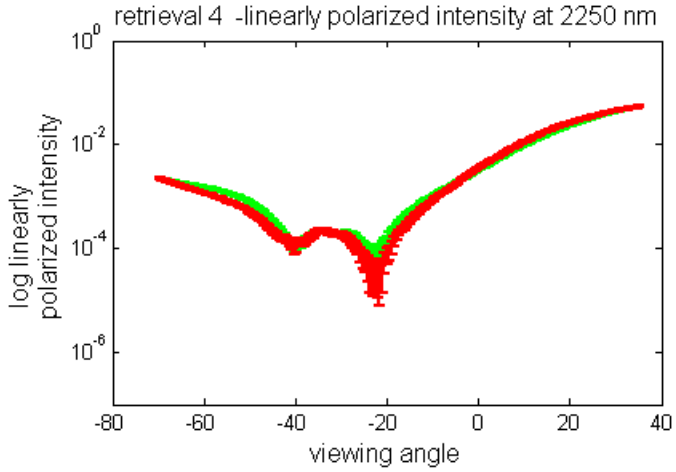

RSP file #51 - fit of total intensity RSP measurements

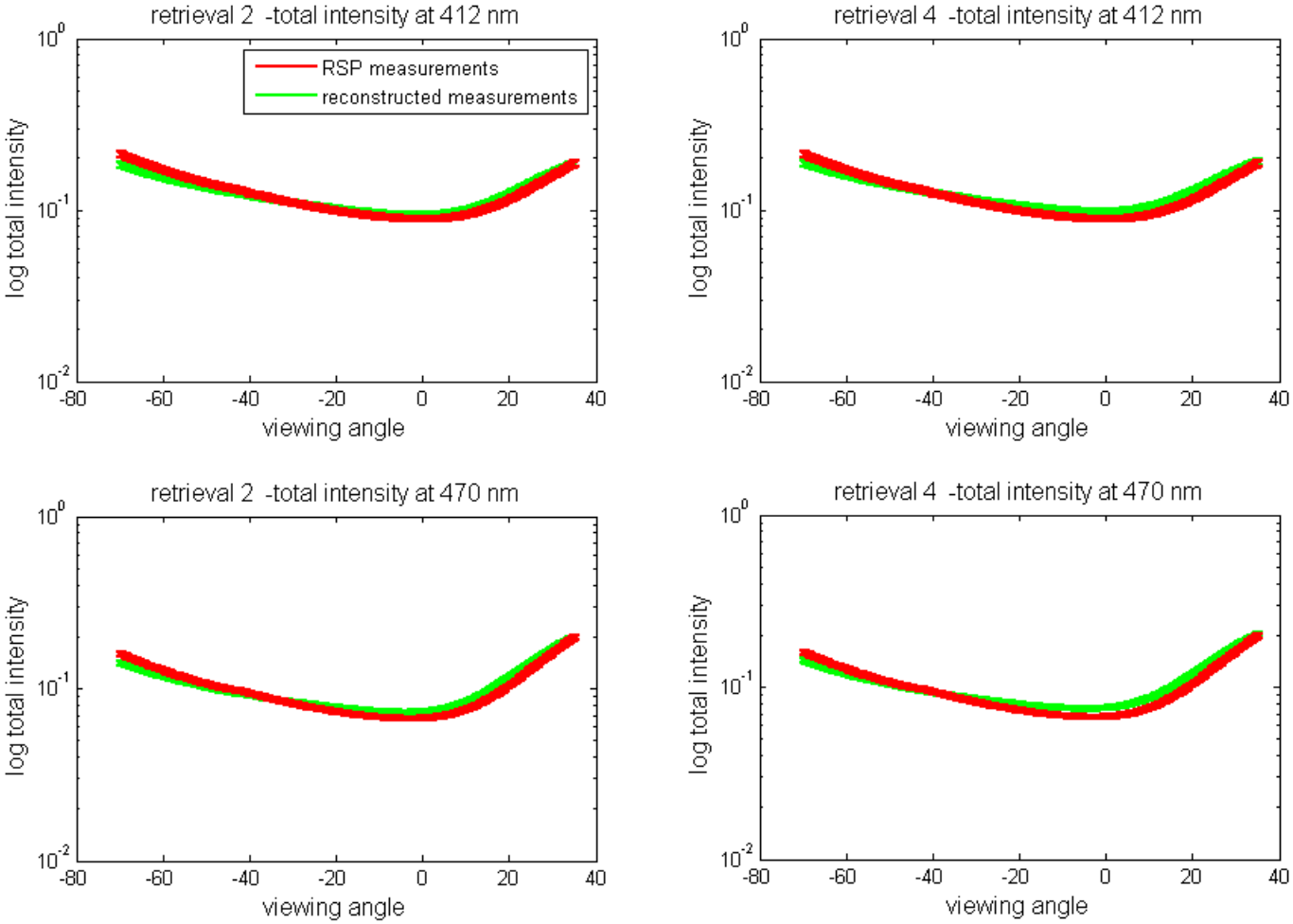

RSP file #51 - fit of total intensity RSP measurements (continue)

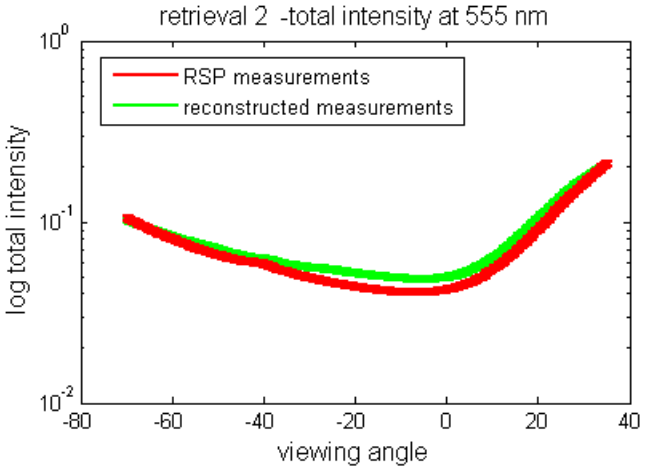

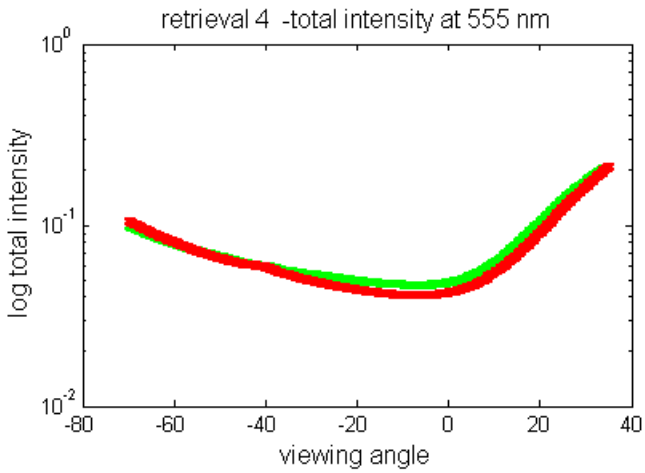

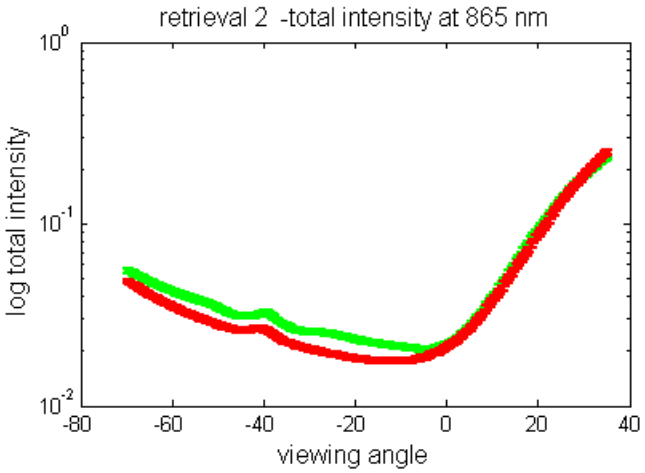

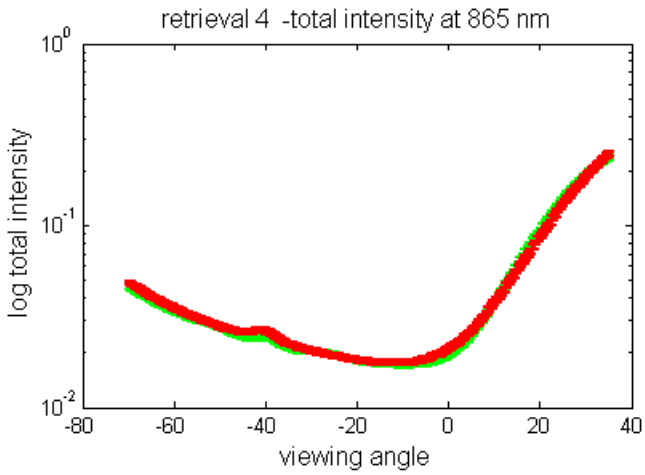

RSP file #51 - fit of total intensity RSP measurements (continue)

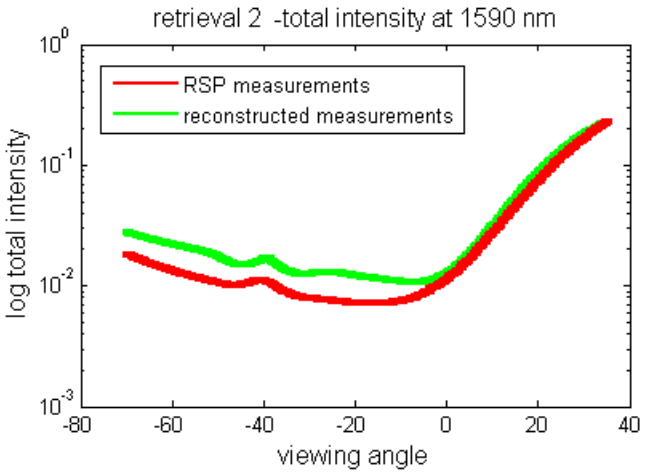

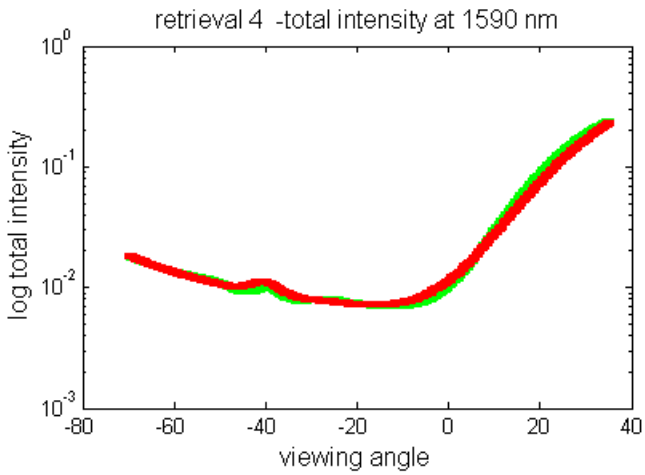

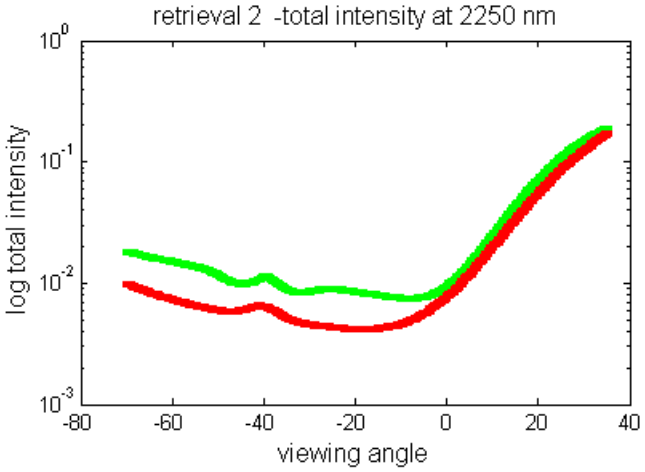

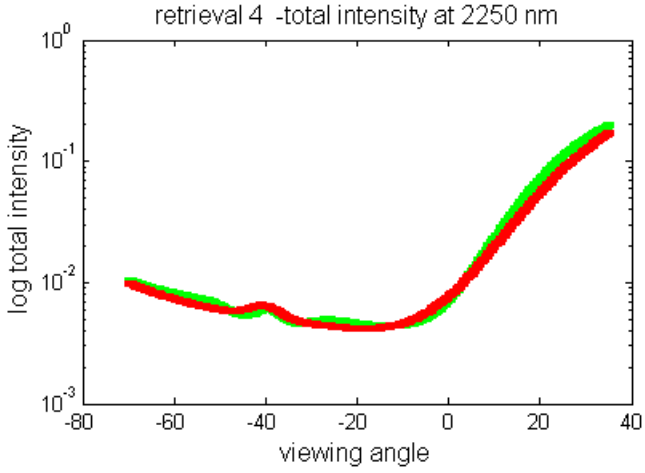

RSP file #51 - fit of linearly polarized intensity RSP measurements

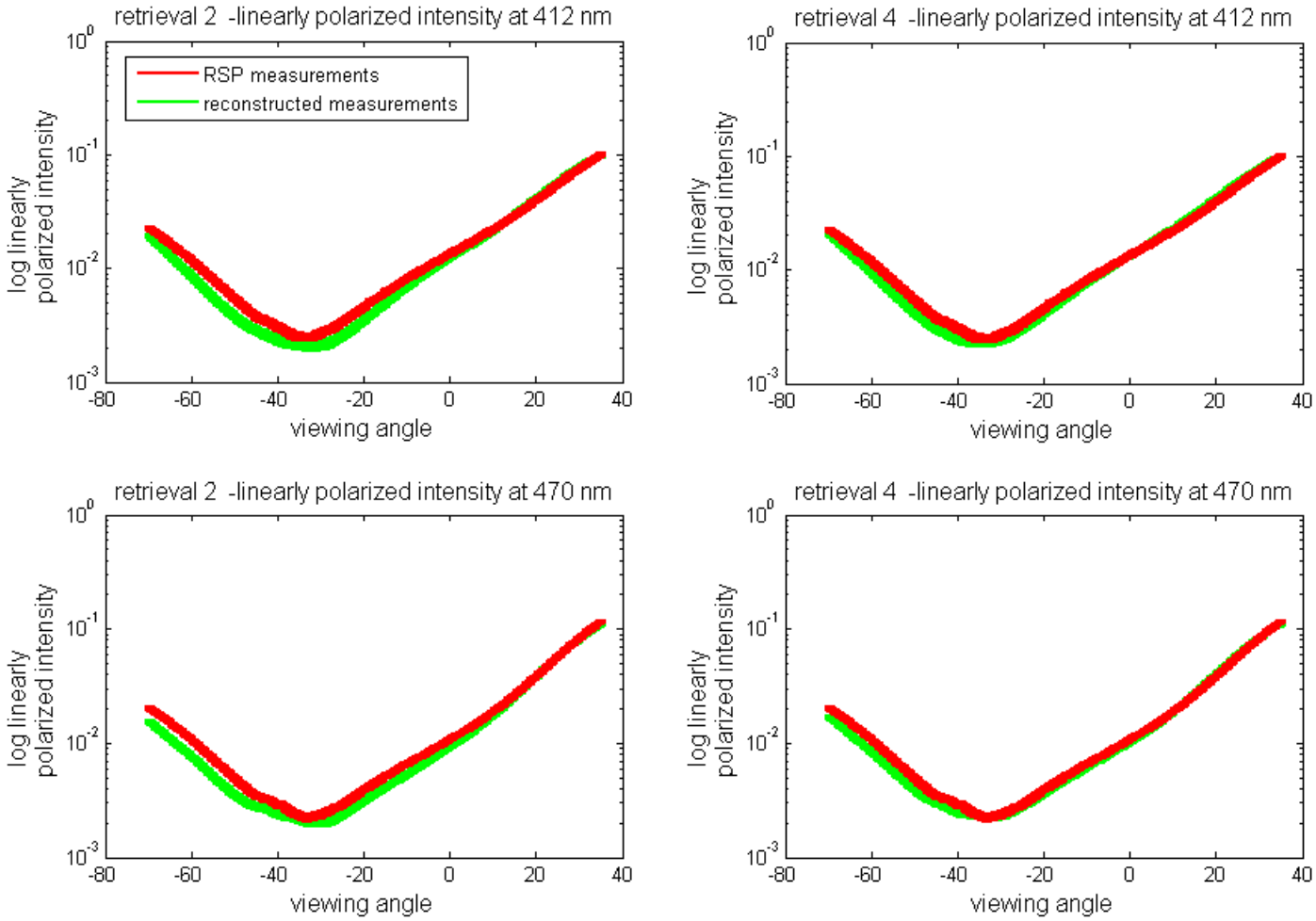

RSP file #51 - fit of linearly polarized intensity RSP measurements (continue)

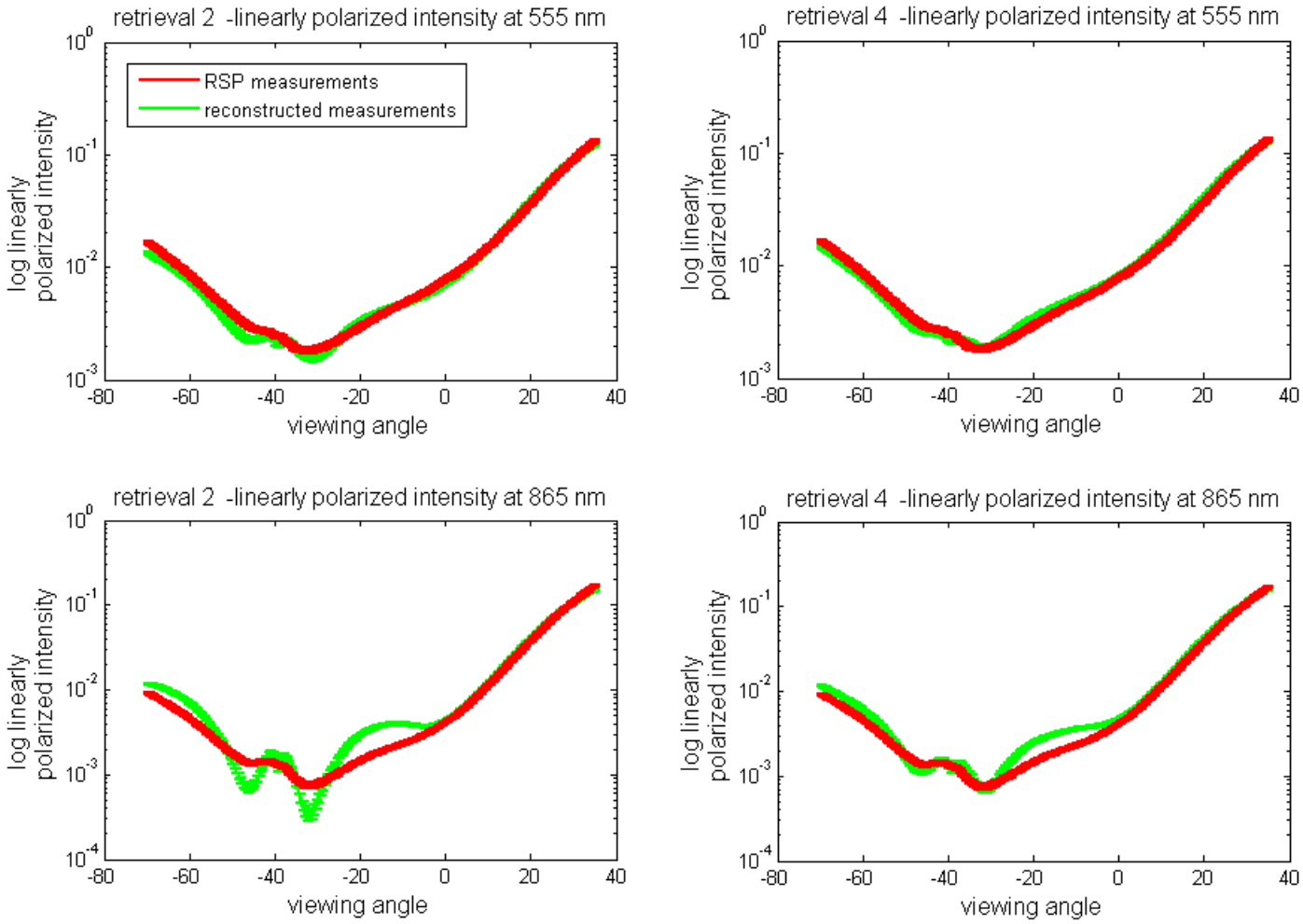

RSP file #51 - fit of linearly polarized intensity RSP measurements (continue)

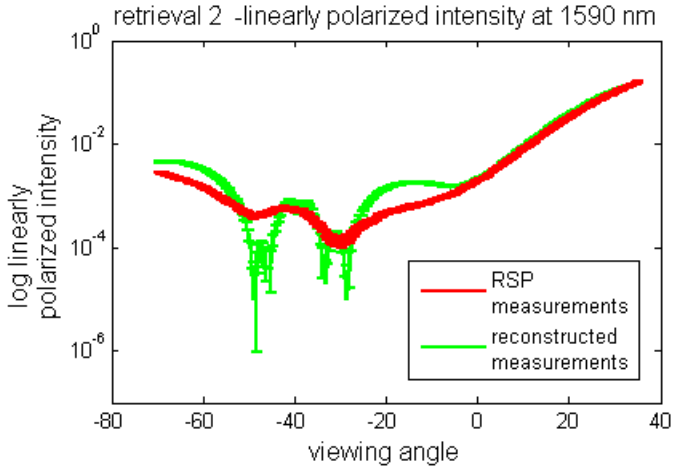

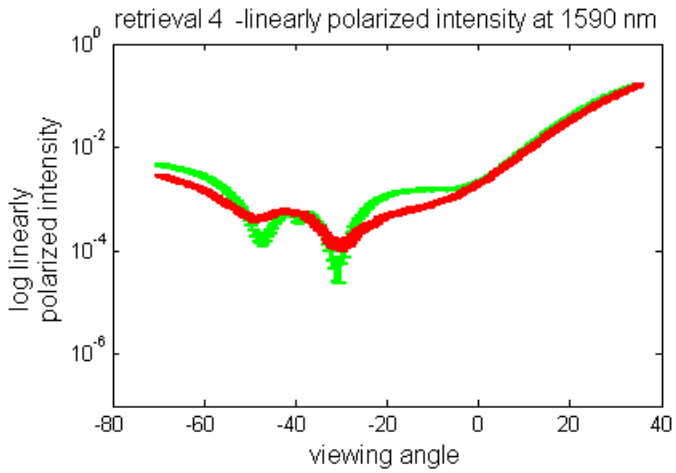

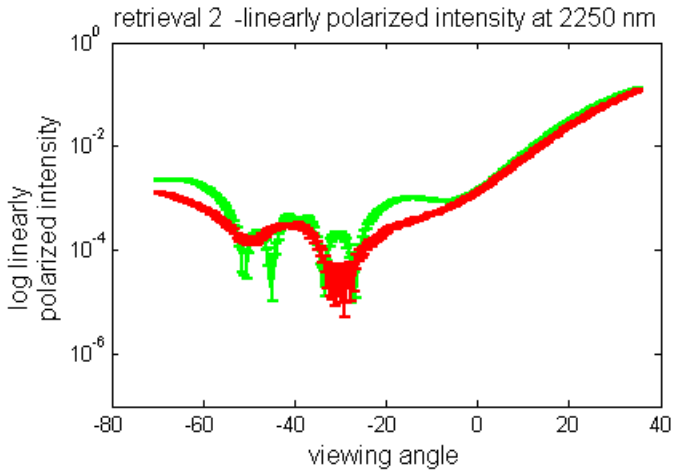

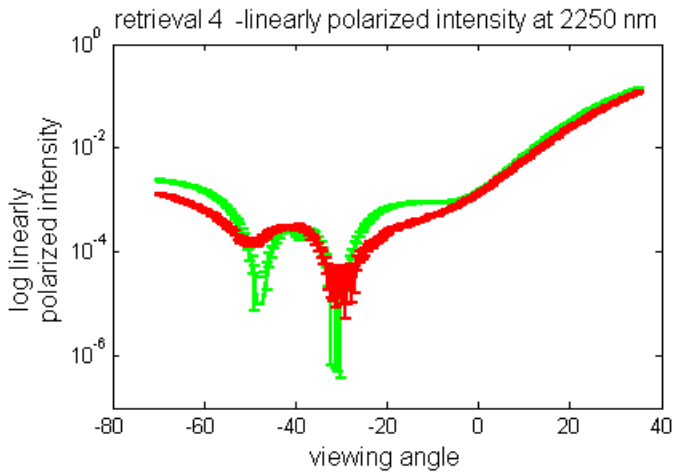

Bibliography

Aires, F., C. Prigent, W.B. Rossow and M. Rothstein (2001), A neural network approach including first guess for retrieval of atmospheric water vapor, cloud liquid water path, surface temperature, and emissivities over land from satellite microwave observations, *J. Geoph. Res., 106*, 14887-14907.

Aires, F., W.B. Rossow and A. Chédin (2002), Rotation of EOFs by the Independent Component Analysis: Toward a Solution of the Mixing Problem in the Decomposition of Geophysical Time Series, *J. Atmos. Sci., 59*, 111–123.

Aires, F., C. Prigent, and W.B. Rossow (2004), Neural network uncertainty assessment using Bayesian statistics: A remote sensing application, *Neural Comput., 16*, 2415-2458.

Anderson, T., R.J. Charlson, N. Bellouin, O. Boucher, M. Chin, S.A. Christopher, J. Haywood, Y.J. Kaufman, S. Kinne, J.A. Orgen, L.A. Remer, T. Takemura, D. Tanré, O. Torres, C.R. Trepte. B.A. Wielicki, D.M. Winker and H. Yu (2005), An "A-Train" Strategy for Quantifying Direct Climate Forcing by Anthropogenic Aerosols, *Bull. Amer. Meteor. Soc., 86***,** 1795–1809

Bergstrom, R.W., K.S. Schmidt, O. Coddington, P. Pilewskie, H. Guan, J.M. Livingston, J. Redemann and P.B. Russell (2010), Aerosol spectral absorption in the Mexico City area: results from airborne measurements during MILAGRO/INTEX B, *Atmos. Chem. Phys., 10*, 6333-6343.

Born, M. and E. Wolf (1959), *Principles of Optics*, Pergamon Press, New York.

Cairns, B., L.D. Travis and E.E. Russell (1999), Research Scanning Polarimeter: Calibration and ground-based measurements, *Proc. SPIE, 3754*, 186-197, Denver.

Chowdhary, J., B. Cairns, M. I. Mishchenko and L. D. Travis (2001), Retrieval of aerosol properties over the ocean using multispectral and multiangle photopolarimetric measurements from the Research Scanning Polarimeter, *Geophys. Res. Lett., 28*, 234-246.

Chowdhary, J., B. Cairns, and L. D. Travis (2002), Case studies of aerosol retrievals from multi-angle, multi-spectral photo-polarimetric remote sensing data, *J. Atmos. Sci.*, 383-397.

Chowdhary, J., B. Cairns, M. I. Mishchenko, P.V. Hobbs, G.F. Cota, J. Redemann, K. Rutledge, B.N. Holben and E. Russell (2005), Retrieval of aerosol scattering and absorption properties from photopolarimetric observations over the ocean during CLAMS experiment, *J. Atmos. Sci., 62*, 1093-1117.

Chowdhary, J., B. Cairns, and L. D. Travis (2006), Contribution of water-leaving radiances to multiangle, multispectral polarimetric observations over the open oceans: Bio-optical model results for Case I waters, *Appl. Opt., 45*, 5542-5567.

Chowdhary, J., B. Cairns, F. Waquet, K. Knobelspiesse, M. Ottaviani, J. Redemann, L. Travis and M. Mishchenko (2011), Sensitivity of multiangle, multispectral polarimetric remote sensing over open oceans to water-leaving radiance: Analyses of RSP data acquired during the MILAGRO campaign, *Remote Sens. Environ.*, submitted.

Cox, C. and W. Munk (1954), The measurements of the roughness of the sea surface from photographs of the sun's glitter, *J. Opt. Soc. Am., 44*, 838-850.

Cybenko, G. (1989), Approximation by superpositions of a sigmoidal function, *Math. Control Signals Syst., 2*, 303-314.

De Haan, J.F., P.B. Bosma and J.W. Hovenier (1987), The adding method for multiple scattering calculations of polarized light, *Astron. Astrophys., 183*, 371-391.

Deuzé, J.L., P. Goloub, M. Herman, A. Marchand, G. Perry, S. Susana and D. Tanré (2000), Estimate of the aerosol properties over the ocean with POLDER, *J. Geophys. Res., 105(D12)*, 15329–15346.

Deuzé, J.L., F.M. Bréon, C. Devaux, P. Goloub, M. Herman, B. Lafrance, F. Maignan, A. Marchand, F. Nadal, G. Perry and D. Tanré (2001), Remote sensing of aerosols over land surfaces from POLDER-ADEOS-1 polarized measurements, *J. Geophys. Res., 106*, 4913–4926.

Diner, D.J., B. Cairns and J. Vanderlei Martins (2010), Decadal Survey Tier 2 Mission Study Summative Progress Report: ACE Polarimeter Development, http://dsm.gsfc.nasa.gov/ace/documents/ACE_Report11_Polarimeter_v6.pdf

Doerffer R. and H. Schiller (2008), MERIS Regional coastal and lake case 2 water project - atmospheric correction ATBD, GKSS research center 21502 Geesthacht, version 1.0. May 2008.

Dubovik, O., B. Holben, T.F. Eck, A. Smirnov, Y.J. Kaufman, M.D. King, D. Tanré and I. Slutsker (2002), Variability of absorption and optical properties of key aerosol types observed in worldwide locations, *J. Atmos. Sci.*, *59*, 590-608.

Dubovik, O. (2004), Optimization of numerical inversion in photopolarimetric remote sensing, *Photopolarimetry in Remote Sensing*, edited by G. Videen, Y. Yatskiv, and M. Mishchenko, 65-106, Springer, New York.

Dubovik, O., A. Sinyuk, T. Lapyonok, B.N. Holben, M. Mishchenko, P. Yang, T.F. Eck, H. Volten, O. Munoz, B. Veihelmann, W.J. van der Zande, J.F. Leon, M. Sorokin and I. Slutsker (2006),

Application of spheroid models to account for aerosol particle nonsphericity in remote sensing of desert dust, *J. Geophys. Res.*, *111*, D11208.

EPA (1996), Air quality criteria for particulate matter. Office of Research and Development, EPA/600/P-95/001aF, Volumes I-III.

Gasteiger, J., S. Groß, V. Freudenthaler and M. Wiegner (2011), Volcanic ash from Iceland over Munich: mass concentration retrieved from ground-based remote sensing measurements, *Atmos. Chem. Phys., 11*, 2209-2223.

Gelman, A.B., J.S. Carlin, H.S. Stern and D.B. Rubin (1995), *Bayesian data analysis*, Chapman & Hall, London.

Gordon, H.R., O.B. Brown and M.M. Jacobs (1975), Computed relationships between inherent and apparent optical properties of a flat homogeneous ocean, *Appl. Opt. 14*, 417-427.

Hair, J.W., C.A. Hostetler, A.L. Cook, D.B. Harper, R.A. Ferrare, T.L. Mack, W. Welch, L.R. Izquierdo and F.E. Hovis (2008), Airborne High Spectral Resolution Lidar for profiling aerosol optical properties, *Appl. Opt., 47*, 6734-6752.

Hansen, J.E. (1969), Radiative transfer by doubling very thin layers, *Astrophys. J., 155*, 565-573.

Hansen, J.E. (1971a), Multiple scattering of polarized light in planetary atmospheres. Part I. The doubling method, *J. Atmos. Sci., 28*, 120-125.

Hansen, J.E. (1971b), Multiple scattering of polarized light in planetary atmospheres. Part II. Sunlight reflected by terrestrial water clouds, *J. Atmos. Sci., 28*, 1400-1426.

Hansen, J.E., and L.D. Travis (1974), Light scattering in planetary atmospheres, *Space Sci. Rev., 16,* 527-610.

Hansen, J.E., W. Rossow, B. Carison, A. Lacis, L. Travis, A. Del Genio, I. Fung, B. Cairns, M. Mishchenko and Mki. Sato (1995), Low-cost long-term monitoring of global climate forcings and feedbacks, *Climatic Change, 31*, 247-271.

Hansen, J.E., A. Lacis and V. Oinas (1997), Global warming in the twenty-first century: An alternative scenario, *Proc. Natl. Acad. Sci. USA, 97*, 9875-9880.

Haykin, S. (1999), *Neural Networks: a comprehensive foundation* (2nd edition), Prentice-Hall, NJ.

Hecht, E. (2001). *Optics* (4th Edition), Addison Wesley, Reading, Massachusetts.

Hornik, K., M. Stinchcombe and H. White (1989), Multilayer feedforward networks are universal approximators, *Neural Networks, 2*, 359-366.

Hovenier, J.W. (1971), Multiple scattering of polarized light in planetary atmospheres, *Astron. Astrophys., 13*, 7-29.

Hovenier, J.W., C. van der Mee and H. Domke (2004), *Transfer of polarized light in planetary atmospheres –basic concepts and practical methods*. Springer, Berlin.

Husar, R.B., J.M. Prospero and L.L. Stowe (1997), Characterization of tropospheric aerosols over the oceans with the NOAA advanced very high resolution radiometer optical thickness operational product, *J. Geophys. Res., 102(D14)*, 16889–16910.

Ignatov, A. and L. Stowe (2002), Aerosol retrievals from individual AVHRR channels. Part I: Retrieval algorithm and transition from Dave to 6S Radiative Transfer Model, *J. Atmos. Sci., 59*, 313–334.

IPCC (2007), *Climate Change 2007 - The Physical Science Basis : Contribution of the Working Group I to the Fourth Assessment Report of the IPCC*, Cambridge University Press, New York, NY.

Jolliffe, I.T. (2002), *Principal component analysis* (2nd edition), Springer, New York.

Kahn, R., P. Banerjee and D. McDonald (2001), Sensitivity of multiangle imaging to natural mixtures of aerosols over ocean, *J. Geophys. Res., 106(D16)*, 18219–18238.

Kaufman, Y.J., D. Tanré, L.A. Remer, E.F. Vermote, A. Chu and B.N. Holben (1997), Operational remote sensing of tropospheric aerosols over the land from EOS-MODIS, *J. Geophys. Res., 102(D14)*, 17051–17068.

Knobelspiesse, K.D. (2010), *Atmospheric Aerosol Property Retrieval with Scanning Polarimeters*, Ph.D. thesis. Columbia University.

Knobelspiesse, K., B. Cairns, M. Ottaviani, R. Ferrare, J. Hair, C. Hostetler, M. Obland, R. Rodgers, J. Redemann, Y. Shinozuka, A. Clarke, S. Freitag, S. Howell, V. Kapustin and C. McNaughton (2011a), Combined retrievals of boreal forest fire aerosol properties with a polarimeter and lidar, *Atmos. Chem. Phys.* doi:10.5194/acp-11-7045-2011.

Knobelspiesse, K., B. Cairns, J. Redemann, R.W. Bergstrom and A. Stohi (2011b), Simultaneous retrieval of aerosol and cloud properties during the MILAGRO field camapaign, *Atmos. Chem. Phys.* doi:10.5194/acp-11-7045-2011.

Lohmann, U. and C. Hoose (2009), Sensitivity studies of different aerosol indirect effects in mixed-phase clouds, *Atmos. Chem. Phys., 9*, 8917–8934.

Martonchik, J.V., D.J. Diner, R. Kahn and B. Gaitley (2004), Comparison of MISR and AERONET aerosol optical depths over desert sites, *Geophys. Res. Lett., 31*, L16102.

Mobley, C.D. (1994), *Light and Water: Radiative Transfer in Natural Waters*, Academic Press, San Diego.

Mishchenko, M.I., L.D. Travis and D.W. Mackowski (1996), T-Matrix computations of light scattering by nonspherical particles: a review, *J. Quant. Spectrosc. Radiat. Transfer, 55,* 535-575.

Mishchenko, M.I., and L.D. Travis (1997a), Satellite retrieval of aerosol properties over the ocean using polarization as well as intensity of reflected sunlight, *J. Geophys. Res., 102,* 16989-17013.

Mishchenko, M.I., and L.D. Travis (1997b), Satellite retrieval of aerosol properties over the ocean using polarization as well as intensity of reflected sunlight: Effect of instrumental errors and aerosol absorption, *J. Geophys. Res., 102,* 13543-13553.

Mishchenko, M.I., L.D. Travis, R.A. Kahn, and R.A. West (1997c), Modeling phase functions for dustlike tropospheric aerosols using a mixture of randomly oriented polydisperse spheroids. *J. Geophys. Res.*, *102*, 16831-16847.

Mishchenko, M.I., L.D. Travis and A.A. Lacis (2002), *Scattering, Absorption, and Emission of Light by Small Particles*, Cambridge University Press.

Mishchenko, M.I., B. Cairns, J.E. Hansen, L.D. Travis, R. Burg, Y.J Kaufman, J.V. Martins and E.P. Shettle (2004), Monitoring of aerosol forcing of climate from space: Analysis of measurement requirements, *J. Quant. Spectrosc. Radiat. Transfer, 88*, 149-161.

Mishchenko, M.I., L.D. Travis and A.A. Lacis (2006), *Multiple Scattering of Light by Particles: Radiative Transfer and Coherent Backscattering*, Cambridge University Press.

Mishchenko, M.I., B. Cairns, G. Kopp, C.F. Schueler, B.A. Fafaul, J.E. Hansen, R.J. Hooker, T. Itchkawich, H.B. Maring and L.D. Travis (2007), Accurate monitoring of terrestrial aerosols and total solar irradiance: Introducing the Glory mission, *Bull. Amer. Meteorol. Soc., 88*, 677-691.

Molina, L.T., S. Madronich, J.S. Gaffney, E. Apel, B. de Foy, J. Fast, R. Ferrare, S. Herndon, J.L. Jimenez, B. Lamb, A.R. Osornio-Vargas, P. Russell, J.J. Schauer, P.S. Stevens and M. Zavala (2010), An overview of the MILAGRO 2006 campaign: Mexico City emissions and their transport and transformation, *Atmos. Chem. Phys. Discuss., 10*, 7819-7983.

Morel, A., L. Prieur (1977), Analysis of variations in ocean color, *Limnology and Oceanography, 22*, 709-722.

Morel, A., S. Maritorena (2001), Bio-optical properties of oceanic waters: A reappraisal, *J. Geophys. Res., 106*, 7163-7180.

Omar, A.H., D.M. Winker, C. Kittaka, M.A. Vaughan, Z. Liu, Y. Hu, C.R. Trepte, R.R. Rogers, R.A. Ferrare, K.P. Lee, R.E. Kuehn and C.A. Hostetler (2009), The CALIPSO automated aerosol classification and Lidar ratio selection algorithm, *J. Atmos. Oceanic Technol., 26*, 1994-2014.

Penndorf, R. (1957), Tables of the refractive index of standard air and the Rayleigh scattering coefficient for the spectral region between 0.2 and 20.0 μ and their application to atmospheric optics, *J. Opt. Soc. Amer., 47*, 176-182.

Pope, R.M. and E.S. Fry (1997), Absorption spectrum (380-700 nm) of pure water, II, Integrating cavity measurements, *Appl. Opt., 36*, 8710-8723.

Prieur, L. (1976), Transfert radiatif dans les eaux de meur, D. Sc. Thesis, Pierre et Marie Curie Univ., Paris.

Purcell, E.M. and C.R. Pennypacker (1973), Scattering and absorption of light by nonspherical dielectric grains, *Astrophys. J., 186*, 705-714.

Rao, C.R.N., L. Stowe and P. McClain (1989), Remote sensing of aerosols over oceans using AVHRR data: Theory, practice and applications, *International Journal of Remote Sensing*, *10*, 743-749.

Redemann, J., Q. Zhang, J. Livingston, P. Russell, Y. Shinozuka, A. Clarke, R. Johnson and R. Levy (2009), Testing aerosol properties in MODIS Collection 4 and 5 using airborne sunphotometer observations in INTEX-B/MILAGRO, *Atmos. Chem. Phys. Discuss., 9*, 11753-11781.

Riedmiller, M. and H. Braun (1993), A direct adaptive method for faster backpropagation learning: the RPROP algorithm, *Proc. of the IEEE Int. Conf. on Neur. Net. (ICNN), vol. 1*, 586-591

Rodgers, C.D. (2000), *Inverse methods for atmospheric sounding: Theory and practice,* World Scientific.

Russell, P., J. Redemann, J. Livingston, Q. Zhang, S. Ramirez, B. Cairns, C. Gatebe, O. Torres, M. King, L. Remer, B. Holben, P. Pilewskie, S. Schmidt, R. Dominguez, W. Gore, R. Kahn, C. Hostetler, J. Hair, R. Ferrare, E. Browell, A. Clarke, Y. Shinozuka, C. McNaughton (2007), An overview of J-31 measurements during the INTEX-B/MILAGRO campaign, Second MILAGRO Science Meeting, 15 May 1007, Mexico City.

Seinfeld J.H. and S.N. Pandis (1998), *Atmospheric Chemistry and Physics: From Air Pollution to Climate Change*, 1st edition, J. Wiley, New York.

Starr, D.O.'C., "NASA's Aerosol-Cloud-Ecosystems (ACE) Mission", in *Hyperspectral Imaging and Sounding of the Environment*, OSA Technical Digest (CD) (Optical Society of America, 2011), paper HMA4, http://www.opticsinfobase.org/abstract.cfm?URI=HISE-2011-HMA4

Szykman, J. J., C. Kittaka, R. Bradley Pierce, J. Al-Saadi, D.O. Neil, J. White, D. A. Chu, and L.A. Remer (2004), Use of MODIS Satellite Observations in Near-Real-Time to Improve Forecast of Fina Particulate Matter (PM2.5): An Experimental Forecast Tool, 2004 National Air Quality, Baltimore, MD, February 22-25, 2004

Tang, I.N. and H.R. Munkelwitz (1996), Chemical and size effects of hydroscopic aerosols on light scattering coefficients. *J. Geophys. Res., 101*, 19245-19250.

Tanré, D., Y.J. Kaufman, M. Herman and S. Mattoo (1997) Remote sensing of aerosol properties over oceans using the MODIS/EOS spectral radiances, *J. Geophys. Res., 102(D14)*, 16971–16988.

Torres, O., P.K. Bhartia, J.R. Herman, A. Sinyuk, P. Ginoux and B. Holben (2002), A long-term record of aerosol optical depth from TOMS: Observations and comparison to AERONET measurements, *J. Atmos. Sci., 59*, 398–413.

Twomey, S. (1980), Cloud nucleation in the atmosphere and the influence of nucleus concentration levels in atmospheric physics, *J. Phys. Chem., 84*, 1459-1463.

Van de Hulst, H.C. (1957), *Light Scattering by Small Particles*. Wiley, New York.

Van de Hulst, H.C. (1963), A new look at multiple scattering, Tech. Rept., Goddard Institute for Space Studies, Nasa, New York.

Van de Hulst, H.C. (1980), *Multiple light scattering*. Academic Press, New York.

Waquet, F., B. Cairns, K. Knobelspiesse, J. Chowdhary, L.D. Travis, B. Schmid and M.I. Mishchenko (2009), Polarimetric remote sensing of aerosols over land, *J. Geophys. Res., 114*, D01206.

Yang, P. and K.N. Liou (1996), Geometric-optics-equation method for light scattering by nonspherical ice particles, *Appl. Opt., 35*, 6568-6584.

Yee, K. (1966), Numerical solution of initial boundary value problems involving maxwell's equations in isotropic media, *IEEE Trans. Ant. Propag., 14*, 302-307.

Zhang, H., R.M. Hoff and J.A. Engel-Cox (2009) The relation between Moderate Resolution Imaging Spectroradiometer (MODIS) aerosol optical depth and PM2.5 over the United States: a geographical comparison by EPA regions, *J.Air & Waste Manage. Assoc., 59*, 1358-1369.

Zeng, X., M.A., Brunke, M. Zhou, C. Fairfall, N.A. Bond and D.H. Lenschow (2004), Marine atmospheric boundary layer height over the eastern Pacific: Data analysis and model evaluation, *J. of Clim., 17,* 4159-4170.